OPTIMAL KINETIC ENERGY RECOVERY ALGORITHMS FOR ELECTRIC MACHINES

A Dissertation
Presented to
The Academic Faculty

By

Aravind Samba Murthy

In Partial Fulfillment
of the Requirements for the Degree
Doctor of Philosophy in the
School of Electrical and Computer Engineering

Georgia Institute of Technology

August 2017

OPTIMAL KINETIC ENERGY RECOVERY ALGORITHMS FOR ELECTRIC MACHINES

Approved by:

Dr. David G Taylor, Advisor
School of Electrical and Computer Engineering
Georgia Institute of Technology

Dr. Thomas Habetler
School of Electrical and Computer Engineering
Georgia Institute of Technology

Dr. Yorai Wardi
School of Electrical and Computer Engineering
Georgia Institute of Technology

Dr. Nader Sadegh
School of Mechanical Engineering
Georgia Institute of Technology

Dr. Ronald Harley
School of Electrical and Computer Engineering
Georgia Institute of Technology

Date Approved: June 21, 2017

The present is theirs; the future, for which I really worked, is mine.

Nikola Tesla

To my loving wife, Rajatha.

ACKNOWLEDGEMENTS

This dissertation would not have been possible without the guidance and the help of several individuals who in one way or another contributed and extended their valuable assistance in the preparation and completion of this study.

First and foremost, my utmost gratitude to my advisor, Dr. David G Taylor, whose continuous guidance and support has been invaluable to me. His patience, motivation, enthusiasm, and immense knowledge has helped me during the research and writing of this dissertation. He gave me the freedom to pursue my own ideas and I could not have asked for a better advisor and mentor. It was certainly a pleasure working with him. I have been greatly influenced by his discipline and dedication to his work, both in teaching and research, and look up to him as a role model.

I would like to acknowledge support from Texas Instruments for funding this research. I would also like to thank Dave Magee, the project liaison from Texas Instruments, for his insights and guidance during this research project. Our monthly project review meetings with Dave were instrumental in keeping this research on track. I would also like to thank Prof. Yorai Wardi and Prof. Thomas Habetler for serving on my reading committee and providing valuable feedback during the proposal phase of this research. I also thank ThyssenKrupp Elevators for supporting the final phase of this research.

I would like to thank my close friends Shweta Srinivaz, Naveen Brahmi, Amritha-Alladi Joesph, Jis Joseph, and Maurice Cousar for their friendship and support. I would also like to thank the 2018 Scheller College of Business MBA cohort for being great classmates and friends. A special thanks to Barbara Lindquist from the Scheller MBA Career Services office for her guidance and advisement during my job search.

Finally, and most importantly, I would acknowledge the ones closest to my heart, my family. My wife, Rajatha, has been my source of strength during these six long years of graduate school and I could not have achieved this without her patience, love, and support.

This dissertation is as much hers as it is mine. My mother, who is the strongest woman I know, I owe her my everything. I would like to thank my sister and grandmother for always believing in me and being pillars of emotional support throughout my life. I would like to thank my father for inspiring me to be the best. I would also like to thank my wife's grandfather, N.B. Bhat, for his words of encouragement and wisdom during these years.

TABLE OF CONTENTS

LIST OF TABLES

LIST OF FIGURES

SUMMARY

Electric machines are used to accelerate and decelerate mechanical loads. During deceleration events, a significant portion of stored kinetic energy can be converted into electrical form for storage in a battery or capacitor, through the use of regenerative braking. By reducing the net energy flow out of the electric power source, regenerative braking is one of the mechanisms by which the overall efficiency of an application can be improved. This research details the development, analysis, and implementation of optimal kinetic energy recovery algorithms for surface permanent-magnet synchronous machines, interior permanent-magnet synchronous machines and induction machines. Braking events over user-defined time-interval lengths that include both stopping and slowing down to non-zero speeds are considered. Mechanical loads that include viscous friction, Coulomb friction, and aerodynamic drag are considered in the development of the algorithms. The trade-off between braking time and energy recovery is clearly illustrated and closed-form expressions for the optimal length of the braking time-interval are developed wherever possible to help control engineers design optimal braking trajectories. A universal optimal kinetic energy recovery algorithm is developed for all three types of electric machines under constant-flux operation. The theory is extended to include braking with final position constraints and braking under variable-flux methods of operation such as maximum-torque-per-amp and flux-weakening. The optimal control solutions are implemented using standard feedback controllers and are validated through simulations and experiments.

CHAPTER 1
INTRODUCTION AND BACKGROUND

The world's consumption of electricity is growing every day. The world total electricity consumption in the year 2015 was about 21.5 trillion kWh [1], with the United States accounting for 3.8 trillion kWh [2]. This demand is steadily increasing year by year with a projected 25% increase by the year 2040 [2]. About 42% of the world's electricity is used by industries [1] and 40% of this is used to power electric motors [3]. Residential and commercial sectors together use about 56% of the world's electricity [1] and electric motors account for about 25% of that power [4]. Therefore, electric motors contribute to about 31% of the world's electricity consumption. A study in [3] shows that there are about 300 million industrial electric motors being used worldwide today, not including the millions of electric machines that are installed in electric and hybrid-electric vehicle powertrains, and a significant number of them are used in start-stop or variable-speed applications. This sort of operation involves accelerating and decelerating mechanical loads. Through the use of efficient motor control systems, about 1.72 trillion kWh of electricity could potentially be saved annually [4].

Electric machines have two main modes of operation, i.e. motoring and braking. The machine is said to produce motoring torque if mechanical power flows out of its mechanical port, and the machine is said to produce braking torque if mechanical power flows into its mechanical port. The load coupled to the machine's mechanical port may consist of inertia loading and/or torque loading (e.g. due to friction, gravity or other active torque sources). In traction applications, such as electric vehicles and trains, the electric machine would be motoring during intervals of cruising or acceleration, and it would be braking during intervals of deceleration.

A more complete classification of electric machine operating modes is possible if the

direction of electric power flow is considered. Motoring always requires that electric power flow into the machine's electrical port, since the source of mechanical power for motoring is the converted electric power. On the other hand, braking can occur in two distinct ways: if electric power flows out of the machine's electrical port when braking, then this mode of operation is referred to as regenerative braking; if electric power flows into the machine's electrical port when braking, then this mode of operation is referred to as non-regenerative braking. Each of these operating modes is visually summarized in Figure 1.1.

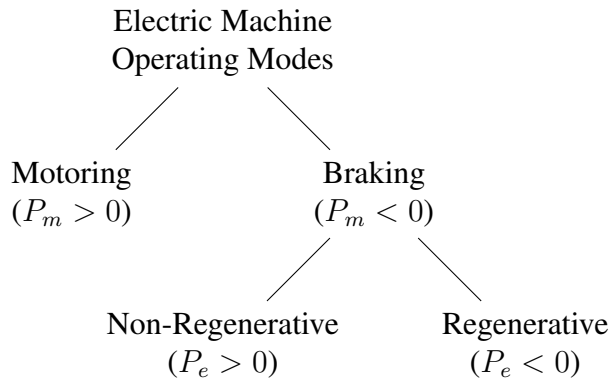

Figure 1.1: Summary of electric machine operating modes, where $P_m > 0$ indicates mechanical power flow out of the machine, and $P_e > 0$ indicates electric power flow into the machine.

Through the use of regenerative braking, a significant portion of the kinetic energy removed from an inertia load due to deceleration may be converted into electrical form and stored in a battery or capacitor. By reducing the net energy flow out of the electric power source, regenerative braking is one of the mechanisms by which the overall efficiency of an application can be improved. This translates directly into energy savings for the consumer and, in the case of hybrid-electric vehicles, this translates into more watt-hours remaining in the vehicle's electrical energy storage system, thereby increasing the distance that the vehicle can travel on a "full charge" and also improving the fuel economy (miles/gallon).

In addition to providing energy savings, regenerative braking also helps reduce the wear and tear associated with mechanical brakes that are used to assist the braking operation in applications such as elevators, electric subway trains, electric and hybrid-electric vehicles.

As the electric machine braking assists the braking event, the mechanical friction brake is subject to less wear and hence its components last longer.

1.1 Problem Definition

As discussed previously, regenerative braking provides an opportunity to recover a significant portion of the kinetic energy stored in a moving mechanical load, thereby improving the overall efficiency of a motion control application. Consider the connection of an electric machine with a power source at its electrical terminals and a mechanical load at its mechanical port as shown in Figure 1.2. The mechanical load is characterized by an inertia coefficient, J, and friction loss component, B. The mechanical losses due to friction are proportional to the square of the rotation speed. The electric machine has losses due to resistance R that are proportional to the square of the current flowing through the machine. Assume that the load is spinning at an initial speed of ω_{r0}. The kinetic energy stored in the spinning load is

$$KE = \frac{1}{2} J \omega_{r0}^2 \tag{1.1}$$

In the absence of an external mechanical brake, the objective of bringing the rotor to a complete stop can be achieved using two distinct choices. The first choice is let the rotor freely decelerate without the application of an electric braking torque. The rotor takes a long time to come to a stop and all of the kinetic energy is lost in the form of heat due to the mechanical friction losses, with none of it being converted to electricity and returned to the electric power source. The second choice is to apply an electrical braking torque using the electric machine. In doing so, a current that is proportional to the applied braking torque flows through the machine and the mechanical power $P_m < 0$. Depending on the magnitude of losses in the electromagnetic system, the steady state electrical power can be

positive or negative according to

$$P_e = P_m + P_{\text{loss}} \tag{1.2}$$

The loss term P_{loss} is always positive regardless of whether the machine is motoring or braking. If the magnitude of losses is greater than the mechanical power, then the sign of the electric power term is positive ($P_e > 0$). As discussed earlier, this type of operation is non-regenerative in nature, i.e. electric power flows into the electric machine during the braking event. In this situation, the kinetic energy that was stored in the spinning mechanical load prior to the braking event is dissipated in the form of heat due to resistance losses in the electric machine and mechanical friction losses in the load. On the other hand, if the magnitude of the loss term is less than the mechanical power, then the sign of the electric power term is negative ($P_e < 0$). This type of braking is regenerative in nature since electric power flows out of the electric machine and into the power source. Some of the kinetic energy is lost in the electric machine resistance and mechanical load friction loss mechanisms. The kinetic energy that remains after feeding the losses is captured by the electric power source where the electricity can be stored or used to power other electrical loads.

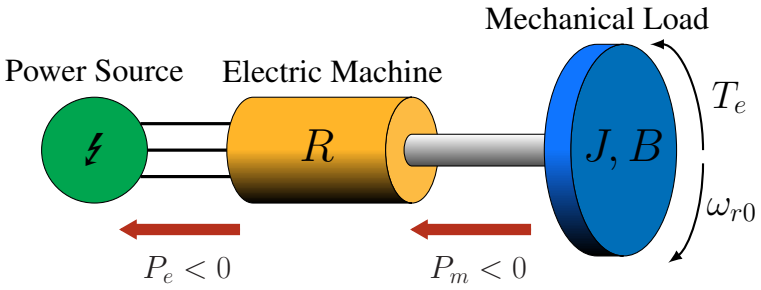

Figure 1.2: Schematic diagram showing the power flow between electrical power source, electric machine, and mechanical load.

Further investigation of the application of electrical braking torque reveals the trade-off between braking time and energy recovery. If the objective is to reach zero speed quickly,

this necessitates the application of a large braking torque and consequently larger electric machine currents. Since the electrical losses are proportional to the square of the current, this results in a large amount of energy being dissipated in the resistance of the electric machine and results in low (or zero) kinetic energy recovery. On the other hand, application of small braking torques with smaller currents results in lower energy dissipation in the machine resistance. Consequently, the rotor takes longer to come to a stop. This increases the mechanical friction losses in the load that are proportional to the square of the rotation speed magnitude and causes a large amount of energy to be dissipated in the form of heating due to friction resulting in low kinetic energy recovery. This forms the basis of the optimal control problem that is solved in detail in the subsequent chapters. By avoiding the deceleration events that are too fast (high electrical losses) or too slow (high mechanical losses), the optimal torque trajectory is one that balances the conflicting objectives of braking time and energy recovery. The optimal torque also balances the energy dissipation in the electrical and mechanical loss mechanisms such that maximum kinetic energy is recovered during the braking interval. Another key distinction that must be made relates to the concept of optimizing operation at every instant in time or optimizing operation over a time-interval. As explained in [5], the former strategy is greedy since it tends to make optimal choices at every time instant by being misled by the prospect of short-term gains resulting in a sub-optimal solution. The latter on the other hand is based on the theory of optimal control wherein the optimal control law is obtained as a result of achieving an objective (kinetic energy recovery in this case) over the entire time-interval rather than on a time-instant basis.

The key questions that are answered as a part of this research are as follows: Can kinetic energy be recovered during the braking process? If the answer is affirmative, how much of the initial kinetic energy can be recovered during the braking process? Is there a limit to the maximum kinetic energy that can be recovered? What is the limit and what factors does it depend on? Is there an ideal braking time-interval length? How can maximum kinetic

energy recovery be achieved?

1.2 Structure of Field-Oriented Control Motor Drives

Field-oriented control is a method of control in which the stator excitation inputs of an electric machine are separated into two orthogonal components, one that controls the flux and one that controls the torque [63]. The component that controls flux is aligned with the rotor's flux axis which is called the direct axis (d-axis); an orthogonal axis, associated with torque production, is called the quadrature axis (q-axis).

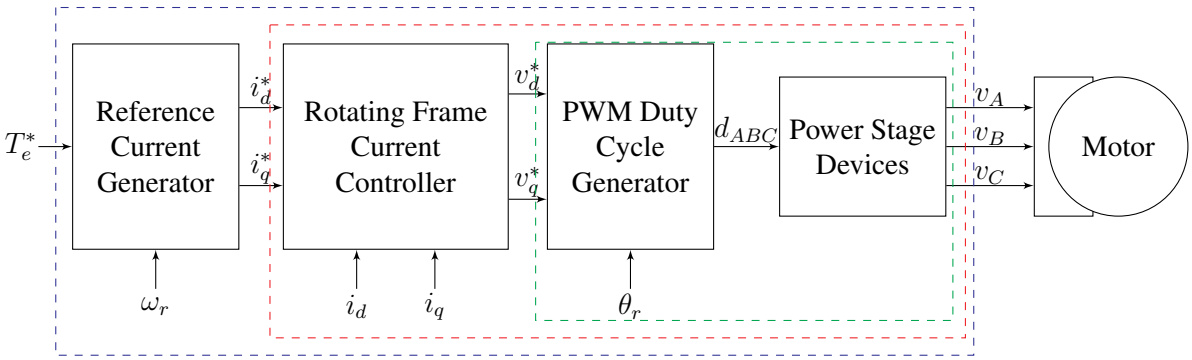

Figure 1.3: Block diagram of a field-oriented torque controller for a synchronous machine, showing various possible levels of control authority; commercial off-the-shelf equipment offers only a scalar torque command input, whereas custom-built equipment may be based on vector-valued current or voltage command inputs.

Figure 1.3 shows a block-diagram representation of a field-oriented torque controller for a synchronous machine. A torque reference command, T_e^*, is given as the input to a reference current generator block. The rotor speed ω_r (measured or estimated) is then used by the reference current generator block to determine the direct- and quadrature-axis current references, i_d^* and i_q^*; this block incorporates an algorithm that selects one reference current vector, from among an infinite number of feasible current vectors, that can achieve the requested torque at the given speed. The direct- and quadrature-axis reference currents are then fed to their respective current controllers. Measured values of the stator currents are then transformed to the direct- and quadrature-axis for use by the current controllers,

which regulate the machine's currents by producing the appropriate direct- and quadrature-axis reference voltages, v_d^* and v_q^*. The voltage reference commands, along with the rotor angle θ_r (measured or estimated), are then used to produce the appropriate PWM duty cycles, d_{ABC}, that dictate the switching of the power stage. The resulting power stage leg voltages are then applied to the stator windings to influence the current flow, and hence the torque and flux within the machine.

Most commercial drives have their control interface limited to the outer blue box shown in Figure 1.3 [7]. These drives can only accept reference torque values, and they produce the appropriate stator voltages to achieve that torque; the user has little or no control of the inner workings of the drive. The user would not know if the reference current generator was operating in a purely constant flux mode or if a loss-minimization algorithm was being used; the drive is essentially a black box which accepts reference torque commands and produces stator voltages.

Now consider the control interface defined by the red box in Figure 1.3. This interface has two distinct reference signals—i_d^* which controls flux, and i_q^* which controls torque—implying that the user has individual control of the flux and torque. The user can now completely determine the relationship between the reference torque command and the corresponding reference currents to control flux and torque at a given rotor speed, permitting the use of user-defined optimization functions that would achieve objectives such as maximum-torque-per-amp (MTPA) and flux weakening.

For even finer control, consider the innermost green box which comprises only the PWM duty cycle generator and the power stage. At this level of control, the user has complete freedom to determine the mapping between the stator currents and voltages, and can thus control the current dynamics in the electric machine by manipulating the direct- and quadrature-axis voltage references. Motor drives which allow this level of control offer opportunities to optimize control operation of the whole process, while being able to completely define the relationships between individual components of the block diagram

in Figure 1.3. However, the validity of the assumptions related to the mapping between the stator currents and voltages must be verified. For example, quasi-steady-state relationships between voltages and currents is a valid assumption for electric machines with higher electrical resistance, but this is not the case for low-resistance machines which require closed-loop current regulation for oscillation-free operation.

The control engineer who is responsible for the design of the software blocks of the drive is faced with answering the question: is the drive just a three-phase voltage amplifier (innermost box), a three-phase current regulating system (intermediate box) or a torque regulating system (outermost box). The design of the control algorithms depends on the answer to this question.

1.3 Objectives of this Research

The primary goal of this research is to study the topic of kinetic energy recovery using the optimal control framework. Key questions related to the limits of kinetic energy recovery for user-defined braking parameters are answered using closed-form expressions. Optimal kinetic energy recovery algorithms are developed for permanent-magnet synchronous machines and induction machines; driving linear and non-linear mechanical loads; for motion control that involves slowing down to a non-zero speed as well as stopping; with and without position constraints imposed on motion control; for low-speed and high-speed operation; under constant-flux and variable-flux operation. A detailed framework for implementing the optimal control algorithms is also discussed and demonstrated.

CHAPTER 2
LITERATURE SURVEY

The studies related to regenerative braking in the existing literature can be classified into application specific studies, e.g. automotive vehicles and electric trains, and analyses based on machine physics.

2.1 Applications of Regenerative Braking

2.1.1 Automotive Vehicles

Electric and hybrid-electric automotive vehicles have the ability of using electrical braking (provided by electric machines in the vehicle's powertrain) in combination with conventional mechanical friction brakes. Several papers study the manner in which the braking effort is shared between the electrical and mechanical braking components.

Different energy recovery strategies for electric vehicles are studied in [8] where the braking effort between electric and mechanical brakes is shared in parallel and series schemes. In the parallel scheme, for every value of torque requested by the controller, both the electric and mechanical brakes work together. In the series scheme, only the electric brake is functional for braking torque requests up to its maximum value and mechanical brakes are applied only if the electric brakes cannot meet the requested torque due to actuator saturation. Several authors have designed strategies that apply maximum electrical braking torque for speeds above a certain threshold speed and then provide only mechanical friction brakes at low speeds [9, 10, 11, 12, 13, 14, 15]. A method of using maximum electrical braking torque for some duration during the braking operation and then smoothly reducing the electrical braking torque to zero is studied in [16, 17]. However, no physical interpretation is provided to explain the choice of the threshold speed or the choice

of ramp rate of reducing the electrical braking torque to zero. An optimal regenerative braking torque controller is designed in [18] such that the braking torque provided by the motor is maximized and cooperates with the hydraulic braking torque to maintain the longitudinal wheel slip at a desired value. It is implied that maximizing regenerative braking torque maximizes the energy captured. Although this might result in the recovery of some energy, there is potential to lose energy if the braking trajectory is allowed to enter the non-regenerative braking regions defined in [19, 20, 21]. In [19, 22], the concept of steady-state regenerative braking boundaries is used to design vehicle braking strategies that determine how braking effort is shared between the electrical and mechanical braking systems. The vehicle braking strategies that are developed avoid operation of the electric machine in the non-regenerative braking regions so as to recover as much electrical energy as possible during braking events.

In [23, 24, 25], steady-state regenerative braking control is studied in the context of maximum regeneration power, constant current regeneration, maximum braking current, and maximum regeneration efficiency for a BLDC drive system and concludes that in the interest of safety and saving energy, the constant current control mode is more suitable. However, no justification to support this conclusion is provided. The authors of [26] and [27] study the speed control operation of IPMs used in electric and hybrid-electric vehicle powertrains using the maximum-torque-per-amp (MTPA) algorithm and [27] studies the regenerative braking operation in particular. Maximum-torque-per-amp maps the shortest length current vector for the requested level of torque and rotor speed so as to minimize stator winding copper losses. The authors of [28] provide an algorithm which finds the current vector that minimizes stator windings copper losses as well as iron-core loss. However, [26, 27] do not provide torque commands that would improve kinetic energy recovery through regenerative braking.

In [29], braking control strategies are considered for a hybrid electric vehicle with a continuously variable transmission (CVT) to maximally use regenerative braking. Although

the authors claim that the control strategies are optimal, they do not show the formulation and solution of either a static optimization problem or an optimal control problem. In [30], a regenerative braking system with a brake resistor for a hybrid-electric bus is studied and it is concluded that the function of the regenerative braking system is expanded due to the introduction of the brake resistor which dissipates energy if the battery charging current limit is reached. A method of extracting kinetic energy by operating an induction machine in the negative slip region is proposed in [31], but the only variable that is manipulated is the excitation frequency while the voltages are kept constant.

The authors of [32] study the minimization of energy losses for an externally-excited synchronous machine (EESM) traction drive that is used in a hybrid-electric vehicle. An optimal adaptive state-feedback controller based on a linearized state-space model of the current dynamics around a given operating point is developed. A linear quadratic regulator (LQR) problem is then formulated to minimize a weighted sum of the energy of the state and control variables. The results of this LQR controller are compared to that of a conventional PI controller and it is shown that the LQR controller results in less energy being consumed and has a better transient performance while accelerating to higher speeds.

The authors of [33] study the torque control of a high-speed flywheel energy storage system that is used in electric vehicles. The system consists of a high-speed composite flywheel directly connected to a high speed interior permanent magnet synchronous machine (IPM). The IPM is torque controlled using the maximum-torque-per-amp (MTPA) algorithm to transfer and extract kinetic energy from the flywheel depending on the vehicle's operating state. The authors do not consider the effect of electric and mechanical loss mechanisms during the kinetic energy transfer process and studies such as [33] will benefit from the results of this research which includes development of optimal regenerative braking control for IPMs.

2.1.2 Electric Trains

Regenerative braking is discussed in [34] - [40] in the context of application in trains. In [34], a flywheel energy storage system with an induction machine is used to store regenerative braking energy during braking events instead of wasting it as heat, and releasing the energy when it is required to support the DC bus instead of supplying extra energy from external sources. However, optimal methods for kinetic energy transfer to and from the flywheel using the electric machine are not considered. The authors of [35], [36] and [38] develop optimization methods to control the speed profiles and timetables of a railway network such that the energy recovered during the braking of one train can be transferred to an accelerating train that is connected to the same line. The authors of [37] study energy efficient train control while assuming that all of the braking energy can be recovered. An energy saving speed profile is constructed through optimal control methods and is simulated for an Automatic Train Operation (ATO) system. The authors of [39, 40] describe linear programming methods to optimize the speed trajectory of a train; however they do not consider electric machine physics in the planning of optimal trajectories. In [41], the authors study the analysis of transient and steady-state operation of a traction motor drive using direct torque control. The paper proposes the use of energy storage devices to store recovered energy when the DC link voltage is in the normal operating range and the use of dynamic braking to dissipate energy in overvoltage conditions. Since this research develops optimal energy recovery strategies from a machine-physics perspective, applications such as electric trains which use electric machines for propulsion will benefit from the results. Optimal speed profiles can then be developed holistically without neglecting the important role that the electric machine plays in the kinetic energy recovery process.

2.1.3 Storage of Recovered Energy

The effect of feeding active power back into the electrical grid during regenerative braking in gantry crane applications is studied in [42]. The system uses three-phase induction

machines that are controlled using 12-pulse frequency controllers that can be operated in regenerative braking mode to hoist and lower heavy loads at the seaport, and reported that about 10%-16% of the energy is returned to the grid due to regenerative braking. However, the power is returned to the grid intermittently and this rapid power fluctuation causes unwanted effects such as voltage rise, leading power factor, harmonic distortions, etc. The authors suggest the installation of an on-board energy storage device, such as an ultra-capacitor, that stores the energy recovered through regenerative braking and supplies the stored energy to the drive during peak energy demands. The results of this research will provide benefits for applications such as the one studied in [42], i.e. a gantry crane, by developing methods to maximally recuperate the stored kinetic energy in the rotor of the electric machine during its regular hoist-and-lower operation. A method of regulating the DC bus voltage by using an additional energy storage capacitor and power electronic switches has been studied in [43, 44, 45, 46, 47, 48].

2.2 Regenerative Braking and Electric Machine Physics

Studies related to regenerative braking from a machine physics perspective are discussed in this section. Some authors use steady-state machine physics models to study regenerative braking whereas others use dynamic models of the mechanical subsystem to formulate kinetic energy recovery methods. There are no published results in the existing literature that use both electrical and mechanical dynamic models for any type of electric machine in the formulation of optimal regenerative braking control. This aspect is one of the unique contributions of this research.

2.2.1 Steady-State Analysis

The authors of [49] suggest modifications to the dimensions of the stator conductors to maximize the power density of an induction motor. As a result of the modifications, the constant torque region of the torque-speed capability of the machine is extended to a

higher rotor speed for a fixed terminal voltage. The authors claim an increase of about 18% in the energy recovered in a simulation example where the modified machine functions as a traction motor in an electric commuter vehicle. The authors of [50] define "critical braking" of an induction machine such that no power flow to or from the power source occurs, but there is no consideration of the influence of frequency-dependent machine reactance.

In [19, 20, 21], it is shown that the nature of electric braking can either be regenerative or non-regenerative. Using steady-state models, it is shown that the braking quadrants of the torque-speed plane of: separately-excited DC machines, permanent-magnet DC machines, surface permanent-magnet synchronous machines, and interior permanent-magnet synchronous machines, are divided into regions of regenerative braking and non-regenerative braking. In [19, 20], detailed derivations of the expressions that define the boundaries between regenerative and non-regenerative braking are developed for surface permanent-magnet synchronous machines accounting for the effect of iron-loss in the stator's core. Closed-form expressions could not be derived for IPMs, however a methodology to obtain the regenerative braking boundaries using numerical methods is described. Both [19] and [20] also describe a curve of maximum regenerative braking current in the torque-speed plane which describes the steady-state torque that results in the flow of maximum regenerative braking recharge current to the DC power source. In [21], steady-state models are used to derive similar boundaries between regenerative and non-regenerative braking regions in the braking quadrants of the torque-speed plane of induction machines.

However, braking is a transient phenomenon. Although the use of steady-state models is useful in determining steady-state regenerative braking boundaries, transient models must be used while formulating regenerative braking control strategies to effectively capture the effect of speed transients (and current transients) on kinetic energy recovery.

2.2.2 A Variational Approach

The authors of [51] study the minimum energy control of a DC traction motor with current as the control variable. The paper uses constrained optimal control methods considering the effects of armature current limits. In the special case where the armature resistance is neglected, the resulting control law is a switching function between minimum and maximum armature currents, with singular subarcs along which velocity is constant.

In [43]-[48] and [52]-[58], which deal with induction machines, an optimal control method is developed to realize optimal torque trajectories for power regeneration under constant flux operation. The authors also have subsequent publications which expand the topic to include amplitude and speed limits [46, 54, 55, 56], varying stopping time [47], final conditions on rotation angle [53, 55, 56], and smoothing the transition from motoring to braking at the beginning of the braking event [57, 58]. In [48], a numerical design methodology of optimal trajectories based on a loss map is presented for induction machine drives. The loss map includes stator and rotor copper losses as well as iron-core and other unmodeled losses. The numerical design methodology determines a smoothed optimal speed trajectory based on the loss map and it is shown that the numerical method outperforms the analytical method described in [43]-[47] and [52]-[58] in terms of energy consumption during an accelerating event. The methodology presented in [43]-[48] and [52]-[58] produces a scalar optimal torque trajectory that can be supplied as the input to a motor drive with a control interface akin to that of the outermost box of Figure 1.3. The authors of [43]-[48] and [52]-[58] also limit the study to induction machines with constant-flux operation only, while the scope of this research extends to surface-permanent magnet synchronous machines, interior permanent magnet synchronous machines, as well as induction machines, and addresses both constant flux and variable flux modes of operation.

2.3 Unique Contributions of this Research

The current state-of-the-art in the area of optimal kinetic energy recovery will now be summarized. Several authors have suggested using maximum braking torque as a means to recover maximum kinetic energy. However, this claim must be verified for electromechanical systems with electrical and mechanical losses. Some authors use steady-state analysis to develop energy recovery algorithms. However, since they neglect mechanical dynamics they perform static optimization rather than using optimal control, resulting in sub-optimal solutions. Although Inoue et al. have investigated this topic using a variational approach, there are several shortcomings. Their work is limited only to induction machines under constant-flux operation. Their work does not incorporate the dynamic model of an induction machine or a current-regulating power converter. They do not expose the trade-off between energy recovery and braking time-interval length. They also limit their work to simple mechanical loads that are characterized only by viscous friction. To fill these gaps in the knowledge base, this research contributes to the topic of optimal kinetic energy recovery as follows:

1. Developing a simplified optimal kinetic energy recovery algorithm for SPMs based on fractional back-EMF voltage feedback [59].

2. Comparing maximum power braking and maximum energy braking, thereby exposing the difference between static optimization and optimal control in the context of kinetic energy recovery using electric machines [59].

3. Developing a common optimal kinetic energy recovery algorithm for surface permanent-magnetic synchronous machines, interior permanent-magnet synchronous machines, and induction machines under constant-flux operation.

4. Developing closed-form expressions that show the kinetic energy recovery performance under optimal braking.

5. Considering the internal behavior of the system, thereby exposing the role of design parameters and enabling the investigation of robustness to parameter uncertainty.

6. Developing a simplified optimal kinetic energy recovery algorithm which can be implemented using simple speed feedback control for current-controlled PMSMs and induction machines [60, 61].

7. Providing control engineers a framework to study the trade-off between kinetic energy recovery and braking time.

8. Determining the optimal braking time-interval length for a set of initial and final rotor speeds.

9. Including position constraints in the optimal kinetic energy recovery problem framework that can be used in applications such as robotic manufacturing, elevator drives, etc.

10. Including the effect of flux-weakening in the optimal kinetic energy recovery problem framework for high-speed operation of electric machines.

11. Including variable-flux operation in the optimal kinetic energy recovery problem framework for interior permanent-magnet synchronous machines in accordance with algorithms such as maximum-torque-per-amp (MTPA).

2.4 Dissertation Outline

Chapter 3 provides details of the electric machine modeling, control, and mechanical load modeling that will be used in this dissertation. In Chapter 4, the procedures for identifying electrical and mechanical parameters that are essential for the design of optimal kinetic energy recovery algorithms are outlined and experimentally demonstrated. Chapter 5 is the first time the optimal kinetic energy recovery algorithm framework is

introduced using a simple electromechanical system consisting of a surface permanent-magnet synchronous machine and a viscous friction inertial mechanical load. This chapter also outlines a framework to implement the optimal kinetic energy recovery algorithm. Chapter 6 expands the optimal kinetic energy algorithm developed in Chapter 5 to include constant-flux operation of interior permanent-magnet synchronous machines and induction machines. This chapter also studies the inclusion of a Coulomb friction mechanical load in addition to the viscous friction model that was studied in Chapter 5 and experimental results for all three electric machine types are reported. In Chapter 7, position constraints are included in the optimal kinetic energy recovery problem framework. The augmented optimal control problem is solved and experimental results are reported. Chapter 8 studies the optimal kinetic energy recovery problem for high-speed operation of electric machines under flux-weakening. The optimal control problem is formulated, solved, and implemented experimentally. In Chapter 9, the optimal kinetic energy recovery algorithm is studied for an interior permanent-magnet synchronous machine operating under variable-flux in the constant-torque region of the torque-speed plane. The dissertation is concluded in Chapter 10 with a summary of the completed work and topics for future research.

CHAPTER 3
ELECTRIC MACHINES AND MECHANICAL LOADS

This chapter discusses the modeling and control of the different types electric machines used for this research and the typical mechanical loads that they drive.

3.1 Electric Machine Modeling

The prevalence of permanent-magnet synchronous machines and induction machines in the electric machine market has justified limiting this research to consider just those two electric machine families. A three-phase DC-AC power converter is used to control the three-phase electric machines. A schematic diagram of the electric machine drive system is shown in Figure 3.1. A DC power source (e.g. a battery pack) and bus capacitance are connected to the DC side of the power converter, and an electric machine is connected to the AC side of the power converter. The bus voltage and current are denoted by v_{bus} and i_{bus}, the power converter voltages and currents are denoted by v_{ABC} and i_{ABC}, and the electric machine voltages and currents are denoted by v_{abc} and i_{abc}. The machine stator windings can be either Δ-connected or Y-connected. The converter applies effort v_{ABC}, the motor experiences effort v_{abc}, physics results in machine current flow i_{abc}, and the converter experiences current flow i_{ABC}. The reference node used to determine the converter output voltage values v_{ABC} is the negative terminal of the power supply [62].

3.1.1 Relationship Between Converter and Machine Electrical Variables

Delta-Connected Electric Machines

Analysis of the schematic diagram for the Δ-connected machine in Figure 3.1(a) shows that the application of converter leg voltages (v_A, v_B, v_C) produces corresponding machine

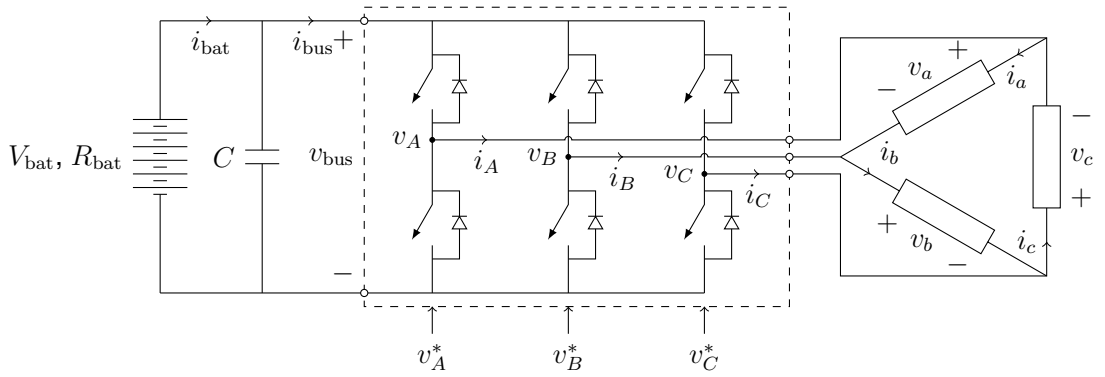

(a) Delta (Δ)-connected machine

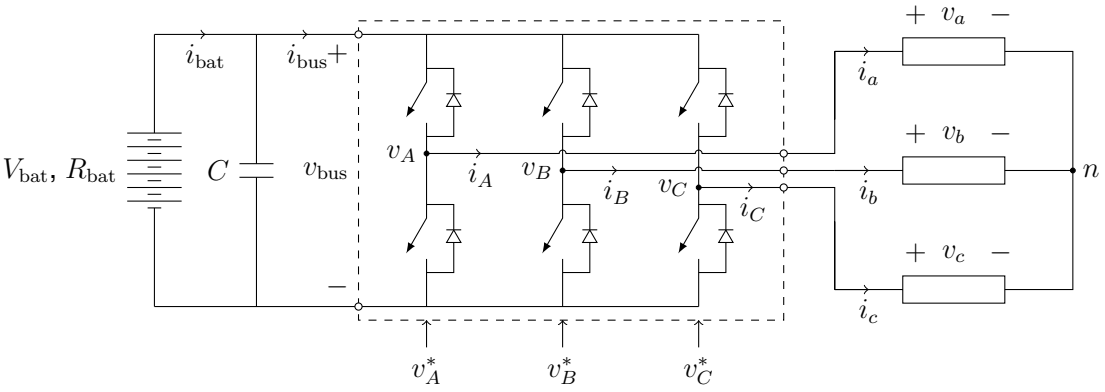

(b) Wye (Y)-connected machine

Figure 3.1: Schematic diagram of an electric machine drive system.

phase voltages (v_a, v_b, v_c) according to

$$\begin{aligned} v_a &= v_A - v_B \\ v_b &= v_B - v_C \\ v_c &= v_C - v_A \end{aligned} \tag{3.1}$$

Machine phase currents will flow as a consequence and are related to the converter leg currents (i_A, i_B, i_C) as

$$\begin{aligned} i_A &= i_a - i_c \\ i_B &= i_b - i_a \\ i_C &= i_c - i_b \end{aligned} \tag{3.2}$$

Shunt resistors located within the converter are used to measure the leg currents. Computing the inverse relationship between phase currents and leg currents is useful in determining the phase currents from measured leg currents. Assuming that $i_a + i_b + i_c = 0$, the phase currents are determined as

$$\begin{aligned} i_a &= \frac{1}{3} i_A - \frac{1}{3} i_B \\ i_b &= \frac{1}{3} i_B - \frac{1}{3} i_C \\ i_c &= \frac{1}{3} i_C - \frac{1}{3} i_A \end{aligned} \tag{3.3}$$

The desired machine phase voltages are applied using converter leg voltages

$$\begin{aligned} v_A &= \frac{1}{2} v_{\text{bus}} + \tilde{v}_A \\ v_B &= \frac{1}{2} v_{\text{bus}} + \tilde{v}_B \\ v_C &= \frac{1}{2} v_{\text{bus}} + \tilde{v}_C \end{aligned} \tag{3.4}$$

where the leg voltage deviations from mid-point, $\tilde{v}_{ABC}$, satisfy

$$\tilde{v}_A + \tilde{v}_B + \tilde{v}_C = 0 \tag{3.5}$$

and the inverse relationship of (3.1) results in

$$\tilde{v}_A = \frac{1}{3}v_a - \frac{1}{3}v_c \tag{3.6}$$

$$\tilde{v}_B = \frac{1}{3}v_b - \frac{1}{3}v_a \tag{3.7}$$

$$\tilde{v}_C = \frac{1}{3}v_c - \frac{1}{3}v_b \tag{3.8}$$

Wye-Connected Electric Machines

Analysis of the schematic diagram for the Y-connected machine in Figure 3.1(b) shows that the application of converter leg voltages (v_A, v_B, v_C) produces corresponding machine phase voltages (v_a, v_b, v_c) according to

$$\begin{aligned} v_a &= \frac{2}{3}v_A - \frac{1}{3}v_B - \frac{1}{3}v_C \\ v_b &= \frac{2}{3}v_B - \frac{1}{3}v_C - \frac{1}{3}v_A \\ v_c &= \frac{2}{3}v_C - \frac{1}{3}v_A - \frac{1}{3}v_B \end{aligned} \tag{3.9}$$

Machine phase currents will flow as a consequence and are related to the converter leg currents (i_A, i_B, i_C) as

$$\begin{aligned} i_A &= i_a \\ i_B &= i_b \\ i_C &= i_c \end{aligned} \tag{3.10}$$

Therefore, measuring leg currents using shunt resistor current sensors results in direct measurements of phase current values, without the need for further calculations. As shown earlier in (3.4), the leg voltages are applied using deviation voltages

$$\begin{aligned}\tilde{v}_A &= \frac{2}{3}v_a - \frac{1}{3}v_b - \frac{1}{3}v_c \\ \tilde{v}_B &= \frac{2}{3}v_b - \frac{1}{3}v_c - \frac{1}{3}v_a \\ \tilde{v}_C &= \frac{2}{3}v_c - \frac{1}{3}v_a - \frac{1}{3}v_b\end{aligned} \tag{3.11}$$

3.1.2 Machine Modeling in the DQ-Reference Frame

Permanent-Magnet Synchronous Machine Modeling (PMSMs)

Permanent-magnet synchronous machines (PMSMs) are characterized by a rotor that has a permanent-magnet which is the source of magnetic flux in the rotor. Copper windings are wound around a stator, which is made up of steel laminations. An air gap separates the stator and the rotor. The permanent-magnet of the rotor can either be stuck onto the surface of the rotor, or embedded inside the rotor. A PMSM with permanent-magnets on the surface of the rotor is called a surface-mounted permanent-magnet synchronous machine (abbreviated as SPM), and a PMSM with permanent-magnets embedded inside the rotor is called an interior permanent-magnet synchronous machine (abbreviated as IPM). Figure 3.2 shows the cross-section geometry of both types of PMSMs, where θ_r is the rotor angle and the rotor direct (d) and quadrature (q) axes are displayed.

The governing equations that describe the electrical dynamics of PMSMs in the dq reference frame are

$$\begin{aligned}L_d\frac{di_d}{dt} &= v_d - R_s i_d + N\omega_r L_q i_q \\ L_q\frac{di_q}{dt} &= v_q - R_s i_q - N\omega_r\left(\Lambda + L_d i_d\right)\end{aligned} \tag{3.12}$$

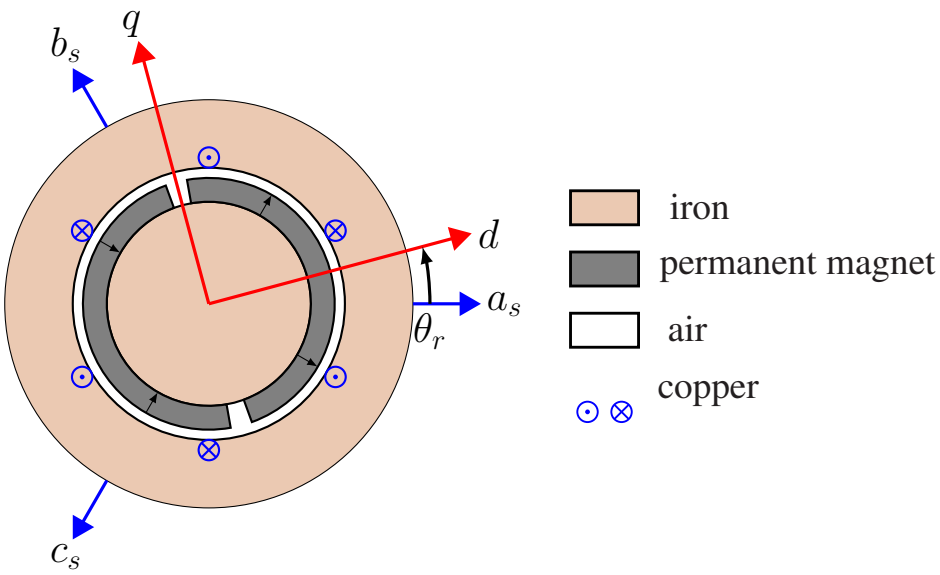

(a) SPM

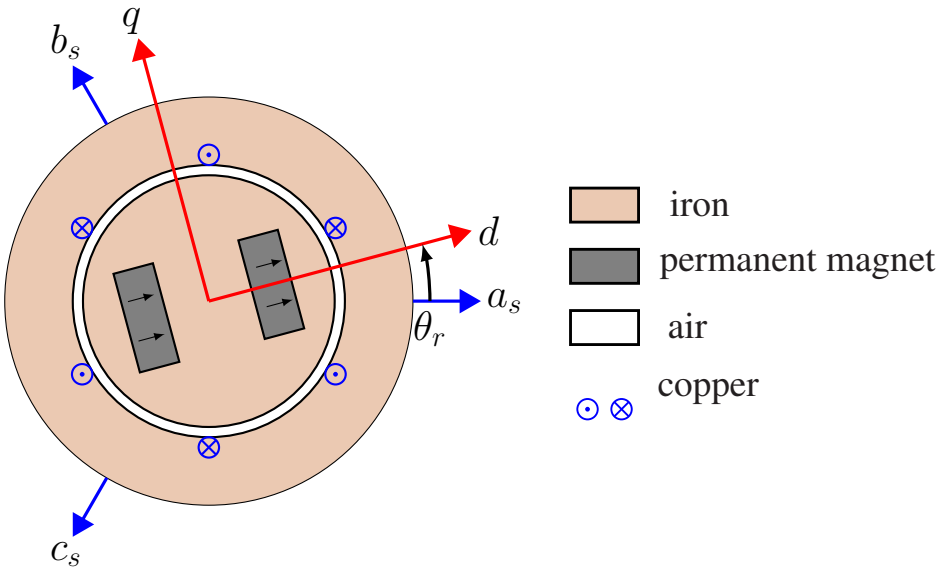

(b) IPM

Figure 3.2: Cross-sectional diagrams of the two types of PMSMs.

and the electromagnetic torque is expressed as

$$T_e = N\left(\Lambda + \left(L_d - L_q\right) i_d\right) i_q \tag{3.13}$$

where ω_r is the rotor speed, i_d and i_q are the stator currents, and v_d and v_q are the stator voltages expressed in the rotor (or synchronous) frame, N is the number of rotor pole-pairs, R_s is the stator winding resistance, L_d and L_q are the stator winding inductances in the dq reference frame, and Λ is the permanent-magnet flux in the dq reference frame. This model is based on the power-invariant form of dq-transformation

$$\mathbf{K}(\theta_r) = \sqrt{\frac{2}{3}} \begin{bmatrix} \cos\left(N\theta_r\right) & \cos\left(N\theta_r - \frac{2\pi}{3}\right) & \cos\left(N\theta_r + \frac{2\pi}{3}\right) \\ -\sin\left(N\theta_r\right) & -\sin\left(N\theta_r - \frac{2\pi}{3}\right) & -\sin\left(N\theta_r + \frac{2\pi}{3}\right) \\ \sqrt{\frac{1}{2}} & \sqrt{\frac{1}{2}} & \sqrt{\frac{1}{2}} \end{bmatrix}, \tag{3.14}$$

and the phase voltages and currents are transformed to the dq reference frame as

$$\begin{aligned} v_{dq0} &= \mathbf{K}(\theta_r) v_{abc} \\ i_{dq0} &= \mathbf{K}(\theta_r) i_{abc} \end{aligned} \tag{3.15}$$

Delta-Connected Machines

For delta-connected electric machines, a desired stator voltage vector, v^*_{dq}, is implemented using three-phase power converter voltage commands, v^*_{ABC}, according to

$$\begin{aligned} v^*_A &= \frac{1}{2} v_{\text{bus}} + \sqrt{\frac{2}{9}} |v^*_{dq}| \cos\left(\vartheta_A + \angle v^*_{dq}\right) \\ v^*_B &= \frac{1}{2} v_{\text{bus}} + \sqrt{\frac{2}{9}} |v^*_{dq}| \cos\left(\vartheta_B + \angle v^*_{dq}\right) \\ v^*_C &= \frac{1}{2} v_{\text{bus}} + \sqrt{\frac{2}{9}} |v^*_{dq}| \cos\left(\vartheta_C + \angle v^*_{dq}\right) \end{aligned} \tag{3.16}$$

where

$$\begin{aligned}\vartheta_A &= N\theta_r - \frac{\pi}{6} \\ \vartheta_B &= N\theta_r - \frac{\pi}{6} - \frac{2\pi}{3} \\ \vartheta_C &= N\theta_r - \frac{\pi}{6} + \frac{2\pi}{3}\end{aligned} \tag{3.17}$$

The maximum length of the voltage and current vectors in the dq reference frame are bounded by the bus voltage and the maximum current through the power converter switches respectively. According to [19], the application of three-phase voltages without the third-harmonic component for a delta-connected machine shown in (3.16) results in a maximum voltage vector of length

$$V_{\max} = \sqrt{\frac{9}{8}} v_{\text{bus}} \tag{3.18}$$

and the corresponding maximum length of the current vector for the delta-connected machine is defined according to

$$I_{\max} = \sqrt{\frac{1}{2}} I_{\text{sw,max}} \tag{3.19}$$

where $I_{\text{sw,max}}$ is the magnitude of the maximum allowable current that can flow through the switch.

Wye-Connected Machines

For wye-connected electric machines, a desired stator voltage vector, v^*_{dq}, is implemented using three-phase power converter voltage commands, v^*_{ABC}, according to

$$\begin{aligned} v^*_A &= \frac{1}{2}v_{\text{bus}} + \sqrt{\frac{2}{3}}|v^*_{dq}|\cos\left(\vartheta_A + \angle v^*_{dq}\right) \\ v^*_B &= \frac{1}{2}v_{\text{bus}} + \sqrt{\frac{2}{3}}|v^*_{dq}|\cos\left(\vartheta_B + \angle v^*_{dq}\right) \\ v^*_C &= \frac{1}{2}v_{\text{bus}} + \sqrt{\frac{2}{3}}|v^*_{dq}|\cos\left(\vartheta_C + \angle v^*_{dq}\right) \end{aligned} \tag{3.20}$$

where

$$\begin{aligned} \vartheta_A &= N\theta_r \\ \vartheta_B &= N\theta_r - \frac{2\pi}{3} \\ \vartheta_C &= N\theta_r + \frac{2\pi}{3} \end{aligned} \tag{3.21}$$

The voltage limit corresponding to the application of three-phase voltages without the third-harmonic component for a wye-connected machine shown in (3.20) is

$$V_{\max} = \sqrt{\frac{3}{8}}v_{\text{bus}} \tag{3.22}$$

and the corresponding maximum length of the current vector for the wye-connected machine is defined according to

$$I_{\max} = \sqrt{\frac{3}{2}}I_{\text{sw,max}} \tag{3.23}$$

where $I_{\text{sw,max}}$ is the magnitude of the maximum allowable current that can flow through the switch.

A summary of the voltage and current limits for delta and wye-connected electric machines that use three-phase voltages in (3.16) and (3.20) is shown in Table 3.1

Table 3.1: Voltage and Current Limits for Electric Machines

	$V_{\max}/v_{\text{bus}}$	$I_{\max}/I_{\text{sw,max}}$
Δ	$\sqrt{\frac{9}{8}}$	$\sqrt{\frac{1}{2}}$
Y	$\sqrt{\frac{3}{8}}$	$\sqrt{\frac{3}{2}}$

Induction Machines

Induction machines do not have permanent-magnets present in or on the rotor. Instead, the laminated rotor iron either has copper bars (squirrel-cage rotor) embedded on its surface or is wound with copper windings (wound-rotor). Copper windings are wound around a stator that is made of steel laminations, similar to synchronous machines [65]. Applying three-phase stator voltages sets up a rotating magnetic field in the air-gap. This induces currents in the rotor that create a rotor magnetic field that opposes the stator magnetic field (due to Lenz's law). As a result, the rotor starts rotating in the direction of the stator magnetic field and reaches a speed that is close to but less than the synchronous speed of the stator rotating magnetic field. The difference between the two speeds is called "slip speed." The essential characteristic of an induction machine is that the rotor magnetic field is created solely by induction instead of being sourced by materials such as permanent-magnets. Figure 3.3 shows the cross-section geometry of the induction machine, where θ_r is the rotor angle and θ_e is the excitation angle of the stator magnetic field (defined with respect to the stator phase-a magnetic axis). The direct-axis in the synchronous reference frame of an induction machine is aligned with the excitation angle of the stator magnetic field.

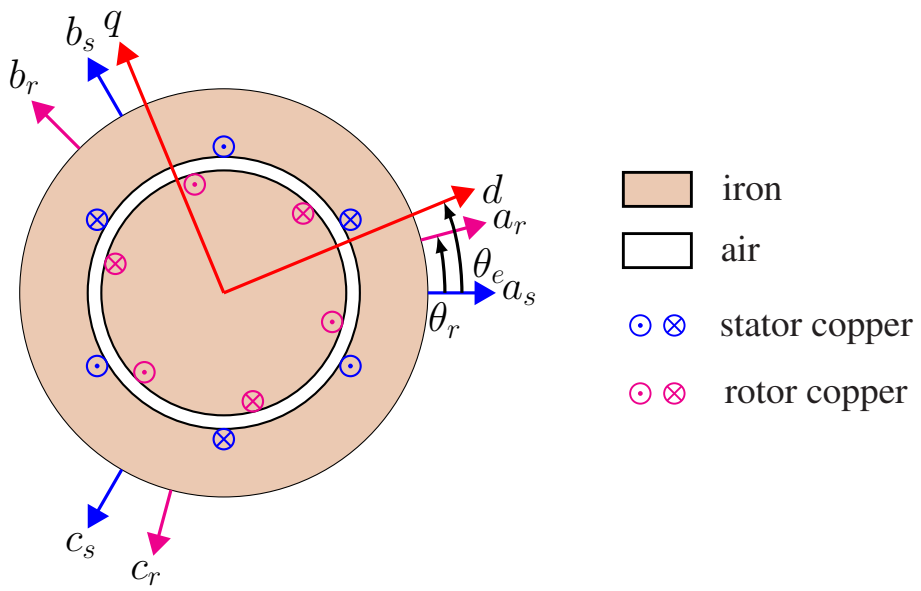

Figure 3.3: Cross-sectional diagram of an induction machine.

The stator electrical dynamic equations in the synchronous dq reference frame are

$$\begin{aligned}\sigma L_s L_r^2 \frac{di_d}{dt} &= L_r^2 v_d - \left(L_m^2 R_r + L_r^2 R_s\right) i_d + \omega_e \sigma L_s L_r^2 i_q + L_m R_r \lambda_d + N\omega_r L_m L_r \lambda_q \\ \sigma L_s L_r^2 \frac{di_q}{dt} &= L_r^2 v_q - \left(L_m^2 R_r + L_r^2 R_s\right) i_q - \omega_e \sigma L_s L_r^2 i_d + L_m R_r \lambda_q - N\omega_r L_m L_r \lambda_d,\end{aligned} \tag{3.24}$$

the rotor electrical dynamics are

$$\begin{aligned}L_r \frac{d\lambda_d}{dt} &= -R_r \lambda_d + \omega_s L_r \lambda_q + L_m R_r i_d \\ L_r \frac{d\lambda_q}{dt} &= -R_r \lambda_q - \omega_s L_r \lambda_d + L_m R_r i_q,\end{aligned} \tag{3.25}$$

and the electromagnetic torque is

$$T_e = \frac{NL_m}{L_r}\left(\lambda_d i_q - \lambda_q i_d\right) \tag{3.26}$$

where ω_r is the rotor speed, λ_d and λ_q are the rotor flux components, i_d and i_q are the stator current components, v_d and v_q are the stator voltage components, ω_e is the excitation

frequency, ω_s is the slip frequency which satisfies

$$\omega_s = \omega_e - N\omega_r, \tag{3.27}$$

N is the number of pole pairs, L_m is the mutual inductance, L_s and R_s are the stator inductance and resistance, L_r and R_r are the rotor inductance and resistance, and σ is the leakage coefficient given by

$$\sigma = 1 - \frac{L_m^2}{L_s L_r} \tag{3.28}$$

A desired stator voltage vector, v_{dq}^*, is implemented using three-phase power converter voltage commands that are similar to (3.16) and (3.20) for delta and wye-connected machines respectively with the exception of θ_e replacing $N\theta_r$ in (3.17) and (3.21). The excitation angle is used instead of the rotor electrical angle ($N\theta_r$) in the power-invariant transformation matrix shown in (3.14) according to

$$\mathbf{K}(\theta_e) = \sqrt{\frac{2}{3}} \begin{bmatrix} \cos(\theta_e) & \cos\left(\theta_e - \frac{2\pi}{3}\right) & \cos\left(\theta_e + \frac{2\pi}{3}\right) \\ -\sin(\theta_e) & -\sin\left(\theta_e - \frac{2\pi}{3}\right) & -\sin\left(\theta_e + \frac{2\pi}{3}\right) \\ \sqrt{\frac{1}{2}} & \sqrt{\frac{1}{2}} & \sqrt{\frac{1}{2}} \end{bmatrix}, \tag{3.29}$$

and the phase voltages and currents are transformed to the dq reference frame as

$$\begin{aligned} v_{dq0} &= \mathbf{K}(\theta_e) v_{abc} \\ i_{dq0} &= \mathbf{K}(\theta_e) i_{abc} \end{aligned} \tag{3.30}$$

3.1.3 Field-Oriented Control and Torque Control

The electrical dynamics of a three-phase electric machine were transformed to a two-axis dq reference frame previously. Therefore, the three-phase stator currents are identified as two orthogonal components of a vector in the dq reference frame. The theory of field-

oriented control (or vector control) states that one component of the current vector is used to control the magnetic flux, and the other component is used to control the electromagnetic torque of the machine [63]. As such, the direct-axis current component which is defined in Figures 3.2 and 3.3 to be aligned in direction of the rotor magnetic-flux, is used to control flux and the orthogonal quadrature-axis current component controls the torque produced. Since closed-loop current control is used to regulate the currents in the d and q axes, the measured three-phase stator winding currents must be transformed to the dq reference frame. The output of the current controller must also be accurately transformed from the dq reference frame to the three-phase reference frame for implementation using a three-phase power converter as shown in Figure 3.1. To do this accurately, the position of the rotor must be known at all times. Therefore, rotor position sensors or estimators are essential to implement field-oriented control.

PMSMs

The block diagram of a field-oriented control based torque controller for permanent-magnet synchronous machines is shown in Figure 3.4. The input to the block diagram is the desired torque reference, T_e^*. The rotor speed is estimated (or measured directly) from the rotor position sensor output, θ_r, and is given as an input to a current selector block which then determines suitable rotor-frame current reference signals i_{dq}^*. Feedback of measured stator currents and subsequent transformation to the dq reference frame, i_{dq}, lead to error signals, which are then used to determine suitable rotor-frame voltage reference signals v_{dq}^*. An inverse rotor-frame transformation is used to determine the desired converter leg voltages v_{ABC}^* from v_{dq}^* as shown in (3.16) and (3.20).

The current control loop is defined by PI compensation of the form

$$\begin{aligned} v_d^* &= -k_{c1} i_d - k_{c2} \xi_d \\ \dot{\xi}_d &= i_d - i_d^* \end{aligned} \tag{3.31}$$

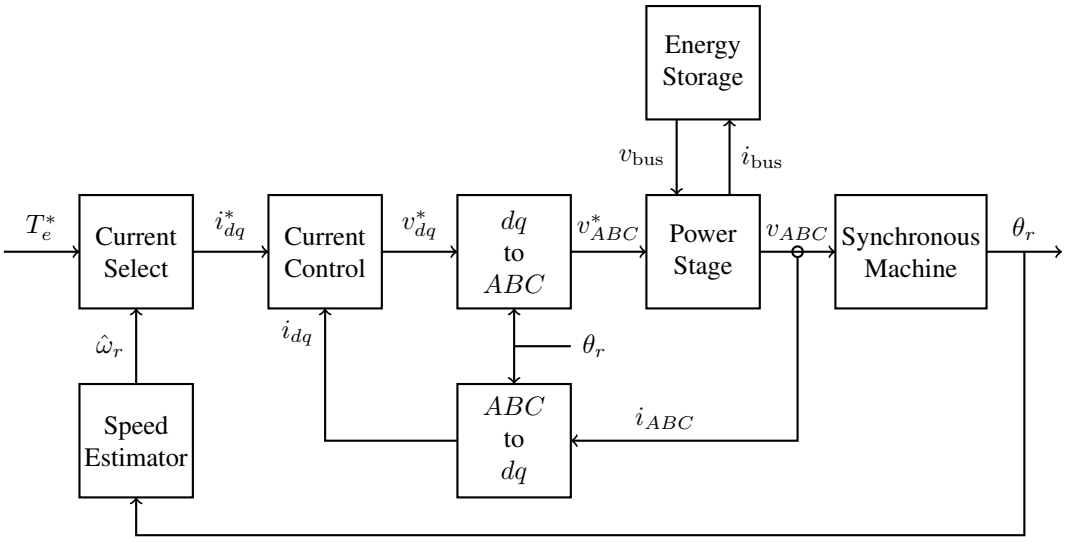

Figure 3.4: Block diagram of the closed-loop current controller used to achieve desired torque for PMSMs.

and

$$\begin{aligned} v_q^* &= -k_{c1} i_q - k_{c2} \xi_q \\ \dot{\xi}_q &= i_q - i_q^* \end{aligned} \tag{3.32}$$

where ξ_d and ξ_q are the current-error integrals. Feedback gains k_{c1} and k_{c2} are selected to satisfy

$$\begin{aligned} k_{c1} &= 4 \frac{L_d L_q}{L_d + L_q} \alpha_s - R \\ k_{c2} &= \sqrt{L_d L_q} \alpha_s^2 \end{aligned} \tag{3.33}$$

where α_s represents the desired nominal bandwidth for stator current control. For the case of SPMs, where $L_d = L_q = L$, the choice of controller gains simplifies to

$$\begin{aligned} k_{c1} &= 2L\alpha_s - R \\ k_{c2} &= L\alpha_s^2 \end{aligned} \tag{3.34}$$

With this choice of feedback gains, the stator current dynamics in (3.12) augmented with

the error integrator dynamics in (3.31)-(3.32) is characterized by the coefficient matrix

$$\begin{bmatrix} -2\alpha_s & N\omega_r & -\alpha_s^2 & 0 \\ -N\omega_r & -2\alpha_s & 0 & -\alpha_s^2 \\ 1 & 0 & 0 & 0 \\ 0 & 1 & 0 & 0 \end{bmatrix} \tag{3.35}$$

and the associated characteristic polynomial

$$(s + \alpha_s)^4 + (N\omega_r s)^2 \tag{3.36}$$

If the commanded current i_{dq}^* is constant, which corresponds to constant-torque constant-speed equilibrium conditions, then the actual current i_{dq} will converge to i_{dq}^* with a settling time of approximately $5/\alpha_s$, assuming ω_r is relatively small.

Induction Machines

Indirect field-oriented control for induction machines follows the same principle as for PMSMs, i.e. one component of the current vector i_{dq} is used to control flux (the d-axis component) and the other component is used to manipulate torque (the q-axis component) [64]. As a consequence, synchronous reference frame rotor flux vector is controlled such that the quadrature-axis component is of zero length and the direct-axis component has all the rotor flux according to

$$\begin{aligned} \lambda_d^* &= \bar{\lambda}_d \\ \lambda_q^* &= 0 \end{aligned} \tag{3.37}$$

The block diagram of a indirect field-oriented control based torque and flux controller for an induction machine is shown in Figure 3.5. The inputs to the system are the desired torque and direct-axis rotor flux reference signal. Unlike PMSMs where the rotor flux was

sourced using permanent-magnets, the stator currents in induction machines induce rotor currents which in turn produce rotor flux which is essential to produce torque.

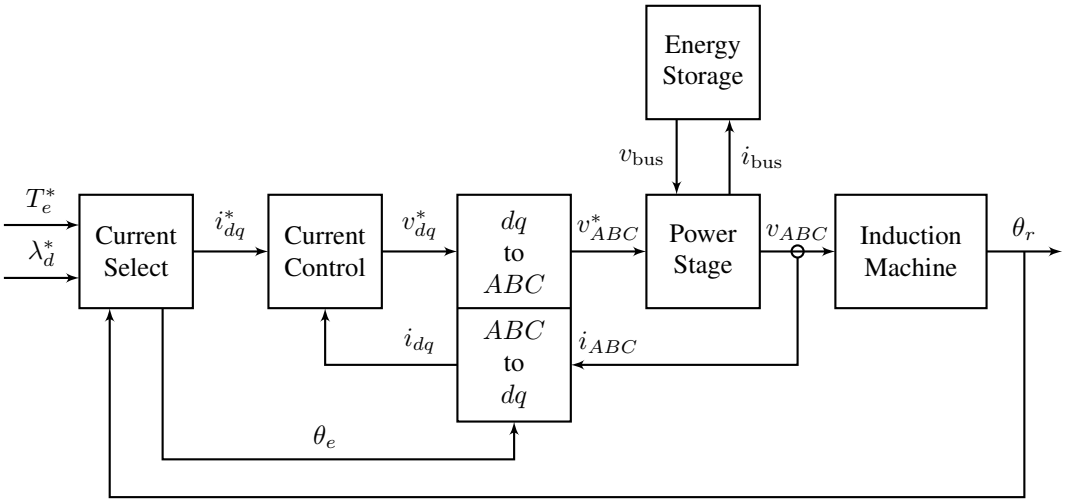

Figure 3.5: Block diagram of the internal architecture for control of torque and flux of an induction machine.

The current selector assigns synchronous frame stator winding current references according to

$$\begin{aligned} i_d^* &= \frac{\lambda_d^*}{L_m} \\ i_q^* &= \frac{L_r}{N L_m} \frac{T_e^*}{\lambda_d^*} \end{aligned} \tag{3.38}$$

The synchronous frame reference angle, θ_e, is obtained from measurements of the rotor angle, θ_r, according to

$$\begin{aligned} \theta_e &= N\theta_r + \theta_s \\ \omega_s &= \dot{\theta}_s = \frac{R_r T_e^*}{N \lambda_d^{*2}} \end{aligned} \tag{3.39}$$

The current reference choices in (3.38) and excitation angle in (3.39) are obtained by solving three algebraic equations (equilibrium version of rotor electrical dynamics in (3.25) and the torque equation in (3.26)) for the three variables i_d^*, i_q^*, and θ_e.

The current control loop is defined by the same PI compensators shown in (3.31) and (3.32). Feedback gains k_{c1} and k_{c2} are selected to satisfy

$$\begin{aligned} k_{c1} &= 2\sigma L_s \alpha_s - \left(R_s + \left(\frac{L_m}{L_r} \right)^2 R_r \right) \\ k_{c2} &= \sigma L_s \alpha_s^2 \end{aligned} \tag{3.40}$$

where α_s represents the nominal bandwidth of the current controller. With this choice of feedback gains, the stator current dynamics (3.24) augmented with the error integrator dynamics (3.31)-(3.32) is characterized by the coefficient matrix

$$\begin{bmatrix} -2\alpha_s & \omega_e & -\alpha_s^2 & 0 \\ -\omega_e & -2\alpha_s & 0 & -\alpha_s^2 \\ 1 & 0 & 0 & 0 \\ 0 & 1 & 0 & 0 \end{bmatrix} \tag{3.41}$$

and the associated characteristic polynomial

$$(s + \alpha_s)^4 + (\omega_e s)^2 \tag{3.42}$$

If the commanded current i_{dq}^* is constant, corresponding to constant-torque constant-speed equilibrium conditions, then the actual current i_{dq} will converge to i_{dq}^* with a settling time of approximately $5/\alpha_s$. The rotor flux dynamics (3.25) is in turn influenced by i_{dq}^*, according to the coefficient matrix

$$\begin{bmatrix} -\alpha_r & \omega_s \\ -\omega_s & -\alpha_r \end{bmatrix} \tag{3.43}$$

and the associated characteristic polynomial

$$(s + \alpha_r)^2 + \omega_s^2 \tag{3.44}$$

with the rotor electrical bandwidth

$$\alpha_r = \frac{R_r}{L_r} \tag{3.45}$$

Consequently, the rotor flux λ_{dq} will converge to its equilibrium with settling time of approximately $5/\alpha_r$. The takeaway from this analysis is that although high-bandwidth current control can result in quick convergence of stator currents, the rate of the rotor flux convergence cannot be influenced by user-defined bandwidth selection and the rate of convergence is a function of the rotor electrical parameters alone.

3.2 Mechanical Load Modeling

Electric machines usually drive mechanical loads. The movement of the mechanical load requires changing its speed or position, which implies that a torque must be applied to overcome its resistance to motion, i.e. inertia, so as to accelerate or decelerate the load. The inertia of the mechanical load is denoted by J. Mechanical loads are usually mounted on or attached to the shaft of the rotor of the electric machine. If T_{load} is the load torque and T_e is the electromagnetic torque of the electric machine, then the load dynamics are represented as

$$\dot{\omega}_r = \frac{1}{J}\left(T_e - T_{\text{load}}\right) \tag{3.46}$$

This section discusses the characteristics of two common types of mechanical loading due to friction effects, viscous friction and Coulomb friction [66].

3.2.1 Viscous Friction

A common mechanical load that electric motors operate on are viscous friction loads. An electric machine, even without any external mechanical loading, inherently experiences viscous friction loading due the mechanical bearing that is used to mount the rotor shaft. The bearing applies a mechanical linear damping effect to the rotation of the rotor shaft as it rotates. The magnitude of viscous fiction loading increases linearly with rotor speed according to

$$T_{\text{load}} = B_1 \omega_r \tag{3.47}$$

where B_1 is the viscous friction coefficient of the load. Figure 3.6 shows the speed characteristics of a viscous friction mechanical load.

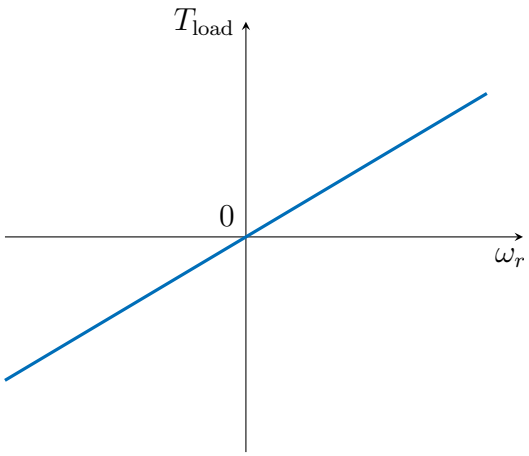

Figure 3.6: Speed characteristics of a viscous friction load.

3.2.2 Coulomb Friction

Another type of mechanical load that is typically encountered during electric machine operation is Coulomb friction. This is a type of constant mechanical load in which energy is absorbed through sliding friction, as the load slides over the mechanical bearing. The classical Coulomb friction model is described by a discontinuous relationship between the

friction force and the relative velocity between the sliding surfaces and is modeled as

$$T_{\text{load}} = B_0 \, \text{sgn}(\omega_r) \tag{3.48}$$

where B_0 is the Coulomb friction coefficient of the load. The Coulomb friction load is constant (equal to B_0) for all non-zero speeds. Figure 3.7 shows the speed characteristics of a Coulomb friction mechanical load.

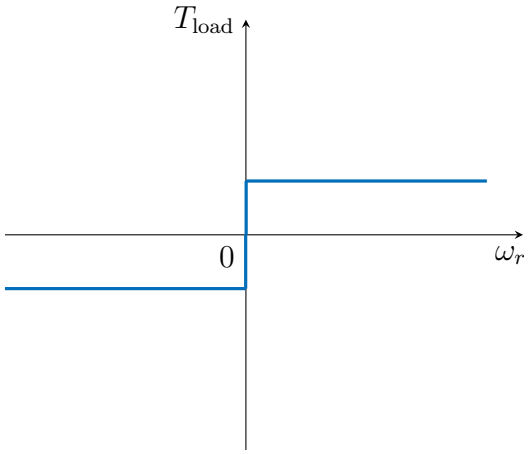

Figure 3.7: Speed characteristics of a Coulomb friction load.

A combination of viscous friction and Coulomb friction loading is represented as

$$T_{\text{load}} = B_1 \omega_r + B_0 \, \text{sgn}(\omega_r). \tag{3.49}$$

Figure 3.8 shows the speed characteristics of a mechanical load model that has both viscous and Coulomb friction components.

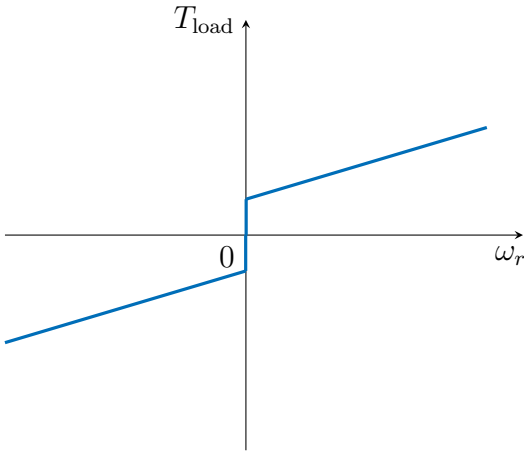

Figure 3.8: Speed characteristics of a viscous friction load combined with Coulomb friction loading.

3.3 Speed Control

Certain applications require the electrical machine to regulate the speed of a mechanical load. Figure 3.9 shows the block diagram of a closed-loop speed controller which has an inner current loop (from Section 3.1.3) to regulate the speed of the mechanical load. The speed reference, ω_r^*, is given as the input to the speed controller. Sensor measurements or estimates of the rotor speed are used to compute the speed error which is used to determine an electromagnetic torque reference signal, T_e^*.

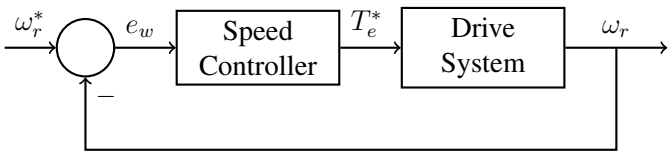

Figure 3.9: Block diagram of closed-loop speed controller.

A mechanical load model that includes the effect of both viscous and Coulomb friction results in rotor speed dynamics

$$\dot{\omega}_r = \frac{1}{J}\left(T_e^* - B_1\omega_r - B_0\,\mathrm{sgn}(\omega_r)\right) \tag{3.50}$$

The speed control loop is defined by an error-based PI compensator of the form

$$\begin{aligned} T_e^* &= k_{w1} e_w + k_{w2} \sigma_w \\ \dot{\sigma}_w &= e_w \\ e_w &= \omega_r^* - \omega_r \end{aligned} \tag{3.51}$$

The compensator gains k_{w1} and k_{w2} are selected to satisfy

$$\begin{aligned} k_{w1} &= 2J\alpha_w - B_1 \\ k_{w2} &= J\alpha_w^2 \end{aligned} \tag{3.52}$$

where α_w is the desired speed controller bandwidth. With this choice of controller gains, the rotor speed error dynamics in (3.50) augmented with the error integrator dynamics in (3.51) is characterized by

$$\begin{bmatrix} \dot{e}_w \\ \dot{\sigma}_w \end{bmatrix} = \begin{bmatrix} -2\alpha_w & -\alpha_w^2 \\ 1 & 0 \end{bmatrix} \begin{bmatrix} e_w \\ \sigma_w \end{bmatrix} + \begin{bmatrix} \frac{B_1}{J}\omega_r^* + \frac{B_0}{J}\,\mathrm{sgn}(\omega_r^* - e_w) \\ 0 \end{bmatrix} \tag{3.53}$$

and the associated characteristic polynomial is

$$(s + \alpha_w)^2 \tag{3.54}$$

If the commanded ω_r^* is constant, then ω_r will converge to ω_r^* with a settling time of approximately $5/\alpha_w$ and will reject constant disturbances such as the Coulomb friction.

CHAPTER 4

IDENTIFICATION OF ELECTROMECHANICAL PARAMETERS

Accurate control of the electromechanical system requires knowledge of the electrical and mechanical parameters of the system. Moreover, the design of the optimal kinetic energy recovery algorithms, that will be developed in the later chapters, relies on accurate electrical and mechanical load models for maximum effectiveness. The electrical parameters may be obtained from the data sheet of the electric machine or measured by conducting simple tests. Once the electrical parameters have been determined, a constant electromagnetic torque pulse is then used to excite the mechanical load using closed-loop current controllers that were discussed earlier. The dynamic response of the rotor speed is measured and the data is logged. Since a torque sensor is not available, the power converter leg currents are measured and logged and the electromagnetic torque is calculated using the formulas from Chapter 3. A schematic representation of the torque-pulse experiment is shown in Figure 4.1. Now that the input (T_e) and output (ω_r) to the physical plant are logged, a least-squares based parameter estimation algorithm is used to determine the parameters of the mechanical load. The following section will discuss the identification of electrical and mechanical parameters for three types of electric machines: SPMs, IPMs, and induction machines.

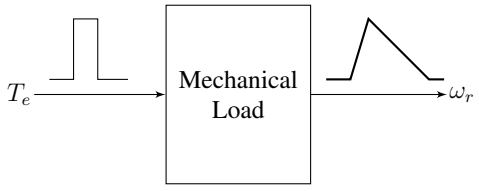

Figure 4.1: Schematic representation of the torque-pulse experiment.

4.1 SPM

The SPM electromechanical system shown in Figure 4.2 consists of an SPM electrical machine manufactured by Anaheim Automation (BLY172D-24V-4000) and a set of aluminum discs that are fastened together to form an inertia wheel. The inertia wheel is mounted on the rotor shaft of the electric machine to act as a mechanical load. This section discusses the process of determining the electrical and mechanical parameters of the SPM system.

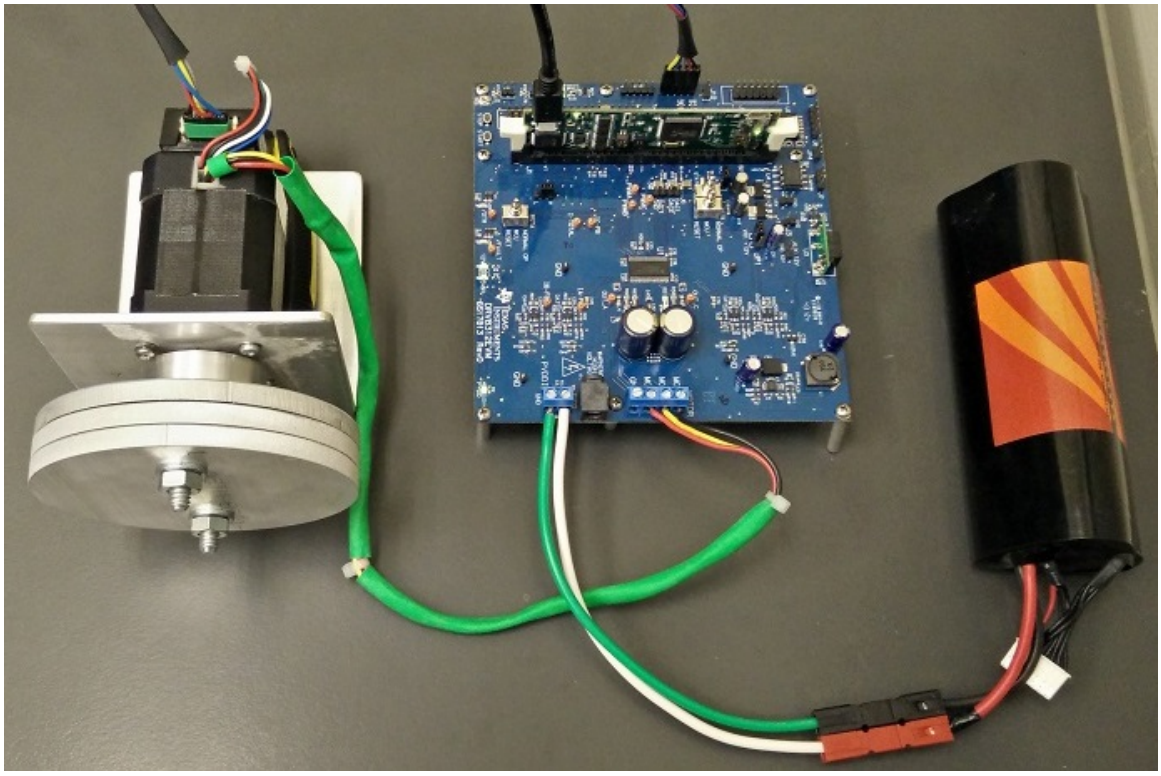

Figure 4.2: The Anaheim SPM experimental system.

4.1.1 Electrical Parameters

The data sheet for the Anaheim Automation SPM electrical machine indicates the stator windings are Δ-connected and the rotor has eight poles, so the number of pole-pairs is

$$N = 4 \tag{4.1}$$

The data sheet also indicates that the line-to-line resistance and inductance are $0.8\ \Omega$ and 1.2 mH. These values are verified using an RLC-meter by measuring the series resistance and inductance across any two of the three terminals of the stator windings. Since the stator windings are Δ-connected, this measurement puts one phase winding in parallel across a series connection of the other two phase windings. The per-phase values of the resistance and inductance are determined as

$$R_{\mathrm{LL}} = \frac{2}{3} R_s = 0.8\ \Omega \quad \Longrightarrow \ R_s = 1.2\ \Omega \tag{4.2}$$

and

$$L_{\mathrm{LL}} = \frac{2}{3} L = 1.2\ \mathrm{mH} \quad \Longrightarrow \ L = 1.8\ \mathrm{mH} \tag{4.3}$$

For the SPM, the permanent-magnets are stuck onto the surface of the rotor. This means that the presence of permanent magnets (low-permeability material) presents equal reluctance to the magnetic-flux path at all rotor positions. This results in an equal value of stator inductance along both the direct and quadrature axes

$$L_d = L_q = L = 1.8\ \mathrm{mH} \tag{4.4}$$

To determine the value of permanent-magnet flux parameter, Λ_m, the following test is conducted. The rotor is made to spin at a constant speed ω_r with the stator windings open

circuited. This results in the production of an induced sinusoidal voltage across any two terminals of the stator winding, with the peak value given by

$$V_P = \Lambda_m N \omega_r \tag{4.5}$$

The data sheet ratio of the back EMF constant, which is the ratio of the induced voltage to the rotor speed, is equal to 3.32 V/krpm, so it follows that

$$\Lambda_m N = 3.72 \text{ V/krpm} = 35.5 \text{ mWb} \quad \Longrightarrow \quad \Lambda_m = 8.9 \text{ mWb} \tag{4.6}$$

Using the power-invariant version of the dq transformation matrix in (3.14), the permanent-magnet flux coefficient in the dq reference frame is

$$\Lambda = \sqrt{\frac{3}{2}} \Lambda_m = 10.9 \text{ mWb} \tag{4.7}$$

and the associated back EMF constant is

$$K = N\Lambda = 43.6 \text{ mV/rad/s} \tag{4.8}$$

The maximum current through the power converter switches is set to $I_{\text{sw,max}} = 6$ A and the maximum length of the current vector in the dq reference frame for the Δ-connected machine from Table 3.1 is

$$I_{\max} = \sqrt{\frac{1}{2}} I_{\text{sw,max}} = 4.24 \text{ A} \tag{4.9}$$

The maximum electromagnetic torque that can be produced by the SPM under this current limit constraint is

$$T_{e,\max} = K I_{\max} = 0.185 \text{ Nm} \tag{4.10}$$

A summary of the electrical parameters is shown in Table 4.1(a).

4.1.2 Mechanical Parameters

The mechanical parameters of the SPM system shown in Figure 4.2 are determined using a torque-pulse test. The electrical parameters that were determined in the previous section are used to produce a torque-pulse for a short duration. The mechanical load is excited and responds by accelerating for the duration of the torque-pulse, which is then followed by a period of free-deceleration. The response of the rotor speed dynamics is measured and logged. The electromagnetic torque is also measured or estimated from current measurements and logged. A least-squares parameter estimation algorithm is used to process the logged values of rotor speed and electromagnetic torque to determine the parameters of the mechanical load. This section describes the development of the least-squares parameter estimation algorithm used to determine the mechanical parameters and the experimental results.

Least-Squares Parameter Estimation

Since a small amount of Coulomb friction is generally present in any mechanical system, a mechanical load model that includes the effect of both viscous friction and Coulomb friction is used

$$T_{\text{load}} = B_1 \omega_r + B_0 \, \text{sgn}(\omega_r) \tag{4.11}$$

where B_1 is the viscous friction coefficient and B_0 is the Coulomb friction coefficient. The rotor speed dynamics are

$$\dot{\omega}_r = \frac{1}{J} \left(T_e - T_{\text{load}} \right) \tag{4.12}$$

which is rewritten as

$$\dot{\omega}_r = \frac{1}{J}\left(T_e - B_1\omega_r - B_0\ \mathrm{sgn}(\omega_r)\right) \tag{4.13}$$

This can be represented using a generic non-linear scalar system as

$$\dot{x} = af(x) + bg(x) + cu \tag{4.14}$$

where

$$x = \omega_r,\ \ u = T_e,\ \ f(x) = \omega_r,\ \ g(x) = \mathrm{sgn}(\omega_r) \tag{4.15}$$

and

$$a = -\frac{B_1}{J},\ \ b = -\frac{B_0}{J},\ \ c = \frac{1}{J} \tag{4.16}$$

The non-linear system described in (4.14) can be rewritten as

$$\dot{x} = \hat{\theta}^T\phi \tag{4.17}$$

where

$$\hat{\theta} = \begin{bmatrix}\hat{a} & \hat{b} & \hat{c}\end{bmatrix}^T,\ \ \phi = \begin{bmatrix}f(x) & g(x) & u\end{bmatrix}^T \tag{4.18}$$

Using a method that is similar to the one described in [69], a first-order filtered equation of the system can be written as

$$z = \hat{\theta}^T\phi_f \tag{4.19}$$

where $z = H_1(s)\ x$ and $\phi_f = H_0(s)\ \phi$ with

$$H_i(s) = \frac{\lambda\ s^i}{s + \lambda} \tag{4.20}$$

where λ is the filter cutoff frequency. The $H_0(s)$ filter is implemented by using the following state-space model

$$A_0 = -\lambda, \quad B_0 = 1, \quad C_0 = \lambda, \quad D_0 = 0 \tag{4.21}$$

and $H_1(s)$ is implemented using

$$A_1 = -\lambda, \quad B_1 = 1, \quad C_1 = -\lambda^2, \quad D_1 = \lambda \tag{4.22}$$

Using (4.19), the parameter vector, $\hat{\theta}$, is obtained using the expression

$$\hat{\theta} = \left[\phi_f \phi_f^T\right]^{-1} \phi_f z \tag{4.23}$$

In the above equation, z and ϕ_f are stacked versions of (4.19). The mechanical parameters are extracted from the elements of $\hat{\theta}$ as

$$\hat{J} = \frac{1}{\hat{c}} \quad \hat{B}_1 = -\frac{\hat{a}}{\hat{c}}, \quad \hat{B}_0 = -\frac{\hat{b}}{\hat{c}} \tag{4.24}$$

Experimental Results

The DRV-8312 Motor Control Board with the F28069 microcontroller from Texas Instruments is used for the experiments. The power converter switching frequency is 30 kHz, the current-controller update frequency is 12.5 kHz, and the current-controller bandwidth is 2500 rad/s. The rotor speed is measured using a shaft-mounted quadrature encoder, with signal processing that combines two forms of differentiation; variable position over fixed

time, and fixed position over variable time. The encoder measurement is also used for electronic commutation to ensure synchronous three-phase operation of the electric machine. The leg currents are measured by sampling the voltage across shunt resistors located between the low-side switches and the negative battery terminal. Torque-pulses that are fractions of the maximum electromagnetic torque of the machine are applied for small duration. The closed-loop current-controller in Figure 3.4 is used to regulate the machine currents. The measured leg currents are transformed to the dq reference frame using the measured rotor angle and the electromagnetic torque is calculated as $T_e = Ki_q$ and is logged. The response of the rotor speed is also measured and logged. The data-logging frequency is 50 Hz. Torque-pulses equal to 20%, 30%, 40%, and 50% of $T_{e,\max}$ are applied for 0.5 seconds and zero torque is applied after $t = 0.5$ seconds. The data is then used in the least-squares parameter estimation algorithm described in the previous section to determine the values of J, B_1, and B_0. Figure 4.3(a) shows the application of 40% of the maximum torque for 0.5 seconds and Figure 4.3(b) compares the rotor speed response from the experiment (blue) and simulation using the least-squares estimation parameters (dashed red) which show good agreement with each other. Table 4.1(b) shows the average values of the mechanical parameters for four different experiments using 20%, 30%, 40%, and 50% of the maximum torque.

The experimental observation that the permanent-magnet synchronous machine apparently exhibits a significant Coulomb friction term, especially evident during the free deceleration interval of Figure 4.3(b), requires some explanation. This friction term arises primarily due to magnetic, rather than mechanical, phenomena. During free deceleration the stator current is zero, but the stator iron experiences a relatively large level of magnetic hysteresis due to the rotation of the rotor magnets; the rotor iron also experiences a relatively small level of magnetic hysteresis due to the stator saliency seen by the rotor magnets (which also gives rise to cogging torque). During free deceleration, the sole source of magnetic hysteresis in both the stator iron and the rotor iron is rotor magnet rotation, and

therefore the power loss associated with this magnetic hysteresis must be supplied by the kinetic energy of the rotor, rather than by the electric energy stored in the battery pack; this power loss is proportional to rotor speed, so the constant torque associated with this power loss represents a magnetic effect that is indistinguishable from Coulomb friction (a constant torque opposing motion). A finite-element method for computation of hysteresis torque is presented in [70]. The Coulomb friction-like term that was identified only accounts for the permanent-magnet hysteresis loss and does not account for electromagnetic hysteresis loss.

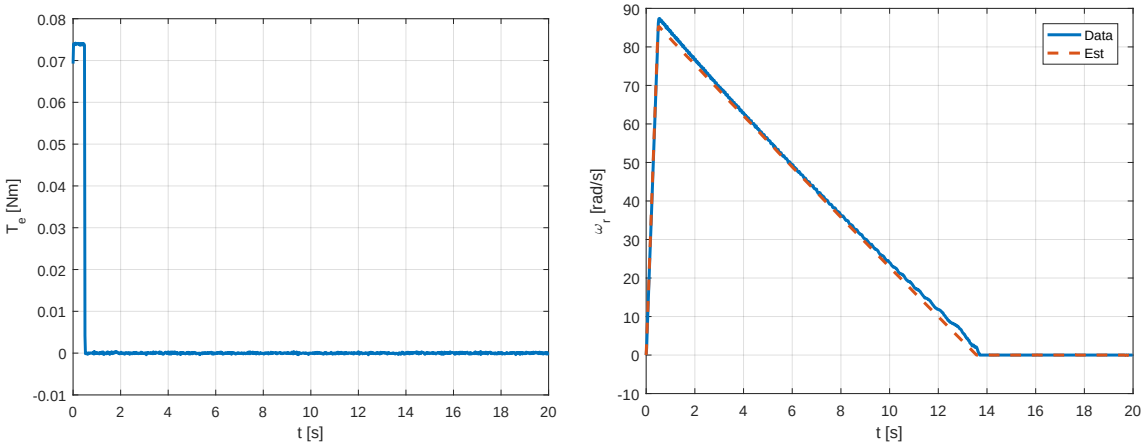

(a) 40% of $T_{e,\max}$ torque-pulse

(b) Rotor speed response

Figure 4.3: Comparison of the electromagnetic torque and rotor speed data from the experiment and simulation using estimated parameters for the Anaheim SPM system.

4.2 IM

The IM electromechanical system shown in Figure 4.4 consists of an induction electrical machine manufactured by Motorsolver and a set of aluminum discs that form an inertia wheel which acts as the mechanical load, similar to the SPM system. The identification of the electrical and mechanical parameters of the induction machine system is discussed in this section.

Table 4.1: Electrical and Mechanical Parameters of the Anaheim SPM System.

(a) Anaheim Automation SPM Electrical Parameters (BLY172D-24V-4000)

Parameter	Value	Units
N	4	-
R_s	1.2	Ohm
$L_d = L_q = L$	1.8	mH
Λ	10.9	mWb
K	43.6	mV/rad/s
$I_{\max}$	4.24	A
$T_{e,\max}$	0.185	Nm

(b) Estimated Mechanical Parameters

Parameter	Value	Units
J	4.11×10^{-4}	kg-m^2
B_1	7.73×10^{-6}	Nm/rad/s
B_0	2.38×10^{-3}	Nm

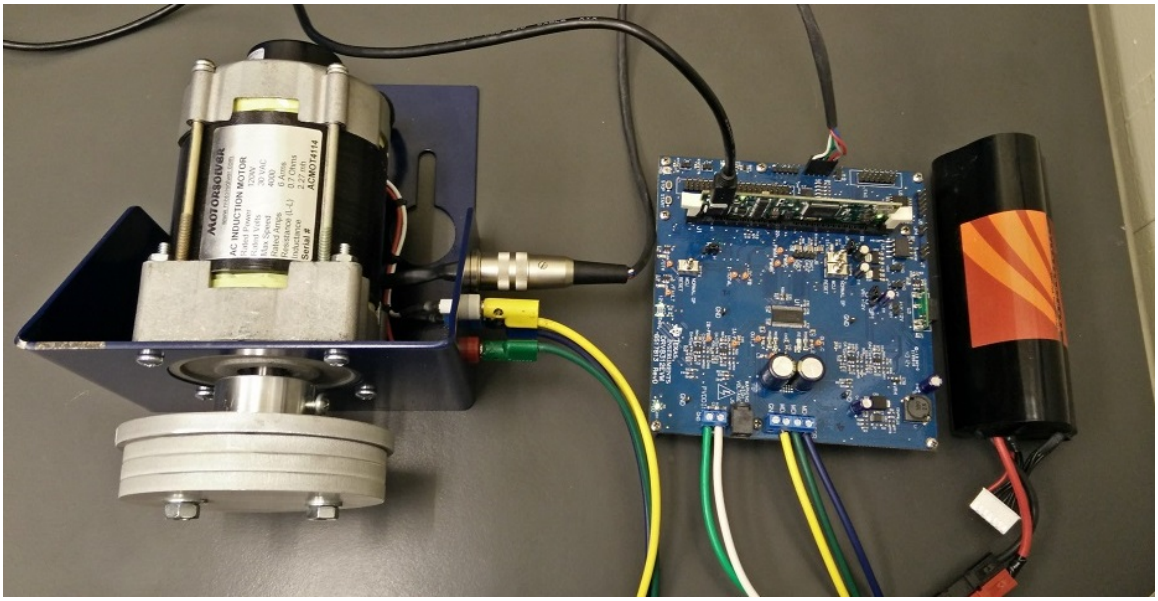

Figure 4.4: The Motorsolver induction machine experimental system.

4.2.1 Electrical Parameter Estimation

The electrical parameters of the induction machine were determined using a set of steady-state AC measurement tests and a DC measurement test. The steady-state forms of the electrical dynamics in (3.24) and (3.25) reveal the relationship between the applied stator voltages, rotor flux, and stator currents, which can be summarized as

$$\begin{aligned} v_d &= R_{\text{eq}} i_d - \omega_e L_{\text{eq}} i_q \\ v_q &= R_{\text{eq}} i_q + \omega_e L_{\text{eq}} i_d \end{aligned} \tag{4.25}$$

where R_{eq} and L_{eq} are the equivalent resistance and inductance values defined by

$$\begin{aligned} R_{\text{eq}} &= R_s + R_r \frac{\omega_e \omega_s L_m^2}{R_r^2 + \omega_s^2 L_r^2} \\ L_{\text{eq}} &= L_s - L_r \frac{\omega_s^2 L_m^2}{R_r^2 + \omega_s^2 L_r^2} \end{aligned} \tag{4.26}$$

The AC impedance tests that are used to determine the electrical parameters, rely on the ability to apply known stator voltages and measure corresponding values of stator currents in (4.25). This can be achieved by applying a constant excitation frequency, ω_e. The slip frequency, ω_s, is related to the excitation frequency and rotor mechanical speed, ω_r, according to

$$\omega_s = \omega_e - N\omega_r \tag{4.27}$$

where N is the number of pole-pairs. To conduct the AC impedance measurement experiments, the induction machine is mechanically coupled to a second speed controlled permanent-magnet DC machine, which is used to impose the desired slip values. The two-machine experimental system is shown in Figure 4.5. The tests that were conducted are described in the following series of steps.

1. To determine the number of pole-pairs, the induction machine was excited using

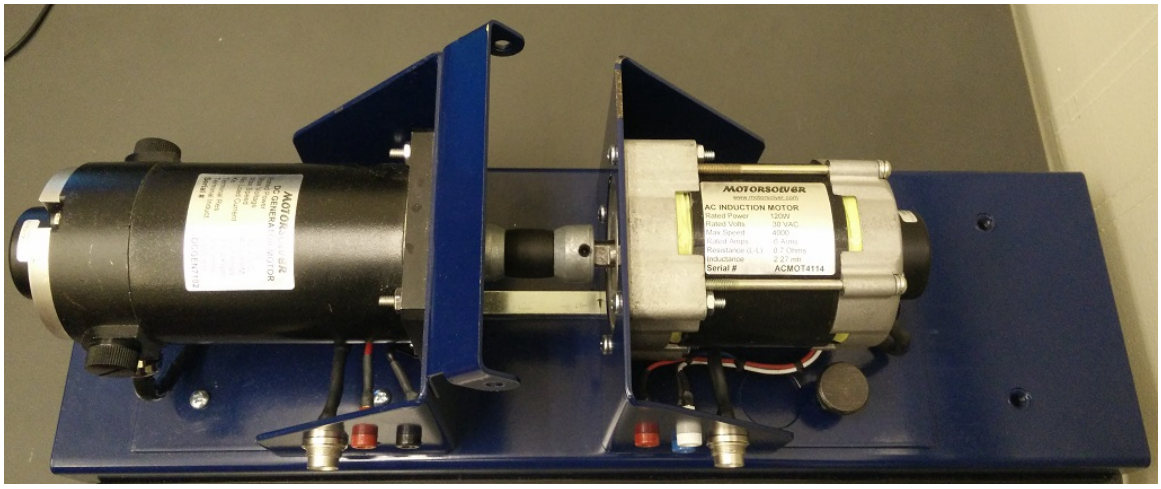

Figure 4.5: The two-machine experimental system consisting of the induction machine and the PMDC machine.

a constant-frequency excitation, resulting in low slip. For this test, an excitation-frequency of $\omega_e = 120\pi$, is used and the steady-state rotor mechanical speed was measured to be $\omega_r = 179.86$ rad/s. The number of pole-pairs, N, is determined as the largest integer not exceeding ω_e/ω_r,

$$\frac{\omega_e}{\omega_r} = 2.096, \quad \Longrightarrow \; N = 2 \tag{4.28}$$

2. The next test performed was a DC resistance test to determine the stator-winding resistance. Two stator winding terminals of the induction machine were connected to the power converter at two of its legs. The power converter was used to apply a DC voltage v_{LL} across the two stator winding terminals, and the resulting current i_{LL} flowing through the windings was measured for several trials. The stator windings of the induction machine are Δ-connected, resulting in

$$R_{LL} = \frac{v_{LL}}{i_{LL}} = \frac{2}{3}R_s = 0.62\ \Omega \quad \Longrightarrow \; R_s = 0.93\ \Omega \tag{4.29}$$

3. The third test performed was a zero-slip test. The induction machine was excited

using constant-frequency, ω_e. Then, the rotor speed of the mechanically-connected PMDC machine was speed-controlled to achieve a speed $\omega_r \approx \omega_e/N$. This results in zero-slip from (4.27), and the expressions in (4.26) reduce to

$$R_{\text{eq}} \approx R_s, \quad L_{\text{eq}} \approx L_s \tag{4.30}$$

Measuring the direct and quadrature axes currents and voltages, a known excitation frequency, and previously measured stator winding resistance can be used to determine L_{eq}. Several trials are conducted and a least-square data fitting results in

$$L_{\text{eq}} \approx L_s = 34.19 \text{ mH} \tag{4.31}$$

4. The final test that is conducted is the unity-slip test. In this test, the induction machine is excited using a constant frequency ω_e. The PMDC machine is used in closed-loop speed control mode to regulate the rotors of the combined two-machine system at zero speed. Imposing $\omega_r \approx 0$ achieves unity-slip from (4.27) and the equivalent resistance and inductance in (4.26) simplify to

$$\begin{aligned} R_{\text{eq}} &= R_s + R_r \frac{L_m^2}{L_r^2} \\ L_{\text{eq}} &= L_s - L_r \frac{L_m^2}{L_r^2} \end{aligned} \tag{4.32}$$

assuming $\omega_e >> R_r/L_r$. Measuring the direct and quadrature axes currents and voltages and a known excitation frequency can be used to determine both R_{eq} and L_{eq}. Using the values of R_s and L_s from the previous steps, R_r, L_r, and L_m can be determined using algebraic expressions. Several trials are conducted and a least-square data fitting results in

$$R_r = 1.76\ \Omega, \quad L_r = 34.19 \text{ mH}, \quad L_m = 32.15 \text{ mH} \tag{4.33}$$

The maximum allowable current through the power converter switches is $I_{\mathrm{sw,max}} = 6$ A and the maximum length of the stator current vector in the dq reference frame for the Δ-connected machine from Table 3.1 is

$$I_{\max} = \sqrt{\frac{1}{2}} I_{\mathrm{sw,max}} = 4.24 \text{ A} \tag{4.34}$$

The maximum electromagnetic torque that can be produced by the induction machine under current constraints is determined using stator winding current references

$$i^*_{d,\max} = i^*_{q,\max} = \sqrt{\frac{1}{2}} I_{\max} = 3 \text{ A} \tag{4.35}$$

This choice is in accordance with the maximum-torque-per-amp (MTPA) logic discussed in [67] and [68]. The resulting value of maximum electromagnetic torque is calculated using

$$T_{e,\max} = \frac{NL_m^2}{L_r} i^*_{d,\max} i^*_{q,\max} = \frac{NL_m^2}{2L_r} I^2_{\max} = 0.544 \text{ Nm} \tag{4.36}$$

A summary of the estimated electrical parameters of the induction machine is reported in Table 4.2(a).

4.2.2 Mechanical Parameter Estimation

The mechanical parameters of the induction machine system are determined using a torque-pulse test. The estimated electrical parameters that were determined in the previous section were used to implement indirect field-oriented control. A constant direct-axis current is used to set up a constant rotor-flux in the air-gap. The quadrature-axis current is then used to command a desired value of electromagnetic torque. The current commands

used to produce constant torque from (3.26) are

$$\begin{aligned} i_d^* &= \bar{i}_d \\ i_q^* &= \frac{L_r}{NL_m^2}\frac{T_e^*}{\bar{i}_d} \end{aligned} \tag{4.37}$$

The torque-pulse is applied for a duration of 0.5 seconds and the response of the rotor speed is measured and logged. The leg currents were also measured and transformed to the synchronous dq reference frame using measurements of the rotor angle and estimation of slip-angle. Constant direct-axis currents equal to $\bar{i}_d = 1.5$ A and $\bar{i}_d = 2.0$ A were used with quadrature-axis currents to produce constant torque-pulses equal to 20%, 30%, 40%, and 50% of the maximum electromagnetic torque. For each trial the responses of the rotor speed and dq currents were logged. Since a torque sensor is not available, the electromagnetic torque is estimated from the stator dq currents using the formula from (3.26). The least-squares parameter estimation algorithm discussed in the previous section requires experimental data of the electromagnetic torque and rotor speed to determine the parameters of a mechanical load of the form

$$T_{\text{load}} = B_1\omega_r + B_0\ \text{sgn}(\omega_r) \tag{4.38}$$

The experimental rotor speed and electromagnetic torque data is used in the least-squares parameter estimation algorithm to determine the values of J, B_1, and B_0. Figure 4.6(b) compares experiment and estimated parameter simulation of the rotor speed response to a 40% of maximum torque pulse with $\bar{i}_d = 1.5$ A. The average of four different least-squares parameter estimation results using 20%, 30%, 40%, and 50% of the maximum torque with $\bar{i}_d = 1.5$ A is listed in Table 4.3(b). The results of the mechanical parameter estimation algorithm show that the mechanical load in Figure 4.4 is characterized by both a viscous friction and a Coulomb friction component. However, the effect of the Coulomb friction is less pronounced with a B_0/B_1 ratio of approximately 23. In comparison, the Anaheim SPM

system has $B_0/B_1 \approx 308$ due to the effect of magnetic hysteresis. The exponential shape of the free deceleration response of the induction machine system in Figure 4.6(b) compared to the straight-line free deceleration response of the SPM system in Figure 4.3(b), also indicates that the latter has a dominant Coulomb friction-like component in its mechanical characteristics.

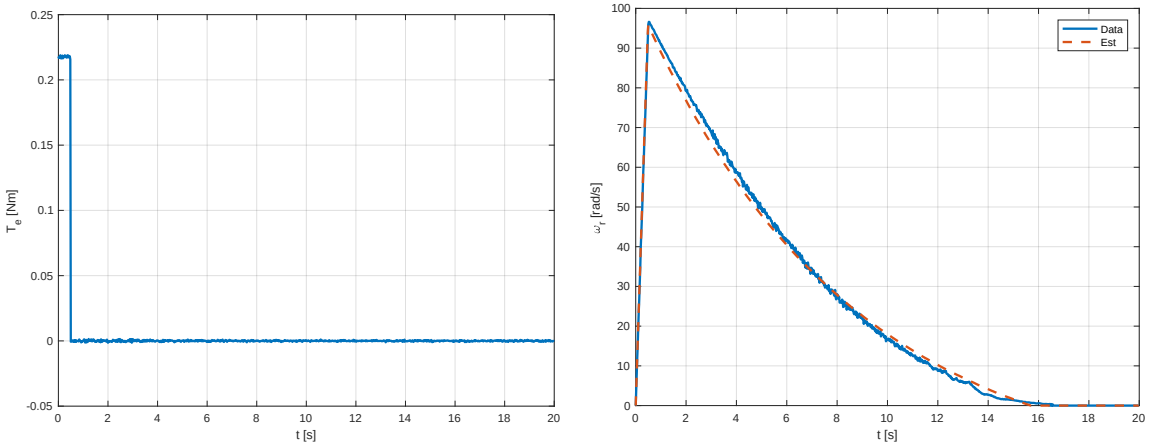

(a) 40% of $T_{e,\max}$ torque-pulse

(b) Rotor speed response

Figure 4.6: Comparison of the electromagnetic torque and rotor speed data from the experiment and simulation using estimated parameters for the Motorsolver induction machine system with $\bar{i}_d = 1.5$ A.

Table 4.2: Electrical and Mechanical Parameters of the Motorsolver Induction Machine System.

(a) Mototsolver IM Electrical Parameters (4-Pole AC Induction Motor)

Parameter	Value	Units
N	2	-
R_s	0.93	Ohm
R_r	1.76	Ohm
L_m	32.15	mH
L_s	34.19	mH
L_r	34.19	mH
$I_{\max}$	4.24	A
$T_{e,\max}$	0.54	Nm

(b) Estimated Mechanical Parameters

Parameter	Value	Units
J	10.11×10^{-4}	kg-m^2
B_1	1.29×10^{-4}	Nm/rad/s
B_0	2.59×10^{-3}	Nm

4.3 IPM

The IPM electromechanical system shown in Figure 4.7 consists of an IPM electrical machine from Motorsolver and a set of aluminum discs which act as the mechanical load. This section discusses the procedures to determine the electrical and mechanical parameters of the IPM system.

4.3.1 Electrical Parameter Estimation

The data sheet from the electrical machine manufacturer indicates that the rotor steel has four permanent-magnets embedded in it, resulting in $N = 2$ pole-pairs. The data sheet also indicates that the stator windings are wye-connected. The identification of the electrical system parameters such as resistance, inductance, permanent-magnet flux coefficient, and maximum electromagnetic torque is described as follows:

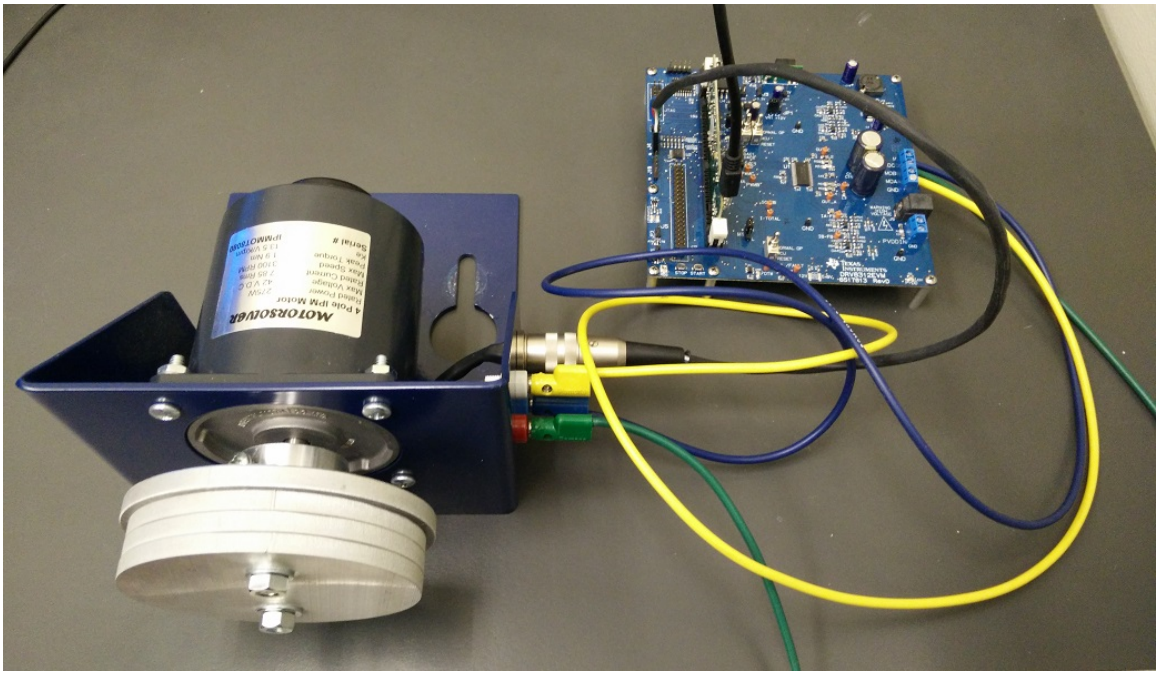

Figure 4.7: The Motorsolver IPM machine experimental system.

Measurement of Resistance

The per-phase stator winding resistance is determined by measuring the resistance between any two terminals. Measurements between the three pairs of terminals are taken and the average value is reported as

$$R_{LL} = 2R_s = 365.5 \text{ m}\Omega, \quad \Longrightarrow \quad R_s = 182.75 \text{ m}\Omega \tag{4.39}$$

Measurement of Inductance

Interior permanent-magnet synchronous machines have permanent-magnets embedded inside the rotor steel as seen in Figure 3.2(b). The permanent-magnets, which are made of low-permeability material, are aligned along the direct-axis of the machine. As a result, the magnetic reluctance along the direct-axis is more than that along the quadrature-axis (which has more high-permeability steel). The inductance, which is inversely proportional to magnetic reluctance, is greater along the q-axis than the d-axis, i.e. $L_d < L_q$. This also

means that the per-phase stator winding inductance is a function of the rotor position. If the self inductances of the stator windings are L_{aa}, L_{bb} and L_{cc}, and the mutual inductances are L_{ab}, L_{ba}, L_{ac}, L_{ca}, L_{bc} and L_{cb}, then the three-phase inductance matrix for an IPM is written as

$$\mathbf{L}_{abc}(\theta_r) = \begin{bmatrix} L_{aa} & L_{ab} & L_{ac} \\ L_{ba} & L_{bb} & L_{bc} \\ L_{ca} & L_{cb} & L_{cc} \end{bmatrix} = \begin{bmatrix} L_{ls}+L_{0s} & -\frac{1}{2}L_{0s} & -\frac{1}{2}L_{0s} \\ -\frac{1}{2}L_{0s} & L_{ls}+L_{0s} & -\frac{1}{2}L_{0s} \\ -\frac{1}{2}L_{0s} & -\frac{1}{2}L_{0s} & L_{ls}+L_{0s} \end{bmatrix} - L_{2s} \begin{bmatrix} \cos(2N\theta_r) & \cos\left(2N\theta_r - \frac{2\pi}{3}\right) & \cos\left(2N\theta_r + \frac{2\pi}{3}\right) \\ \cos\left(2N\theta_r - \frac{2\pi}{3}\right) & \cos\left(2N\theta_r + \frac{2\pi}{3}\right) & \cos\left(2N\theta_r\right) \\ \cos\left(2N\theta_r + \frac{2\pi}{3}\right) & \cos\left(2N\theta_r\right) & \cos\left(2N\theta_r - \frac{2\pi}{3}\right) \end{bmatrix} \tag{4.40}$$

where N is the number of pole-pairs in the rotor, θ_r is the rotor angular position, L_{ls} is the leakage inductance, L_{0s} is the zero-order harmonic of the self-inductance, and L_{2s} is the second-order harmonic of the self-inductance. Using the power-invariant transformation matrix

$$\mathbf{K}(\theta_r) = \sqrt{\frac{2}{3}} \begin{bmatrix} \cos\left(N\theta_r\right) & \cos\left(N\theta_r - \frac{2\pi}{3}\right) & \cos\left(N\theta_r + \frac{2\pi}{3}\right) \\ -\sin\left(N\theta_r\right) & -\sin\left(N\theta_r - \frac{2\pi}{3}\right) & -\sin\left(N\theta_r + \frac{2\pi}{3}\right) \\ \sqrt{\frac{1}{2}} & \sqrt{\frac{1}{2}} & \sqrt{\frac{1}{2}} \end{bmatrix}, \tag{4.41}$$

the rotor angle-dependent three-phase (abc) inductance matrix is transformed to a rotor angle-independent $dq0$ inductance matrix

$$\begin{aligned} \mathbf{L}_{dq0} &= \mathbf{K}(\theta_r)\mathbf{L}_{abc}(\theta_r)\mathbf{K}(\theta_r)^{-1} \\ &= \begin{bmatrix} L_{ls}+\frac{3}{2}L_{0s}-\frac{3}{2}L_{2s} & 0 & \\ 0 & L_{ls}+\frac{3}{2}L_{0s}+\frac{3}{2}L_{2s} & 0 \\ 0 & 0 & L_{ls} \end{bmatrix} \end{aligned} \tag{4.42}$$

To summarize, the direct-axis inductance is

$$L_d = L_{ls} + \frac{3}{2}L_{0s} - \frac{3}{2}L_{2s} \tag{4.43}$$

and the quadrature-axis inductance is

$$L_q = L_{ls} + \frac{3}{2}L_{0s} + \frac{3}{2}L_{2s} \tag{4.44}$$

An LCR meter is used to measure the series inductance between two of the three terminals of the wye-connected IPM as shown in Figure 4.8. The two leads of the LCR meter are connected to stator winding terminals A and B.

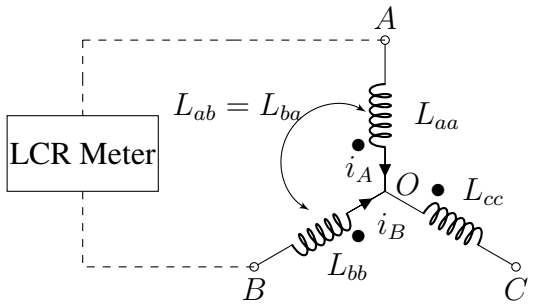

Figure 4.8: Measurement of the stator-winding inductance using an LCR meter.

The dot convention used in Figure 4.8 is explained as follows:

- If current "enters" the dotted terminal of a coil, the reference polarity of the induced voltage in the other coil is positive at its dotted terminal.
- If current "leaves" the dotted terminal of a coil, the reference polarity of the induced voltage in the other coil is negative at its dotted terminal.

The figure shows that current i_B "leaves" the dot, therefore the polarity of the induced voltage in phase A due to the current in phase B is negative at the location of the dot. According to Kirchhoff's voltage law, the polarity of the self-induced emf in phase A is

positive at the A terminal and negative at the O terminal. Therefore, the total voltage drop across phase A is

$$V_{AO} = R_s i_A + L_{aa}\frac{di_A}{dt} + L_{ab}\frac{di_B}{dt} \tag{4.45}$$

Similarly, the voltage drop across phase B is

$$V_{BO} = R_s i_B + L_{bb}\frac{di_B}{dt} + L_{ba}\frac{di_A}{dt} \tag{4.46}$$

The LCR meter applies a voltage V_{AB} across the two-terminals which can be calculated using KVL as

$$\begin{aligned} V_{AB} &= V_{AO} - V_{BO} \\ &= R_s i_A + L_{aa}\frac{di_A}{dt} + L_{ab}\frac{di_B}{dt} - R_s i_B - L_{bb}\frac{di_B}{dt} - L_{ba}\frac{di_A}{dt} \end{aligned} \tag{4.47}$$

and the resulting current flow is

$$i_A = -i_B = i \tag{4.48}$$

The voltage equation in (4.47) is simplified as

$$\begin{aligned} V_{AB} &= R_s i + L_{aa}\frac{di}{dt} - L_{ab}\frac{di}{dt} + Ri + L_{bb}\frac{di}{dt} - L_{ba}\frac{di}{dt} \\ &= R_{AB} i + L_{AB}\frac{di}{dt} \end{aligned} \tag{4.49}$$

where $R_{AB} = 2R_s$ and $L_{AB} = L_{aa} - L_{ab} - L_{ba} + L_{bb}$. Substituting the values of L_{aa},L_{ab},L_{ba}

and L_{bb} from (4.40), results in

$$\begin{aligned} L_{AB} &= L_{ls} + L_{0s} - L_{2s}\cos\left(2N\theta_r\right) + \frac{1}{2}L_{0s} + \frac{1}{2}L_{0s} \\ &\quad + L_{ls} + L_{0s} - L_{2s}\cos\left(2N\theta_r + \frac{2\pi}{3}\right) \\ &= 2L_{ls} + 3L_{0s} - 3L_{2s}\cos\left(2N\theta_r + \frac{\pi}{3}\right) \end{aligned} \tag{4.50}$$

The minimum and maximum values of L_{AB} are obtained by substituting $N\theta_r = \frac{5\pi}{6}$ and $N\theta_r = \frac{\pi}{3}$ respectively,

$$\begin{aligned} \min(L_{AB}) &= 2L_{ls} + 3L_{0s} - 3L_{2s} \\ \max(L_{AB}) &= 2L_{ls} + 3L_{0s} + 3L_{2s} \end{aligned} \tag{4.51}$$

The expressions for the direct and quadrature axis inductances from (4.43) and (4.44) are related to minimum and maximum values of the line-to-line inductance measurements as follows

$$\begin{aligned} L_d &= \frac{1}{2}\min(L_{AB}) = L_{ls} + \frac{3}{2}L_{0s} - \frac{3}{2}L_{2s} \\ L_q &= \frac{1}{2}\max(L_{AB}) = L_{ls} + \frac{3}{2}L_{0s} + \frac{3}{2}L_{2s} \end{aligned} \tag{4.52}$$

Therefore, the values for L_d and L_q are obtained from the minimum and maximum line-to-line inductance measurements as the rotor is slowly rotated. The measurements are repeated for the other two pairs of stator winding terminals BC and CA and the average values of the direct and quadrature axis inductances are calculated as

$$\begin{aligned} L_d &= \frac{1}{3}\left(\frac{1}{2}\min(L_{AB}) + \frac{1}{2}\min(L_{BC}) + \frac{1}{2}\min(L_{CA})\right) = 0.55 \text{ mH} \\ L_q &= \frac{1}{3}\left(\frac{1}{2}\max(L_{AB}) + \frac{1}{2}\max(L_{BC}) + \frac{1}{2}\max(L_{CA})\right) = 1.31 \text{ mH} \end{aligned} \tag{4.53}$$

Measurement of Back-EMF Constant

To determine the back-EMF constant of the Motorsolver IPM machine, the open-circuit voltage of the machine is measured using a two-machine dynamometer kit. The IPM is mounted on a two-machine dynamometer kit and mechanically coupled to a PMDC machine. The speed of the PMDC machine is regulated using a closed-loop controller. The three stator terminals of the IPM are connected directly to an oscilloscope and the frame of the motor is used for grounding the oscilloscope signals. The PMDC machine is made to rotate at a fixed speed, that is measured using a shaft-mounted quadrature encoder and the rotor speed is estimated as discussed earlier. The open-circuit voltage of the IPM is obtained on the oscilloscope and measurements from all three phases are logged using the built-in function of the oscilloscope. Data are logged for 100 ms at 625 kHz. A schematic representation of the back EMF voltage measurement experiment setup is shown in Figure 4.9.

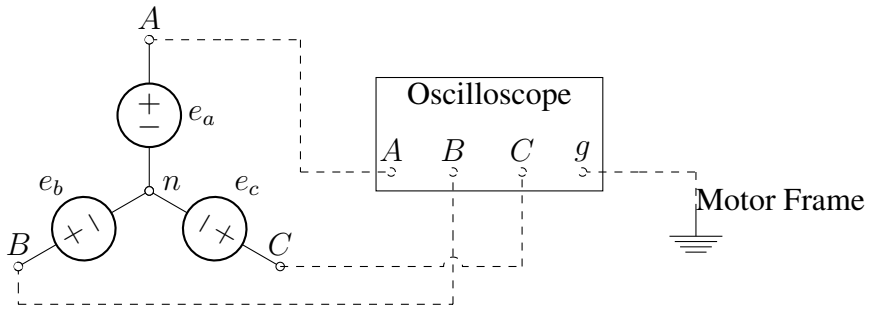

Figure 4.9: Schematic representation of the back-EMF voltage measurement experiment.

The symbols e_a, e_b, and e_c represent the internal phase voltages; A, B, and C are the three terminals of the stator winding; and n is the floating neutral of the wye-connected system. The three stator terminals are connected to the oscilloscope and the motor frame is used to ground the oscilloscope signals which is represented as g. According to Kirchhoff's

voltage law

$$\begin{aligned} v_A &= v_{Ag} = e_a + v_{ng} \\ v_B &= v_{Bg} = e_b + v_{ng} \\ v_C &= v_{Cg} = e_c + v_{ng} \end{aligned} \tag{4.54}$$

If the stator windings are assumed to be balanced and symmetric, then $e_a + e_b + e_c = 0$, resulting in

$$v_{ng} = \frac{1}{3}\left(v_A + v_B + v_C\right) \tag{4.55}$$

Substituting this in (4.54) and solving for e_a, e_b, and e_c, results in

$$\begin{bmatrix} e_a \\ e_b \\ e_c \end{bmatrix} = \frac{1}{3}\begin{bmatrix} 2 & -1 & -1 \\ -1 & 2 & -1 \\ -1 & -1 & 2 \end{bmatrix}\begin{bmatrix} v_A \\ v_B \\ v_C \end{bmatrix} \tag{4.56}$$

The desired speed of the PMDC machine in the two-machine system is set to 100 rad/s and the open-circuit voltage of the IPM machine is measured and logged. The three-phase open-circuit voltages are plotted for one electrical cycle in Figure 4.10. Observe that the profile of the back-emf voltage is not perfectly sinusoidal. To extract the harmonics that characterize the non-sinusoidal back-emf voltage, a fast Fourier Transform (FFT) algorithm is used. The open-circuit voltage for one of the phases was used in the FFT algorithm to extract the frequency-domain information from the raw data. Figure 4.11 shows the relative amplitude of sinusoids at harmonic frequencies of the fundamental frequency for the Motorsolver IPM. The FFT results show that the 5^{th}, 7^{th}, and 11^{th} harmonics are dominant after the fundamental frequency. The FFT analysis also gives the phase angle associated with the sinusoids at harmonic frequencies which can be used to obtain a closed-form expression for the back EMF voltages. Let K_m represent the back-EMF constant, ω_r the rotor speed,

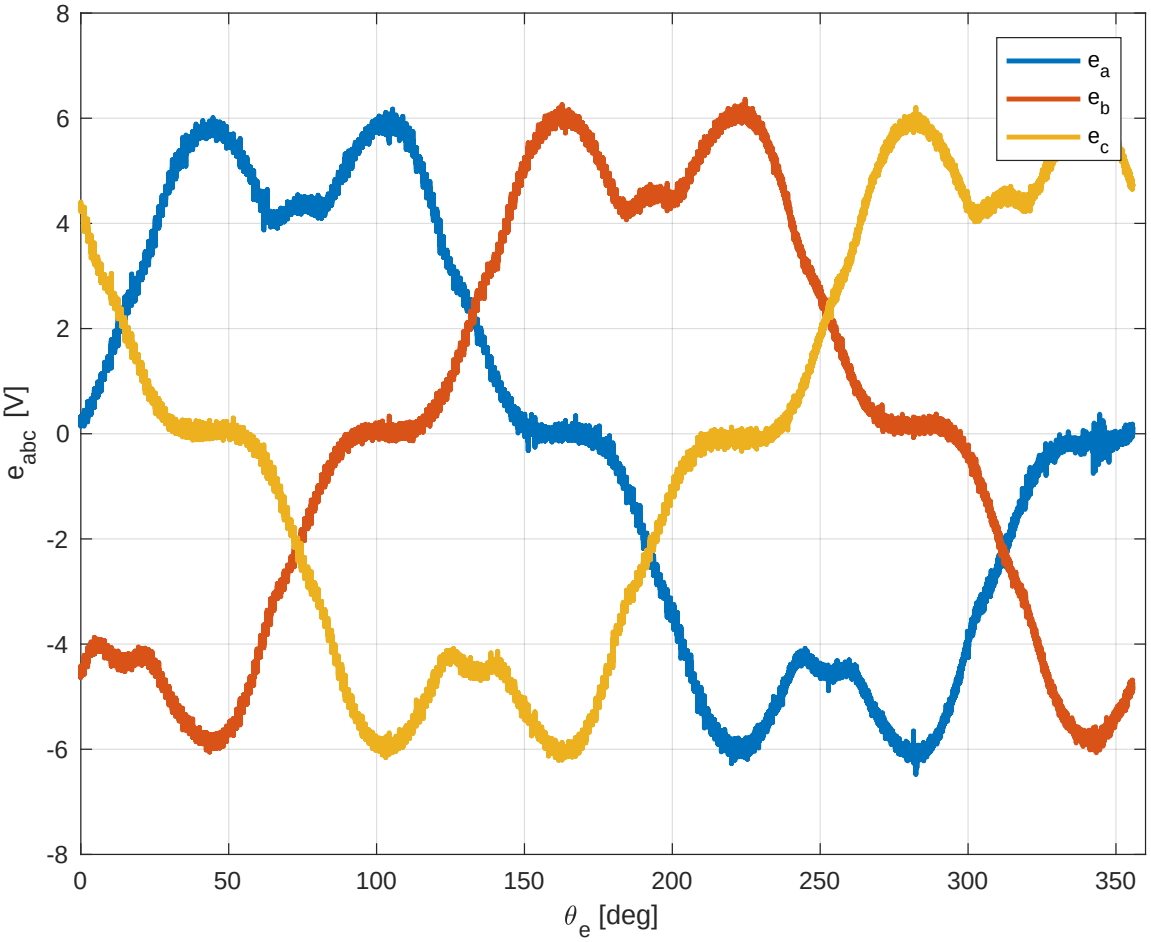

Figure 4.10: Open-circuit voltage for one electrical cycle for the Motorsolver IPM at a rotor speed of 100 rad/s.

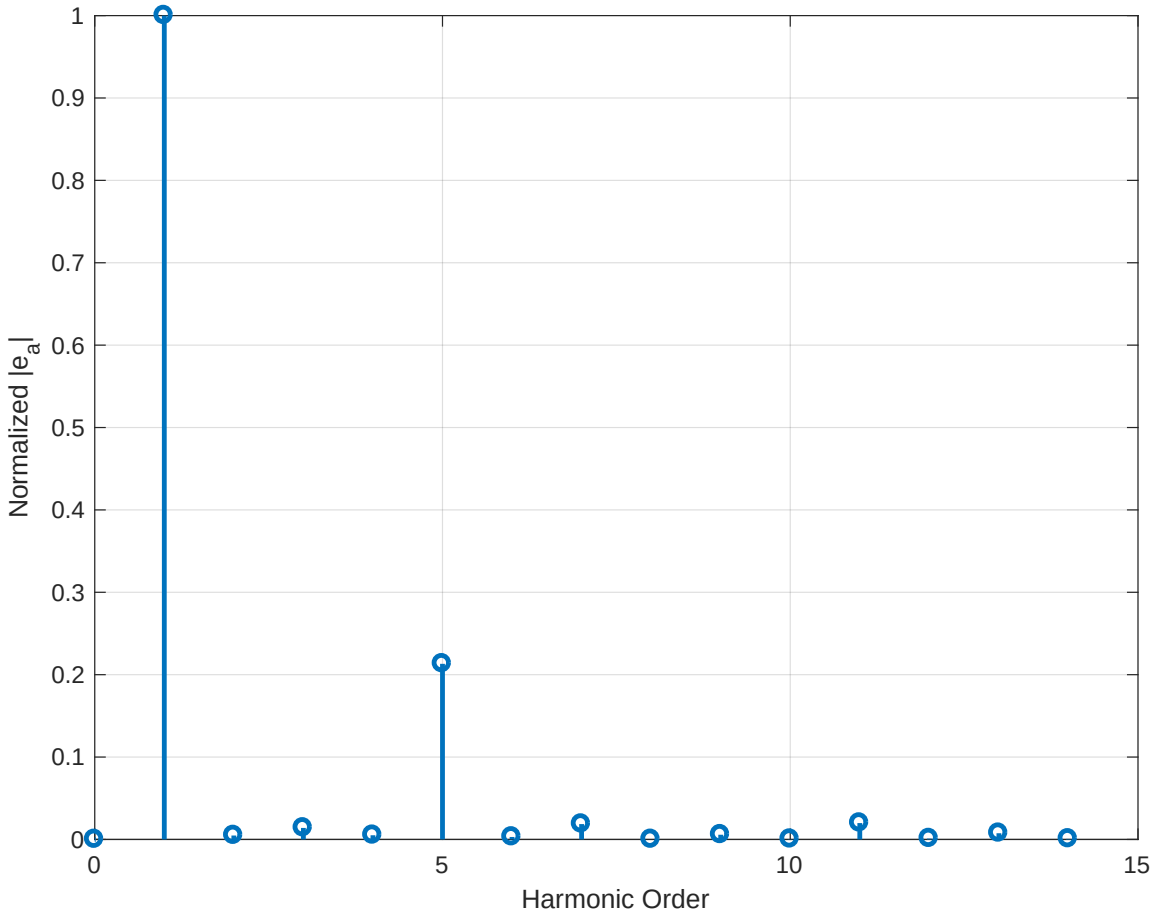

Figure 4.11: FFT analysis results of the open-circuit voltage for the Motorsolver IPM.

and θ_r the rotor angle. Then the back-EMF voltage, e_{abc} can be written as

$$\begin{aligned} e_a &= -K_m \omega_r f(\theta_a) \\ e_b &= -K_m \omega_r f(\theta_b) \\ e_c &= -K_m \omega_r f(\theta_c) \end{aligned} \tag{4.57}$$

The generic form for the non-sinusoidal function $f(\theta_{abc})$ is expressed as

$$f(\theta_{abc}) = \sin(\theta_{abc}) + a_5 \sin(5\theta_{abc}) + a_7 \sin(7\theta_{abc}) + a_{11} \sin(11\theta_{abc}) \tag{4.58}$$

and for the IPM,

$$K_m = 56.57 \text{ mV/rad/s}, \quad a_5 = -0.21, \quad a_7 = 0.02, \quad a_{11} = -0.02 \tag{4.59}$$

with

$$\theta_a = N\theta_r, \;\; \theta_b = N\theta_r - \frac{2\pi}{3}, \;\; \theta_c = N\theta_r + \frac{2\pi}{3} \tag{4.60}$$

Using the formula for the sinusoids for the Motorsolver IPM in (4.57) and (4.58), the back EMF profile can be reconstructed and compared to the experiment data as shown in Figure 4.12. The reconstructed voltage profile shows good agreement with the experimental data, verifying that the formulas used for reconstruction are accurate.

The fundamental component of the permanent-magnet flux coefficient is calculated from the FFT analysis as

$$\Lambda_m = \frac{K_m}{N} = 28.28 \text{ mWb} \tag{4.61}$$

Using the power-invariant version of the dq transformation matrix in (3.14), the permanent-

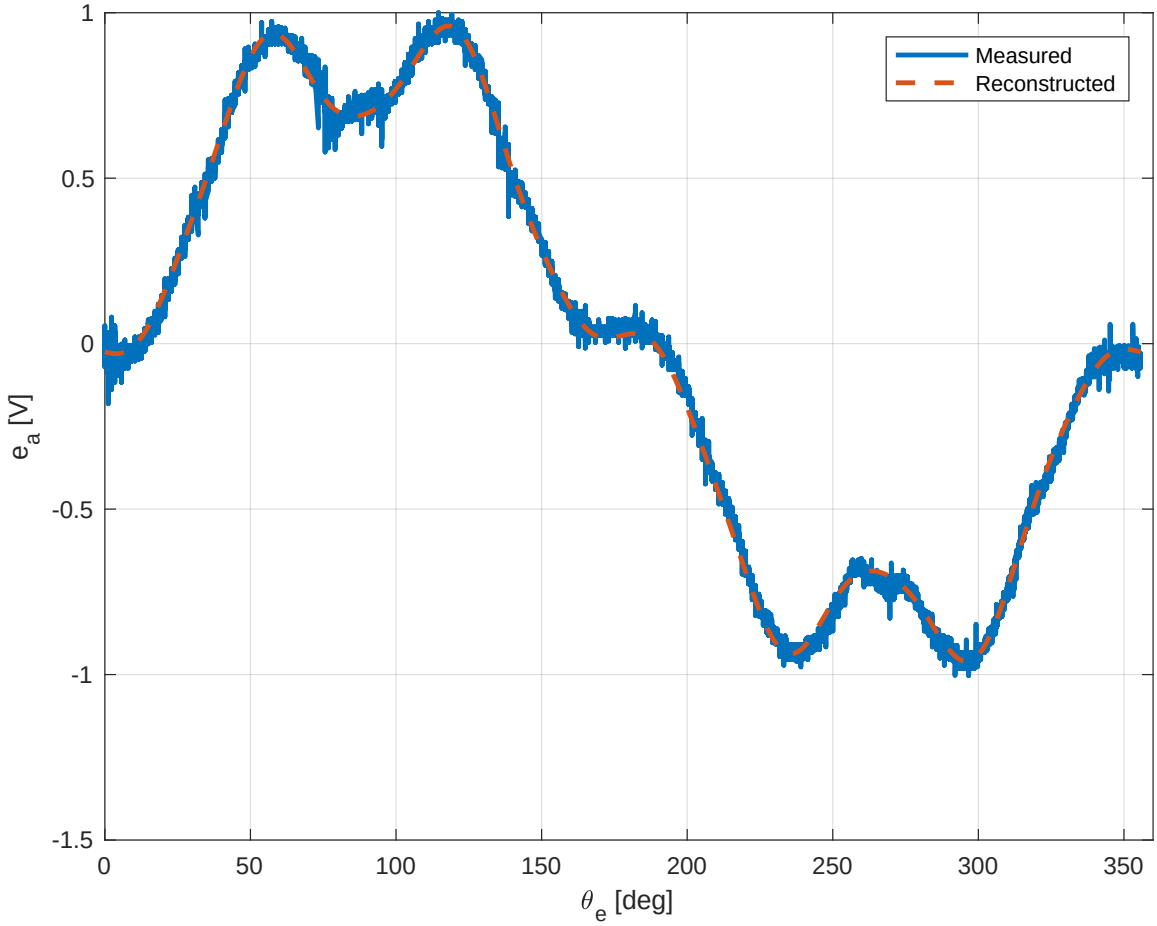

Figure 4.12: FFT-based reconstruction of the open-circuit voltage for the Motor-solver IPM.

magnet flux coefficient in the dq reference frame is

$$\Lambda = \sqrt{\frac{3}{2}}\Lambda_m = 34.64 \text{ mWb} \tag{4.62}$$

and the associated back-EMF constant is

$$K = N\Lambda = 69.28 \text{ mV/rad/s} \tag{4.63}$$

Maximum Current and Torque

The maximum current through the power converter switches is $I_{\text{sw,max}} = 6$ A. The resulting maximum length of the current vector in the dq reference frame for the wye-connected machine from Table 3.1 is

$$I_{\text{max}} = \sqrt{\frac{3}{2}} I_{\text{sw,max}} = 7.35 \text{ A} \tag{4.64}$$

At low speeds, maximum torque is achieved using a maximum-length current vector. When the current constraint is active, the coordinates of the current vector in the dq reference frame are related by

$$i_d^2 + i_q^2 = I_{\text{max}}^2, \quad \Longrightarrow \; i_q = \pm\sqrt{I_{\text{max}}^2 - i_d^2} \tag{4.65}$$

The formula for electromagnetic torque for an IPM, assuming ideal sinusoidal back-EMF voltage, from (3.13) is

$$T_e = N\left(\Lambda + \left(L_d - L_q\right) i_d\right) i_q \tag{4.66}$$

Unlike SPMs which can only produce torque due the presence of permanent-magnets, IPMs have an additional source of electromagnetic torque due the variation of magnetic reluctance between the direct and quadrature axes as seen in the second term of (4.66).

Substituting the value of i_q from (4.65) in (4.66)

$$T_e = \pm N \left(\Lambda + \left(L_d - L_q\right) i_d\right) \sqrt{I_{\max}^2 - i_d^2} \tag{4.67}$$

To maximize torque, the partial derivative of T_e with respect to i_d is set to zero, resulting in

$$\begin{aligned} \frac{\partial T_e}{\partial i_d} = 0, \quad \Longrightarrow \; i_d = i_{d,\mathrm{MTPA,max}} &= \frac{-\Lambda + \sqrt{\Lambda^2 + 8\left(L_d - L_q\right)^2 I_{\max}^2}}{4\left(L_d - L_q\right)} \\ i_q = i_{q,\mathrm{MTPA,max}} &= \sqrt{I_{\max}^2 - i_{d,\mathrm{MTPA,max}}^2} \end{aligned} \tag{4.68}$$

The resulting value of maximum torque is

$$T_{e,\max} = N \left(\Lambda + \left(L_d - L_q\right) i_{d,\mathrm{MTPA,max}}\right) i_{q,\mathrm{MTPA,max}} \tag{4.69}$$

Based on the values of the electrical parameters that were obtained in the previous sections,

$$i_{d,\mathrm{MTPA,max}} = -1.14 \text{ A}, \quad i_{q,\mathrm{MTPA,max}} = \pm 7.26 \text{ A} \tag{4.70}$$

which results in

$$T_{e,\max} = 0.516 \text{ Nm} \tag{4.71}$$

The maximum torque that can be produced using $i_d = 0$, i.e. torque produced only due to the effect of permanent-magnets, is

$$T_{e,\max,i_{d0}} = N\Lambda I_{\max} = 0.51 \text{ Nm} \tag{4.72}$$

The contribution of the reluctance-torque component for the Motorsolver IPM under the current limit constraints that were chosen is 0.006 Nm. An IPM with a higher saliency ratio (L_q/L_d) and higher current limit constraints will have a significant reluctance-torque

contribution to the maximum torque of the drive system.

Torque formula for non-sinusoidal permanent-magnet excitation

The Motorsolver IPM electrical machine has non-sinusoidal back-EMF characteristics, and as such the electromagnetic torque will also have some harmonic content associated with it. This harmonic content manifests itself in the form of a torque-ripple when sinusoidal currents are commanded using a closed-loop current controller. For a non-sinusoidal IPM, the formula for electromagnetic torque can be expressed in the ABC frame as

$$T_e = -K_m \, i_{abc}^T f(\theta_{abc}) + \frac{1}{2} i_{abc}^T \frac{dL(\theta)}{d\theta} i_{abc} \tag{4.73}$$

The above formula includes the effect of spatial harmonics due to non-sinusoidal permanent-magnet flux, however, it does not include the effect of magnetic saturation. Transforming the expression to the dq reference frame with the following transformation

$$\begin{bmatrix} i_d \\ i_q \\ i_0 \end{bmatrix} = \begin{bmatrix} \cos(\theta_a) & \cos(\theta_b) & \cos(\theta_c) \\ -\sin(\theta_a) & -\sin(\theta_b) & -\sin(\theta_c) \\ \frac{1}{\sqrt{2}} & \frac{1}{\sqrt{2}} & \frac{1}{\sqrt{2}} \end{bmatrix} \begin{bmatrix} i_a \\ i_b \\ i_c \end{bmatrix}, \tag{4.74}$$

results in

$$\begin{aligned} T_e = K\big(i_q - a_5 \left(i_d \sin(6N\theta_r) + i_q \cos(6N\theta_r)\right) - a_7 \left(i_d \sin(6N\theta_r) - i_q \cos(6N\theta_r)\right) \\ - a_{11} \left(i_d \sin(12N\theta_r) + i_q \cos(12N\theta_r)\right)\big) + N \left(L_d - L_q\right) i_d i_q \end{aligned} \tag{4.75}$$

where $K = \sqrt{\frac{3}{2}} K_m$. The above formula assumes ideal sinusoidal variation of stator winding inductance with rotor angle. A summary of the Motorsolver IPM electrical parameters is listed in Table 4.3(a).

4.3.2 Mechanical Parameter Estimation

The mechanical parameters of the IPM system shown in Figure 4.7 are determined using a torque-pulse test. The electrical parameters that were determined in the previous section are used to produce a torque-pulse for a short duration. The mechanical load is excited by the applied torque and responds by accelerating first and then freely decelerates after the torque-pulse ceases. The response of the rotor speed dynamics is measured and logged. The electromagnetic torque is also measured or estimated from current measurements and logged. A least-squares parameter estimation algorithm then uses the logged data of rotor speed and electromagnetic torque to determine the parameters of the mechanical load. The mechanical load for the Motorsolver IPM system was found to have significant cogging torque. This required a modification to the least-squares parameter estimation algorithm described in Section 4.1.2 to include rotor angle dynamics as well. This section describes the modified parameter estimation algorithm and experimental results.

4.3.3 Second-Order Least-Squares Based Mechanical Parameter Estimation

A mechanical load model which includes the effect of cogging torque, viscous friction, and Coulomb friction is described by

$$T_{\text{load}} = B_1\omega_r + B_0\ \text{sgn}(\omega_r) + T_{e,\text{cogg}} \sin\left(N_{\text{cogg}}\theta_r + \phi_{\text{cogg}}\right) \tag{4.76}$$

where $T_{e,\text{cogg}}$ is the magnitude of cogging torque, N_{cogg} is the frequency of cogging torque, and ϕ_{cogg} is the cogging phase angle. The frequency of cogging torque is the least common multiple of the number of stator winding slots and the number of poles in the rotor. The number of stator winding slots and the cogging phase angle are determined from a cross-sectional diagram of the electric machine, which is usually provided by the manufacturer. For the Motorsolver IPM, the number of stator winding slots is 12 and the number of poles

is 4, which results in

$$N_{\text{cogg}} = \textbf{LCM}\,(12, 4) = 12, \tag{4.77}$$

and the phase angle is $\phi_{\text{cogg}} = 0$. The rotor position and speed dynamics are

$$\begin{aligned} \dot{\theta}_r &= \omega_r \\ \dot{\omega}_r &= \frac{1}{J}\left(T_e - T_{\text{load}}\right) \end{aligned} \tag{4.78}$$

The second-order rotor position dynamics are expressed as

$$\ddot{\theta}_r = \frac{1}{J}\left(T_e - B_1\dot{\theta}_r - B_0\ \text{sgn}(\dot{\theta}_r) - T_{e,\text{cogg}}\ \sin(12\theta_r)\right) \tag{4.79}$$

This expression can be rewritten using a generic non-linear second-order system as

$$\ddot{x} = af(\dot{x}) + bg(\dot{x}) + ch(x) + du \tag{4.80}$$

where

$$x = \theta_r,\ u = T_e,\ f(\dot{x}) = \dot{x} = \omega_r,\ g(\dot{x}) = \text{sgn}(\dot{x}) = \text{sgn}(\omega_r),\ h(x) = \sin(12\theta_r) \tag{4.81}$$

and

$$a = -\frac{B_1}{J},\ \ b = -\frac{B_0}{J},\ \ c = -\frac{T_{e,\text{cogg}}}{J},\ \ d = \frac{1}{J} \tag{4.82}$$

The non-linear system described in (4.80) can be rewritten as

$$\ddot{x} = \hat{\theta}^T\phi \tag{4.83}$$

where $\hat{\theta}$ is the vector of estimated coefficients

$$\hat{\theta} = \begin{bmatrix} \hat{a} & \hat{b} & \hat{c} & \hat{d} \end{bmatrix}^T \tag{4.84}$$

and ϕ is the vector of measured signals

$$\phi = \begin{bmatrix} f(\dot{x}) & g(\dot{x}) & h(x) & u \end{bmatrix}^T \tag{4.85}$$

Since the system is described by second-order dynamics, a second-order filter is applied to both sides of (4.80) to obtain

$$z = \hat{\theta}^T \phi_f \tag{4.86}$$

where $z = H_2(s)x$, and $\phi_f = \begin{bmatrix} H_1(s)x & H_0(s)\text{sgn}(\dot{x}) & H_0(s)\sin(12x) & H_0(s)u \end{bmatrix}$, and

$$H_i(s) = \frac{\lambda_0 s^i}{s^2 + \lambda_1 s + \lambda_0} \tag{4.87}$$

with $\lambda_1 = 2\lambda$ and $\lambda_0 = \lambda^2$. The symbol λ is the cut-off frequency of the second-order filter. The $H_0(s)$ filter is implemented using the following state-space model

$$A_0 = \begin{bmatrix} 0 & 1 \\ -\lambda_0 & -\lambda_1 \end{bmatrix}, \quad B_0 = \begin{bmatrix} 0 \\ 1 \end{bmatrix}, \quad C_0 = \begin{bmatrix} \lambda_0 & 0 \end{bmatrix}, \quad D_0 = 0 \tag{4.88}$$

The $H_1(s)$ filter is implemented using

$$A_1 = \begin{bmatrix} 0 & 1 \\ -\lambda_0 & -\lambda_1 \end{bmatrix}, \quad B_1 = \begin{bmatrix} 0 \\ 1 \end{bmatrix}, \quad C_1 = \begin{bmatrix} 0 & \lambda_0 \end{bmatrix}, \quad D_1 = 0 \tag{4.89}$$

and the $H_2(s)$ filter is implemented using

$$A_2 = \begin{bmatrix} 0 & 1 \\ -\lambda_0 & -\lambda_1 \end{bmatrix}, \quad B_2 = \begin{bmatrix} 0 \\ 1 \end{bmatrix}, \quad C_2 = \begin{bmatrix} -\lambda_0^2 & -\lambda_0\lambda_1 \end{bmatrix}, \quad D_2 = \lambda_0 \tag{4.90}$$

Using a stacked version of (4.86), the estimated parameter vector is obtained using

$$\hat{\theta} = \left[\phi_f \phi_f^T\right]^{-1} \phi_f z \tag{4.91}$$

and the mechanical parameters are estimated as

$$\hat{J} = \frac{1}{\hat{d}}, \quad \hat{B}_1 = -\frac{\hat{a}}{\hat{d}}, \quad \hat{B}_0 = -\frac{\hat{b}}{\hat{d}}, \quad \hat{T}_{e,\text{cogg}} = -\frac{\hat{c}}{\hat{d}} \tag{4.92}$$

Experimental Results

The DRV-8312 Motor Control Board with the F28069 microcontroller shown in Figure 4.7 is used for the torque-pulse experiments. The power converter switching frequency is 30 kHz, the current-controller update frequency is 12.5 kHz, and the current-controller bandwidth is 4500 rad/s. The rotor position is measured using a shaft-mounted quadrature encoder and the rotor speed is estimated from the encoder signals as discussed earlier. The encoder position measurement is used for electronic commutation to ensure synchronous three-phase operation of the electric machine. The leg currents are measured by sampling the voltage across shunt resistors located between the low-side switches and the negative terminal of the DC power supply. The direct and quadrature axes currents are obtained by transforming the measured leg currents using the measure rotor angle as described in (3.15). Torque-pulses that are fractions of the maximum electromagnetic torque with zero direct-axis current, $T_{e,\max,i_{d0}}$, are applied for 0.5 seconds and the response of the rotor mechanical dynamics is measured and logged. The current reference commands for the closed-loop

current controller are

$$i_d^* = 0$$
$$i_q^* = \begin{cases} \dfrac{\xi T_{e,\max,i_{d0}}}{K}, & \text{if } 0 \leq t \leq 0.5 \text{ s} \\ 0, & \text{if } t > 0.5 \text{ s} \end{cases} \tag{4.93}$$

where ξ is the fraction of maximum torque that is applied. The parameter estimation algorithm discussed in the previous section requires logged data of rotor position, rotor speed, and electromagnetic torque to determine the mechanical parameter. The rotor position and speed are obtained from the encoder signals as explained earlier. To determine the torque, the formula from (4.75) that includes the effect of non-sinusoidal back-EMF is used. Measurements of direct and quadrature axes currents along with the rotor position data are used to estimate the electromagnetic torque produced in the air-gap and the data is logged. The data are fed to the second-order least-squares based parameter estimation algorithm to determine the mechanical characteristics of the rotor-load combination. The data logging frequency is 800 Hz. Torque-pulses of magnitudes equal to 30%, 40%, and 50% of the maximum torque are applied for 0.5 seconds. The forced acceleration and free deceleration responses of the rotor dynamics are measured and logged. Figure 4.13(b) compares the experiment (blue) and simulation (dashed red) responses of the rotor dynamics to the application of 50% of maximum torque for 0.5 seconds. The simulation response uses the value of mechanical parameters obtained from the least-squares algorithm. Figure 4.13(a) shows the estimated electromagnetic torque that is applied to the mechanical load during the torque-pulse test. The torque is estimated from (4.75) using the direct and quadrature axes currents and the rotor position information. Observe that the non-sinusoidal back-EMF adds significant harmonics to the torque-pulse. Also observe in Figure 4.13(b) that the free deceleration response at low-speeds has a ripple - this is due to the effect of cogging torque. The parameter estimation algorithm provides an estimate of the magnitude of

cogging torque in addition to the inertia (J), viscous friction (B_1), and Coulomb friction (B_0). Table 4.3(b) lists the average results of the parameter estimation algorithm using 30%, 40%, and 50% of the maximum torque pulse tests.

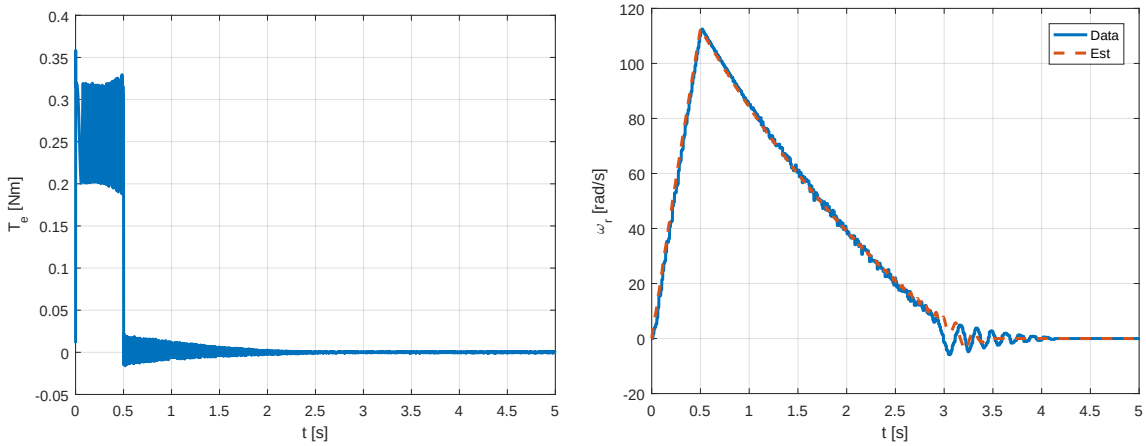

(a) 50% of $T_{e,\max,i_{d0}}$ torque-pulse

(b) Rotor speed response

Figure 4.13: Comparison of the electromagnetic torque and rotor speed data from the experiment and simulation using estimated parameters for the Motorsolver IPM system.

4.4 Conclusion

This chapter discussed the systematic procedures used to determine the electrical and mechanical parameters of the three experimental systems that are used in this research. These parameters will be used to design, implement, and evaluate the optimal kinetic energy recovery algorithms in the chapters that follow.

Table 4.3: Electrical and Mechanical Parameters of the Motorsolver IPM System.

(a) Mototsolver IPM Electrical Parameters
(4-Pole IPM PMAC Synchronous Motor)

Parameter	Value	Units
N	2	-
R_s	182.75	mOhm
L_d	0.55	mH
L_q	1.31	mH
Λ	34.64	mWb
K	69.28	mV/rad/s
$I_{\max}$	7.35	A
$T_{e,\max}$	0.516	Nm
$T_{e,\max,i_{d0}}$	0.51	Nm

(b) Estimated Mechanical Parameters

Parameter	Value	Units
J	9.58×10^{-4}	kg-m^2
B_1	3.15×10^{-4}	Nm/rad/s
B_0	2.49×10^{-2}	Nm
$T_{e,\text{cogg}}$	0.119	Nm

CHAPTER 5

OPTIMAL KINETIC ENERGY RECOVERY ALGORITHMS FOR SPMS

The objective of recovering maximum kinetic energy during the braking time-interval is studied using the optimal control framework that is discussed in [5].

5.1 Optimal Control Framework

The rotor speed mechanical dynamics can be described as

$$\dot{\omega}_r = \frac{1}{J}\left(T_e^* - T_{\text{load}}\right) \tag{5.1}$$

where T_e^* is the desired electromagnetic torque, T_{load} is the load torque, and J is the mechanical inertia. If it is assumed that the mechanical load is characterized by only the viscous friction (B_1) component, then

$$T_{\text{load}} = B_1\omega_r \tag{5.2}$$

and the rotor speed dynamics are now expressed as

$$\dot{\omega}_r = \frac{1}{J}\left(T_e^* - B_1\omega_r\right) \tag{5.3}$$

For an SPM machine, the electrical power is given as

$$P_e = v_d i_d + v_q i_q \tag{5.4}$$

where v_d and v_q are the direct and quadrature axes voltages, and i_d and i_q are the direct and quadrature axes currents. Through the use of high-bandwidth current control, the actual

direct and quadrature axes currents are approximately equal to the reference currents, i.e. $i_d \approx i_d^*$ and $i_q \approx i_q^*$. The approximate quasi-steady-state voltage equations are

$$v_d \approx R_s i_d^* - N\omega_r L i_q^*$$
$$v_q \approx R_s i_q^* + N\omega_r L i_q^* + K i_q^*$$

The time-scale separation resulting from current feedback can be interpreted in the context of singular perturbation theory [72]. This results in the electric power equation simplifying to

$$P_e \approx R_s \left(i_d^{*2} + i_q^{*2}\right) + K i_q^* \omega_r \tag{5.5}$$

and the electromagnetic torque reference for an SPM is written as

$$T_e^* = K i_q^* \tag{5.6}$$

where $K = N\Lambda$.

The objective of the optimal control problem is described as follows: if the initial rotor speed is ω_{r0} (> 0), maximize the energy that can be recovered as the rotor slows down to a speed ω_{rT} $(< \omega_{r0})$ in a braking time-interval of T seconds. This can be mathematically described as

$$\text{Minimize } \; E = \int_0^T P_e \, dt, \quad \omega_r(0) = \omega_{r0} \; \text{ and } \; \omega_r(T) = \omega_{rT} \tag{5.7}$$

under rotor dynamics (5.3). This belongs to the category of optimal control problems that is characterized by fixed final state and fixed final time, since both $\omega_r(T)$ and T are determined by the user.

Let i_d^* and i_q^* be the control variables for the unconstrained optimal control problem.

According to the theory of optimal control, a Hamiltonian function H can be formulated as

$$H = P_e + \chi \, \dot{\omega}_r \tag{5.8}$$

where χ is the costate variable. Substituting the values of P_e and $\dot{\omega}_r$ from (5.5) and (5.3), the Hamiltonian can be expanded as

$$H = R_s \left(i_d^{*2} + i_q^{*2} \right) + K i_q^* \omega_r + \frac{\chi}{J} \left(K i_q^* - B_1 \omega_r \right) \tag{5.9}$$

Assuming that current magnitude constraints are not active, the optimal current commands are determined by setting partial derivatives

$$\begin{aligned} \frac{\partial H}{\partial i_d^*} &= 2 R_s i_d^* \\ \frac{\partial H}{\partial i_q^*} &= 2 R_s i_q^* + K \left(\omega_r + \frac{\chi}{J} \right) \end{aligned} \tag{5.10}$$

equal to zero, yielding

$$\begin{aligned} i_{d,\mathrm{opt}}^* &= 0 \\ i_{q,\mathrm{opt}}^* &= -\frac{K}{2R_s} \left(\omega_{r,\mathrm{opt}} + \frac{\chi_{\mathrm{opt}}}{J} \right) \end{aligned} \tag{5.11}$$

The state and costate dynamics can be derived in terms of the state and costate variables by taking the partial derivatives

$$\begin{aligned} \dot{\omega}_{r,\mathrm{opt}} &= \frac{\partial H}{\partial \chi} = \frac{1}{J} \left(K i_{q,\mathrm{opt}}^* - B_1 \omega_{r,\mathrm{opt}} \right) \\ \dot{\chi}_{\mathrm{opt}} &= -\frac{\partial H}{\partial \omega_r} = -K i_{q,\mathrm{opt}}^* + \frac{B_1}{J} \chi_{\mathrm{opt}} \end{aligned} \tag{5.12}$$

Now that the optimal values of the control variables and the optimal state and costate dynamic equations have been obtained, the optimal speed and costate trajectories can be obtained by formulating a two-point boundary value problem as described in the next sec-

tion.

5.1.1 Two-Point Boundary Value Problem

The optimal values of the control variables, i_d^* and i_q^*, from (5.11) are substituted into (5.12) to obtain a two-point boundary value problem as shown below

$$\begin{bmatrix} \dot{\omega}_{r,\text{opt}} \\ \dot{\chi}_{\text{opt}} \end{bmatrix} = \frac{K^2}{2JR_s} \begin{bmatrix} -(1+2\gamma) & -J^{-1} \\ J & (1+2\gamma) \end{bmatrix} \begin{bmatrix} \omega_{r,\text{opt}} \\ \chi_{\text{opt}} \end{bmatrix}, \quad \begin{matrix} \omega_{r,\text{opt}}(0) = \omega_{r0} \\ \omega_{r,\text{opt}}(T) = \omega_{rT} \end{matrix} \tag{5.13}$$

where $\gamma = \dfrac{B_1 R_s}{K^2}$ is a dimensionless electromechanical loss parameter that captures the effect of both the mechanical loss (through B_1) and electrical loss (through R_s). The system described in (5.13) has two eigenvalues at $\pm\alpha$, where

$$\alpha = \frac{K^2}{JR_s}\sqrt{\gamma(1+\gamma)} \tag{5.14}$$

The general solution of the two-point boundary value problem in (5.13) is of the form

$$\begin{aligned} \omega_{r,\text{opt}} &= c_1 e^{-\alpha t} + c_2 e^{\alpha t} \\ \chi_{\text{opt}} &= c_3 e^{-\alpha t} + c_4 e^{\alpha t} \end{aligned} \tag{5.15}$$

with the following relationships between the coefficients

$$\frac{c_1}{c_3} = -\frac{\gamma_1}{J}, \quad \frac{c_2}{c_4} = -\frac{\gamma_2}{J} \tag{5.16}$$

where

$$\begin{aligned} \gamma_1 &= 1 + 2\gamma + 2\sqrt{\gamma(1+\gamma)} \\ \gamma_2 &= 1 + 2\gamma - 2\sqrt{\gamma(1+\gamma)} \\ \gamma_1\gamma_2 &= 1 \end{aligned} \tag{5.17}$$

Therefore, only two boundary conditions are required to determine all coefficients, c_1 through c_4. Applying the boundary conditions $\omega_{r,\text{opt}}(0) = \omega_{r0}$ and $\omega_{r,\text{opt}}(T) = \omega_{rT}$, results in

$$\begin{aligned} c_1 &= \frac{\omega_{r0}e^{\alpha T} - \omega_{rT}}{e^{\alpha T} - e^{-\alpha T}} \\ c_2 &= \frac{\omega_{rT} - \omega_{r0}e^{-\alpha T}}{e^{\alpha T} - e^{-\alpha T}} \end{aligned} \tag{5.18}$$

Substituting the values of the coefficients in (5.15) results in the following optimal trajectories for the rotor speed and costate

$$\begin{aligned} \omega_{r,\text{opt}} &= \frac{\omega_{r0}\left(e^{\alpha(T-t)} - e^{-\alpha(T-t)}\right) + \omega_{rT}\left(e^{\alpha t} - e^{-\alpha t}\right)}{e^{\alpha T} - e^{-\alpha T}} \\ \chi_{\text{opt}} &= -J\left(\frac{\omega_{r0}\left(\gamma_2 e^{\alpha(T-t)} - \gamma_1 e^{-\alpha(T-t)}\right) + \omega_{rT}\left(\gamma_1 e^{\alpha t} - \gamma_2 e^{-\alpha t}\right)}{e^{\alpha T} - e^{-\alpha T}}\right) \end{aligned} \tag{5.19}$$

The optimal direct and quadrature axes current references are then calculated from (5.11) as

$$\begin{aligned} i^*_{d,\text{opt}} &= 0 \\ i^*_{q,\text{opt}} &= -\frac{K}{2R_s}\left(\omega_{r,\text{opt}} + \frac{\chi_{\text{opt}}}{J}\right) \end{aligned} \tag{5.20}$$

and the corresponding electromagnetic torque reference is calculated as

$$T^*_{e,\text{opt}} = Ki^*_{q,\text{opt}} = -\frac{K^2}{2R_s}\left(\omega_{r,\text{opt}} + \frac{\chi_{\text{opt}}}{J}\right) \tag{5.21}$$

5.1.2 Energy Recovered

To evaluate the cost function, i.e. kinetic energy recovered during the braking interval, consider the energy equation from (5.7)

$$\begin{aligned} E &= \int_0^T P_e \, dt \\ &= \int_0^T \left(R_s \left(i_{d,\text{opt}}^{*2} + i_{q,\text{opt}}^{*2} \right) + K i_{q,\text{opt}}^{*} \omega_{r,\text{opt}} \right) \quad dt \end{aligned} \tag{5.22}$$

Substituting the values of the optimal currents from (5.11) and optimal state and costate trajectories from (5.19) and solving the integral from $t = 0$ to $t = T$ results in

$$E = -\frac{J}{2(1 - e^{-2\alpha T})} \left(\omega_{r0}^2 (\gamma_2 - \gamma_1 e^{-2\alpha T}) + \omega_{rT}^2 (\gamma_2 e^{-2\alpha T} - \gamma_1) - 2\omega_{r0}\omega_{rT}(\gamma_2 - \gamma_1) e^{-\alpha T} \right) \tag{5.23}$$

Let the ratio of the final rotor speed, ω_{rT} to the initial rotor speed ω_{r0} be defined as

$$\rho = \frac{\omega_{rT}}{\omega_{r0}} \tag{5.24}$$

For braking, the value of ρ is bounded between 0 and 1. The kinetic energy available for conversion is the difference between the kinetic energies stored in the rotor at the two speeds, ω_{r0} and ω_{rT},

$$E_{\text{avail}} = \frac{1}{2} J \omega_{r0}^2 - \frac{1}{2} J \omega_{rT}^2 = \frac{1}{2} J \omega_{r0}^2 (1 - \rho^2) \tag{5.25}$$

An energy ratio can then be defined as the ratio of the electrical energy recovered (E) to the kinetic energy available for conversion

$$\begin{aligned} E_{\text{ratio}} &= -\frac{E}{E_{\text{avail}}} \\ &= \frac{\gamma_2 - \gamma_1 e^{-2\alpha T} + \rho^2(\gamma_2 e^{-2\alpha T} - \gamma_1) - 2\rho(\gamma_2 - \gamma_1)e^{-\alpha T}}{(1 - e^{-2\alpha T})(1 - \rho^2)} \end{aligned} \tag{5.26}$$

The above expression for energy ratio has a unique feature, viz. that the ratio of kinetic energy recovery is independent of value of the initial rotor speed and depends only on the ratio between the final and initial speeds of the rotor. Moreover, the formula for energy ratio shows that any pair of final and initial rotor speeds with the same value of ρ is characterized by the same value of energy recovery ratio. For example, a rotor speed of 500 rad/s braking to 250 rad/s in T seconds has the same energy recovery ratio as a rotor of 100 rad/s braking to 50 rad/s in the same T seconds.

The sign convention for the energy recovery ratio is described below:

- Positive Energy Recovery Ratio: Kinetic energy that was stored in the spinning rotor is converted to electrical energy by the electric machine and enters the terminals of the electrical power supply. This energy is now available for storage in an energy storage system if there is such a provision. The energy lost in the electromechanical losses in the duration of the braking interval is less than the total kinetic energy initially available for conversion.

- Negative Energy Recovery Ratio: In this case the energy lost in the electromechanical loss mechanisms in the system is greater than the initial kinetic energy that is available for conversion. Additional electrical energy is drawn from the electrical supply to compensate for the losses that are incurred during the braking process.

- Zero Energy Recovery Ratio: This is a special case in which the energy lost due to electromechanical losses during the braking time-interval is exactly equal to the difference in the levels of kinetic energy of the rotor at the initial and final speeds. In

this case electrical energy neither enters nor exits the electrical power supply during the braking time-interval.

The expression for energy recovery ratio in (5.26) shows the optimal energy that can be recovered for any user-defined braking time-interval length, T. However, not all choices of T result in positive energy recovery ratios, i.e. at least some of the kinetic energy being converted to useful electrical energy on the power supply side. The minimum length of the braking time-interval that results in positive energy recovery ratios can be obtained by solving for the value of T that has a zero energy recovery ratio.

$$E_{\text{ratio}} = 0, \implies T_{\min} = \left(\frac{1}{\alpha}\right) \ln\left(\frac{\rho^2 + \rho\left(\gamma_1 - \gamma_2\right) - 1}{\rho^2\gamma_1 - \gamma_2}\right) \tag{5.27}$$

Special Case: $\rho = 0$

In the special case of braking to a full stop, i.e. $\omega_{rT} = 0$, the expressions for the optimal state and costate trajectories are

$$\begin{aligned} \omega_{r,\text{opt}} &= \frac{\omega_{r0}\left(e^{\alpha(T-t)} - e^{-\alpha(T-t)}\right)}{e^{\alpha T} - e^{-\alpha T}} \\ \chi_{\text{opt}} &= -\frac{J\omega_{r0}\left(\gamma_2 e^{\alpha(T-t)} - \gamma_1 e^{-\alpha(T-t)}\right)}{e^{\alpha T} - e^{-\alpha T}} \end{aligned} \tag{5.28}$$

The formula for energy recovery ratio simplifies to

$$E_{\text{ratio}} = \frac{\gamma_2 - \gamma_1 e^{-2\alpha T}}{1 - e^{-2\alpha T}} \tag{5.29}$$

In this case, the minimum value of the length of the braking time-interval that achieves positive energy recovery ratios is

$$T_{\min} = \left(\frac{1}{\alpha}\right) \ln\left(\gamma_1\right) \tag{5.30}$$

For this special case of $\rho = 0$, another level of simplification of expressions can be obtained by assuming the braking time-interval to be infinite in length, i.e. $T \to \infty$. For this case, the optimal state and costate trajectories are

$$\begin{aligned} \omega_{r,\text{opt}} &= \omega_{r0} e^{-\alpha t} \\ \chi_{\text{opt}} &= -J\gamma_2 \omega_{r0} e^{-\alpha t} \end{aligned} \tag{5.31}$$

The optimal direct axis current is zero as obtained earlier. However, in this case, the optimal quadrature axis current simplifies to

$$i^*_{q,\text{opt}}(t) = -\frac{K}{2R_s}\left(\omega_{r,\text{opt}} + \frac{\chi_{,\text{opt}}}{J}\right) = -\frac{K}{2R_s}\left(1-\gamma_2\right)\omega_{r,\text{opt}} \tag{5.32}$$

The simplified electromagnetic torque trajectory is obtained as

$$T^*_{e,\text{opt}} = -\frac{K^2}{2R_s}\left(1-\gamma_2\right)\ \omega_{r,\text{opt}} \tag{5.33}$$

which is a straight line passing through the origin in second and fourth quadrants of the torque-speed plane. The optimal energy recovery ratio in this case is

$$E_{\text{ratio}} = \gamma_2 \tag{5.34}$$

which is a constant that only depends on the electromechanical loss parameter, γ.

5.2 Design of Braking Trajectories

The method of designing optimal braking trajectories that was described in the previous sections can be applied to any length of the braking time-interval, T. However, not all choices for T result in well-designed braking trajectories. For example, consider a situation where the initial rotor speed is ω_{r0} and it is desired to slow down to a rotor speed of $\omega_{rT} = \rho\omega_{r0}$. The optimal braking trajectories are designed for two distinct braking time-interval

lengths, T_1 and T_2. The two optimal braking trajectories are shown in Figure 5.1, one in blue and the other in red (dashed). The trajectory shown in blue is designed for a braking time-interval of length T_1, and the one shown in dashed red is designed for a braking time-interval length of T_2. Notice that the braking trajectory shown in blue does not go below ω_{rT} at any time instant, i.e. the operation of the electric machine is purely in the braking mode for the entire length of the braking interval. This optimal braking trajectory is considered to be a "good" design. Contrary to this, the optimal braking trajectory shown in dashed red, goes below ω_{rT} for a significant time-interval and then starts accelerating towards ω_{rT} so that the rotor speed is at the desired final speed at time $t = T_2$. This braking trajectory, although optimal, is a mix of both braking and motoring, and is considered to be a "bad" design of the trajectory. Therefore, care must be taken while choosing the length of the braking time-interval, T, while designing the optimal braking trajectory.

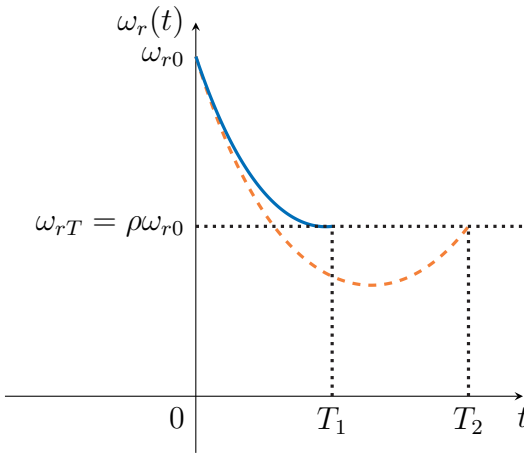

Figure 5.1: Comparison of good (blue) and bad (red dashed) braking trajectory designs.

5.3 Optimal Braking Time

The formulas derived in the previous section, allow the user to develop optimal braking trajectories for any user-specified braking time-interval, T. However, if the objective is to maximize the kinetic energy recovered by braking from ω_{r0} to ω_{rT}, the length of the

braking time-interval must also be optimized.

5.3.1 Deriving T_{opt} from E_{ratio} Expression

One method of deriving the length of the braking time-interval is to set the partial derivative of the energy ratio expression from (5.26) with respect to T equal to zero and solving for $T = T_{\text{opt}}$.

$$\frac{\partial E_{\text{ratio}}}{\partial T} = 0, \implies \rho = e^{-\alpha T_{\text{opt}}} \text{ or } T_{\text{opt}} = \frac{1}{\alpha} \ln\left(\frac{1}{\rho}\right) \tag{5.35}$$

5.3.2 Determining T_{opt} using the Hamiltonian Function

Allowing T to be free, transforms the optimal control problem described earlier in this chapter from one that is characterized by fixed final state and fixed final time to one that is characterized by fixed final state and free final time. According to the methodology described in [5], the free final time variable, T, is obtained by setting the value of the Hamiltonian function at $t = T$ to zero.

$$\begin{aligned} & H\left(\omega_{r,\text{opt}}(T), i^*_{d,\text{opt}}(T), i^*_{q,\text{opt}}(T), \chi_{\text{opt}}(T), T\right) = 0 \\ & \implies R_s\left(i^{*2}_{d,\text{opt}}(T) + i^{*2}_{q,\text{opt}}(T)\right) + K i^*_{q,\text{opt}}(T)\omega_{r,\text{opt}}(T) \\ & + \frac{\chi_{\text{opt}}(T)}{J}\left(K i^*_{q,\text{opt}}(T) - B_1 \omega_{r,\text{opt}}(T)\right) = 0 \end{aligned} \tag{5.36}$$

Using the symbolic manipulation tool in Matlab, the above expression simplifies to

$$\rho = e^{-\alpha T_{\text{opt}}} \text{ or } T_{\text{opt}} = \frac{1}{\alpha} \ln\left(\frac{1}{\rho}\right) \tag{5.37}$$

Therefore, both methods of determining the value of the optimal length of the braking time-interval have the same result. Notice that the expression for T_{opt} does not depend on the explicit values of initial and final speeds of the rotor, but rather depends on their ratio. Every pair of rotor speeds with the same value of ρ have the same optimal braking

time-interval length.

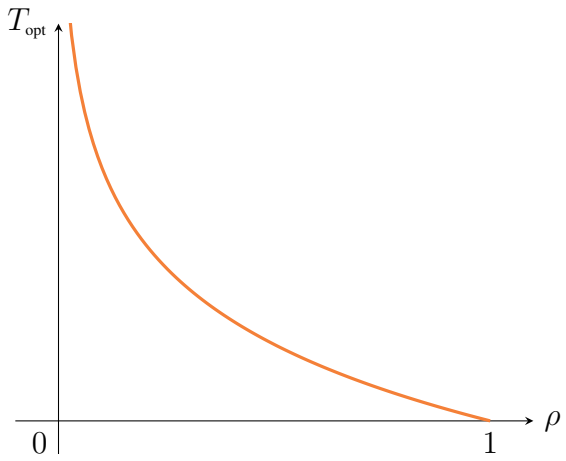

Figure 5.2: Optimal braking time-interval (T_{opt}) as a function of speed ratio ρ.

Figure 5.2 shows the optimal braking time-interval length for different speed ratios. Notice that the braking time-interval length corresponding to stopping ($\rho = 0$) is $T_{\text{opt}} \to \infty$. The optimal state and costate trajectories for the free final time optimal control problem are

$$\begin{aligned} \omega_{r,\text{opt}} &= \omega_{r0} e^{-\alpha t} \\ \chi_{\text{opt}} &= -\gamma_2 J \omega_{r0} e^{-\alpha t} \end{aligned} \tag{5.38}$$

These trajectories have the same form as those obtained earlier in (5.31) for the special case of $\rho = 0$ and $T \to \infty$. Similarly here, the optimal currents and electromagnetic torque are

$$\begin{aligned} i^*_{d,\text{opt}} &= 0 \\ i^*_{q,\text{opt}} &= -\frac{K}{2R_s}\left(\omega_{r,\text{opt}} + \frac{\chi_{\text{opt}}}{J}\right) = -\frac{K}{2R_s}\left(1-\gamma_2\right)\omega_{r,\text{opt}} \\ T^*_{e,\text{opt}} &= -\frac{K^2}{2R_s}\left(1-\gamma_2\right)\omega_{r,\text{opt}} \end{aligned} \tag{5.39}$$

The optimal torque trajectory is a straight line passing through the origin in second and fourth quadrants of the torque-speed plane. The optimal energy recovery ratio in this case

is

$$E_{\text{ratio}} = \gamma_2 \tag{5.40}$$

which is a constant that only depends on the electromechanical loss parameter, γ. Every braking event that slows down to ρ times the initial speed in the optimal time T_{opt} from (5.35) recovers the same energy ratio.

Figure 5.3 shows the optimal speed trajectory for a non-zero value of ρ (orange). This trajectory is superimposed on the optimal speed trajectory corresponding to $\rho = 0$, shown in dotted blue. The blue curve asymptotically approaches zero as time goes to infinity. Both curves have the same trajectory $\omega_r(t) = \omega_{r0}e^{-\alpha t}$, however, the orange curve is only valid from $0 \leq t \leq T_{\text{opt}} = \dfrac{1}{\alpha}\ln\left(\dfrac{1}{\rho}\right)$.

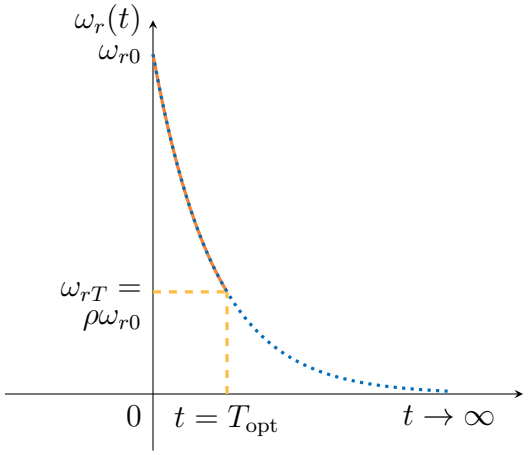

Figure 5.3: Optimal speed trajectory as a function of time.

5.4 Constant-Torque Braking

The method of applying constant torque (including maximum torque) has been recommended by several authors [9, 10, 11, 12, 13, 14, 15]. The expression for braking torque

reference can be written as

$$T_e^* = -\xi T_{e,\max}; \tag{5.41}$$

where ξ is the fraction of maximum braking torque that is applied. If the initial rotor speed is ω_{r0}, this value of braking torque is applied until the rotor speed equals ω_{rT}, which is less than ω_{r0}. Assuming that the load model only includes viscous friction, as in (5.2), the rotor speed dynamics can be written as

$$\dot{\omega}_r = \frac{1}{J}\left(-\xi T_{e,\max} - B_1\omega_r\right) \tag{5.42}$$

The solution to the above differential equation is

$$\omega_r(t) = -\frac{\xi T_{e,\max}}{B_1} + \frac{1}{B_1}\left(\xi T_{e,\max} + B_1\omega_{r0}\right) e^{-\frac{B_1}{J}t} \tag{5.43}$$

The time at which the rotor speed equals ω_{rT} can be calculated by setting the above equation to ω_{rT} and solving for $t = T_{\text{brk}}$

$$\omega_r(t = T_{\text{brk}}) = \omega_{rT}, \quad \Longrightarrow \; T_{\text{brk}} = \frac{J}{B_1}\ln\left(\frac{\xi T_{e,\max} + B_1\omega_{r0}}{\xi T_{e,\max} + B_1\omega_{rT}}\right) \tag{5.44}$$

Suppose the braking torque is achieved through closed-loop current control using the following current commands for the direct and quadrature axes

$$\begin{aligned} i_d^* &= 0 \\ i_q^* &= -\frac{\xi T_{e,\max}}{K}, \end{aligned} \tag{5.45}$$

then the energy recovered during the braking process is calculated by integrating the electric power from $t = 0$ to $t = T_{\text{brk}}$

$$\begin{aligned} E &= \int_0^{T_{\text{brk}}} \left(R_s(i_d^{*2} + i_q^{*2}) + T_e\omega_r \right) \, dt \\ &= \frac{J}{B_1^2}\xi^2 T_{e,\max}^2 \ln\left(\frac{\xi T_{e,\max} + B_1\omega_{r0}}{\xi T_{e,\max} + B_1\omega_{rT}}\right) \\ &- \frac{J}{B_1 K^2}\xi T_{e,\max}\left(K^2\left(\omega_{r0} - \omega_{rT}\right) - \xi R T_{e,\max}\ln\left(\frac{\xi T_{e,\max} + B_1\omega_{r0}}{\xi T_{e,\max} + B_1\omega_{rT}}\right)\right) \end{aligned} \tag{5.46}$$

which simplifies to

$$E = \frac{1}{B_1}\xi^2 T_{e,\max}^2 T_{\text{brk}}\left(1 + \gamma\right) - \frac{J}{B_1}\xi T_{e,\max}\left(\omega_{r0} - \omega_{rT}\right) \tag{5.47}$$

The kinetic energy available for conversion is represented by the same equation as (5.25). The associated energy recovery ratio is defined as

$$E_{\text{ratio}} = -\frac{E}{E_{\text{avail}}} \tag{5.48}$$

Implementation of Constant Torque Braking

To implement the constant torque braking, the fraction of the maximum braking torque that is desired is given as the input of a torque controller as shown in Figure 3.4.

$$T_e^* = \xi T_{e,\max}, \text{if } \omega_r > \omega_{rT} \tag{5.49}$$

The constant braking torque is applied until the rotor speed reaches the desired final rotor speed, ω_{rT}. Once the rotor speed reaches ω_{rT}, the closed-loop speed controller shown in Figure 3.9 takes over to regulate the rotor speed at $\omega_r = \omega_{rT}$.

5.5 Example System

The theories that were developed in the previous sections will now be tested on an example SPM machine system. The electrical parameters that are used are of the Anaheim Automation SPM machine, however, the mechanical parameters are example values and not representative of an actual mechanical system. The electrical parameters for the system are listed in Table 4.1(a) and the example mechanical parameters are shown in Table 5.1.

Table 5.1: Example Mechanical Parameters

Parameter	Value	Units
J	4×10^{-4}	kg-m^2
B_1	2×10^{-5}	Nm/rad/s

5.5.1 Performance of Constant-Torque Braking

The performance of the constant braking torque controller is studied first. The rotor speed of the example system described in the previous section is at an initial value of 100 rad/s. This corresponds to an initial kinetic energy of 2 Joules for this system. Now constant braking torques which are percentages of the maximum braking torque are applied to the system until the rotor reaches zero speed, i.e. $\omega_{rT} = 0$. The percentage of kinetic energy recovered and the time taken to come to a complete halt for a set of constant braking torque values are shown in Figure 5.4(a) and 5.4(b) respectively. In accordance with the sign convention chosen for the energy recovery ratio term earlier, constant braking torque values that correspond to positive energy recover ratios are shown in green and those corresponding to negative energy recovery ratios are shown in red. Values of constant braking torque that are greater than 40% of the maximum braking torque do not recover any of the kinetic energy for this example system. The highest energy recovery for the set of constant braking torque values that were considered corresponds to 10% of the maximum braking

torque, which recovers 71.15% of the kinetic energy. Another observation that can be made is that the length of the braking time-interval decreases with the application of higher levels of constant braking torques, with 10% of maximum braking torque taking 2.05 seconds to reach zero speed and 100% of maximum braking torque taking only 0.21 seconds to come to a complete stop.

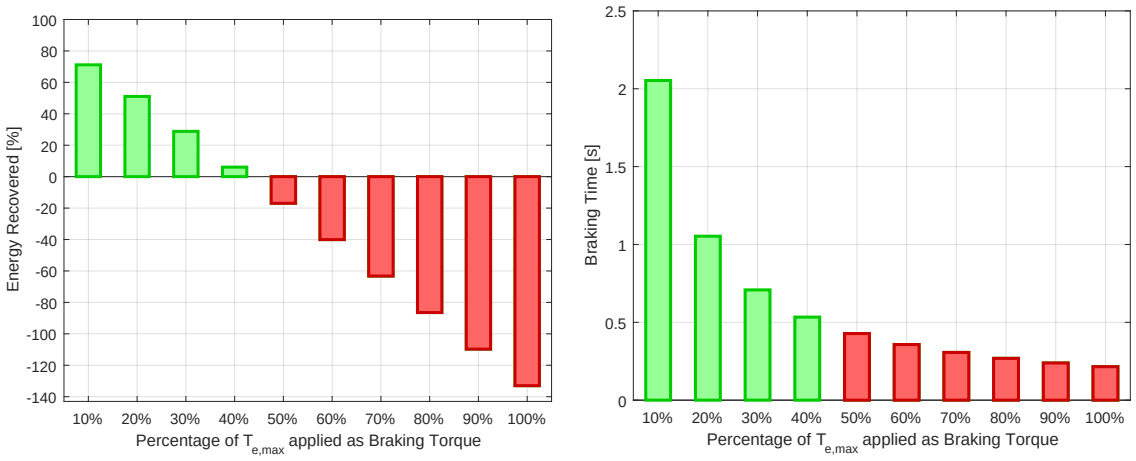

(a) Percentage of kinetic energy recovered

(b) Braking time-interval

Figure 5.4: Performance of constant torque braking on the example electromechanical system for an initial rotor speed of 100 rad/s.

5.5.2 Performance of the Optimal Braking

The performance of the optimal regenerative braking controller for the example system will be discussed in this section. Table 5.2 lists the values of the various parameters used in the design of the optimal braking trajectory.

Table 5.2: Regenerative Braking Parameter Values for the Example System

Parameter	Value
α	0.45 rad/s
γ	1.26×10^{-2}
γ_1	1.25
γ_2	79.91×10^{-2}

Figure 5.5 shows the energy recovery ratios for different values of braking time-interval length (T), for the special case of braking to zero speed ($\rho = 0$) from equation (5.29). The minimum length of the braking time-interval that ensures positive energy recovery ratios is $T_{\min} = 0.50$ seconds. Only positive energy recovery ratios are shown in Figure 5.5.

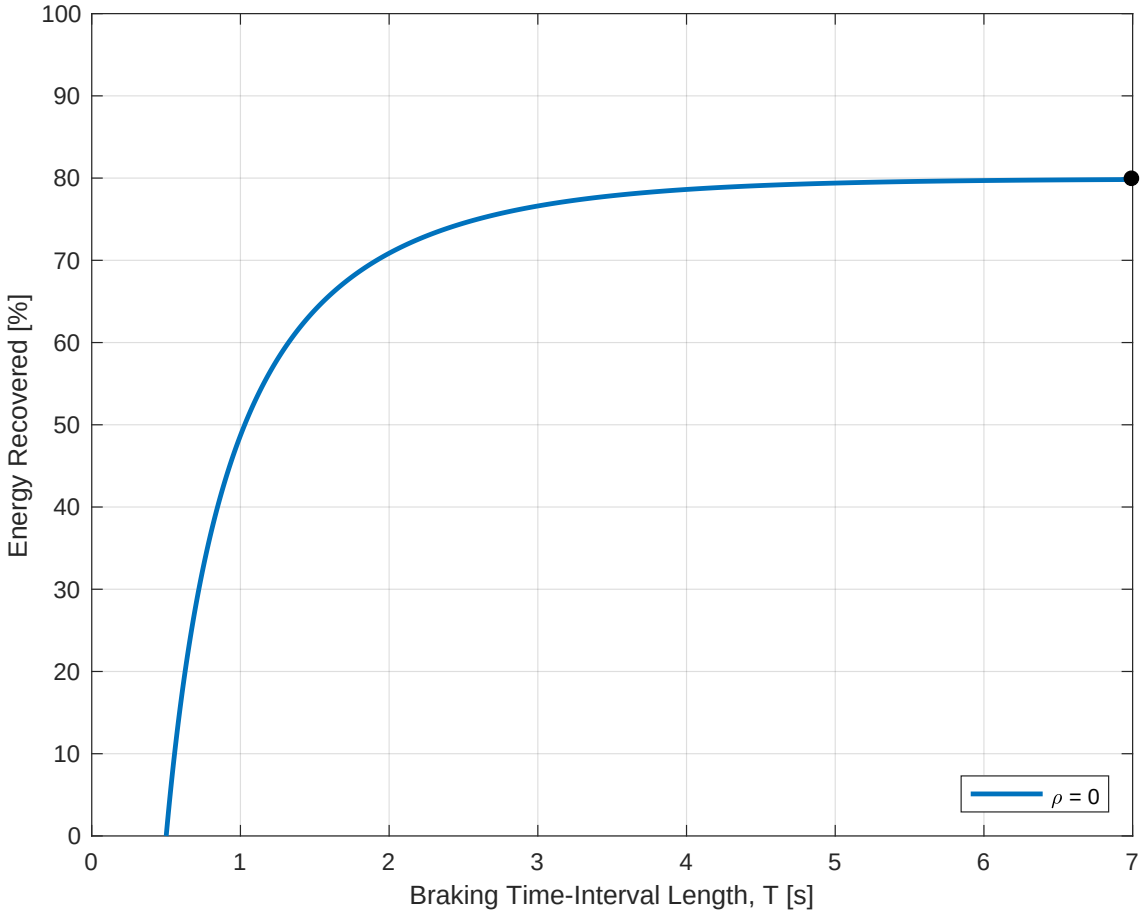

Figure 5.5: Energy recovery ratios as a function of braking time-interval length for $\rho = 0$ for the example system.

Since the rotor is braking to zero speed ($\rho = 0$), the optimal length of the braking time-interval from (5.35) or (5.37) is $T_{\text{opt}} \to \infty$. However, for a practical case as in the example system, this corresponds to about $T = 6$ seconds, above which an appreciable increase in energy recovery is not observed. For the infinite time horizon case of braking to zero speed, the optimal energy recovery ratio is given by γ_2 which in this case is 79.91% of the initial kinetic energy that was stored in the spinning rotor. As discussed earlier, the graph shown

in Figure 5.5 is independent of the initial rotor speed.

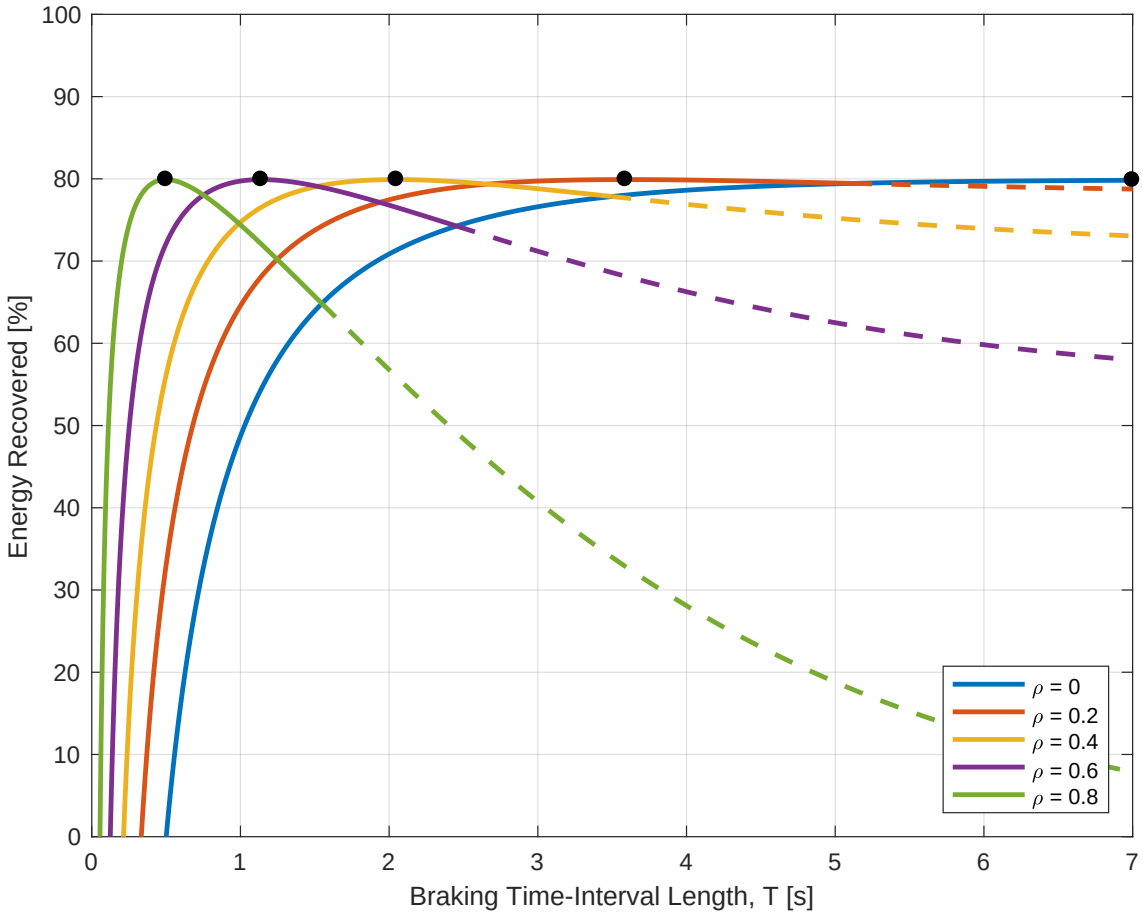

Figure 5.6: Energy recovery ratios as a function of braking time-interval length using various values of ρ for the example system.

Similar graphs of energy recovery ratio versus braking time-interval length can be drawn for various values of ρ as shown in Figure 5.6. Notice that the maximum energy recovery ratio that can be achieved for all values of ρ is $\gamma_2 = 79.91\%$. The optimal length of the braking time-interval that achieves the optimal energy recovery ratio is indicated using a black dot for each value of ρ. These curves are also independent of the initial rotor speed as with Figure 5.5. Notice that some of the curves have a dashed portion, e.g. $\rho = 0.8$ shown in green. The dashed portions of the energy recovery curves correspond to values of T that result in "bad" braking trajectory designs as described in Section 5.2. Designers of the braking trajectory should avoid choosing values of T that lie in the dashed portions of

the energy recovery ratio curves in Figure 5.6.

5.5.3 Comparison of Constant Torque Braking and Optimal Regenerative Braking

The application of a constant braking torque does not always guarantee recovery of kinetic energy as seen in Figure 5.4(a). For the example system, application of a constant braking torque that is more than 40% of the maximum braking torque results in energy being expended rather than recovered during the braking interval. However, as seen earlier there are certain levels of constant braking torque that recover kinetic energy during braking. The performance of the constant braking torque method and the optimal regenerative braking method are compared in this section for the case of $\rho = 0$. A braking torque corresponding to 10% of the maximum braking torque is used for the constant braking torque method. For the optimal regenerative braking method the length of the braking time-interval is chosen to be $T = 5$ s. Figures 5.7(a) and 5.7(b) compare the rotor speed and braking torque trajectories for the two methods. Table 5.3 compares the energy recovery ratios and braking times for the two methods. The trajectories are drawn using the expressions in (5.43) and (5.28) for constant torque braking and optimal braking respectively. The energy recovered is calculated using (5.47) and (5.29) for the two methods. The comparison of the performance in Table 5.3 shows that there is a trade-off between energy recovery and braking time. The optimal regenerative braking method outperforms the constant braking torque method by recovering more than 8% of the stored kinetic energy, however, it takes an additional 3 seconds to reach zero speed. The optimal braking trajectory in the torque-speed plane is shown in Figure 5.7(b) for $T = 5$ seconds. If larger values of T were chosen, this curve would approach a straight line with a slope of $-\dfrac{K^2}{2R_s}(1-\gamma_2)$ as seen in (5.39).

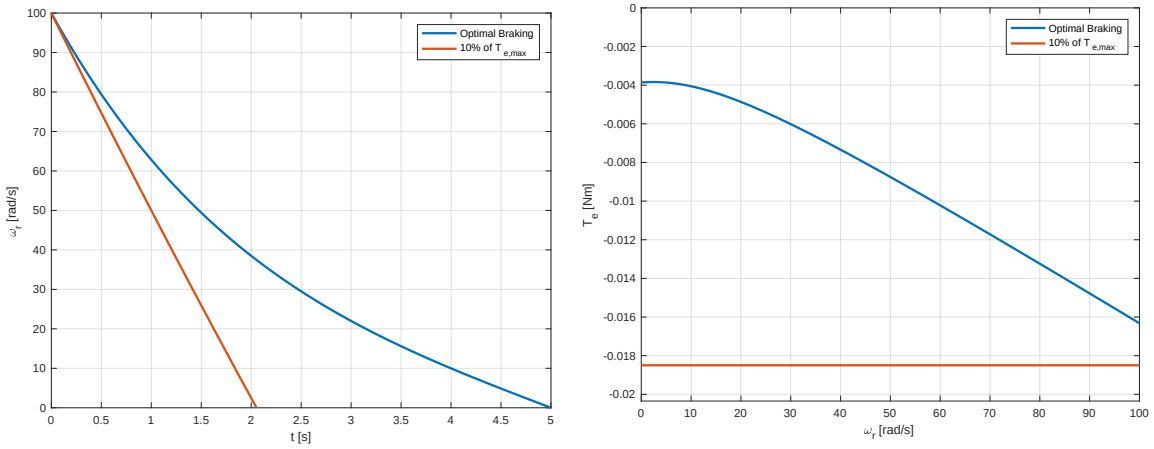

(a) Rotor speed trajectories

(b) Torque trajectories in the torque-speed plane

Figure 5.7: Rotor speed and braking torque trajectories using constant torque braking and optimal regenerative braking methods on the example electromechanical system from an initial rotor speed of 100 rad/s and braking to zero speed.

Table 5.3: Comparison of Performance of Constant-Torque Braking and Optimal Kinetic Energy Recovery Methods for the Example System

Method	Energy Recovered [%]	Braking Time [s]
10% of $T_{e,\max}$	71.15	2.05
Optimal Braking	79.39	5

5.5.4 Simulation of Example System

Implementation

Now that the optimal braking controller for the example system has been designed and its performance has been analyzed and compared with that of a constant braking torque controller, the next task is to implement the algorithm on the system. One method of implementing the optimal braking control algorithm is to use the closed-loop torque controller shown in Figure 3.4 to implement the optimal torque trajectory (5.39) during the braking interval. However, this is not advisable for two reasons:

1. The system was operating under closed-loop speed control before the braking event to regulate the rotor speed at $\omega_r = \omega_{r0}$. At the end of the braking interval, the system will again operate under closed-loop speed control to regulate the rotor speed at $\omega_r = \omega_{rT}$. Therefore, it seems unnatural for the system to transition from speed control to torque control (during the braking interval) and then back to speed control again. Moreover, switching between controllers may result in undesirable speed transients which could affect the performance of the optimal kinetic energy recovery algorithm.

2. The design of the optimal braking trajectory is based on knowledge of electrical and mechanical parameters. If there is a mismatch between the design parameters and actual parameters, the braking trajectory will no longer be optimal. Moreover, using closed-loop torque control with mismatched parameters during the braking interval will result in a final rotor speed that is not ω_{rT} at the end of the braking interval. The closed-loop speed controller will have to kick into action to bring the rotor speed to $\omega_r = \omega_{rT}$ which will result in undesirable speed transients.

To avoid these problems, the optimal braking trajectory can be realized by using the optimal time-dependent speed trajectory in (5.19) as the reference speed input of a closed-loop speed controller as shown in Figure 3.9. If the braking event starts at $t = T_0$ and ends at

$t = T_0 + T$, then the rotor speed reference signal is

$$\omega_r^*(t) = \begin{cases} \omega_{r0} & \text{if } 0 \leq t < T_0 \\ \dfrac{\omega_{r0}\left(e^{\alpha(T-t+T_0)} - e^{-\alpha(T-t+T_0)}\right) + \omega_{rT}\left(e^{\alpha(t-T_0)} - e^{-\alpha(t-T_0)}\right)}{e^{\alpha T} - e^{-\alpha T}} & \text{if } T_0 \leq t < T_0 + T \\ \omega_{rT} & \text{if } t \geq T_0 + T \end{cases} \tag{5.50}$$

For the case where $T = T_{\text{opt}} = \dfrac{1}{\alpha} \ln\left(\dfrac{1}{\rho}\right)$, the rotor speed reference signal can be simplified as

$$\omega_r^*(t) = \begin{cases} \omega_{r0} & \text{if } 0 \leq t < T_0 \\ \omega_{r0}\, e^{-\alpha(t-T_0)} & \text{if } T_0 \leq t < T_0 + T_{\text{opt}} \\ \omega_{rT} & \text{if } t \geq T_0 + T_{\text{opt}} \end{cases} \tag{5.51}$$

Using the closed-loop speed controller to implement the optimal braking control algorithm eliminates the undesirable transients that arise from switching between controllers as discussed previously. It also ensures that the rotor speed at the end of the braking interval is regulated accurately to $\omega_r = \omega_{rT}$ even in the presence of parameter mismatch.

Simulation Results

Simulations are performed to test the effectiveness of using a feedback speed controller to implement the optimal braking control algorithm. The example system is assumed to be at an initial speed of $\omega_{r0} = 100$ rad/s. The requirements of the braking event are to reduce the rotor speed to half its initial speed in 1.5 seconds, i.e. $\omega_{rT} = 50$ rad/s and $T = 1.5$ s. The bandwidth of the speed controller is chosen to be 5 rad/s and that of the current controller is 2500 rad/s. The feedback gains for speed and current controllers are chosen according to (3.52) and (3.34) respectively. For the given braking parameters, the ideal energy recovery

ratio according to (5.26) is 79.90%. Figure 5.8(a) compares the simulation speed trajectory (blue) with the reference trajectory (dashed red) for a speed controller with bandwidth $\alpha_w = 5$ rad/s. Observe that the reference trajectory is not followed accurately using the feedback speed controller. Not following the optimal braking reference trajectory also affects the energy recovery performance; in this case the energy recovery ratio is 79.6%. Trajectory tracking can be improved by cranking up the speed controller bandwidth as seen in Figure 5.8(b), where the speed controller bandwidth is $\alpha_w = 15$ rad/s. This also improves the energy recovery ratio to 79.76%. However, using high-bandwidth gains can lead to aggressive responses, especially to step reference commands, and cause undesirable response overshoots. High-bandwidth gains can also excite high-frequency unmodeled parasitic dynamics which can render the system unstable according to the theory of singular perturbation in [72].

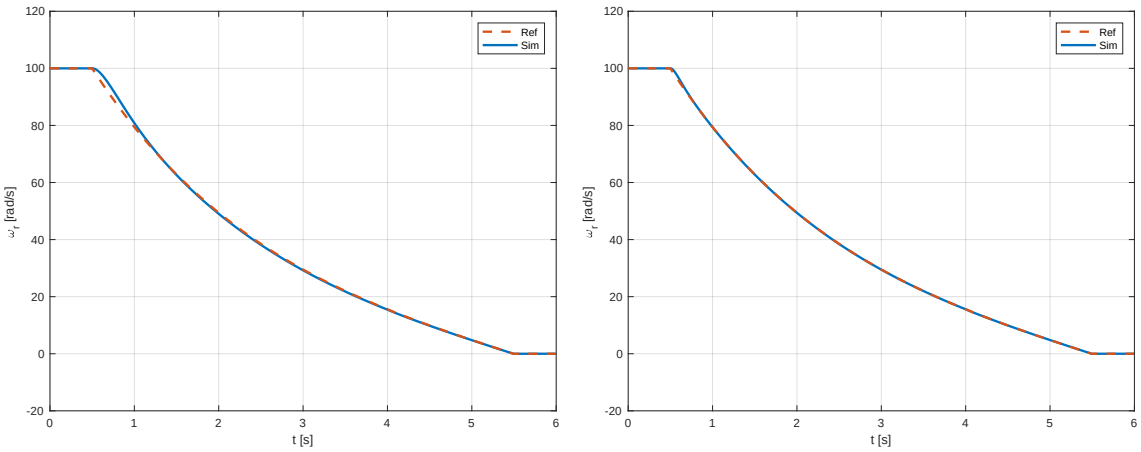

(a) $\alpha_w = 5$ rad/s (b) $\alpha_w = 15$ rad/s

Figure 5.8: Simulation results of optimal braking control using a closed-loop feedback speed controller with different bandwidth selections.

To avoid using high-bandwidth speed controller gains and ensure accurate trajectory tracking, a feedforward signal is used in combination with the feedback speed controller. The block diagram of the optimal braking controller is modified as shown in Figure 5.9.

The user-defined braking parameters such as initial rotor speed (ω_{r0}), final rotor speed (ω_{rT}), and braking time-interval length (T) are given as inputs to the optimal trajectory

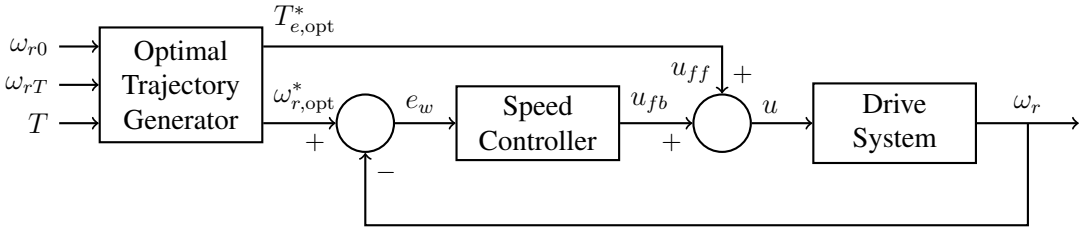

Figure 5.9: Block diagram of the modified speed controller with feedforward torque reference signal.

generator block. This block then uses the inputs and the electromechanical parameters of the system to generate time-dependent speed reference command, $\omega^*_{r,\text{opt}}$, as in (5.19) and corresponding optimal braking torque reference trajectory, $T^*_{e,\text{opt}}$, as in (5.21). The speed reference command is given as the reference input of a closed-loop feedback speed controller as shown in Figure 3.9 which uses the measured or estimated rotor speed to compute an error signal e_w to generate a feedback torque reference u_{fb}. The optimal braking torque reference trajectory, T^*_e, is then added to the feedback torque reference in the form of a feedforward signal u_{ff} to generate an overall torque reference command u which is then given as an input to the drive system.

The dynamics of the overall system will now be analyzed. The rotor speed dynamics assuming only viscous friction mechanical loading is written as

$$\dot{\omega}_r = \frac{1}{J}\left(T_e - B_1\omega_r\right) \tag{5.52}$$

The dynamics of the reference signal satisfies

$$\dot{\omega}^*_{r,\text{opt}} = \frac{1}{J}\left(T^*_{e,\text{opt}} - B_1\omega^*_{r,\text{opt}}\right) \tag{5.53}$$

where $\omega^*_{r,\text{opt}}$ and $T^*_{e,\text{opt}}$ are outputs of the optimal trajectory generator. The output of the

feedback speed controller is

$$u_{fb} = k_{w1} e_w + k_{w2} \sigma_w \tag{5.54}$$

where

$$\begin{aligned} e_w &= \omega^*_{r,\text{opt}} - \omega_r \\ \dot{\sigma}_w &= e_w \end{aligned} \tag{5.55}$$

and the compensator gains are chosen according to (3.52) as

$$\begin{aligned} k_{w1} &= 2J\alpha_w - B_1 \\ k_{w2} &= J\alpha_w^2 \end{aligned} \tag{5.56}$$

where α_w is the user-defined speed controller bandwidth. The feedforward torque reference is defined as

$$u_{ff} = T^*_{e,\text{opt}} \tag{5.57}$$

and the overall torque reference command u is defined as

$$u = u_{ff} + u_{fb} = T^*_{e,\text{opt}} + k_{w1} e_w + k_{w2} \sigma_w \tag{5.58}$$

The signal u is given as the input to the drive system which produces an electromagnetic

torque that satisfies $T_e = u$. The overall system dynamics are now represented as

$$\begin{aligned}
\dot{\omega}_r &= \frac{1}{J}\left(T_e - B_1\omega_r\right) \\
&= \frac{1}{J}\left(T^*_{e,\text{opt}} + k_{w1}e_w + k_{w2}\sigma_w - B_1\omega_r\right) \\
&= \frac{1}{J}\left(T^*_{e,\text{opt}} - B_1\omega^*_{r,\text{opt}} + B_1\omega^*_{r,\text{opt}} + k_{w1}e_w + k_{w2}\sigma_w - B_1\omega_r\right) \\
&= \dot{\omega}^*_{r,\text{opt}} + \frac{1}{J}\left(B_1\omega^*_{r,\text{opt}} + k_{w1}e_w + k_{w2}\sigma_w - B_1\omega_r\right) \\
&= \dot{\omega}^*_{r,\text{opt}} + \frac{1}{J}\left(\left(k_{w1} + B_1\right)e_w + k_{w2}\sigma_w\right)
\end{aligned} \tag{5.59}$$

The speed error dynamics are

$$\begin{aligned}
\dot{e}_w &= \dot{\omega}^*_{r,\text{opt}} - \dot{\omega}_r = -\frac{1}{J}\left(\left(k_{w1} + B_1\right)e_w + k_{w2}\sigma_w\right) \\
\dot{\sigma}_w &= e_w
\end{aligned} \tag{5.60}$$

Substituting the compensator gains from (5.56) results in

$$\begin{aligned}
\dot{e}_w &= -2\alpha_w e_w - \alpha_w^2\sigma_w \\
\dot{\sigma}_w &= e_w
\end{aligned} \tag{5.61}$$

which is rewritten in matrix form as

$$\begin{bmatrix} \dot{e}_w \\ \dot{\sigma}_w \end{bmatrix} = \begin{bmatrix} -2\alpha_w & -\alpha_w^2 \\ 1 & 0 \end{bmatrix} \begin{bmatrix} e_w \\ \sigma_w \end{bmatrix} \tag{5.62}$$

which is represented by the characteristic polynomial

$$(s + \alpha_w)^2. \tag{5.63}$$

The above analysis shows that the addition of the feedforward term results in unforced error and integrator dynamics staying at zero if the system started with zero error at the

beginning of the braking interval and the initial condition of the error integrator is zero, regardless of the choice of speed controller bandwidth, α_w. The revised simulation result with the feedforward reference torque signal included is shown in Figure 5.10. The speed controller bandwidth is the same as that used to produce Figure 5.8(a), i.e. $\alpha_w = 5$ rad/s. Observe that optimal reference trajectory is followed perfectly even for low bandwidth speed control and the energy recovery ratio is 79.90% which is the ideal energy recovery ratio for the chosen set of braking parameters. Therefore, the addition of the feedforward signal ensures accurate tracking of the designed trajectory.

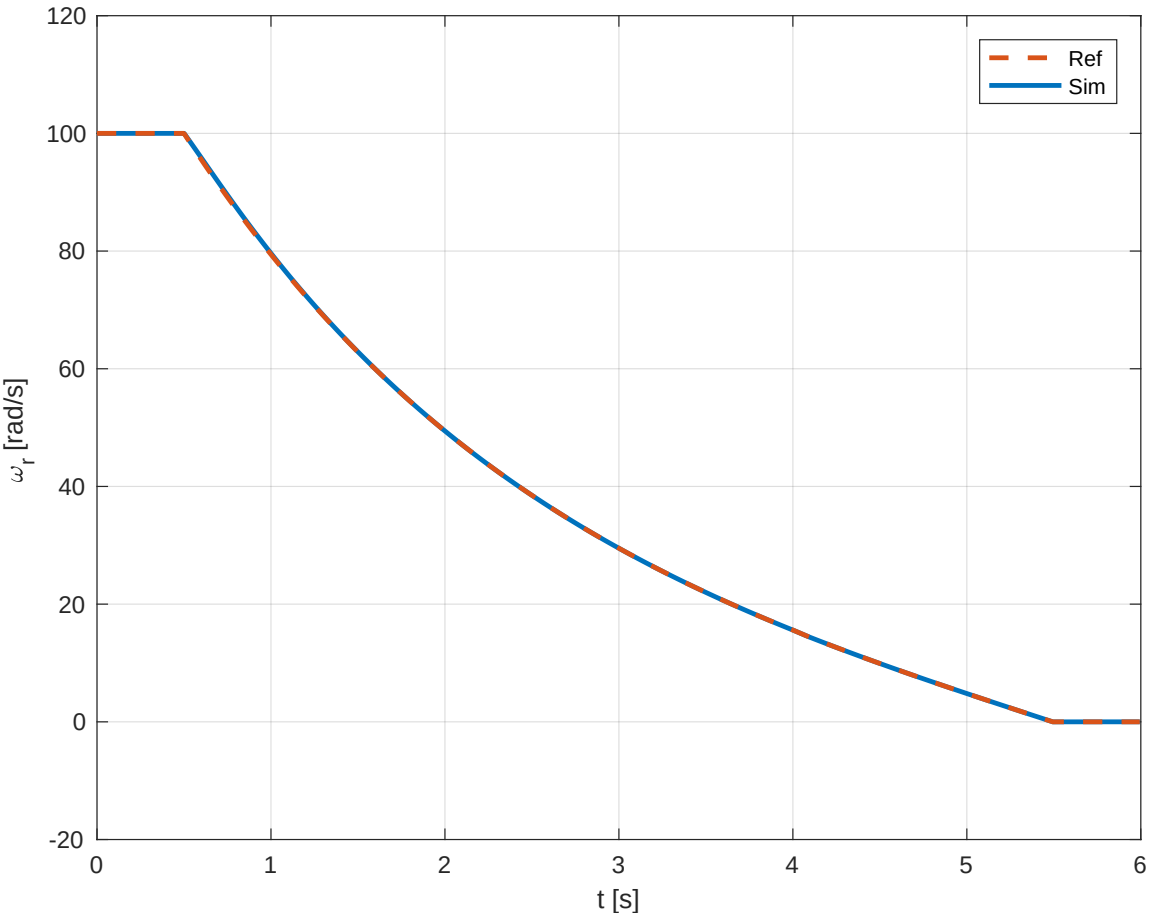

Figure 5.10: Simulation results of optimal braking control using a closed-loop feedback speed controller with the addition of the feedforward torque reference signal for $\alpha_w = 5$ rad/s.

CHAPTER 6
OPTIMAL KINETIC ENERGY RECOVERY ALGORITHMS FOR ELECTRIC MACHINES UNDER CONSTANT-FLUX OPERATION

This chapter discusses optimal regenerative braking for SPMs, IPMs, and induction machines operating under constant-flux. A common framework will be developed that can be applied to all three machine types to achieve optimal regenerative braking. Moreover, the theory will be expanded to include another type of mechanical load, i.e. Coulomb friction. As explained earlier, for permanent magnet synchronous machines, this Coulomb friction component in the mechanical load is due to magnetic hysteresis that presents an effect that is indistinguishable from Coulomb friction during the mechanical parameter identification process.

6.1 Current Reference Signals for Constant-Flux Operation

As discussed earlier in Chapter 3, field-oriented control will be used to control the electric machines, which means that the rotor flux is controlled using the direct-axis current and the electromagnetic torque is controlled using the quadrature-axis current. The reference currents that will be used to achieve a desired electromagnetic torque, T_e, under constant-flux operation will be discussed in this section. Constant-flux operation in this context means that the rotor flux is constant during the operation of the machine. The rotor flux is not influenced by either the rotor speed or the desired electromagnetic torque. As a consequence of current and voltage limits, constant-flux operation is confined to the constant-torque region of the electric machine.

SPM

For SPMs, it is well-known that the most efficient operation in the constant-flux region is characterized by direct and quadrature axes currents equal to

$$\begin{aligned} i_d^* &= 0 \\ i_q^* &= \frac{T_e^*}{N\Lambda} \end{aligned} \tag{6.1}$$

where T_e^* is the desired electromagnetic torque in the constant-flux region of the torque-speed plane. This choice of current reference signals is consistent with the concept of Maximum-Torque-Per-Amp (MTPA) as well as optimal kinetic energy recovery methodology that was derived in a previous chapter.

IPM

In the case of IPMs characterized by ideal sinusoidal permanent-magnet flux, if constant-flux operation is desired, then the choice of direct and quadrature currents that can be used to achieve a desired torque reference, T_e^* are

$$\begin{aligned} i_d^* &= \zeta_d \; i_{d,\mathrm{MTPA,max}} \\ i_q^* &= \frac{T_e^*}{N\left(\Lambda + \left(L_d - L_q\right) i_d^*\right)} \end{aligned} \tag{6.2}$$

where ζ_d is a fraction of the maximum d-axis current that can be applied in the constant-flux region ($i_{d,\mathrm{MTPA,max}}$) according to MTPA

$$\begin{aligned} 0 \leq \zeta_d &\leq 1 \\ i_{d,\mathrm{MTPA,max}} &= \frac{-\Lambda + \sqrt{\Lambda^2 + 8\left(L_d - L_q\right)^2 I_{\max}^2}}{4\left(L_d - L_q\right)} \end{aligned} \tag{6.3}$$

Zero direct-axis current is a valid choice for constant-flux operation in this case.

Induction Machines (IM)

Unlike permanent-magnet synchronous machines, induction machines cannot produce electromagnetic torque with zero direct-axis current. The rotor flux that is essential to produce electromagnetic torque is not sourced through permanent-magnets in this case, but is sourced through the direct-axis component of the stator current vector. The quadrature-axis current is used to achieve the desired torque reference, T_e^*. In other words, flux and torque are manipulated independently by the direct and quadrature axis respectively. This method is called the indirect field orientation method of control.

$$\begin{aligned} i_d^* &= \zeta_d \; i_{d,\mathrm{MTPA,max}} \\ i_q^* &= \left(\frac{L_r}{NL_m}\right)\frac{T_e^*}{\lambda_d^*} \end{aligned} \tag{6.4}$$

where λ_d^* is the desired rotor flux and ζ_d is a fraction of the maximum d-axis current that can be applied in the constant-flux region ($i_{d,\mathrm{MTPA,max}}$) according to MTPA.

$$\begin{aligned} 0 < \zeta_d &\leq 1 \\ i_{d,\mathrm{MTPA,max}} &= \frac{I_{\max}}{\sqrt{2}} \\ \lambda_d^* &= L_m i_d^* \end{aligned} \tag{6.5}$$

A value of $\zeta_d = 0$ is not an option for induction machines if a non-zero value of electromagnetic torque is desired.

A summary of the current references for the three types of electric machines is shown in Table 6.1. Notice that the formula for i_d^* in all cases does not depend on the torque reference signal. In other words, the direct-axis current references are set to a predetermined value and are not altered during the operation of the electric machine.

Table 6.1: Current References for Constant-Flux Operation

Machine Type	i_d^*	i_q^*
SPM	0	$\dfrac{T_e^*}{N\Lambda}$
IPM	$\zeta_d \left(\dfrac{-\Lambda + \sqrt{\Lambda^2 + 8\left(L_d - L_q\right)^2 I_{\max}^2}}{4\left(L_d - L_q\right)} \right)$	$\dfrac{T_e^*}{N\left(\Lambda + \left(L_d - L_q\right) i_d^*\right)}$
IM	$\zeta_d \left(\dfrac{I_{\max}}{\sqrt{2}} \right)$	$\left(\dfrac{L_r}{N L_m^2} \right) \dfrac{T_e^*}{i_d^*}$

6.2 Electric Power and Controllable Electric Power

The expression for electric power entering or leaving all three types of electric machines is given by

$$P_e = v_d i_d + v_q i_q \tag{6.6}$$

Using the quasi-steady-state expressions from the current dynamic equations, the electric power can be simplified for each machine type as follows:

SPM

$$P_e \approx \underbrace{T_e^* \omega_r + \frac{R_e}{K_e^2} T_e^{*2}}_{P_c} \tag{6.7}$$

where $R_e = R_s$ and $K_e = N\Lambda$. Notice that all of the terms in the expression for electric power are influenced (or controlled) by the torque reference signal T_e^*. Therefore, a term called controllable electric power, P_c, can be defined as the portion of the total electric power that is influenced by T_e^*. In this case, the controllable electric power and the total electric power are the same.

IPM

$$P_e \approx R_s i_d^{*2} + \underbrace{T_e^* \omega_r + \frac{R}{K_r^2} T_e^{*2}}_{P_c} \tag{6.8}$$

where $R_e = R_s$ and $K_e = N\left(\Lambda + \left(L_d - L_q\right) i_d^*\right)$. In this case, there is one term in the total electric power expression that is not influenced by the torque reference signal, T_e^*. This is the power that is associated with the production of a direct-axis current for constant-flux operation as shown in Table 6.1. As discussed earlier, the value of i_d^* can be set to zero for the IPM, resulting in an operation principle that is identical to an SPM. However, if i_d^* is non-zero, this portion of electric power ($R_s i_d^{*2}$) is incurred during the entire operation of the IPM and this power is sourced from the electrical supply.

IM

$$P_e \approx R_s i_d^{*2} + \underbrace{T_e^* \omega_r + \frac{R_e}{K_e^2} T_e^{*2}}_{P_c} \tag{6.9}$$

where $R_e = R_s + R_r \frac{L_m^2}{L_r^2}$ and $K_e = \frac{N L_m^2}{L_r} i_d^*$. Again in this case, there is one term in the total electric power expression that is not influenced by the torque reference signal, T_e^*. This is the power that is associated with the production of a direct-axis current for constant-flux operation as shown in Table 6.1. For induction machines, the direct-axis current cannot be set to zero and this portion of the electric power is always incurred during the operation of the induction machine. However, the remaining portion of the electric power expression, the controllable electric power P_c, can be influenced through the reference torque signal, T_e^*.

The expression for controllable electric power for all three types of electric machine is given by a common expression, viz.

$$P_c = T_e^* \omega_r + \frac{R_e}{K_e^2} T_e^{*2} \tag{6.10}$$

where R_e is the effective stator resistance and K_e is the effective back-EMF constant whose expressions are listed in Table 6.2 for each type of electric machine operating under field-oriented control.

Table 6.2: Effective Resistance and Back-EMF Constants for Different Electric Machines Under Constant-Flux Operation

Machine Type	R_e	K_e
SPM	R_s	$N\Lambda$
IPM	R_s	$N\left(\Lambda + \left(L_d - L_q\right) i_d^*\right)$
IM	$R_s + R_r \dfrac{L_m^2}{L_r^2}$	$\dfrac{N L_m^2}{L_r} i_d^*$

6.3 A Common Optimal Kinetic Energy Recovery Control Framework

The optimal kinetic energy recovery framework is revisited in this section with two important changes:

1. The cost function now uses only the controllable electric power, i.e.

$$E = \int_0^T P_c \, dt \tag{6.11}$$

The objective is to minimize the controllable electrical energy during a braking interval of length of T seconds, subject to the constraints of initial rotor speed, $\omega_r(0) = \omega_{r0}$, and final rotor speed, $\omega_r(T) = \omega_{rT}$.

2. The mechanical load model now includes both a viscous friction component (B_1)

and a Coulomb friction component (B_0)

$$T_{\text{load}} = B_1\omega_r + B_0\ \text{sgn}(\omega_r) \tag{6.12}$$

The rotor speed dynamics are now written as

$$\dot{\omega}_r = \frac{1}{J}\left(T_e^* - B_1\omega_r - B_0\ \text{sgn}(\omega_r)\right) \tag{6.13}$$

According to the theory of optimal control, a Hamiltonian function can be formulated as

$$H = P_c + \chi\dot{\omega}_r \tag{6.14}$$

where χ is the costate variable. Substituting the expressions for controllable electric power and rotor speed dynamics, the Hamiltonian is expanded as

$$\begin{aligned} H &= P_c + \chi\dot{\omega}_r \\ &= T_e^*\omega_r + \frac{R_e T_e^{*2}}{K_e^2} + \frac{\chi}{J}\left(T_e^* - B_1\omega_r - B_0\ \text{sgn}(\omega_r)\right) \end{aligned} \tag{6.15}$$

The electromagnetic torque reference signal is used as the optimal control variable in this case. This can be done here since the user has already chosen the value of direct-axis current, i_d^*, to be set to a pre-specified constant level that is independent of the rotor speed (ω_r) and the desired electromagnetic torque (T_e^*). The optimal electromagnetic torque reference signal can now be calculated by setting the following partial derivative

$$\frac{\partial H}{\partial T_e^*} = \omega_r + \frac{2R_e}{K_e^2}T_e^* + \frac{\chi}{J} \tag{6.16}$$

equal to zero, resulting in

$$T^*_{e,\text{opt}} = -\frac{K_e^2}{2R_e}\left(\omega_{r,\text{opt}} + \frac{\chi_{\text{opt}}}{J}\right) \tag{6.17}$$

The state and costate dynamics can be derived in terms of the state, costate, and control variables by taking the partial derivatives

$$\begin{aligned} \dot{\omega}_{r,\text{opt}} &= \frac{\partial H}{\partial \chi} = \frac{1}{J}\left(T^*_{e,\text{opt}} - B_1\omega_{r,\text{opt}} - B_0\ \text{sgn}(\omega_{r,\text{opt}})\right) \\ \dot{\chi}_{\text{opt}} &= -\frac{\partial H}{\partial \omega_r} = -T^*_{e,\text{opt}} + \frac{B_1}{J}\chi_{\text{opt}} + \frac{2B_0}{J}\delta(\omega_{r,\text{opt}})\chi_{\text{opt}} \end{aligned} \tag{6.18}$$

where $\delta(\cdot)$ is the Dirac delta function, which appears because of the infinite derivative of the signum function [73]. The factor of 2 in the Dirac function appears because the magnitude of the instantaneous change in the signum function is 2.

6.3.1 Two-Point Boundary Value Problem

The optimal value of the control variable, $T^*_{e,\text{opt}}$, from (6.17) is substituted into the optimal state and costate dynamic equations in (6.18) to obtain a two-point boundary value problem as shown below

$$\begin{bmatrix} \dot{\omega}_{r,\text{opt}} \\ \dot{\chi}_{\text{opt}} \end{bmatrix} = \frac{K_e^2}{2JR_e}\begin{bmatrix} -(1+2\gamma) & J^{-1} \\ J & (1+2\gamma) \end{bmatrix}\begin{bmatrix} \omega_{r,\text{opt}} \\ \chi_{\text{opt}} \end{bmatrix} + \frac{B_0}{J}\begin{bmatrix} -\text{sgn}(\omega_r) \\ 2\delta(\omega_{r,\text{opt}})\chi_{\text{opt}} \end{bmatrix}, \quad \begin{aligned} \omega_{r,\text{opt}}(0) &= \omega_{r0} \\ \omega_{r,\text{opt}}(T) &= \omega_{rT} \end{aligned} \tag{6.19}$$

where $\gamma = \dfrac{B_1 R_e}{K_e^2}$ is a dimensionless electromechanical loss parameter that captures the effect of both the mechanical loss (through B_1) and electrical loss (through R). The system described in (6.19) has two eigenvalues at $\pm\alpha$, where

$$\alpha = \frac{K_e^2}{JR_e}\sqrt{\gamma(1+\gamma)} \tag{6.20}$$

The general solution of the two-point boundary value problem in (6.19) is of the form

$$\begin{aligned} \omega_r(t) &= c_1 e^{-\alpha t} + c_2 e^{\alpha t} + c_{01} \\ \chi(t) &= c_3 e^{-\alpha t} + c_4 e^{\alpha t} + c_{02} \end{aligned} \tag{6.21}$$

where

$$\frac{c_1}{c_3} = -\frac{\gamma_1}{J} \quad \frac{c_2}{c_4} = -\frac{\gamma_2}{J} \quad \frac{c_{01}}{c_{02}} = -\frac{1+2\gamma}{J} \quad c_{01} = -c_0 \quad c_0 = \frac{B_0(1+2\gamma)}{2B_1(1+\gamma)}\mathrm{sgn}(\omega_{r0}) \tag{6.22}$$

and

$$\begin{aligned} \gamma_1 &= 1 + 2\gamma + 2\sqrt{\gamma(1+\gamma)} \\ \gamma_2 &= 1 + 2\gamma - 2\sqrt{\gamma(1+\gamma)} \\ \gamma_1\gamma_2 &= 1 \end{aligned} \tag{6.23}$$

Due to the cross-coupling between the coefficients, only two boundary conditions are required to determine all the coefficients that describe the solution to the two-point boundary value problem. Applying the boundary conditions $\omega_r(0) = \omega_{r0}$ and $\omega_r(T) = \omega_{rT}$, results in

$$\begin{aligned} c_1 &= \frac{\left(\omega_{r0}e^{\alpha T} - \omega_{rT}\right) - c_0\left(1 - e^{\alpha T}\right)}{e^{\alpha T} - e^{-\alpha T}} \\ c_2 &= \frac{\left(\omega_{rT} - \omega_{r0}e^{-\alpha T}\right) + c_0\left(1 - e^{-\alpha T}\right)}{e^{\alpha T} - e^{-\alpha T}} \end{aligned} \tag{6.24}$$

Substituting the values of these coefficients into the general solution for the state and costate trajectories results in specific solutions

$$\omega_{r,\mathrm{opt}} = \frac{\left(\omega_{r0} + c_0\right)\left(e^{\alpha(T-t)} - e^{-\alpha(T-t)}\right) + \left(\omega_{rT} + c_0\right)\left(e^{\alpha t} - e^{-\alpha t}\right)}{e^{\alpha T} - e^{-\alpha T}} - c_0 \tag{6.25}$$

and

$$\chi_{\text{opt}} = \frac{J\ c_0}{1+2\gamma} - J\frac{(\omega_{r0}+c_0)\left(\gamma_2 e^{\alpha(T-t)} - \gamma_1 e^{-\alpha(T-t)}\right) + (\omega_{rT}+c_0)\left(\gamma_1 e^{\alpha t} - \gamma_2 e^{-\alpha t}\right)}{e^{\alpha T} - e^{-\alpha T}} \tag{6.26}$$

for the state and costate trajectories respectively and the corresponding electromagnetic torque reference is obtained from (6.17) as

$$T^*_{e,\text{opt}} = -\frac{K_e^2}{2R_e}\left(\omega_{r,\text{opt}} + \frac{\chi_{\text{opt}}}{J}\right) \tag{6.27}$$

The effect of the Dirac delta function in the costate dynamics will be discussed now. The delta function gives rise to jump discontinuities when the speed trajectory crosses zero speed, i.e. goes from positive to negative. However, as explained earlier such trajectories are considered "bad" designs since they involve both braking and subsequent motoring operation during the braking time-interval and should be avoided. Even with "good" trajectory designs, the jump discontinuity is still encountered for the case where $\omega_{rT} = 0$. This is tackled by setting the value of c_0 to zero at the time-instant the rotor speed $\omega_{r,\text{opt}} = 0$. The other coefficients can be used as they are. For the time-instant when $\omega_{r,\text{opt}} = 0$, the system experiences no Coulomb friction and the mechanical load is characterized by only viscous friction, similar to the system that was discussed in the previous chapter. Notice that the coefficients in (6.24) are identical those in (5.18) with the substitution of $c_0 = 0$.

6.3.2 Energy Recovered

To calculate the kinetic energy that is recovered during the braking interval, the cost function is evaluated as follows

$$\begin{aligned} E &= \int_0^T P_c \, dt \\ &= \int_0^T \left(T^*_{e,\mathrm{opt}} \omega_{r,\mathrm{opt}} + \frac{R_e T^{*2}_{e,\mathrm{opt}}}{K_e^2} \right) \, dt \end{aligned} \tag{6.28}$$

Substituting for the optimal values of T_e^*, ω_r, and χ and computing the integral from $t = 0$ to $t = T$ results in

$$E = E_1 + E_1' + E_1'' + E_2 + E_3 \tag{6.29}$$

where

$$\begin{aligned} E_1 &= -\frac{J}{2(1-e^{-2\alpha T})} \left(\omega_{r0}^2(\gamma_2 - \gamma_1 e^{-2\alpha T}) + \omega_{rT}^2(\gamma_2 e^{-2\alpha T} - \gamma_1) - 2\omega_{r0}\omega_{rT}(\gamma_2 - \gamma_1)e^{-\alpha T} \right) \\ E_1' &= -\frac{J}{(1-e^{-2\alpha T})} c_0 \left(\gamma_2\omega_{r0} - \gamma_1\omega_{rT} - (\omega_{r0} + \omega_{rT})(\gamma_2 - \gamma_1)e^{-\alpha T} + (\gamma_2\omega_{rT} - \gamma_1\omega_{r0})e^{-2\alpha T} \right) \\ E_1'' &= -\frac{J}{2(1-e^{-2\alpha T})} c_0^2(\gamma_2 - \gamma_1)(1 - e^{-\alpha T})^2 \\ E_2 &= \frac{J}{1+2\gamma} c_0 \left(\omega_{r0} - \omega_{rT} \right) \\ E_3 &= -\frac{B_0^2}{4B_1(1+\gamma)} T \end{aligned} \tag{6.30}$$

Notice that the expression for energy recovered in (6.29) and (6.30) simplifies to (5.23) if the B_0 term is set to zero. The above expression for energy recovered is accurate for all trajectory designs (see Section 5.2), except for the subset of "bad" designs that involve zero-speed crossing. The presence of the Dirac delta function causes a jump discontinuity in the optimal speed trajectory at zero-speed and including this jump will result in a complicated expression for energy recovered that is difficult to present in the written form.

An energy recovery ratio can be defined as the ratio between the energy recovered and the kinetic energy available for conversion as

$$E_{\text{ratio}} = -\frac{E}{E_{\text{avail}}} \tag{6.31}$$

where $E_{\text{avail}} = \frac{1}{2} J \omega_{r0}^2 \left(1 - \rho^2\right)$ and $\rho = \frac{\omega_{rT}}{\omega_{r0}}$. In the previous chapter, for the case in which the mechanical load model only included the B_1 term, it was observed that the energy recovery ratio term was independent of the initial rotor speed. This does not apply to the present scenario in which the mechanical load model includes the B_0 term in addition to the B_1 term. In this case, the E_{ratio} depends on the value of the initial rotor speed ω_{r0}.

6.3.3 Performance of Optimal Kinetic Energy Recovery Algorithm

In the previous section, the design of the optimal braking trajectory that recovers maximum kinetic energy for a choice of braking time-interval length, T, was discussed. In this section, the performance of the design will be studied for the three types of electric machines using parameter values from Tables 4.1, 4.2, and 4.3. For each type of electric machine, the energy recovery ratio is plotted as a function of braking time-interval length, T, and speed ratio ρ. This is done for two different values of the initial rotor speed ω_{r0}.

SPM

The energy recovery ratio as a function of braking time-interval length for different speed ratios is shown in Figures 6.1(a) and 6.1(b) for initial rotor speeds of $\omega_{r0} = 100$ rad/s and $\omega_{r0} = 200$ rad/s respectively. The information contained in figures is discussed as follows:

1. The graphs do not start at $T = 0$. This indicates that not all choices of braking time-interval length result in positive energy recovery ratios. For example, the graph shown in blue starts at $T = 0.5$ seconds. Choices of T less than 0.5 seconds end up

losing energy rather than recovering energy, i.e. the losses in the system overwhelm the kinetic energy available for conversion.

2. Solid lines indicate choices of braking time-interval length that result in "good" designs of braking trajectories and the dashed lines correspond to "bad" choices of T according to the discussion in Section 5.2.

3. The black dot in each curve represents the optimal braking time-interval length, T_{opt}, and the corresponding energy recovery ratio. This was determined by running a numerical search that found the maximum energy recovery ratio and the corresponding braking time-interval length from a large array of energy recovery ratios for different values of T. Table 6.3 summarizes the optimal energy recovery ratios corresponding to T_{opt} for different values of ρ.

4. The peak value energy recovery ratio is not the same for every value of ρ. This is different from the observations made in Chapter 5 where the mechanical load model only consisted of viscous friction (B_1). It was observed in Figure 5.6 that the peak value of energy recovery ratio is a constant equal to γ_2 for every value of ρ and is independent of ω_{r0}.

5. The energy recovery ratio depends on the initial rotor speed ω_{r0}. This is evident from Tables 6.3(a) and 6.3(b) where the same value of ρ results in a higher peak energy recovery ratio for $\omega_{r0} = 200$ rad/s when compared to $\omega_{r0} = 100$ rad/s.

IPM

For IPMs, the value of ζ_d influences the optimal braking characteristics through the variable K_e. The choice of $\zeta_d = 0$ for IPMs results in operation that is identical to SPMs. The only source of rotor flux in the air-gap is due to the permanent-magnets that are embedded in the rotor. The variation of energy recovery ratio for the Motorsolver IPM system

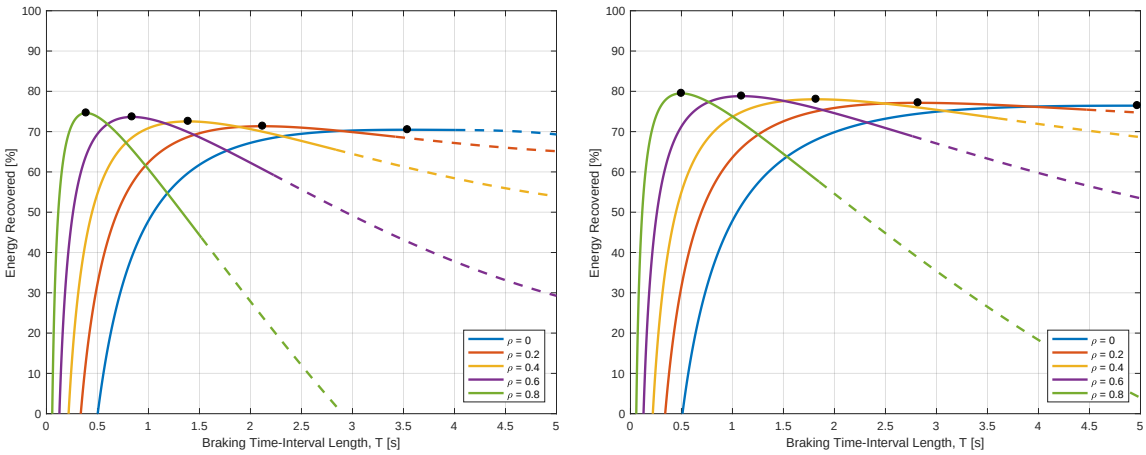

(a) $\omega_{r0} = 100$ rad/s (b) $\omega_{r0} = 200$ rad/s

Figure 6.1: Energy recovery ratio as a function of braking time-interval length for different values of speed ratios for the Anaheim SPM system.

Table 6.3: Peak Energy Recovery Ratio and Optimal Braking Time-Interval Length for Different Speed Ratios for the Anaheim SPM System.

(a) $\omega_{r0} = 100$ rad/s

ρ	E_{ratio} [%]	T_{opt} [s]
0	70.46	3.54
0.2	71.34	2.12
0.4	72.54	1.39
0.6	73.64	0.84
0.8	74.62	0.39

(b) $\omega_{r0} = 200$ rad/s

ρ	E_{ratio} [%]	T_{opt} [s]
0	76.44	4.97
0.2	77.14	2.82
0.4	78.02	1.82
0.6	78.81	1.09
0.8	79.49	0.50

with $\zeta_d = 0$ is shown in Figure 6.2 for initial rotor speeds of 100 rad/s and 200 rad/s. The observations made regarding Figure 6.1 for the SPM system are applicable here as well. The peak energy recovery ratios and the corresponding optimal braking time-interval lengths (T_{opt}) are shown in Tables 6.4(a) and 6.4(b) for initial rotor speed of 100 rad/s and 200 rad/s respectively.

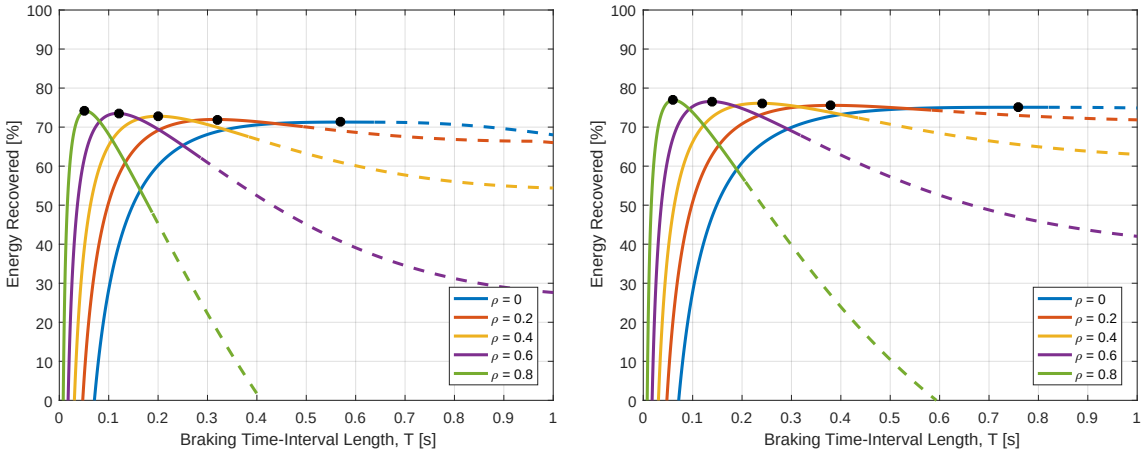

(a) $\omega_{r0} = 100$ rad/s (b) $\omega_{r0} = 200$ rad/s

Figure 6.2: Energy recovery ratio as a function of braking time-interval length for different values of speed ratios for the Motorsolver IPM system with $\zeta_d = 0$.

Table 6.4: Peak Energy Recovery Ratio and Optimal Braking Time-Interval Length for Different Speed Ratios for the Motorsolver IPM system with $\zeta_d = 0$.

(a) $\omega_{r0} = 100$ rad/s

ρ	E_{ratio} [%]	T_{opt} [s]
0	71.28	0.57
0.2	71.96	0.32
0.4	72.80	0.20
0.6	73.52	0.12
0.8	74.14	0.05

(b) $\omega_{r0} = 200$ rad/s

ρ	E_{ratio} [%]	T_{opt} [s]
0	75.08	0.76
0.2	75.57	0.38
0.4	76.11	0.24
0.6	76.56	0.14
0.8	76.94	0.06

With IPMs, there exists an option of injecting a negative d- axis current which either enhances or counteracts the permanent-magnet flux in the air-gap, depending on whether L_d is less than or greater than L_q. For the Motorsolver IPM, the direct-axis stator inductance is less than the quadrature-axis stator inductance ($L_d < L_q$). Therefore, injecting negative

direct-axis current enhances the effect of permanent-magnet flux and results in a larger effective back EMF constant, K_e, according to

$$K_e = N\left(\Lambda + (L_d - L_q)i_d^*\right) \tag{6.32}$$

where $i_d^* = \zeta_d \; i_{d,\mathrm{MTPA,max}}$ is determined by (6.3). For the Motorsolver IPM system, the value of $i_{d,\mathrm{MTPA,max}}$ is -1.15 A (most negative value). Therefore, values of ζ_d between 0 and 1 result in the injection of constant negative d-axis current in the stator windings which enhances the rotor flux in the air-gap. However, this also increases the copper losses due to the Ri_d^{*2} term. The controllable electrical power term, P_c, that was used in the development of the optimal regenerative braking algorithm does not include the copper-loss that is incurred due to the flow of direct-axis current. However, the total electrical power term, P_e, includes the d-axis copper-loss term. Figure 6.3 compares the variation of the energy recovery ratio with braking time-interval length for values of ζ_d between 0 and 1 and $\rho = 0$. The controllable energy recovery ratio is shown in Figure 6.3(a) and the total energy recovery ratio, which includes the energy lost due to d-axis current flow, is shown in Figure 6.3(b). The peak controllable and total energy recovery ratios and the corresponding optimal braking time-interval lengths (T_{opt}) are shown in Tables 6.5(a) and 6.5(b) respectively. Injecting constant levels of negative direct-axis current does not have a significant impact on the controllable energy recovery ratios as seen from Figure 6.3(a). The curve corresponding to $\zeta_d = 1$ slightly outperforms the other curves. The total energy recovery curves in Figure 6.3(b) tell a more complete story. For smaller values of T, the impact of larger values of ζ_d on K_e outweighs the copper-loss due to d-axis current flow and the curve with $\zeta_d = 1$ (light blue) outperforms the other curves. However, as the braking time-interval length increases, the copper winding losses due to the flow of direct-axis current ($R_s i_d^{*2} T$) increases linearly. Therefore, at higher values of T, the energy recovery ratios corresponding to $\zeta_d = 0$ (dark blue) are greater than those with non-zero values of ζ_d

due to the absence of direct-axis current flow and its associated copper-losses for this curve. The injection of direct-axis current will have more pronounced effect on energy recovery ratios for IPMs with larger salience ratios (L_q/L_d) or the ability to handle larger currents or both.

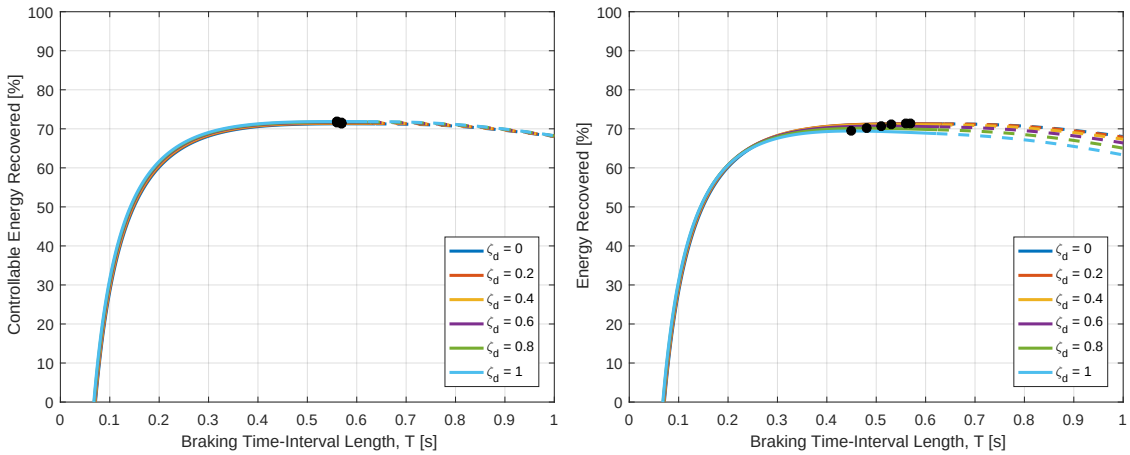

(a) Controllable Energy Recovered (b) Total Energy Recovered

Figure 6.3: Energy recovery ratio as a function of braking time-interval length for different values of ζ_d with $\omega_{r0} = 100$ rad/s and $\rho = 0$ for the Motorsolver IPM system.

Table 6.5: Peak Energy Recovery Ratio and Optimal Braking Time-Interval Length for Different Levels of Constant Direct-Axis Current Injection with $\omega_{r0} = 100$ rad/s and $\rho = 0$ for the Motorsolver IPM System.

(a) Controllable Energy Recovered

ζ_d	E_{ratio} [%]	T_{opt} [s]
0	71.28	0.57
0.2	71.40	0.57
0.4	71.52	0.57
0.6	71.64	0.56
0.8	71.75	0.56
1	71.87	0.56

(b) Total Energy Recovered

ζ_d	E_{ratio} [%]	T_{opt} [s]
0	71.28	0.57
0.2	71.29	0.56
0.4	71.09	0.53
0.6	70.70	0.51
0.8	70.14	0.48
1	69.44	0.45

IM

As discussed earlier, induction machines cannot produce electromagnetic torque with zero direct-axis current. Therefore, $\zeta_d = 0$ is not an option for induction machines. As seen in Table 6.2, the effective back EMF constant, K_e, for an induction machine under constant rotor flux operation is directly proportional to the value of the direct-axis current in the stator. For the Motorsolver induction machine, a value of $\zeta_d = 0.5$ corresponds to a direct-axis current of 1.5 A. This value of d-axis stator current will be used to set up a constant rotor flux of 69.3 mWb in the air-gap. There are copper-losses associated with the flow of direct-axis current, however, the controllable electrical power term is defined in such a way that these losses are neglected during the formulation of the optimal control problem. The variation of controllable energy recovery with the length of the braking time-interval with $\zeta_d = 0.5$ for $\omega_{r0} = 100$ rad/s is shown in Figure 6.4(a) for various speed ratios ρ. As a comparison, the total energy recovery ratio that includes the copper-losses associated with the flow of non-zero direct-axis stator currents is shown in Figure 6.4(b). The peak values of controllable energy recovery and the corresponding values of optimal braking time-interval lengths are shown in Table 6.6(a). There is barely any variation between the peak values of the controllable energy recovery ratios corresponding to different speed ratios ($\approx 1.5\%$) for the induction machine system. In contrast, the SPM system had variations of about 4% for different speed ratios and the IPM system had variations of about 3% between speed ratios. This is due to the less pronounced effect of Coulomb friction in induction machines ($B_0/B_1 \approx 20$ for the Motorsolver IM system). This results in the induction machine system displaying similar trends in the controllable energy recovery curves to the SPM system with only viscous friction in the mechanical load model that was discussed in Chapter 5. On the other hand, the Coulomb friction effect is more pronounced in the SPM ($B_0/B_1 \approx 308$) and IPM ($B_0/B_1 \approx 80$) systems due to the large levels of magnetic hysteresis that the stator experiences due to the rotation of permanent-magnets. The total energy recovery ratio curves in Figure 6.4(b) show the effect of including the copper-losses due to d-axis

current flow in the calculation of energy recovery. The graphs show that there exists a narrow range of values for T such that the energy recovery ratio is positive. In other words, choices of very small or very large values of T result in energy being lost from the system rather than being recovered during the braking interval. Very small values of T result in the production of large q-axis currents which produce significant copper-losses over the short duration of the braking time-interval. On the other hand, large values of T result in large copper-loss energy due to d-axis current flow. Both these effects result in negative energy recovery ratios for very small and very large values of T. The peak energy recovery ratios have significant variation between speed ratios as seen in Table 6.6(b). The optimal braking time-interval length is associated with balancing the d-axis copper losses, q-axis copper losses, and mechanical losses due to B_1 and B_0 for the induction machine system.

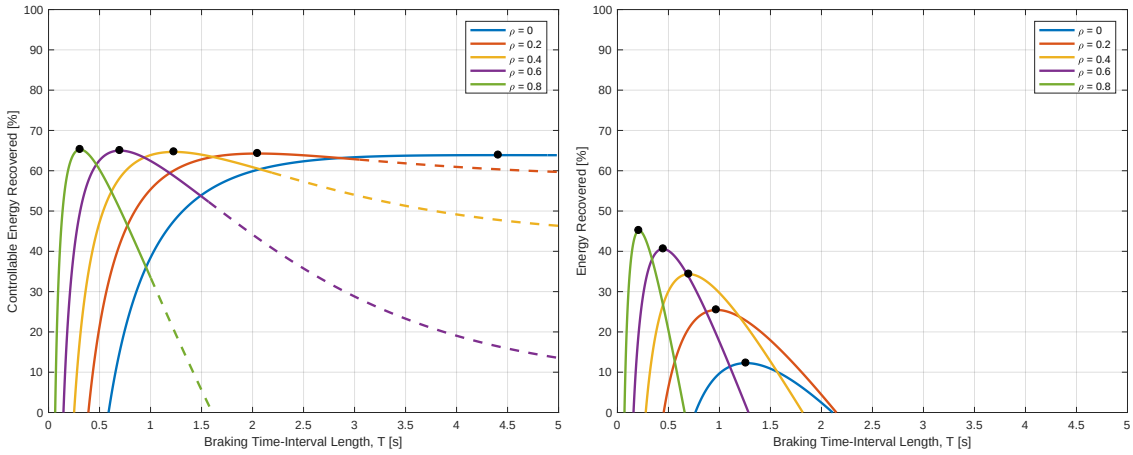

(a) Controllable Energy Recovered (b) Total Energy Recovered

Figure 6.4: Energy recovery ratio as a function of braking time-interval length for different speed ratios with $\zeta_d = 0.5$ and $\omega_{r0} = 120$ rad/s for the Motorsolver IM system.

The choice of ζ_d affects the level of constant rotor flux that is produced in the air gap. This in turn affects the performance of the optimal kinetic energy recovery algorithm through the back EMF constant K_e. The variation of controllable energy recovery and total energy recovery for various values of ζ_d is shown in Figures 6.5(a) and 6.5(b) respectively. The scenario of braking to a standstill from an initial rotor speed of 120 rad/s is considered

Table 6.6: Peak Energy Recovery Ratio and Optimal Braking Time-Interval Length for Different Speed Ratios with $\zeta_d = 0.5$ and $\omega_{r0} = 120$ rad/s for the Motorsolver IM System.

(a) Controllable Energy Recovered

ρ	E_{ratio} [%]	T_{opt} [s]
0	63.87	4.41
0.2	64.27	2.05
0.4	64.67	1.23
0.6	65.00	0.70
0.8	65.27	0.31

(b) Total Energy Recovered

ρ	E_{ratio} [%]	T_{opt} [s]
0	12.26	1.26
0.2	25.46	0.97
0.4	34.33	0.70
0.6	40.59	0.45
0.8	45.16	0.21

here. The choice of $\zeta_d = 0$ is an invalid choice for induction machine operation and is not considered for that reason. The graphs in Figure 6.5(a) show that the controllable energy recovery ratio increases with increasing levels of constant direct-axis current. However, with increasing levels of constant d-axis current, the possibility of choosing values of T that will result in "bad" trajectory designs increases (dashed lines in Figure 6.5(a)). Therefore, the value of T must be chosen carefully to avoid "bad" designs. The total energy recovery ratios that account for the copper losses due to the flow of d-axis current are shown in Figure 6.5(b) for different levels of constant d-axis current. Observe that the feasible range of T that results in positive energy recovery ratios keeps shrinking as the level of constant d-axis current increases. This is because longer lengths of the braking time-intervals result in increased energy losses due to the flow of constant direct-axis current during the entire length of the braking time-interval. The graphs in Figure 6.5(b) can be used as a reference to choose the value of T for the level of constant d-axis current that is desired. Moreover, the peak energy recovery ratio and the choice of T that achieves it (T_{opt}) is shown as a black dot on each curve. These values are also tabulated in Tables 6.7(a) and 6.7(b).

6.4 Comparison with Constant-Torque Braking

As stated in the previous chapter, several authors recommend applying constant braking torque as a means to recover kinetic energy during the braking event. For the example

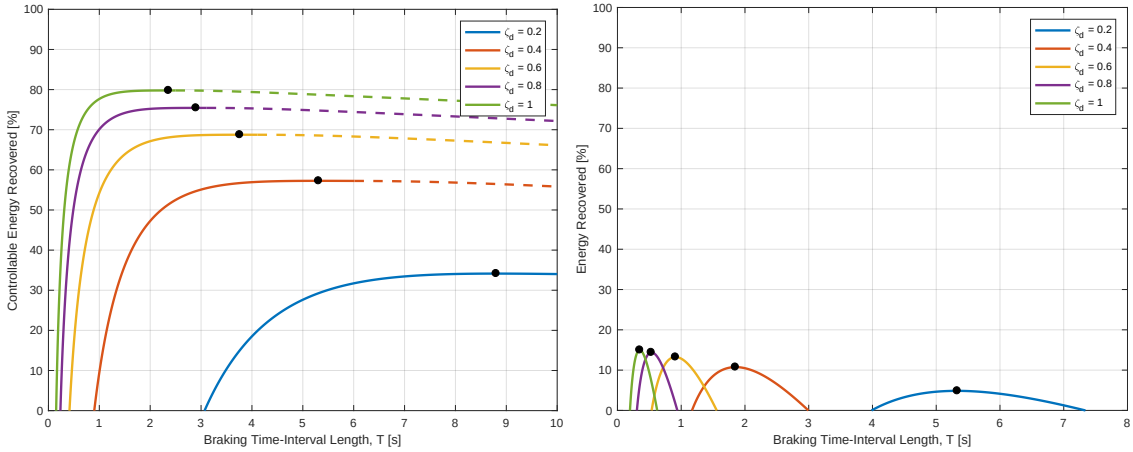

(a) Controllable Energy Recovered (b) Total Energy Recovered

Figure 6.5: Energy recovery ratio as a function of braking time-interval length for different levels of constant d-axis current with $\omega_{r0} = 120$ rad/s and $\rho = 0$ for the Motorsolver IM system.

Table 6.7: Peak Energy Recovery Ratio and Optimal Braking Time-Interval Length for Different Levels of Constant Direct-Axis Current with $\omega_{r0} = 120$ rad/s and $\rho = 0$ for the Motorsolver IM System.

(a) Controllable Energy Recovered

ζ_d	E_{ratio} [%]	T_{opt} [s]
0.2	34.15	8.80
0.4	57.26	5.31
0.6	68.75	3.76
0.8	75.44	2.90
1	79.78	2.36

(b) Total Energy Recovered

ζ_d	E_{ratio} [%]	T_{opt} [s]
0.2	4.85	5.33
0.4	10.75	1.85
0.6	13.25	0.91
0.8	14.39	0.53
1	14.99	0.35

system considered in the previous chapter, that includes only viscous friction, constant-torque braking is sub-optimal (Table 5.3), in fact it does not recover any energy in most cases as seen from Figure 5.4(a). The performance of the constant-torque braking controller for a mechanical load that includes both viscous and Coulomb friction will be studied in this section and the results will be compared to those of the optimal kinetic energy recovery algorithm for each machine type. The expression for the braking torque reference can be written as

$$T_e^* = -\xi T_{e,\max} \tag{6.33}$$

where ξ is the fraction of maximum braking torque that is applied. The initial rotor speed is ω_{r0} and this value of braking torque is applied until the rotor speed equals ω_{rT}, which is less that ω_{r0}. The mechanical load model includes the effects of both viscous friction and Coulomb friction and the rotor speed dynamics can be written as

$$\dot{\omega}_r = \frac{1}{J}\left(-\xi T_{e,\max} - B_1\omega_r - B_0\ \mathrm{sgn}(\omega_r)\right) \tag{6.34}$$

The solution to the above differential equation is

$$\omega_r(t) = -\frac{\xi T_{e,\max}}{B_1} - \frac{B_0\ \mathrm{sgn}(\omega_{r0})}{B_1} + \frac{1}{B_1}\left(\xi T_{e,\max} + B_1\omega_{r0} + B_0\ \mathrm{sgn}(\omega_{r0})\right) e^{-\frac{B_1}{J}t} \tag{6.35}$$

The time at which the rotor speed equals ω_{rT} can be calculated by setting the above equation to ω_{rT} and solving for $t = T_{\mathrm{brk}}$

$$\omega_r(t = T_{\mathrm{brk}}) = \omega_{rT}, \quad \Longrightarrow\ T_{\mathrm{brk}} = \frac{J}{B_1}\ln\left(\frac{\xi T_{e,\max} + B_1\omega_{r0} + B_0\ \mathrm{sgn}(\omega_{r0})}{\xi T_{e,\max} + B_1\omega_{rT} + B_0\ \mathrm{sgn}(\omega_{r0})}\right) \tag{6.36}$$

The total electrical power that exits the electrical power supply and enters the electric machine is

$$P_e = R_s i_d^{*2} + \frac{R_e}{K_e^2} T_e^{*2} + T_e^* \omega_r \tag{6.37}$$

The choice of d-axis currents depends on the type of machine and is decided by the user according to Table 6.1. The energy recovered during the braking process is calculated by integrating the electric power from $t = 0$ to $t = T$

$$\begin{aligned} E &= \int_0^{T_{\text{brk}}} \left(R_s i_d^{*2} + \frac{R_e}{K_e^2} T_e^{*2} + T_e^* \omega_r \right) \, dt \\ &= R_s i_d^{*2} T_{\text{brk}} + \frac{J}{B_1^2} \left(\xi T_{e,\max} + B_0 \, \text{sgn}(\omega_{r0}) \right) \ln \left(\frac{\xi T_{e,\max} + B_1 \omega_{r0} + B_0 \, \text{sgn}(\omega_{r0})}{\xi T_{e,\max} + B_1 \omega_{rT} + B_0 \, \text{sgn}(\omega_{r0})} \right) \\ &- \frac{J}{B_1 K_e^2} \xi T_{e,\max} \left(K_e^2 \left(\omega_{r0} - \omega_{rT} \right) - \xi R_e T_{e,\max} \ln \left(\frac{\xi T_{e,\max} + B_1 \omega_{r0} + B_0 \, \text{sgn}(\omega_{r0})}{\xi T_{e,\max} + B_1 \omega_{rT} + B_0 \, \text{sgn}(\omega_{r0})} \right) \right) \end{aligned} \tag{6.38}$$

which simplifies to

$$E = R_s i_d^{*2} T_{\text{brk}} + \frac{1}{B_1} \xi^2 T_{e,\max}^2 T_{\text{brk}} \left(1 + \gamma \right) + \frac{B_0 \, \text{sgn}(\omega_{r0})}{B_1} \xi T_{e,\max} T_{\text{brk}} - \frac{J}{B_1} \xi T_{e,\max} \left(\omega_{r0} - \omega_{rT} \right) \tag{6.39}$$

The kinetic energy available for conversion is represented by the same equation as (5.25). The associated energy recovery ratio is defined as

$$E_{\text{ratio}} = -\frac{E}{E_{\text{avail}}} \tag{6.40}$$

Constant braking torque is applied until the rotor speed reaches the desired final rotor speed, ω_{rT}. Once the rotor speed reaches ω_{rT}, the closed-loop speed controller shown in Figure 3.9 takes over to regulate the rotor speed at $\omega_r = \omega_{rT}$. This operation involves switching from speed control to torque control for the braking event. Although it was

advised to avoid switching between types of controllers (see Section 5.5.4), doing so in this case is the simplest method of implementing constant-torque braking. The results that are shown in the following subsections are based on evaluating (6.36) and (6.39) and do not involve simulation of system dynamics.

6.4.1 SPM

In the previous chapter, the performance of constant-torque braking was compared to optimal braking for the simple case where the mechanical load was only characterized by viscous friction. Here, the two types of braking controllers are compared for an SPM system with a mechanical load that has both viscous and Coulomb frictions. The performance of the constant-torque braking controller for the Anaheim SPM system is shown in Figure 6.6 for an initial rotor speed of $\omega_{r0} = 100$ rad/s and final speed of $\omega_{rT} = 0$ rad/s. The levels of constant braking torque that result in positive energy recovery ratios are shown as green bars and those which correspond to negative or zero energy recovery ratios are shown in red. Values of constant braking torque greater than 40% of $T_{e,\max}$ result in energy being lost from the system rather than recovering any energy. The peak energy recovery ratio is 66.14% and corresponds to a constant torque level of 10% of the maximum braking torque of the system. The rotor takes 1.93 seconds to come to a standstill for this level of constant braking torque. In contrast, the optimal kinetic energy recovery algorithm recovers 70.46% of the available kinetic energy and takes 3.54 seconds to come to a standstill from an initial rotor speed of 100 rad/s as seen from Table 6.3(a). These numbers are obtained by substituting the values of the Anaheim SPM system parameters into (6.31), (6.36), and (6.39). Notice that the time taken to reach a standstill exponentially decreases with increasing levels of constant braking torque. Also, the free deceleration which results from applying zero braking torque recovers zero energy and takes about 15 seconds to come to a standstill from an initial speed of 100 rad/s. Table 6.8 lists the performance comparisons of the constant-torque braking and optimal kinetic energy recovery algorithms. The optimal kinetic energy

recovery algorithm recovers about 4% additional kinetic energy than the constant-torque braking controller and takes an additional 1.5 seconds to come to a standstill.

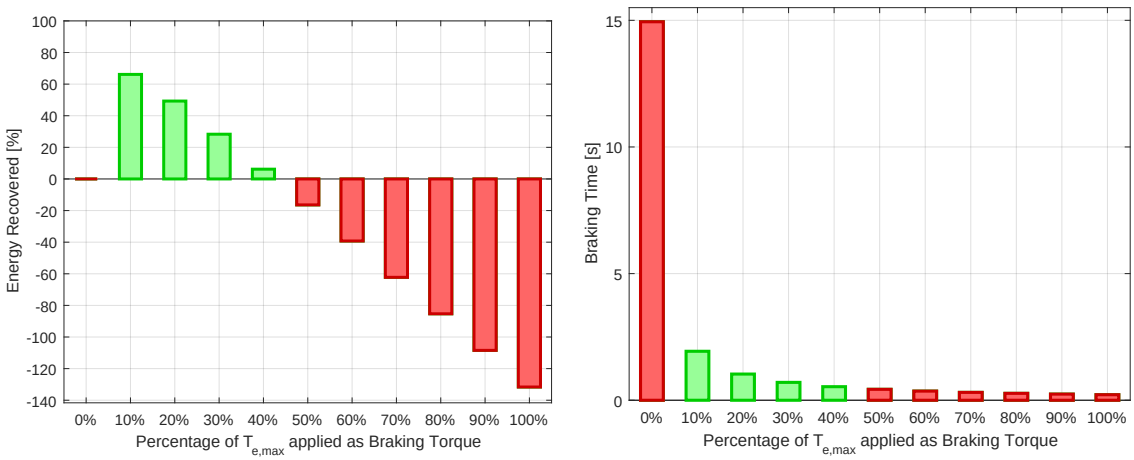

(a) Percentage of kinetic energy recovered

(b) Braking time-interval

Figure 6.6: Performance of constant torque braking on the Anaheim SPM system for initial and final rotor speeds of 100 rad/s and 0 rad/s respectively.

Table 6.8: Comparison of Performance of Constant-Torque Braking and Optimal Kinetic Energy Recovery Methods for the Anaheim SPM System Parameters

Method	Energy Recovered [%]	Braking Time [s]
10% of $T_{e,\max}$	66.14	1.93
Optimal Braking	70.46	3.54

6.4.2 IPM

The performance of the constant-torque braking controller for the Motorsolver IPM system is evaluated by substituting system parameter values into (6.36) and (6.39). The results are shown in Figure 6.7 for an initial rotor speed of $\omega_{r0} = 100$ rad/s and a final speed of $\omega_{rT} = 0$ rad/s. The direct-axis current is set to zero ($\zeta_d = 0$), resulting in an operation that is similar to SPMs. For this system, all levels of constant braking torques (except zero-torque shown in red) result in positive energy recovery ratios which are shown as green bars. This is different from the results for the Anaheim SPM system shown in Figure 6.6, where the application of large constant braking torque levels resulted in no energy recovery, in fact

energy was lost from the system. The reason for this difference between the two systems is explained by looking at the stator winding resistance of the two machines. For the SPM, $R_s = 1.2\ \Omega$ and for the Motorsolver IPM system, $R_s = 182.75\ \text{m}\Omega$. The low resistance value for the Motorsolver IPM, causes the system to incur smaller electrical losses than the Anaheim SPM system resulting in positive energy recovery ratios even at the maximum constant braking torque level. The peak energy recovery ratio is 68.71% and corresponds to a constant torque level of 40% of the maximum braking torque of the system. The rotor takes 0.39 seconds to come to a standstill for this level of constant braking torque. The optimal kinetic energy recovery algorithm recovers 71.28% of the available kinetic energy and takes 0.57 seconds to come to a standstill from an initial rotor speed of 100 rad/s as seen from Table 6.4(a). Therefore, the optimal braking algorithm outperforms constant-torque braking even for this low-resistance system. Free deceleration which results from applying zero braking torque recovers zero energy and takes about 2.5 seconds to come to a standstill from an initial speed of 100 rad/s. Table 6.9 lists the performance comparisons of the constant-torque braking and optimal kinetic energy recovery algorithms. The optimal kinetic energy recovery algorithm recovers about 2.6% additional kinetic energy than the constant-torque braking controller and takes an additional 0.18 seconds to come to a standstill.

Table 6.9: Comparison of Performance of Constant-Torque Braking and Optimal Kinetic Energy Recovery Methods for the Motorsolver IPM System

Method	Energy Recovered [%]	Braking Time [s]
40% of $T_{e,\max}$	68.71	0.39
Optimal Braking	71.28	0.57

6.4.3 IM

The performance of the constant-torque braking controller for the Motorsolver induction machine system is shown in Figure 6.8 for an initial rotor speed of $\omega_{r0} = 120$ rad/s

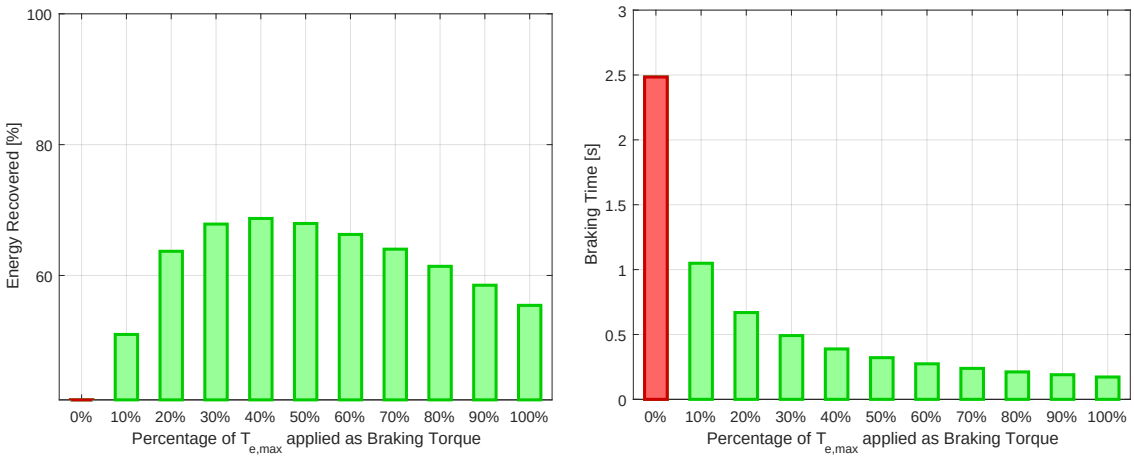

(a) Percentage of kinetic energy recovered

(b) Braking time-interval

Figure 6.7: Performance of constant torque braking on the Motorsolver IPM system for initial and final rotor speeds of 100 rad/s and 0 rad/s respectively.

and final speed of $\omega_{rT} = 0$ rad/s. A direct-axis current equal to 1.5 A is used to set up the rotor flux in the air-gap. The expression for energy recovery in (6.39) accounts for the copper losses due to the flow of non-zero direct-axis current. The levels of constant braking torque that result in positive energy recovery ratios are shown in green and those which correspond to negative or zero energy recovery ratios are shown in red. Constant braking torque values greater than 20% of the maximum braking result in negative energy recovery ratios for this system. The peak energy recovery ratio is 10.02% and corresponds to a constant torque level of 20% of the maximum braking torque of the system. The rotor takes 1.02 seconds to come to a standstill for this level of constant braking torque. In contrast, the optimal kinetic energy recovery algorithm recovers 12.26% of the available kinetic energy and takes 1.26 seconds to come to a standstill from an initial rotor speed of 120 rad/s from Table 6.7(b). Free deceleration which results from applying zero braking torque takes about 14 seconds to come to a standstill from an initial speed of 120 rad/s. However, since a constant direct-axis current is being commanded to produce the rotor flux during the entire braking interval, the associated copper losses result in a negative energy recovery ratio. Table 6.10 lists the performance comparisons of the constant-torque braking and optimal kinetic energy recovery algorithms. The optimal kinetic energy recovery

algorithm recovers about 2.3% additional kinetic energy than the constant-torque braking controller and takes an additional 0.24 seconds to come to a standstill.

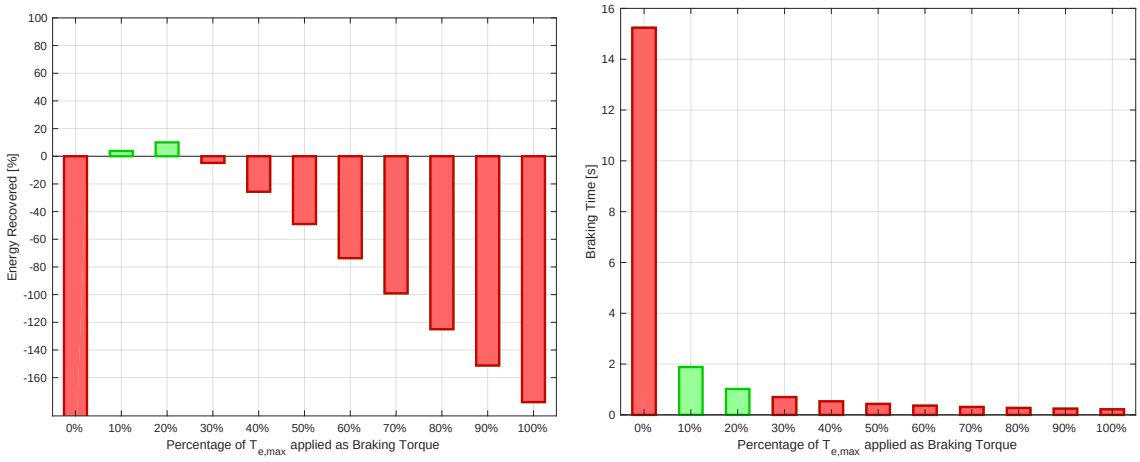

(a) Percentage of kinetic energy recovered (b) Braking time-interval

Figure 6.8: Performance of constant torque braking on the Motorsolver IM system for initial and final rotor speeds of 120 rad/s and 0 rad/s respectively with $i_d^* = 1.5$ A.

Table 6.10: Comparison of Performance of Constant-Torque Braking and Optimal Kinetic Energy Recovery Methods for the Motorsolver IM System with $i_d^* = 1.5$ A

Method	Energy Recovered [%]	Braking Time [s]
20% of $T_{e,\max}$	10.02	1.02
Optimal Braking	12.26	1.26

6.5 Experimental Results

The optimal braking trajectory is implemented through the use of a closed-loop feedback speed controller with a feedforward torque reference signal as shown in Figure 5.9. The reference input to the feedback speed control is obtained from (6.25) and the feedforward torque signal is obtained from (6.27). Since the mechanical load model used in this chapter includes both viscous and Coulomb friction components, the error dynamics of the overall system that includes both feedback and feedforward torque signals must be ana-

lyzed to verify that accurate trajectory tracking can be achieved. The rotor speed dynamics satisfies

$$\dot{\omega}_r = \frac{1}{J}\left(T_e - B_1\omega_r - B_0\ \mathrm{sgn}(\omega_r)\right) \tag{6.41}$$

The dynamics of the reference signal satisfies

$$\dot{\omega}_r^* = \frac{1}{J}\left(T_e^* - B_1\omega_r^* - B_0\ \mathrm{sgn}(\omega_r^*)\right) \tag{6.42}$$

where ω_r^* and T_e^* are outputs of the optimal trajectory generator. The output of the feedback speed controller is

$$u_{fb} = k_{w1}e_w + k_{w2}\sigma_w \tag{6.43}$$

where

$$\begin{aligned} e_w &= \omega_r^* - \omega_r \\ \dot{\sigma}_w &= e_w \end{aligned} \tag{6.44}$$

and the compensator gains are chosen according to (3.52) as

$$\begin{aligned} k_{w1} &= 2J\alpha_w - B_1 \\ k_{w2} &= J\alpha_w^2 \end{aligned} \tag{6.45}$$

where α_w is the user-defined speed controller bandwidth. The feedforward torque reference signal is

$$u_{ff} = T_e^* \tag{6.46}$$

and the overall torque reference command u is defined as

$$u = u_{ff} + u_{fb} = T_e^* + k_{w1} e_w + k_{w2} \sigma_w \tag{6.47}$$

The signal u is given as the input to the drive system which produces an electromagnetic torque that satisfies $T_e = u$. The overall system dynamics are now represented as

$$\begin{aligned}
\dot{\omega}_r &= \frac{1}{J} \left(T_e - B_1 \omega_r - B_0 \, \mathrm{sgn}(\omega_r) \right) \\
&= \frac{1}{J} \left(T_e^* + k_{w1} e_w + k_{w2} \sigma_w - B_1 \omega_r - B_0 \, \mathrm{sgn}(\omega_r) \right) \\
&= \frac{1}{J} \left(T_e^* - B_1 \omega_r^* + B_1 \omega_r^* - B_0 \, \mathrm{sgn}(\omega_r^*) + B_0 \, \mathrm{sgn}(\omega_r^*) + k_{w1} e_w + k_{w2} \sigma_w - B_1 \omega_r - B_0 \, \mathrm{sgn}(\omega_r) \right) \\
&= \dot{\omega}_r^* + \frac{1}{J} \left(B_1 \omega_r^* + B_0 \, \mathrm{sgn}(\omega_r^*) + k_{w1} e_w + k_{w2} \sigma_w - B_1 \omega_r - B_0 \, \mathrm{sgn}(\omega_r) \right) \\
&= \dot{\omega}_r^* + \frac{1}{J} \left(\left(k_{w1} + B_1 \right) e_w + k_{w2} \sigma_w + B_0 \left(\mathrm{sgn}(\omega_r^*) - \mathrm{sgn}(\omega_r) \right) \right)
\end{aligned} \tag{6.48}$$

Assume that the sign of the rotor speed is the same as its reference signal, i.e.

$$\mathrm{sgn}(\omega_r^*) = \mathrm{sgn}(\omega_r) \tag{6.49}$$

Substituting the above expression results in rotor speed dynamics

$$\dot{\omega}_r = \dot{\omega}_r^* + \frac{1}{J} \left(\left(k_{w1} + B_1 \right) e_w + k_{w2} \sigma_w \right) \tag{6.50}$$

The resulting speed error dynamics are

$$\begin{aligned}
\dot{e}_w &= \dot{\omega}_r^* - \dot{\omega}_r = -\frac{1}{J} \left(\left(k_{w1} + B_1 \right) e_w + k_{w2} \sigma_w \right) \\
\dot{\sigma}_w &= e_w
\end{aligned} \tag{6.51}$$

Substituting the compensator gains from (6.45) results in

$$\begin{aligned} \dot{e}_w &= -2\alpha_w e_w - \alpha_w^2 \sigma_w \\ \dot{\sigma}_w &= e_w \end{aligned} \tag{6.52}$$

which is rewritten in matrix form as

$$\begin{bmatrix} \dot{e}_w \\ \dot{\sigma}_w \end{bmatrix} = \begin{bmatrix} -2\alpha_w & -\alpha_w^2 \\ 1 & 0 \end{bmatrix} \begin{bmatrix} e_w \\ \sigma_w \end{bmatrix} \tag{6.53}$$

which is represented by the characteristic polynomial

$$(s + \alpha_w)^2. \tag{6.54}$$

This analysis shows that the addition of the feedforward term results in unforced error and integrator dynamics stay at zero if the system started with zero error and the error integrator is initialized to zero at the beginning of the braking interval, regardless of the choice of speed controller bandwidth, α_w.

The DRV-8312 Motor Drive Kit from Texas Instruments is used to conduct experiments. The three stator winding terminals of the electric machine are connected to the mid-points of the three power converter legs using screw terminals that are provided on the motor-drive board. Leg voltages of the power converter are measured using voltage divider circuitry and subsequent analog-to-digital conversion in the microcontroller. The leg currents are measured by sampling the voltage across shunt resistors located between the low-side switches and the negative battery terminal. The rotor position is measured using a shaft-mounted quadrature encoder and the rotor speed is estimated from the encoder signals as discussed earlier. At the beginning of the experiment, the rotor is made to spin at a user-defined choice of initial speed ω_{r0}. Closed-loop feedback control with zero feedforward reference torque is used to regulate the rotor speed at $\omega_r = \omega_{r0}$. Based

on user-defined choices of initial and final rotor speeds and braking time-interval length, the time-based trajectories of rotor speed and electromechanical torque are calculated on the microcontroller using (6.25) and (6.27). Once the braking command is issued, optimal braking control is implemented using a combination of feedback and feedforward speed control as discussed earlier. The electric power is obtained from measured values of leg currents and voltages using

$$P_e = v_A i_A + v_B i_B + v_C i_C$$

The energy recovered during the braking interval is obtained by integrating the electrical power using Euler's forward integration method. The measured trajectories of rotor speed, dq reference frame currents, estimated electromagnetic torque, and electrical power are logged for comparison with simulation results. This section discusses the experimental results for the three types of electric machines.

6.5.1 SPM

The Anaheim system with the DRV-8312 Motor Drive shown in Figure 4.2 is used for the experiments. The system is operated using a battery pack which has a terminal voltage of about 19.6 V. The switching frequency of the power stage is 30 kHz, current-controller update frequency is 12.5 kHz, speed-controller update frequency is 6.25 kHz. The current-controller bandwidth is 2500 rad/s and the speed-controller bandwidth is 2 rad/s.

The performance of the optimal kinetic energy recovery algorithm is tested on the Anaheim experimental setup for three different speed ratios, $\rho = 0$, $\rho = 0.25$, and $\rho = 0.5$, each starting from an initial rotor speed of $\omega_{r0} = 100$ rad/s. The length of the braking time-interval is $T = 2$ for all cases. The comparison of simulation and experiment trajectories for the $\rho = 0$ case are shown in Figures 6.9 and 6.10. Figures 6.11-6.12 and 6.13-6.14 compare simulation and experiment trajectories for $\rho = 0.25$ and $\rho = 0.5$ respectively with

$T = 2$ seconds. Observe that the rotor speeds stay at $\omega_{rT} = 25$ rad/s and $\omega_{rT} = 50$ rad/s for values of $t > T$. This shows that the optimal kinetic energy recovery algorithm operates only during the braking time-interval, $t \in [0, T]$, and the closed-loop speed controller takes over and ensures that the desired final speed is maintained after the braking time-interval ends. The energy recovery results for the simulation and experiments are tabulated in Table 6.11 for the three choices of ρ with $T = 2$ seconds. The experimental energy recovery ratios are the average of three trials for each case. There is good agreement between the simulation and experimental results for all cases.

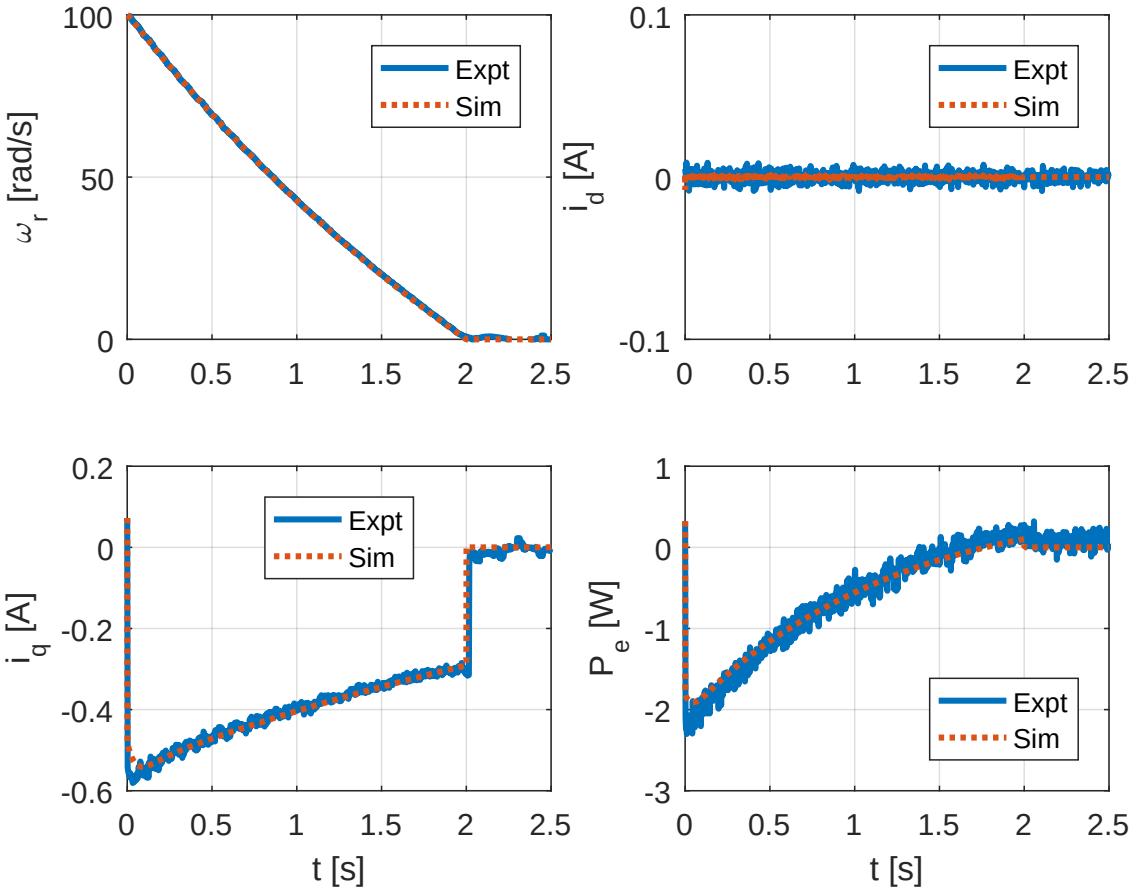

Figure 6.9: Comparison of experiment and simulation implementations using the Anaheim SPM system for $\omega_{r0} = 100$ rad/s, $\rho = 0$, and $T = 2$ s.

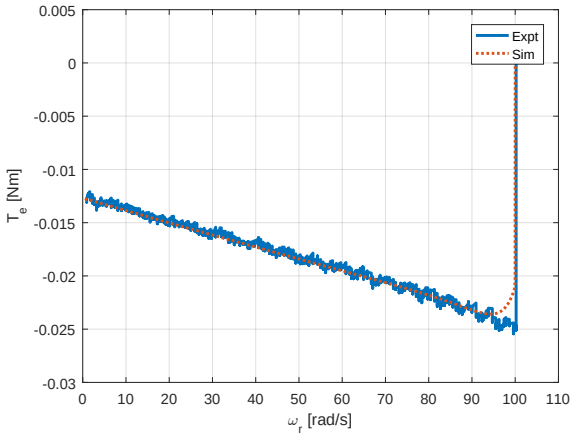

Figure 6.10: Comparison of braking trajectories in the torque-speed plane for experiment and simulation implementations using the Anaheim SPM system for $\omega_{r0} = 100$ rad/s, $\rho = 0$, and $T = 2$ s.

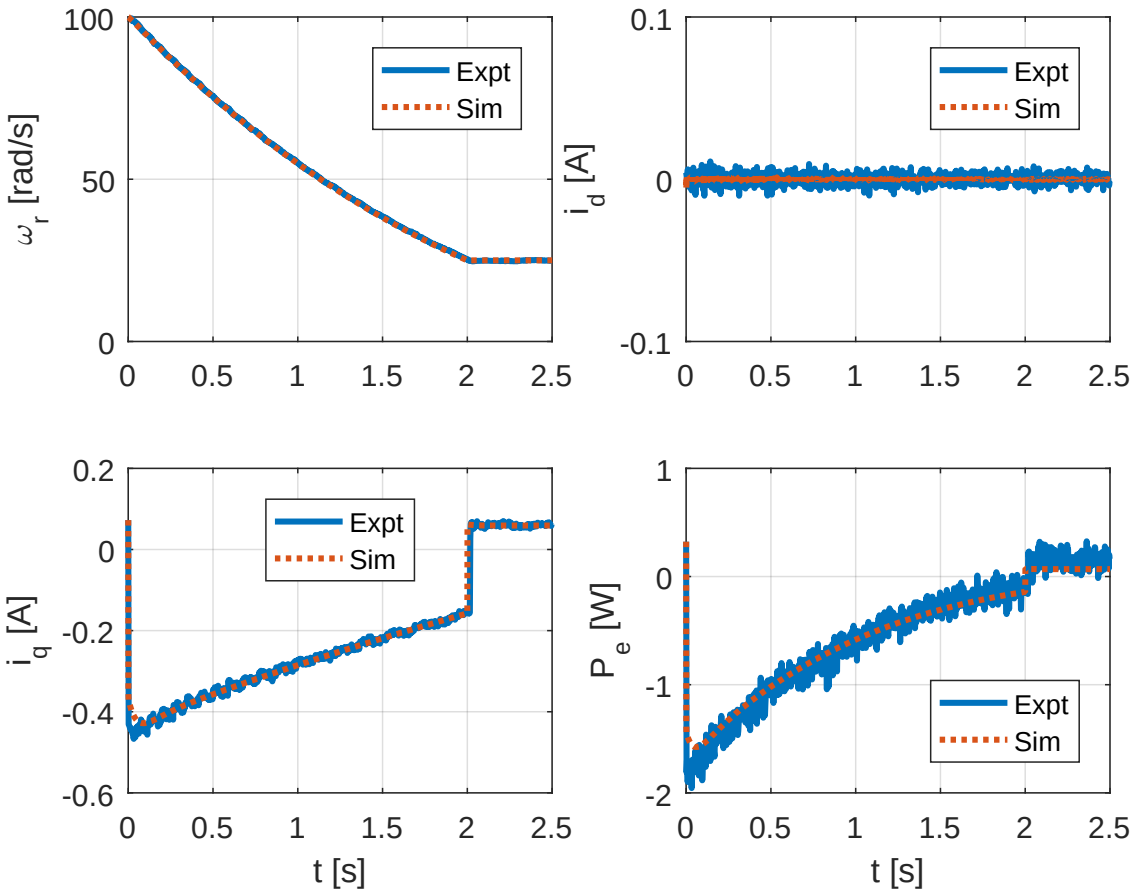

Figure 6.11: Comparison of experiment and simulation implementations using the Anaheim SPM system for $\omega_{r0} = 100$ rad/s, $\rho = 0.25$, and $T = 2$ s.

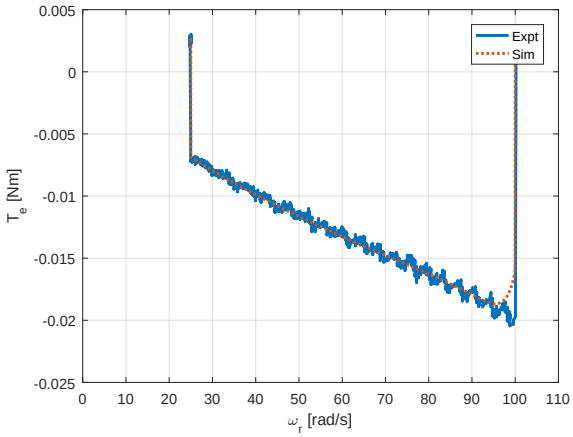

Figure 6.12: Comparison of braking trajectories in the torque-speed plane for experiment and simulation implementations using the Anaheim SPM system for $\omega_{r0} = 100$ rad/s, $\rho = 0.25$, and $T = 2$ s.

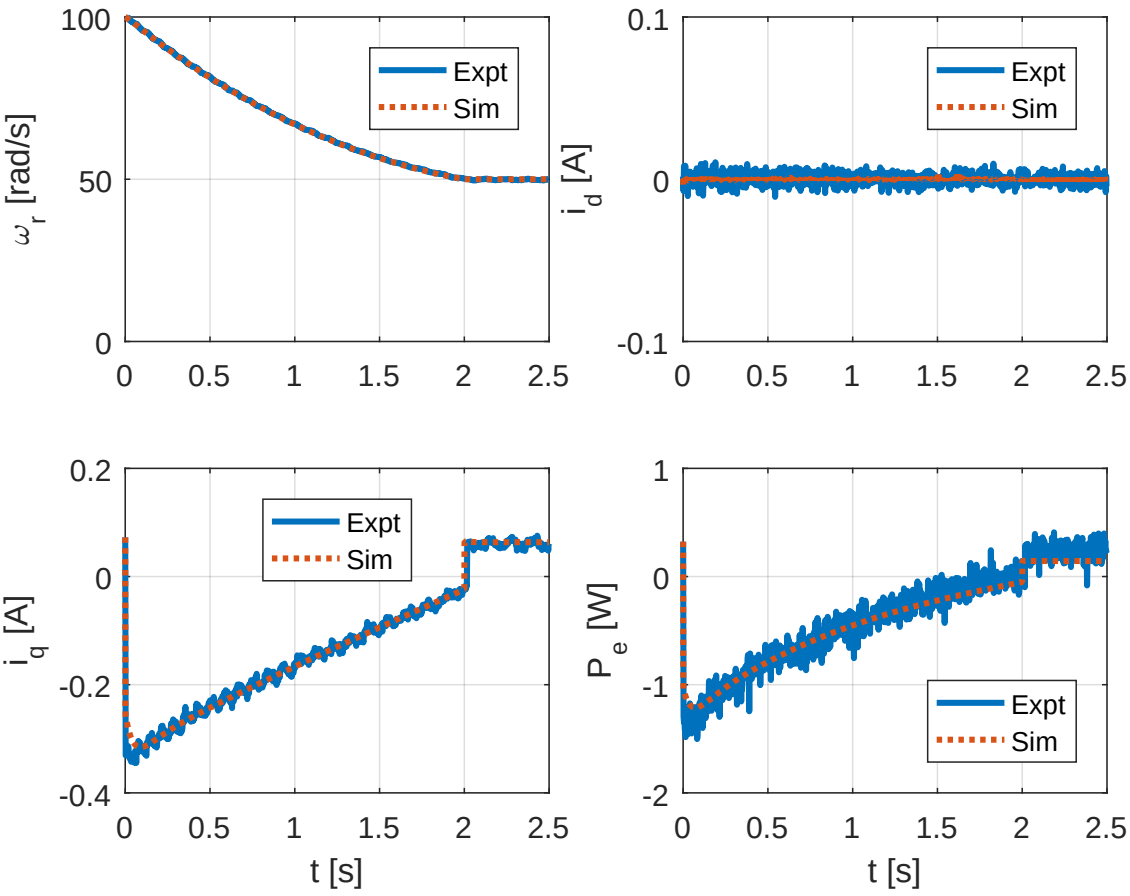

Figure 6.13: Comparison of experiment and simulation implementations using the Anaheim SPM system for $\omega_{r0} = 100$ rad/s, $\rho = 0.5$, and $T = 2$ s.

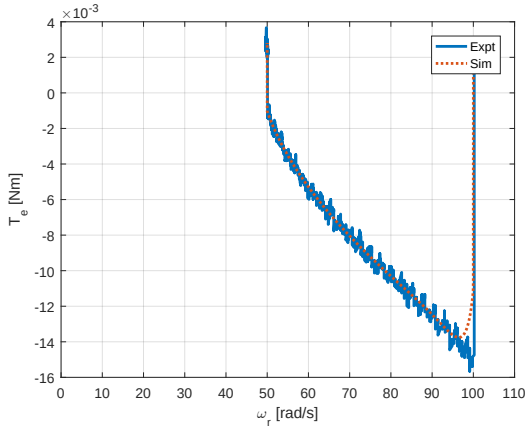

Figure 6.14: Comparison of braking trajectories in the torque-speed plane for experiment and simulation implementations using the Anaheim SPM system for $\omega_{r0} = 100$ rad/s, $\rho = 0.5$, and $T = 2$ s.

Table 6.11: Comparison of Energy Recovery Ratios for Simulations and Experiments for the Anaheim SPM System with $\omega_{r0} = 100$ rad/s and $T = 2$ s

ρ	Simulation	Experiment
0	67.20%	66.94%
0.25	71.60 %	71.34%
0.5	67.83%	67.66%

As an additional exercise, experiments that show the variation of energy recovery with length of the braking time interval were also performed. The objective was to experimentally verify the graphs shown in Figure 6.1 for a set of initial and final rotor speeds. The initial speed was chosen to be $\omega_{r0} = 100$ rad/s and the final speed was $\omega_{rT} = 50$ rad/s, i.e. $\rho = 0.5$ in this scenario. Figure 6.15 shows the variation for the optimal braking experiment for different choices of braking time-interval length. The experiment data points are shown in blue and the simulation, which is a representation of equations (6.30) and (6.31), is shown in red. The experimental energy recovery ratios are the average of three trials for each case. The black dot on the red curve indicates the peak energy recovery ratio and

its corresponding braking time-interval length (T_{opt}) which in this case is 73.11% and 1.1 seconds respectively. There is good agreement between simulation and experiments and the optimal braking time-interval length predicted by the experiments lies between $T = 1$ and $T = 1.25$ seconds.

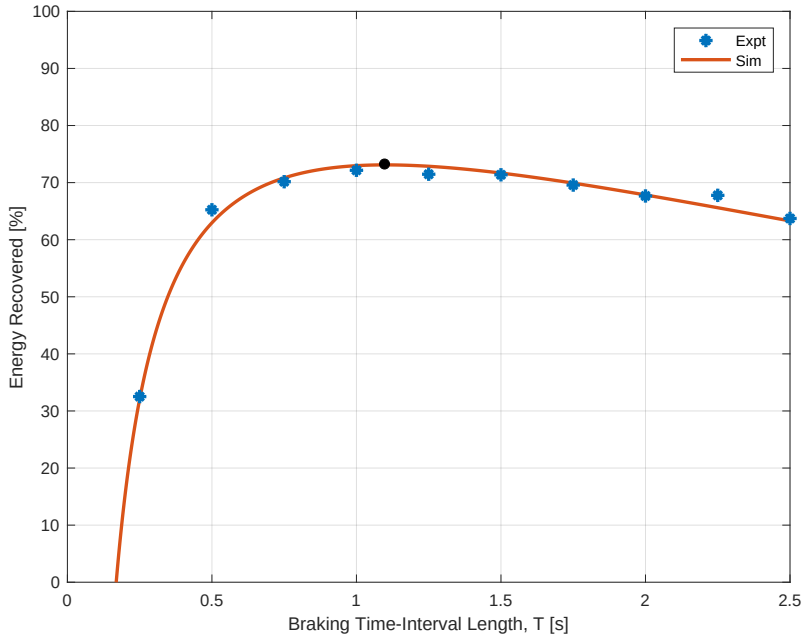

Figure 6.15: Variation of energy recovery ratio with length of braking time-interval for experiment and simulation implementations of the optimal kinetic energy recovery algorithm using the Anaheim SPM system for $\omega_{r0} = 100$ rad/s and $\rho = 0.5$

6.5.2 IPM

The Motorsolver IPM system with the DRV-8312 Motor Drive Kit shown in Figure 4.7 is used to conduct the optimal kinetic energy recovery experiments. The electric power source to the drive is a battery pack as described earlier. The switching frequency of the power converter is 30 kHz, current controller update frequency is 10 kHz, speed-controller update frequency is 5 kHz. The current controller bandwidth is 2500 rad/s and the speed controller bandwidth is 2 rad/s. The performance of the constant-flux optimal kinetic energy recovery algorithm is tested on the Motorsolver IPM system for the case of $\zeta_d = 0$,

$\omega_{r0} = 120$ rad/s, and $\rho = 0$. A braking time-interval length of $T = 0.6$ seconds is chosen for the experiments. The choice of $\zeta_d = 0$ relates to zero direct-axis current, resulting in an SPM-like operation of the IPM system. The comparison of simulation and experiment results for the rotor speed, d-axis current, $q-$ axis current, and electrical power is shown in Figure 6.16. Observe that the rotor speed trajectories for the simulation and experiment show the effect of cogging torque, especially at low speeds. Also observe that the non-sinusoidal back-EMF of the Motorsolver IPM machine produces current ripples in the direct and quadrature axes current trajectories. Figure 6.17 shows the comparison of the braking trajectories for simulation and experiments. The graphs in Figure 6.17(a) shows the estimated average electromagnetic torque uses stator current measurement to calculate torque as shown in (4.66). The more complicated expression for electromagnetic torque that includes the effect of torque-harmonics in (4.75) is used to construct the torque trajectories for simulation and experiments as shown in Figure 6.17(b). The simulation and experiment trajectories show good agreement. The energy recovery performance of simulation and experiments are compared in Table 6.12. The small variation in the experimental energy recovery ratio from the simulation results is due to unmodeled loss mechanisms such as power converter losses and iron losses.

Table 6.12: Comparison of Energy Recovery Ratios for Simulations and Experiments for the Motorsolver IPM System with $\omega_{r0} = 120$ rad/s

ρ	T	Simulation	Experiment
0	0.6	72.41%	71.39%

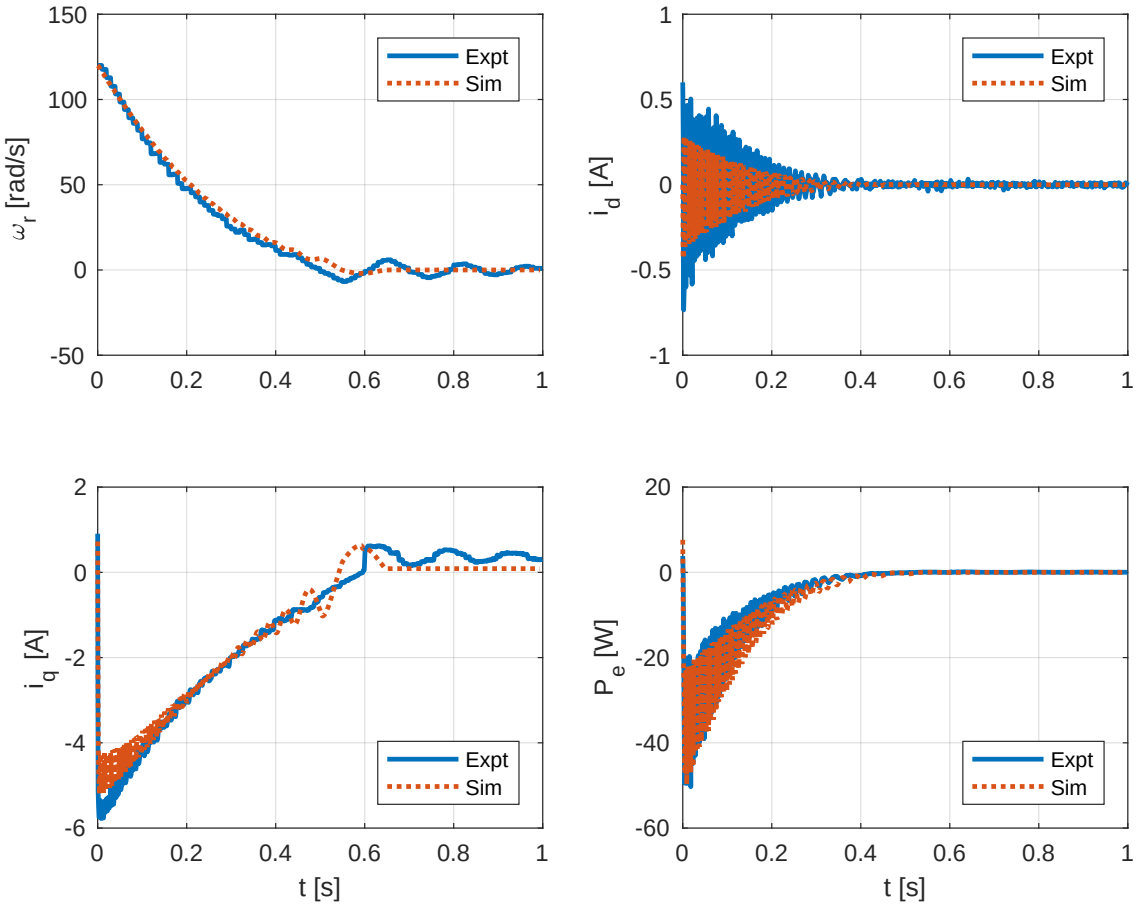

Figure 6.16: Comparison of experiment and simulation implementations using the Motorsolve IPM system for $\omega_{r0} = 120$ rad/s, $\rho = 0$, and $T = 0.6$ s.

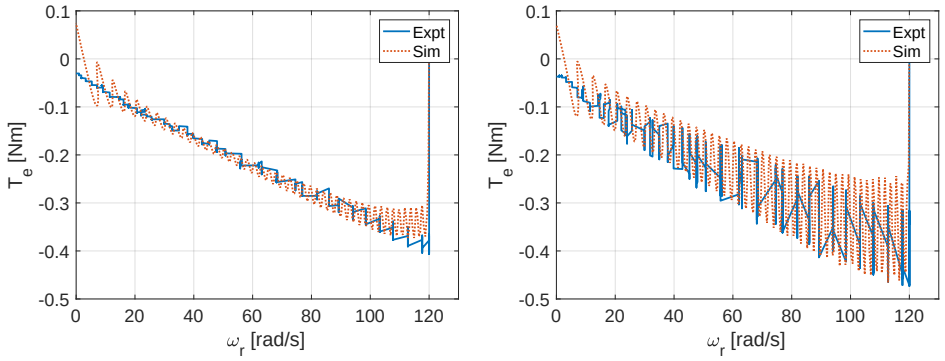

(a) Average torque (b) Including torque-harmonics

Figure 6.17: Comparison of braking trajectories in the torque-speed plane for experiment and simulation implementations using the Motorsolver IPM system for $\omega_{r0} = 120$ rad/s, $\rho = 0$, and $T = 0.6$ s.

6.5.3 IM

The Motorsolver induction machine system with the DRV-8312 Motor Drive Kit shown in Figure 4.4 is used to conduct the optimal kinetic energy recovery experiments. The electric power source to the drive is a low-power battery pack as described earlier. The switching frequency of the power converter is 30 kHz, current controller update frequency is 12.5 kHz, speed-controller update frequency is 6.25 kHz. The current controller bandwidth is 2500 rad/s and the speed controller bandwidth is 5 rad/s. A d-axis current of 1.5 A is used to set up the the rotor flux at the start of the experiment. The rotor is then made to spin at an initial speed of $\omega_{r0} = 120$ rad/s using closed-loop feedback speed control. When the braking command is issued, the optimal braking trajectory is implemented using a combination of closed-loop feedback speed control and a feedforward torque signal as discussed previously. The comparison of simulation and experiment trajectories of rotor speed, d-axis current, q-axis current, and controllable electric power is shown Figure 6.18. The design parameters for the braking trajectory are $\rho = 0$ and $T = 1.5$ seconds. The direct-axis current is maintained at 1.5 A throughout the experiment. There is good agreement between simulation and experiment trajectories. The braking trajectories in the torque-speed plane are shown in Figure 6.19 for simulation and experiment. Also shown in Figure 6.19 is the curve that defines the boundary between regenerative braking ($P_e < 0$) and non-regenerative braking ($P_e > 0$), i.e. the equation that solves for torque-speed operating points that satisfy $P_e = 0$

$$P_e = R_s i_d^{*2} + \underbrace{T_e^* \omega_r + \frac{R_e}{K_e^2} T_e^{*2}}_{P_c} = 0 \tag{6.55}$$

which results in real-valued electromagnetic torque values as a function of rotor speed as

$$T_e^* = \frac{-\omega_r \pm \sqrt{\omega_r^2 - 4R_s i_d^* \left(\frac{R_e}{K_e^2}\right)}}{2\left(\frac{R_e}{K_e^2}\right)}, \quad \forall \quad |\omega_r| \geq \omega_{r,\text{crit}} \tag{6.56}$$

where

$$\omega_{r,\text{crit}} = \frac{2i_d^*\sqrt{R_e R_s}}{K_e} \tag{6.57}$$

For the given system with $i_d^* = 1.5$ A, the value of $\omega_{r,\text{crit}}$ is 50.29 rad/s. During the initial stages of braking the torque-speed operating point is to the right of the zero total input power curve, but the operating point eventually moves to the left of this curve; electric power flows out of the induction machine initially (regenerative), but ultimately electric power flows into the induction machine (non-regenerative) as the rotor speed reduces. Table 6.13 compares the controllable energy recovery ratio (excluding the d-axis current stator copper winding losses) for the simulation and experiment, and shows good agreement.

Table 6.13: Comparison of Controllable Energy Recovery Ratios for Simulations and Experiments for the Motorsolver IM System with $\omega_{r0} = 120$ rad/s

ρ	T	Simulation	Experiment
0	1.5	53.91%	52.81%

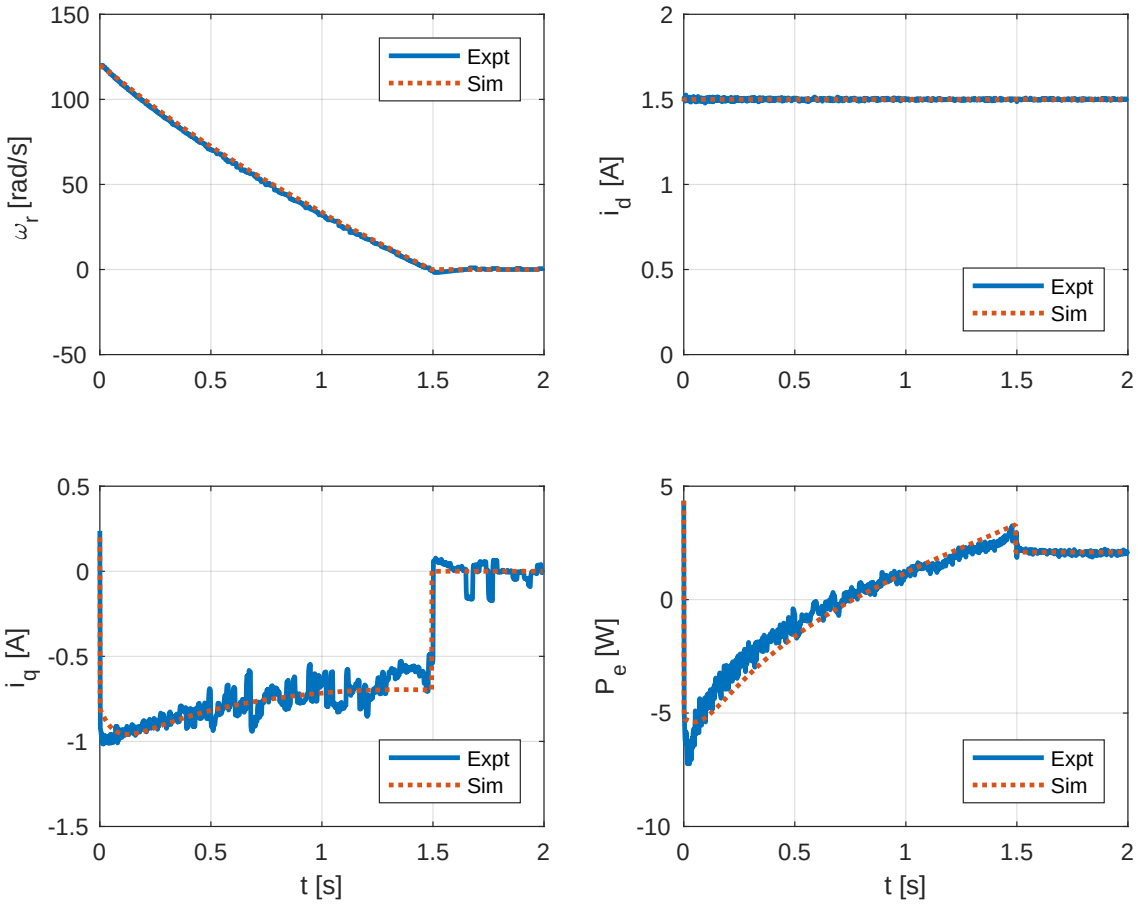

Figure 6.18: Comparison of rotor speed, direct and quadrature axes currents, and electrical power for experiment and simulation implementations of the optimal kinetic energy recovery algorithm using the Motorsolver IM system for $\omega_{r0} = 120$ rad/s, $\rho = 0$, and $T = 1.5$ s.

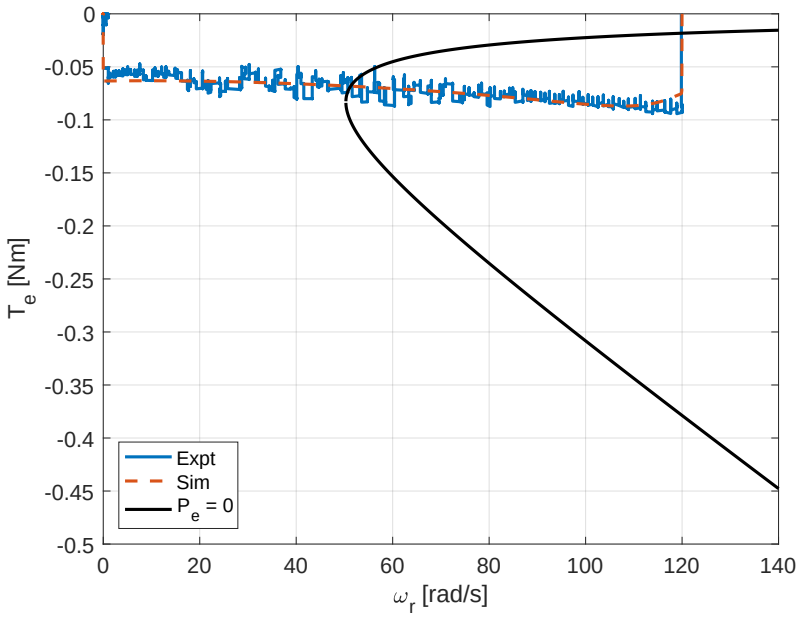

Figure 6.19: Comparison of braking trajectories in the torque-speed plane for experiment and simulation implementations of the optimal kinetic energy recovery algorithm using the Motorsolver IM system for $\omega_{r0} = 120$ rad/s, $\rho = 0$, and $T = 1.5$ s.

CHAPTER 7

OPTIMAL KINETIC ENERGY RECOVERY ALGORITHMS FOR ELECTRIC MACHINES WITH POSITION CONSTRAINTS

Some applications like elevator drives, electric trains, or industrial automation require that the objective of braking to a complete stop aligns with an additional constraint on the final position of the rotor. To extend the optimal kinetic energy recovery algorithm to include these applications, a position constraint is introduced. The initial rotor position at the beginning of the braking interval is $\theta_r(0) = \theta_{r0}$ and the final rotor position is $\theta_r(T) = \theta_{rT}$. This constraint is imposed in addition to the previous constraints on rotor speed, i.e. $\omega_r(0) = \omega_{r0}$ and $\omega_r(T) = \omega_{rT}$. This chapter will discuss the formulation and implementation of the optimal kinetic energy recovery algorithm to include position constraints.

7.1 Optimal Control Problem Formulation

The mechanical system is modeled using the same load model as the previous section. However, an additional state variable for the rotor position is introduced here.

$$\begin{aligned} \dot{\omega}_r &= \frac{1}{J}\left(T_e^* - T_{\text{load}}\right) \\ \dot{\theta}_r &= \omega_r \end{aligned} \tag{7.1}$$

where $T_{\text{load}} = B_1\omega_r + B_0\ \text{sgn}\left(\omega_r\right)$.

The objective function is to minimize the controllable electrical energy during the braking interval which starts at $t = 0$ and ends at $t = T$.

$$E = \int_0^T P_c\ dt \tag{7.2}$$

where P_c is the controllable electric power from the previous chapter and is expressed as

$$P_c = T_e^* \omega_r + \frac{R}{K_r^2} T_e^{*2} \tag{7.3}$$

The boundary conditions on the objective function are

$$\omega_r(0) = \omega_{r0}, \qquad \omega_r(T) = \omega_{rT}, \qquad \theta_r(0) = \theta_{r0}, \qquad \theta_r(T) = \theta_{rT} \tag{7.4}$$

The controllable power only includes the components of the total electric power that is influenced by the control variable T_e^*. It does not include the component of electric power that is incurred due to the production of a constant rotor flux in the case of IPMs and inductions machines. The expressions for R and K_r vary by machine and their expansions can be obtained from Table 6.2.

Following the recipe for optimal control problem formulation that is outlined in [5], a Hamiltonian function can be formulated as

$$H = P_c + \chi_1 \dot{\omega}_r + \chi_2 \dot{\theta}_r \tag{7.5}$$

where χ_1 and χ_2 are the costate variables. Substituting the expressions for controllable electric power and rotor dynamics, the Hamiltonian is expanded as

$$\begin{aligned} H &= P_c + \chi_1 \dot{\omega}_r + \chi_2 \dot{\theta}_r \\ &= T_e^* \omega_r + \frac{R}{K_r^2} T_e^{*2} + \frac{\chi_1}{J} \left(T_e^* - B_1 \omega_r - B_0 \operatorname{sgn}(\omega_r) \right) + \chi_2 \omega_r \end{aligned} \tag{7.6}$$

Since the electromagnetic torque reference signal is used as the optimal control variable, the optimality conditions can be obtained by setting the following partial derivative

$$\frac{\partial H}{\partial T_e^*} = \omega_r + \frac{2R_e}{K_e^2} T_e^* + \frac{\chi_1}{J} \tag{7.7}$$

equal to zero and solving for T_e^* which results in

$$T^*_{e,\text{opt}} = -\frac{K_e^2}{2R_e}\left(\omega_{r,\text{opt}} + \frac{\chi_{1,\text{opt}}}{J}\right) \tag{7.8}$$

The state and costate dynamics can now be derived in terms of the state, costate, and control variables by taking the partial derivatives

$$\begin{aligned}
\dot{\omega}_{r,\text{opt}} &= \frac{\partial H}{\partial \chi_1} = \frac{1}{J}\left(T^*_{e,\text{opt}} - B_1\omega_{r,\text{opt}} - B_0\ \text{sgn}(\omega_{r,\text{opt}})\right) \\
\dot{\theta}_{r,\text{opt}} &= \frac{\partial H}{\partial \chi_2} = \omega_{r,\text{opt}} \\
\dot{\chi}_{1,\text{opt}} &= -\frac{\partial H}{\partial \omega_r} = -T^*_{e,\text{opt}} + \frac{B_1}{J}\chi_{1,\text{opt}} + \frac{2B_0}{J}\delta(\omega_{r,\text{opt}})\chi_{1,\text{opt}} - \chi_{2,\text{opt}} \\
\dot{\chi}_{2,\text{opt}} &= -\frac{\partial H}{\partial \theta_r} = 0
\end{aligned} \tag{7.9}$$

Substituting the value of the optimal control variable, $T^*_{e,\text{opt}}$ from (7.8) results in the formulation of the following two-point boundary value problem

$$\begin{bmatrix} \dot{\omega}_{r,\text{opt}} \\ \dot{\theta}_{r,\text{opt}} \\ \dot{\chi}_{1,,\text{opt}} \\ \dot{\chi}_{2,\text{opt}} \end{bmatrix} = \frac{K_e^2}{2JR_e} \begin{bmatrix} -(1+2\gamma) & 0 & J^{-1} & 0 \\ \frac{2JR_e}{K_e^2} & 0 & 0 & 0 \\ J & 0 & (1+2\gamma) & -\frac{2JR_e}{K_e^2} \\ 0 & 0 & 0 & 0 \end{bmatrix} \begin{bmatrix} \omega_{r,\text{opt}} \\ \theta_{r,\text{opt}} \\ \chi_{1,\text{opt}} \\ \chi_{2,\text{opt}} \end{bmatrix} + \frac{B_0}{J} \begin{bmatrix} -\text{sgn}(\omega_{r,\text{opt}}) \\ 0 \\ 2\delta(\omega_{r,\text{opt}})\chi_{1,\text{opt}} \\ 0 \end{bmatrix} \tag{7.10}$$

with boundary conditions

$$\omega_{r,\text{opt}}(0) = \omega_{r0}, \quad \omega_{r,\text{opt}}(T) = \omega_{rT}, \quad \theta_{r,\text{opt}}(0) = \theta_{r0}, \quad \theta_{r,\text{opt}}(T) = \theta_{rT} \tag{7.11}$$

where $\gamma = \dfrac{B_1 R_e}{K_e^2}$ is a dimensionless electromechanical loss parameter. The system described by the two-point boundary value problem in (7.10) is an LTI system which has four

eigenvalues, two of which are at the origin and the other two are at $\pm\alpha$, where

$$\alpha = \frac{K_e^2}{JR_e}\sqrt{\gamma(1+\gamma)} \tag{7.12}$$

The general solution to the two-point boundary value problem described in (7.10) is of the form

$$\begin{aligned}
\omega_r(t) &= c_1 e^{-\alpha t} + c_2 e^{\alpha t} + c_3 \\
\theta_r(t) &= c_4 e^{-\alpha t} + c_5 e^{\alpha t} + c_6 t + c_7 \\
\chi_1(t) &= c_8 e^{-\alpha t} + c_9 e^{\alpha t} + c_{10} \\
\chi_2(t) &= c_{11}
\end{aligned} \tag{7.13}$$

with the boundary conditions that are described in (7.10). The impulse term causes a jump discontinuity at zero-speed and its effect is captured in the coefficients as discussed in the previous chapter. Although the general solution has 11 coefficients, c_1, ..., c_{11}, the special structure of the two-point boundary value problem imposes algebraic constraints between the coefficients such that only four boundary conditions are required to obtain the values of all the coefficients.

7.2 Numerical Optimization

The specific solution to (7.13) is obtained by substituting the boundary conditions in (7.10) to obtain the expressions for the coefficients, c_1 through c_{11}. Although closed-form expressions for the coefficients can be obtained in terms of the system parameters, this is a tedious process and the expressions that are obtained are too lengthy to be implemented in a simulation or on a microcontroller. Therefore, a numerical optimization tool in Matlab called `bvp4c` [74, 75] is made use of to solve the two-point boundary value problem described in (7.10). The output of the `bvp4c` solver is a mesh grid of time-dependent optimal trajectories of the state and costate variables. The optimal control variable, T_e^*, is then

constructed from the optimal trajectories for rotor speed and its associated costate variable χ_1 using the expression in (7.8). The optimal trajectories for rotor speed, rotor position, and electromagnetic torque reference are then used as lookup tables for simulations and experiments.

7.3 Performance of the Optimal Control Algorithm

The Anaheim SPM electromechanical system in Table 4.1 will be used for the simulations and experiments. To design the optimal braking trajectories, the following set of boundary conditions are chosen

$$\omega_{r0} = 100 \text{ rad/s}, \quad \omega_{rT} = 0 \text{ rad/s}, \theta_{r0} = 0 \text{ rad}, \theta_{rT} = 20\pi \text{ rad} \tag{7.14}$$

As an example case, the braking time-interval length is chosen to be 1.5 seconds. To restate the problem statement in words, the objective of the optimal control problem is bring a rotor that is initially spinning at 100 rad/s to a standstill in 1.5 seconds and completing exactly 10 rotations from the onset of braking, while extracting maximum kinetic energy during the braking interval. The result of using the numerical optimization function to obtain the optimal trajectories for the given boundary conditions is shown in Figure 7.1. The energy recovered during the braking time-interval is determined by computing the area under the electrical power versus time graph and is found to be 60.56% for this case. The variation of energy recovery ratio for different lengths of the braking time-interval is shown in Figure 7.2. The graph shows that smaller values of T significantly affect energy recovery and there is no significant improvement in energy recovery for braking time-interval lengths above $T = 1.6$ seconds. Therefore, the optimal length of the braking time-interval can be assumed to be in the neighborhood of this value. Care must be taken when choosing the value of T since some choices will result in optimal braking trajectories that involve both motoring and braking operations during the braking time-interval. Such designs are

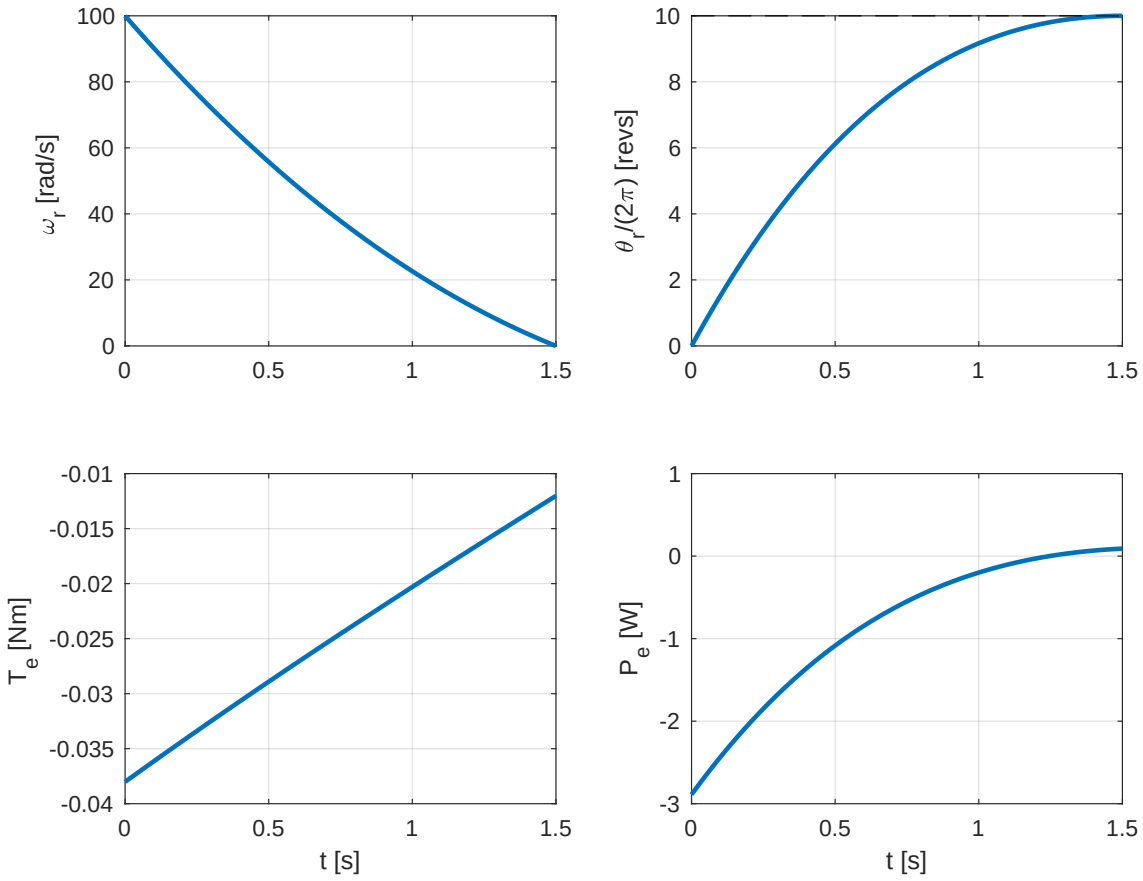

Figure 7.1: Optimal trajectories of rotor speed, rotor position, electromagnetic torque, and electrical power for $\omega_{r0} = 100$ rad/s, $\omega_{rT} = 0$ rad/s, $\theta_{r0} = 0$ rad, $\theta_{rT} = 20\pi$ rad, and $T = 1.5$ seconds using the numerical optimization tool `bvp4c`.

classified as “bad” designs as discussed in Section 5.2 are should be avoided.

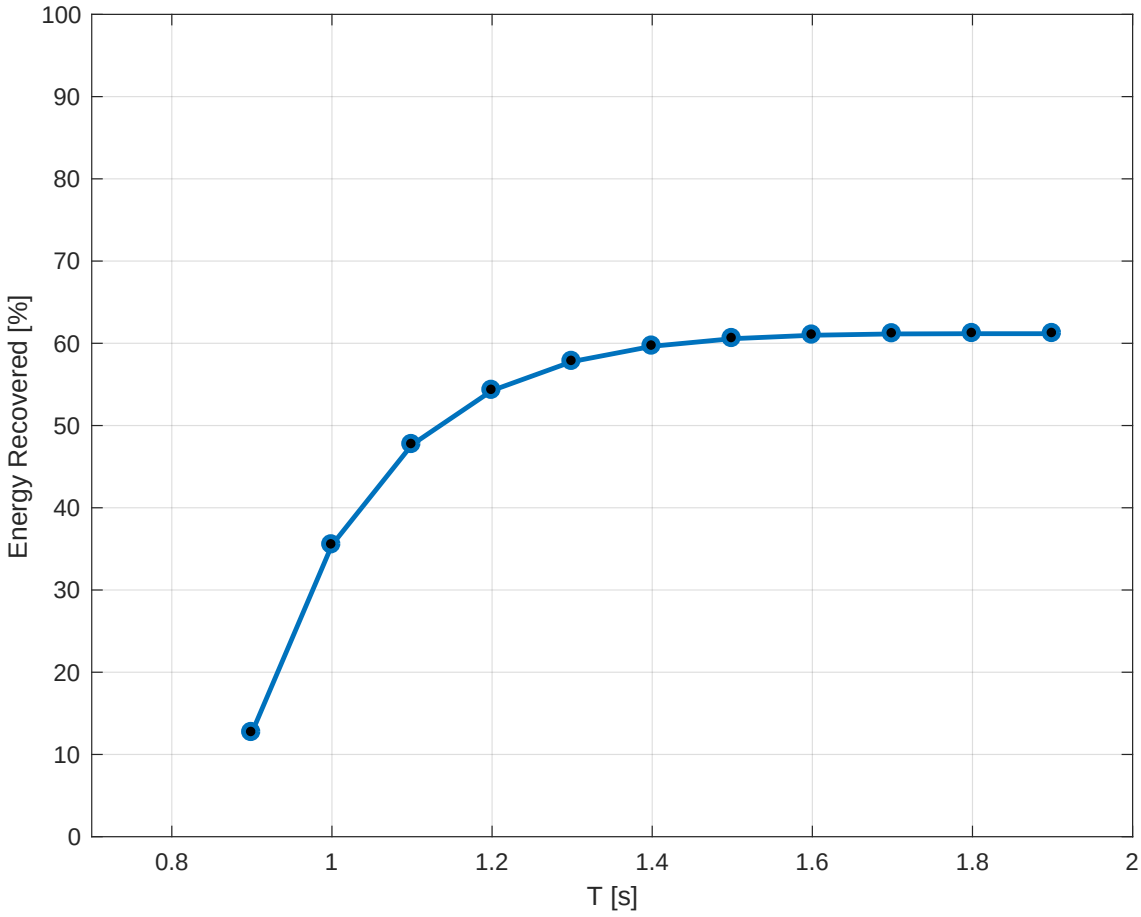

Figure 7.2: Variation of energy recovery with braking time interval length for $\omega_{r0} = 100$ rad/s, $\omega_{rT} = 0$ rad/s, $\theta_{r0} = 0$ rad, and $\theta_{rT} = 20\pi$ rad.

7.4 Implementation of the Optimal Position Control System

To implement the optimal braking controller designed in the previous section, a modified version of a closed-loop feedback position controller to include a feedforward reference torque signal is used as shown in Figure 7.3. The user-defined values of initial rotor position (θ_{r0}), final rotor position (θ_{rT}), initial rotor speed (ω_{r0}), final rotor speed (ω_{rT}), and braking time-interval length (T) are given as inputs to an optimal trajectory generator. The optimal trajectory generator in this case is the `bvp4c` boundary value problem solver which has

three outputs: time-based optimal rotor position trajectory reference (θ_r^*), time-based optimal rotor speed trajectory reference (ω_r^*), and the corresponding optimal electromagnetic torque reference trajectory (T_e^*) which is obtained from the optimal rotor speed trajectory and its associated optimal costate trajectory (χ_1) using (7.8). The optimal rotor speed and position trajectories are given as reference inputs to a closed-loop feedback position controller which computes position and speed errors between reference values and measured (or estimated) signals to generate a feedback torque reference signal u_{fb}. The optimal braking torque reference trajectory, T_e^*, is then added to the feedback torque reference (u_{fb}) in the form a feedforward signal u_{ff} to obtain an overall torque reference command u which is given as the input to the drive system. The addition of the feedforward torque reference signal is to ensure that the optimal braking position and speed trajectories are accurately followed. The dynamics of the overall system is analyzed to verify that the addition of the feedforward torque signal results in accurate trajectory tracking.

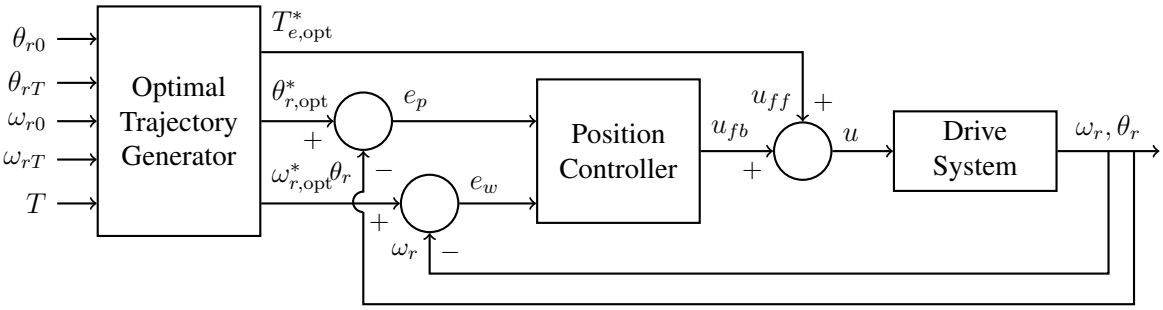

Figure 7.3: Block diagram of a closed-loop feedback position controller with a feedforward torque reference signal.

The rotor mechanical dynamics with both viscous and Coulomb friction loading are defined by

$$\begin{aligned} \dot{\theta}_r &= \omega_r \\ \dot{\omega}_r &= \frac{1}{J}\left(T_e - B_1\omega_r - B_0\,\mathrm{sgn}(\omega_r)\right) \end{aligned} \tag{7.15}$$

The dynamics of the reference signals satisfy

$$\begin{aligned}\dot{\theta}^*_{r,\text{opt}} &= \omega^*_{r,\text{opt}} \\ \dot{\omega}^*_{r,\text{opt}} &= \frac{1}{J}\left(T^*_{e,,\text{opt}} - B_1\omega^*_{r,\text{opt}} - B_0\ \text{sgn}(\omega^*_{r,\text{opt}})\right)\end{aligned} \tag{7.16}$$

where $\theta^*_{r,\text{opt}}$, $\omega^*_{r,\text{opt}}$, and $T^*_{e,\text{opt}}$ are outputs of the optimal trajectory generator. The output of the feedback position controller is

$$u_{fb} = k_{p1}e_p + k_{p2}e_w + k_{p3}\sigma_p \tag{7.17}$$

where

$$\begin{aligned}e_p &= \theta^*_{r,\text{opt}} - \theta_r \\ e_w &= \omega^*_{r,\text{opt}} - \omega_r \\ \dot{\sigma}_p &= e_p\end{aligned} \tag{7.18}$$

and the compensator gains are chosen to satisfy

$$\begin{aligned}k_{p1} &= 3J\alpha_p^2 \\ k_{p2} &= 3J\alpha_p - B_1 \\ k_{p3} &= J\alpha_p^3\end{aligned} \tag{7.19}$$

where α_p is the user-defined position controller bandwidth. The feedforward signal is

$$u_{ff} = T^*_{e,\text{opt}} \tag{7.20}$$

and the overall torque reference command is defined as

$$u = u_{ff} + u_{fb} = T^*_{e,\text{opt}} + k_{p1}e_p + k_{p2}e_w + k_{p3}\sigma_p \tag{7.21}$$

The overall torque reference signal u is given as the input to the drive system which produces an electromagnetic torque that satisfies $T_e = u$ and the overall system dynamics are now represented as

$$\begin{aligned}
\dot{\theta}_r &= \omega_r \\
\dot{\omega}_r &= \frac{1}{J}\Big(T_e - B_1\omega_r - B_0\ \mathrm{sgn}(\omega_r)\Big) \\
&= \frac{1}{J}\Big(T^*_{e,\mathrm{opt}} + k_{p1}e_p + k_{p2}e_w + k_{p3}\sigma_p - B_1\omega_r - B_0\ \mathrm{sgn}(\omega_r)\Big) \\
&= \frac{1}{J}\Big(T^*_{e,\mathrm{opt}} - B_1\omega^*_{r,\mathrm{opt}} - B_0\ \mathrm{sgn}(\omega^*_{r,\mathrm{opt}}) + B_1\omega^*_{r,\mathrm{opt}} + B_0\ \mathrm{sgn}(\omega^*_{r,\mathrm{opt}}) + k_{p1}e_p + k_{p2}e_w + k_{p3}\sigma_p \\
&\quad - B_1\omega_r - B_0\ \mathrm{sgn}(\omega_r)\Big) \\
&= \dot{\omega}^*_{r,\mathrm{opt}} + \frac{1}{J}\Big(k_{p1}e_p + (k_{p2} + B_1)\,e_w + k_{p3}\sigma_p + B_0\left(\mathrm{sgn}(\omega^*_{r,\mathrm{opt}}) - \mathrm{sgn}(\omega_r)\right)\Big)
\end{aligned} \tag{7.22}$$

Assume that the sign of the actual rotor speed is the same as its reference signal,

$$\mathrm{sgn}(\omega^*_{r,\mathrm{opt}}) = \mathrm{sgn}(\omega_r) \tag{7.23}$$

Substituting the above expression results in rotor dynamics

$$\begin{aligned}
\dot{\theta}_r &= \omega_r \\
\dot{\omega}_r &= \dot{\omega}^*_r + \frac{1}{J}\Big(k_{p1}e_p + (k_{p2} + B_1)\,e_w + k_{p3}\sigma_p\Big)
\end{aligned} \tag{7.24}$$

The position error dynamics and speed error dynamics are

$$\begin{aligned}
\dot{e}_p &= \dot{\theta}^*_{r,\mathrm{opt}} - \dot{\theta}_r = e_w \\
\dot{e}_w &= \dot{\omega}^*_{r,\mathrm{opt}} - \dot{\omega}_r = -\frac{1}{J}\Big(k_{p1}e_p + (k_{p2} + B_1)\,e_w + k_{p3}\sigma_p\Big) \\
\dot{\sigma}_p &= e_p
\end{aligned} \tag{7.25}$$

Substituting the feedback compensator gains from (7.19) results in

$$\begin{aligned}\dot{e}_p &= e_w \\ \dot{e}_w &= -\left(3\alpha_p^2 e_p + 3\alpha_p e_w + \alpha^3 \sigma_p\right) \\ \dot{\sigma}_p &= e_p\end{aligned} \tag{7.26}$$

which is rewritten in matrix form as

$$\begin{bmatrix}\dot{e}_p \\ \dot{e}_w \\ \dot{\sigma}_p\end{bmatrix} = \begin{bmatrix}0 & 1 & 0 \\ -3\alpha_p^2 & -3\alpha_p & -\alpha_p^3 \\ 1 & 0 & 0\end{bmatrix}\begin{bmatrix}e_p \\ e_w \\ \sigma_p\end{bmatrix} \tag{7.27}$$

and the associated characteristic polynomial is

$$(s + \alpha_p)^3 \tag{7.28}$$

The conclusion that can be drawn from this analysis is that the addition of the feedforward term results in unforced error dynamics which stays at zero if the system is initialized with zero error at the beginning of the braking interval regardless of the choice of position controller bandwidth, α_p.

7.5 Experiment Results

The position control experiments are conducted using the Anaheim SPM system that is shown in Figure 4.2. The same boundary conditions that were used to produce the optimal trajectories shown in Figure 7.1 are used for the experiments. The output of the numerical optimization function is a mesh grid of 18 points that describe the optimal rotor speed, optimal rotor position, and optimal electromagnetic torque. These trajectories are used as speed and position reference signals and the feedforward torque signal of the optimal regenerative braking position controller shown in Figure 7.3 and are used as lookup tables

on the microcontroller. For the experiments, the current controller bandwidth is 2500 rad/s and the position controller bandwidth is 1 rad/s. The switching frequency is 30 kHz, the current-control loop update frequency is 12.5 kHz, and the position-control loop update frequency is 6.25 kHz. The rotor is made to spin to an initial speed of 100 rad/s. Once the rotor speed has reached its steady-state reference value, a braking command is issued. The time-dependent optimal rotor speed, position, and electromagnetic torque are selected from the lookup table using linear interpolation and are used as reference values to the optimal regenerative braking position controller. The rotor position is measured using a shaft-mounted quadrature encoder. The rotor speed is estimated from the rotor signals as explained earlier. The optimal braking position controller then ensures that the desired trajectory is followed as the rotor comes to a standstill after exactly 10 rotations in 1.5 seconds as desired.

The trajectories of rotor speed, position, power converter leg currents and voltages are measured using sensors during the course of the experiment. The electrical energy recovered during the braking event is calculated as discussed earlier. The trajectories and performance of the experiments are compared with simulation results as shown in Figures 7.4 and 7.5. The black dotted line in Figure 7.5 represents the torque-speed capability boundary. Notice that the rotor speed reaches zero in exactly 10 rotations and 1.5 seconds. Table 7.1 compares the energy recovery ratios of the experiment, which is an average of three trials, and the simulation results. There is good agreement between experiments and simulations for the trajectories and the energy recovery ratios.

Table 7.1: Comparison of Simulation and Experiments for Optimal Braking Control with Position Constraints

Method	E_{ratio} [%]
Simulation	60.56
Experiment	60.07

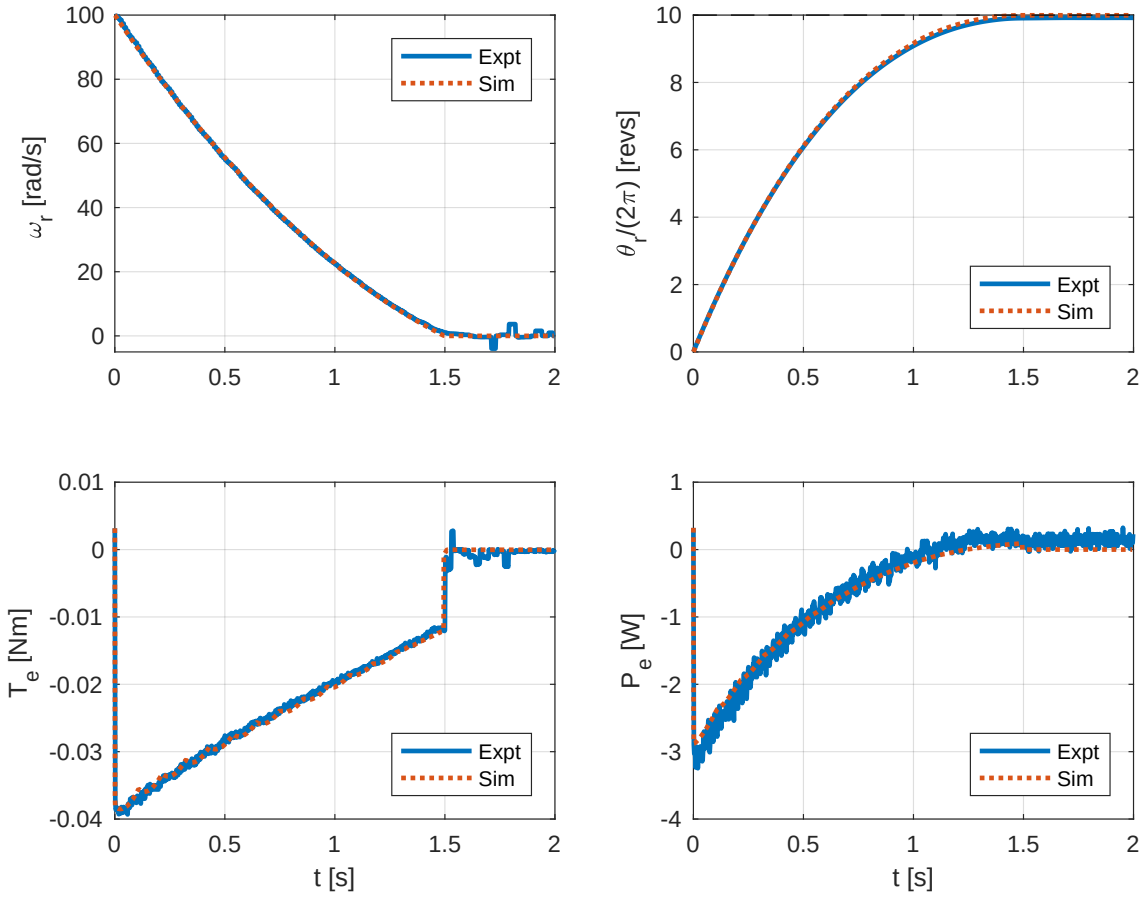

Figure 7.4: Comparison of rotor speed, position, electromagnetic torque, and electrical power for experiment and simulation implementations of the optimal kinetic energy recovery algorithm with position constraints.

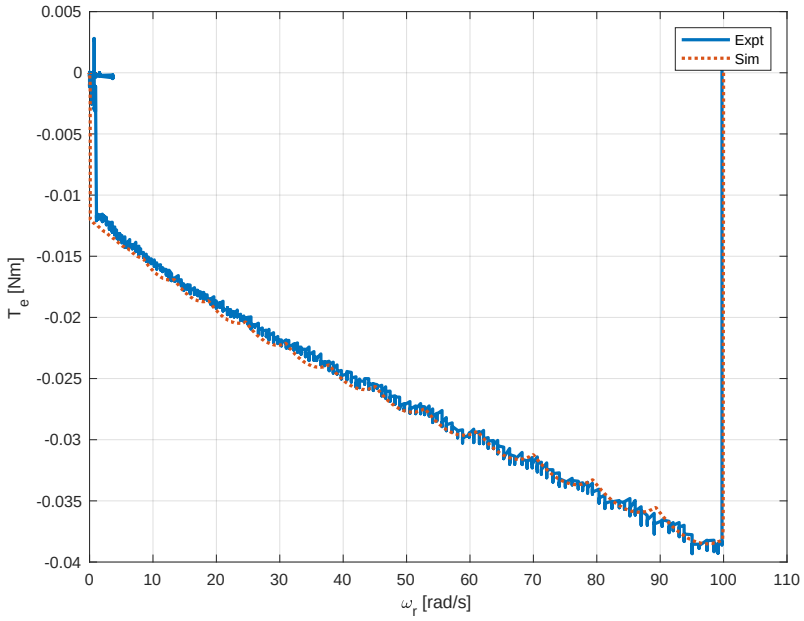

Figure 7.5: Comparison of braking trajectories in the torque-speed plane for experiment and simulation implementations of the optimal kinetic energy recovery algorithm with position constraints.

7.6 Conclusion

The optimal kinetic energy recovery algorithm from earlier was expanded to include position constraints in the problem definition. This resulted in a boundary-value problem with two state variables and two costate variables and four boundary conditions. Although the differential equation system was LTI and could be solved in closed-form, the solution is complicated and lengthy to write down. A numerical optimization tool called `bvp4c` was instead used to obtain the optimal control solution. For an example set of boundary conditions on rotor speed and position, the performance of the optimal braking position controller was studied for a range of braking time-interval lengths. To implement the optimal braking position controller, a standard position controller is modified to include a feedforward torque signal. The outputs of the numerical optimization function, which is a mesh grid of optimal rotor speed and position trajectories, are given as speed and position references to the optimal braking position controller and the optimal torque trajectory is

given as a feedforward signal to the controller. The algorithm was then implemented in simulation and experiments. The results of the simulation and experiments showed good agreement with each other in terms of the speed and position trajectories as well as the energy recovered.

The optimal braking position controller can be applied to any braking operation that has strict position constraints such as conveyor belts and elevator drives. The problem can be expanded to include other non-linear loads such as the aerodynamic drag effect which is prominent in traction applications such as electric vehicles and electric trains. The optimal control problem can be formulated using the guidelines that were described in this chapter and the optimal control solution to the resulting non-linear boundary-value problem can be obtained using numerical optimization tools such as the `bvp4c` function. The solution can then be implemented on an electric train traction drive system to follow the optimally designed speed and position trajectories such that the train comes to a stop from an initial speed in a certain duration, T, while recovering maximum kinetic energy.

CHAPTER 8
OPTIMAL KINETIC ENERGY RECOVERY ALGORITHMS FOR SPMS IN THE FLUX-WEAKENING REGION

The previous chapters studied the problem of optimal kinetic energy recovery under constant-flux operation. For surface permanent-magnet synchronous machines (SPMs), constant-flux operation is characterized by zero direct-axis stator current value ($i_d = 0$). However, as the rotor speed increases and higher torques are requested, this choice of direct-axis current is not feasible and a strategy called flux-weakening will be required.

8.1 Need for Flux-Weakening

The operating capabilities of all electric machines are governed by voltage and current constraints. These constraints are introduced by the DC power supply and the three-phase DC-AC power converter that are used to excite the electric machines. These constraints will in turn manifest themselves as torque and speed limits for the electric drive system [76]. In the dq reference frame, these constraints are expressed as

$$\mathcal{I} = \left\{(i_d, i_q) : i_d^2 + i_q^2 \leq I_{\max}^2\right\}, \mathcal{V} = \left\{(v_d, v_q) : v_d^2 + v_q^2 \leq V_{\max}^2\right\} \tag{8.1}$$

where i_d and i_q are the direct and quadrature axes currents, v_d and v_q are the direct and quadrature axes voltages, $I_{\max}$ is the maximum length of the dq current vector, and $V_{\max}$ is the maximum length of the dq voltage vector. For an SPM, the quasi-steady-state expressions for the direct and quadrature-axis voltages are expressed as

$$\begin{aligned} v_d &= R_s i_d - N\omega_r L i_q \\ v_q &= R_s i_q + N\omega_r \left(\Lambda + L i_d\right) \end{aligned} \tag{8.2}$$

For the sake of simplicity, the value of R_s is assumed to be zero which simplifies the expressions for voltages to

$$\begin{aligned} v_d &\approx -N\omega_r \left(Li_q\right) \\ v_q &\approx N\omega_r \left(\Lambda + Li_d\right) \end{aligned} \tag{8.3}$$

In order to operate the electric machine using a desired current vector of the form (i_d, i_q), the corresponding voltage vector that is required, (v_d, v_q), must scale with rotor speed as seen in (8.3). The permanent magnet on the surface of the rotor induces a voltage in the quadrature-axis that is proportional to Λ. There exists another source of electromagnetically induced voltage in the quadrature-axis in the form of $N\omega_r Li_d$. Therefore, there exists a possibility to intentionally weaken the effect of the permanent magnet flux by using the stator direct-axis current in such a manner that Li_d counteracts Λ. This operation in which $i_d < 0$ and becomes more and more negative with increasing rotor speed, results in reducing the magnitude of quadrature-axis stator voltage and thereby reducing the effective length of the dq voltage vector. This allows the electric machine to operate within the voltage-limit constraint even at high rotor speeds. This operating strategy is called flux-weakening, since the negative direct-axis current "weakens" the effective flux in the quadrature-axis, and allows the machine to reach higher rotor speeds that would not be possible using the $i_d = 0$ strategy due to voltage limits.

8.2 Constant-Power Flux-Weakening

As described above, flux-weakening may be viewed as an operating policy for manipulating the non-torque-producing direct-axis current as a function of rotor speed to enable operation at higher rotor speeds. For the sake of simplicity, it is sometimes preferred to adopt a constant-power flux-weakening policy even though such a policy does not fully exploit the true torque-speed capability of the system. With this approach, the equation that describes the torque that can be produced at each rotor speed is extremely simple and

the torque-speed capability region includes a hyperbolic region. The air-gap power of the machine at any speed is

$$P_m = T_e\ \omega_r \tag{8.4}$$

The maximum power that can be produced by the machine under constant-flux operation ($i_d = 0$) is the product of the maximum electromagnetic torque, $T_{e,\max}$, and a rotor speed called base speed, ω_{rb}. Base speed is defined as the largest rotor speed at which maximum torque, $T_{e,\max}$ can be produced without violating voltage or current-limit constraints. The expression for base speed in terms of the machine parameters and voltage and current-limits is

$$\omega_{rb} = \frac{V_{\max}}{N\sqrt{\Lambda^2 + L^2 I_{\max}^2}} \tag{8.5}$$

The torque-speed operating point $(T_{e,\max}, \omega_{rb})$ is sometimes referred to as the corner-point of the electric drive and the associated air-gap power is

$$P_{m,\text{base}} = T_{e,\max}\ \omega_{rb} \tag{8.6}$$

By definition, constant-power flux-weakening implies that operation beyond base speed will require that air-gap power satisfies

$$T_e\ \omega_r = T_{e,\max}\ \omega_{rb}, \tag{8.7}$$

at every speed above base speed. Under this condition, the maximum permissible value of the torque-producing quadrature-axis current at each rotor speed is

$$i_{q,\max} = I_{\max}\frac{\omega_{rb}}{\omega_r} \tag{8.8}$$

The maximum torque that can be produced with this value of quadrature-axis current is

$$T_{e,\mathrm{fw,max}} = T_{e,\mathrm{max}} \frac{\omega_{rb}}{\omega_r} \tag{8.9}$$

where the subscript fw denotes flux-weakening. The approximate steady-state dq voltages are

$$\begin{aligned} v_d &\approx -N\omega_r L I_{\mathrm{max}} \frac{\omega_{rb}}{\omega_r} \\ v_q &\approx N\omega_r \left(\Lambda + L i_d\right) \end{aligned} \tag{8.10}$$

The voltage constraint that is imposed can be written as

$$\begin{aligned} v_d^2 + v_q^2 &= V_{\mathrm{max}}^2 \\ \left(i_d + \frac{\Lambda}{L}\right)^2 + I_{\mathrm{max}}^2 \frac{\omega_{rb}^2}{\omega_r^2} &= \left(\frac{V_{\mathrm{max}}}{N\omega_r L}\right)^2 \end{aligned} \tag{8.11}$$

Using the expression for base speed from (8.5), the direct-axis current can be isolated and expressed as a current reference signal for positive rotor speeds as

$$i_d^* = \begin{cases} 0 & \text{if } \omega_r \leq \omega_{rb} \\ -\dfrac{\Lambda}{L}\left(1 - \dfrac{\omega_{rb}}{\omega_r}\right) & \text{if } \omega_r > \omega_{rb} \end{cases} \tag{8.12}$$

This is the rule that will be used to implement the constant-power flux-weakening policy.

8.3 Optimal Kinetic Energy Recovery Under Flux-Weakening

The objective of recovering kinetic energy starting from high rotor speeds is discussed in this section. Since the direct-axis current is non-zero for speeds above base speed, the electric power associated with high-speed operation has to include the copper losses associated with the direct-axis current. As the rotor speed goes below base speed during the braking operation, the direct-axis current reference is set to zero and the operation tran-

sitions from flux-weakening to constant-flux operation. For the SPM, the quadrature-axis current reference is determined by the desired electromagnetic torque, T_e^*, as

$$i_q^* = \frac{T_e^*}{K} \tag{8.13}$$

where $K = N\Lambda$. This formula for the q-axis current remains the same regardless of whether the machine is operating in the constant-flux region or flux-weakening region. The steady-state electric power is expressed as

$$P_e = v_d i_d^* + v_q i_q^* = R i_d^{*2} + R i_q^{*2} + T_e^* \omega_r \tag{8.14}$$

where $R = R_s$. Since the formula for i_d^* varies with rotor speed as

$$i_d^* = \begin{cases} 0 & \text{if } \omega_r \leq \omega_{rb} \\ -\dfrac{\Lambda}{L}\left(1 - \dfrac{\omega_{rb}}{\omega_r}\right) & \text{if } \omega_r > \omega_{rb} \end{cases} \tag{8.15}$$

the expression for electric power is also different for the two cases

$$P_e = \begin{cases} R\dfrac{T_e^{*2}}{K} + T_e^* \omega_r & \text{if } \omega_r \leq \omega_{rb} \\ R\dfrac{\Lambda^2}{L^2}\left(1 - \dfrac{\omega_{rb}}{\omega_r}\right)^2 + R\dfrac{T_e^{*2}}{K} + T_e^* \omega_r & \text{if } \omega_r > \omega_{rb} \end{cases} \tag{8.16}$$

The objective of recovering maximum kinetic energy during a braking interval of length T can be defined as

$$\text{minimize } E = \int_0^T P_e \, dt, \;\; \text{subject to } \omega_r(0) = \omega_{r0}, \text{ and } \omega_r(T) = \omega_{rT} \tag{8.17}$$

where E is the electrical energy that is leaving the electrical terminals of the power supply and entering the electric machine. Mechanical rotor speed dynamics that includes the effect

of both viscous friction and Coulomb friction is expressed as

$$\dot{\omega}_r = \frac{1}{J}\left(T_e^* - T_{\text{load}}\right) \tag{8.18}$$

where the load torque is expressed as

$$T_{\text{load}} = B_1\omega_r + B_0\ \text{sgn}(\omega_r) \tag{8.19}$$

The rotor speed dynamics can be rewritten as follows

$$\dot{\omega}_r = \frac{1}{J}\left(T_e^* - B_1\omega_r - B_0\ \text{sgn}(\omega_r)\right) \tag{8.20}$$

According to the theory of optimal control, a Hamiltonian that includes the objective function and the state dynamics must first be defined. However, since the term under the integral sign in the objective function has two different expressions according to whether the rotor speed is above or below base speed, a piece-wise Hamiltonian function is defined as follows

$$H = \begin{cases} R\dfrac{T_e^{*2}}{K^*} + T_e^*\omega_r + \chi\dot{\omega}_r & \text{if } \omega_r \leq \omega_{rb} \\ R\dfrac{\Lambda^2}{L^2}\left(1 - \dfrac{\omega_{rb}}{\omega_r}\right)^2 + R\dfrac{T_e^{*2}}{K^*} + T_e^*\omega_r + \chi\dot{\omega}_r & \text{if } \omega_r > \omega_{rb} \end{cases} \tag{8.21}$$

where χ is the costate variable. The optimality condition for the control variable T_e^* is then obtained by setting the partial derivative of the Hamiltonian function with respect to T_e^* to zero and solving for the optimal control variable. The partial derivative of the Hamiltonian that is described in (8.21) with respect to T_e^* results in the same expression for T_e^* for both cases $\omega_r \leq \omega_{rb}$ and $\omega_r > \omega_{rb}$.

$$\frac{\partial H}{\partial T_e^*} = 0 \implies T_{e,\text{opt}}^* = -\frac{K^2}{2R}\left(\omega_{r,\text{opt}} + \frac{\chi_{\text{opt}}}{J}\right) \tag{8.22}$$

The optimal state dynamics is obtained by taking the partial derivative of the Hamiltonian function with respect to the costate variable, χ as

$$\dot{\omega}_{r,\text{opt}} = \frac{\partial H}{\partial \chi} = \frac{1}{J}\left(T^*_{e,\text{opt}} - B_1\omega_{r,\text{opt}} - B_0\ \text{sgn}(\omega_{r,\text{opt}})\right) \tag{8.23}$$

The state dynamics are has a common expression for both cases. The costate dynamics is obtained by taking the partial derivative of the Hamiltonian function with respect to the state variable, ω_r. This is done for each case since the partial derivatives do not result in a common expression. The piece-wise costate dynamic equation is

$$\dot{\chi}_{\text{opt}} = -\frac{\partial H}{\partial \omega_r} = \begin{cases} -T^*_{e,\text{opt}} + \dfrac{B_1}{J}\chi_{\text{opt}} + \dfrac{2B_0}{J}\delta(\omega_{r,\text{opt}})\chi_{\text{opt}} & \text{if } \omega_{r,\text{opt}} \leq \omega_{rb} \\ -T^*_{e,\text{opt}} + \dfrac{B_1}{J}\chi_{\text{opt}} + \dfrac{2B_0}{J}\delta(\omega_{r,\text{opt}})\chi_{\text{opt}} & \\ \qquad -2R\dfrac{\Lambda^2}{L^2}\omega_{rb}\left(\dfrac{1}{\omega^2_{r,\text{opt}}} - \dfrac{\omega_{rb}}{\omega^3_{r,\text{opt}}}\right) & \text{if } \omega_{r,\text{opt}} > \omega_{rb} \end{cases} \tag{8.24}$$

Substituting the value of the optimal control variable, $T^*_{e,\text{opt}}$, from (8.22) results in the formulation of a piece-wise two-point boundary value problem that depends on the value of the state variable ω_r

Case: $\omega_r \leq \omega_{rb}$

$$\begin{bmatrix} \dot{\omega}_{r,\text{opt}} \\ \dot{\chi}_{\text{opt}} \end{bmatrix} = \frac{K^2}{2JR}\begin{bmatrix} -(1+2\gamma) & J^{-1} \\ J & (1+2\gamma) \end{bmatrix}\begin{bmatrix} \omega_{r,\text{opt}} \\ \chi_{\text{opt}} \end{bmatrix} + \frac{B_0}{J}\begin{bmatrix} -\text{sgn}(\omega_r) \\ 2\delta(\omega_{r,\text{opt}})\chi_{\text{opt}} \end{bmatrix} \tag{8.25}$$

Case: $\omega_r > \omega_{rb}$

$$\begin{aligned}\dot{\omega}_{r,\text{opt}} &= -\frac{K^2}{2JR}\left((1+2\gamma)\omega_{r,\text{opt}} - \frac{\chi_{\text{opt}}}{J}\right) - \frac{B_0}{J}\text{sgn}(\omega_{r,\text{opt}}) \\ \dot{\chi}_{\text{opt}} &= \frac{K^2}{2JR}\left(J\omega_{r,\text{opt}} + (1+2\gamma)\chi_{\text{opt}}\right) + \frac{2B_0}{J}\delta(\omega_{r,\text{opt}})\chi_{\text{opt}} - 2R\frac{\Lambda^2}{L^2}\omega_{rb}\left(\frac{1}{\omega_{r,\text{opt}}^2} - \frac{\omega_{rb}}{\omega_{r,\text{opt}}^3}\right)\end{aligned} \tag{8.26}$$

where $\gamma = \dfrac{B_1 R}{K^2}$ is a dimensionless electromechanical loss parameter. The boundary conditions for the two-point boundary value problem are

$$\omega_{r,\text{opt}}(0) = \omega_{r0}, \quad \text{and} \quad \omega_{r,\text{opt}}(T) = \omega_{rT} \tag{8.27}$$

8.4 Numerical Optimization

Although the expression for the optimal state dynamics, i.e. $\dot{\omega}_{r,\text{opt}}$ is the same for both the cases, the optimal costate dynamics are different. The structure of the two-point boundary value problem for the case where the rotor speed is below base speed in (8.25) is an LTI system and its solution can be obtained in closed-form as seen in Section 6.3.1. However, the boundary value problem in (8.26) is non-linear due to the presence of the $\dfrac{1}{\omega_{r,\text{opt}}^2}$ and $\dfrac{1}{\omega_{r,\text{opt}}^3}$ terms, and therefore its solution cannot be obtained easily in closed-form. The numerical optimization tool in Matlab called `bvp4c` [74, 75] is used to solve the two-point boundary value problem in (8.25) and (8.26). Depending on the value of the rotor speed variable, $\omega_{r,\text{opt}}$, the numerical optimization solves either (8.25) or (8.26) for that time instant $t \in [0, T]$. For example, if the initial rotor speed $\omega_{r0} > \omega_{rb}$, then the numerical optimization function will solve (8.26), and as the rotor slows down to values equal to or below base speed, the numerical optimization function will solve (8.25). The output of the `bvp4c` solver is a time grid and the time-dependent optimal trajectories of the state

and costate variables. The optimal control variable, $T^*_{e,\mathrm{opt}}$, is then constructed from the optimal trajectories for rotor speed and the costate variable χ_{opt} using the expression in (8.22). The optimal trajectories for rotor speed and electromagnetic torque reference are then used as lookup tables for the simulations and experiments. The optimal rotor speed trajectory is given as the speed reference command of a closed-loop speed controller and the optimal torque reference command is used as the feedforward signal to the modified speed controller in Figure 5.9.

8.5 Performance of the Optimal Kinetic Energy Recovery Algorithm

The Anaheim SPM electromechanical system in Table 4.1 is used to test the performance of the optimal kinetic energy recovery algorithm. A DC supply voltage of 19.6 V is used, which translates to a voltage limit constraint value of

$$V_{\max} = \sqrt{\frac{9}{8}}\, V_{\mathrm{DC}} = 20.78 \text{ V} \tag{8.28}$$

for the delta-connected machine. The base speed of the machine is calculated from (8.5) as 390.5 rad/s. For an initial rotor speed of $\omega_{r0} = 600$ rad/s, a final rotor speed of $\omega_{rT} = 0$ rad/s, and a braking time-interval length of $T = 6$ seconds, the solution to the optimal kinetic energy recovery algorithm using the numerical optimization is shown in Figure 8.1.

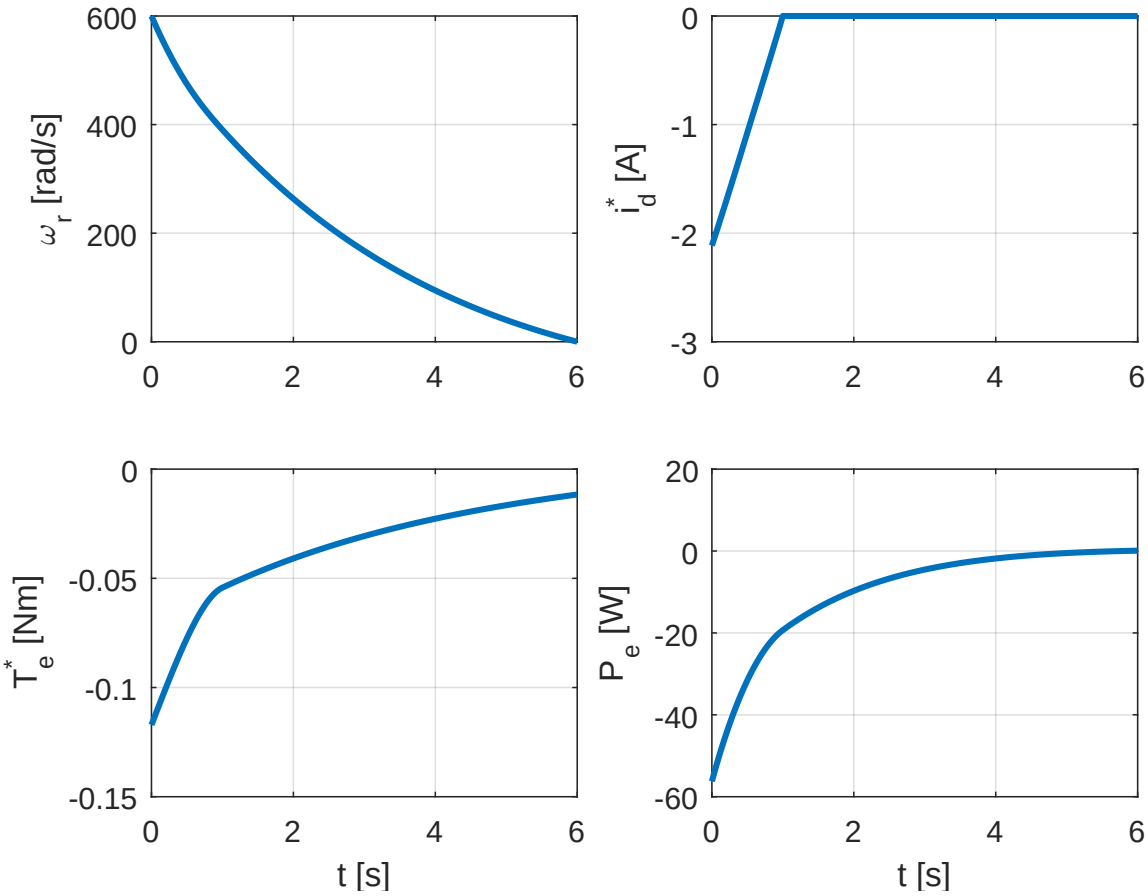

Figure 8.1: Optimal trajectories of rotor speed, direct-axis current, electromagnetic torque, and electrical power for $\omega_{r0} = 600$ rad/s, $\omega_{rT} = 0$ rad/s, and $T = 6$ seconds using the numerical optimization tool `bvp4c`.

Since the initial rotor speed is above base speed, the operation starts off in the flux-weakening region, as seen from the negative direct-axis current trajectory in Figure 8.1. As the rotor speed passes below base speed at around $t = 1$ s, the value of the direct-axis current is zero as the machine enters the constant-flux operating region and stays in this region until the rotor comes to a complete stop. The energy recovered during the braking interval is calculated as the area under the electrical power curve in Figure 8.1. The energy recovery ratio, which is the ratio of the electrical energy recovered during the braking interval to the kinetic energy that is available for conversion, in this scenario is 79.40%. The variation of energy recovery with the length of the braking time-interval for the set of

initial and final rotor speeds chosen earlier is shown in Figure 8.2.

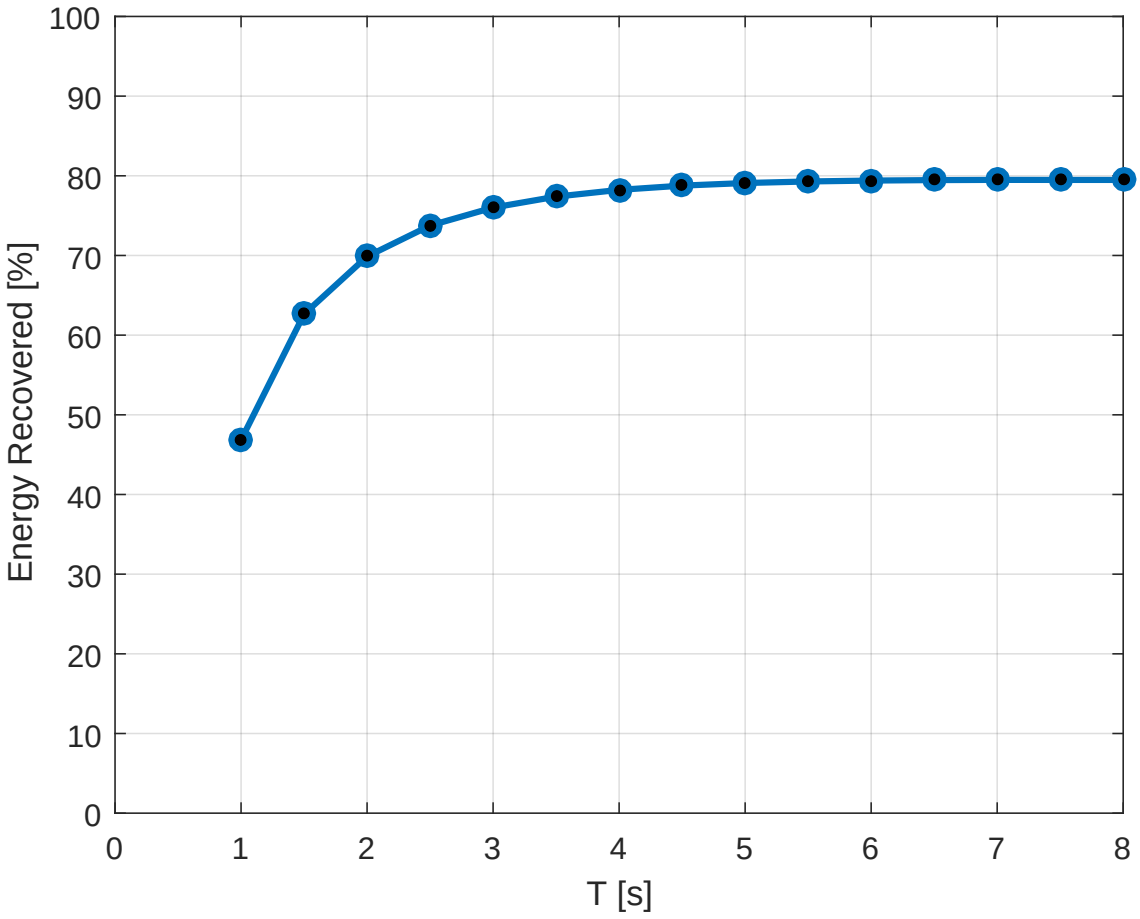

Figure 8.2: Variation of energy recovery with length of the braking time-interval T for $\omega_{r0} = 600$ rad/s, $\omega_{rT} = 0$ rad/s under constant-power flux-weakening.

It can be observed that the energy recovery ratio reaches its optimal value at around $T = 7$ seconds. Therefore, it can be assumed that the optimal braking time-interval length is in the neighborhood of this value.

8.6 Comparison with Constant-Torque Braking

Another option to implement braking is to use constant levels of braking torque. In this strategy, a constant braking torque, which is a fraction of the maximum braking torque, is applied until the rotor speed reaches the desired final speed. This section compares

the performance of a constant-torque braking controller with the optimal kinetic energy recovery algorithm using simulations of the Anaheim SPM system. It should be noted that at rotor speeds above base speed, the flux-weakening operation comes into effect. This impacts the maximum magnitude of electromagnetic torque that can be produced at these high-speeds and is governed by the expression for maximum electromagnetic torque using constant-power flux-weakening operation in (8.9). The performance of the constant-torque braking controller in terms of energy recovery is shown in Table 8.1 at various levels of braking torque. The rotor speed trajectories and the braking trajectories in the torque-speed plane are shown in Figures 8.3(a) and 8.4(b) respectively. The operating boundary in the torque-speed plane under the constant-power flux-weakening operating policy is shown as a black dotted line in Figure 8.4(b). Notice that at constant-torque levels above 60% of the maximum braking torque, the torque trajectory in not a horizontal line in the torque-speed plane. This is because this high-level of constant-braking-torque lies outside the boundary of operation at high-speeds. The braking trajectory is forced to operate on the boundary of the torque-speed capability curve until the rotor speed slows down enough to allow the requested constant level of braking torque to be produced without violating voltage and current limit constraints.

Table 8.1: Energy Recovery Ratio and Braking Time-Interval Length for Constant-Torque Braking Under Flux-Weakening

Constant Braking Torque	E_{ratio} [%]	Braking Time [s]
10% of $T_{e,\max}$	63.86	10.67
20% of $T_{e,\max}$	74.39	5.90
30% of $T_{e,\max}$	76.10	4.10
40% of $T_{e,\max}$	75.28	3.13
50% of $T_{e,\max}$	73.32	2.54
60% of $T_{e,\max}$	70.74	2.13
70% of $T_{e,\max}$	67.82	1.84
80% of $T_{e,\max}$	64.88	1.62
90% of $T_{e,\max}$	62.11	1.44
100% of $T_{e,\max}$	59.57	1.30

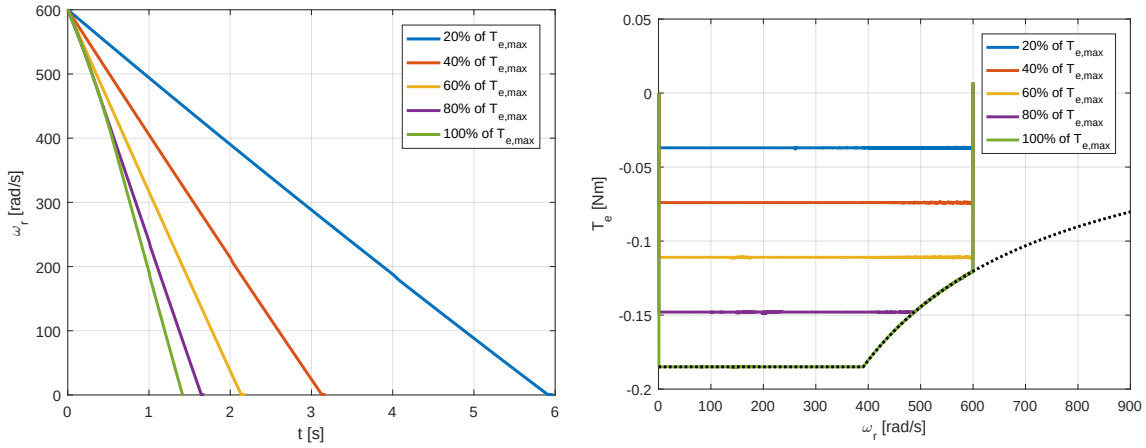

(a) Rotor speed trajectories

(b) Torque trajectories in the torque-speed plane

Figure 8.3: Simulation results showing rotor speed and braking trajectories for the Anaheim SPM system under constant-torque braking.

Table 8.1 shows that highest energy recovery ratio that can be achieved using constant-torque braking is 76.10% using a braking torque level that is 30% of the maximum braking

torque and the rotor takes 4.1 seconds to come to a standstill from an initial speed of 600 rad/s. In contrast, the optimal braking trajectory recovers 79.44% and has an optimal braking time-interval length of $T_{\text{opt}} = 7$ seconds according the simulations. As an additional exercise, the optimal braking trajectory corresponding to a braking time-interval length of $T = 4.1$ seconds was also studied. This provides a direct comparison with the constant-torque braking controller corresponding to 30% of the maximum braking torque since both the controllers now take the same amount of time to reach zero speed, i.e. 4.1 seconds. The superiority of the optimal controller is transparent here since it recovers an additional 2.33% of the kinetic energy that was available for conversion while slowing down to a halt in the same time as the constant braking controller.

Table 8.2: Comparison of Constant-Torque Braking and Optimal Control Under Flux-Weakening

Braking Torque	E_{ratio} [%]	Braking Time [s]
30% of $T_{e,\max}$	76.10	4.1
Optimal Control	78.43	4.1
Optimal Control	79.44	7

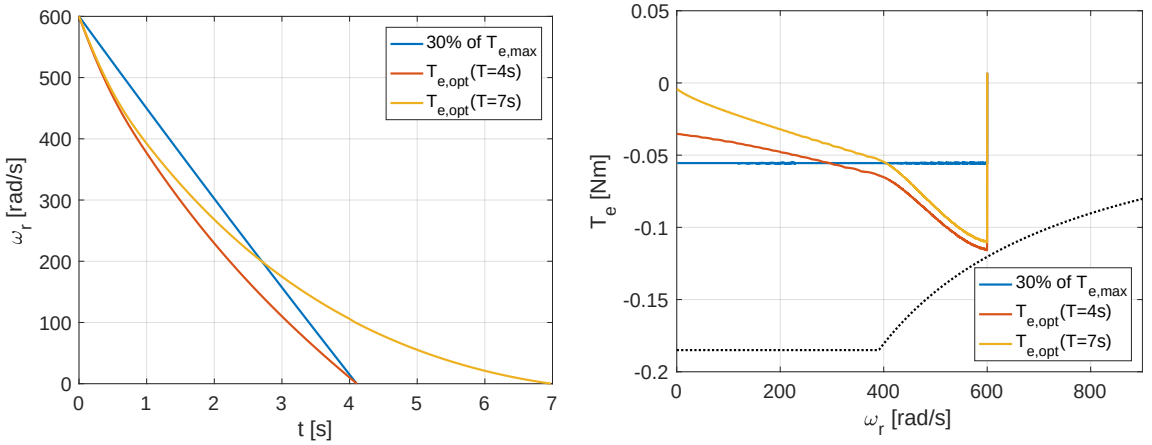

(a) Rotor speed trajectories

(b) Torque trajectories in the torque-speed plane

Figure 8.4: Simulation results comparing constant-torque and optimal braking controllers for the Anaheim SPM system under constant-power flux-weakening operation.

8.7 Experimental Results

In this section, the performance of the optimal kinetic energy recovery algorithm on the experimental Anaheim SPM system pictured in Figure 4.2 will be studied. The current regulator bandwidth is 2500 rad/s, the speed controller bandwidth is 2 rad/s, the power stage switching frequency is 30 kHz, the current-control loop update frequency is 10 kHz and the speed-control loop update frequency is 5 kHz. The output of the numerical optimization function, i.e. the optimal rotor speed and the optimal torque reference values, are implemented on the microcontroller as lookup tables. The electric machine is brought to an initial speed, ω_{r0}, using the closed-loop speed controller. For the experiments that are discussed in this section, the initial rotor speed is above base speed. Therefore, constant-power flux-weakening is used to achieve this high rotor speed using the equations detailed in Section 8.2. Once the rotor speed achieves its target steady-state speed of ω_{r0}, a braking command is issued. The time-dependent optimal rotor speed and torque references are selected from the lookup table using linear interpolation and given as the speed reference signal and the feedforward torque signal to the optimal regenerative braking controller shown in Figure 5.9. The rotor speed is measured using a shaft-mounted quadrature encoder encoder, with signal processing that combines two forms of differentiation; variable position over fixed time, and fixed position over variable time. The encoder measurement is also used for electronic commutation to ensure synchronous three-phase operation of the electric machine. The optimal braking speed controller applies a braking torque that slows the rotor down to a speed of ω_{rT} in T seconds while recovering maximum kinetic energy. For choices of $\omega_{r0} = 450$ rad/s, $\omega_{rT} = 0$ rad/s, and $T = 6.5$ seconds, the output of numerical optimization function is represented on a mesh of 61 data points as determined by the boundary-value problem solver. The optimal rotor speed trajectory, direct-axis current, electromagnetic torque, and electrical power curves for this problem are shown in Figure 8.5.

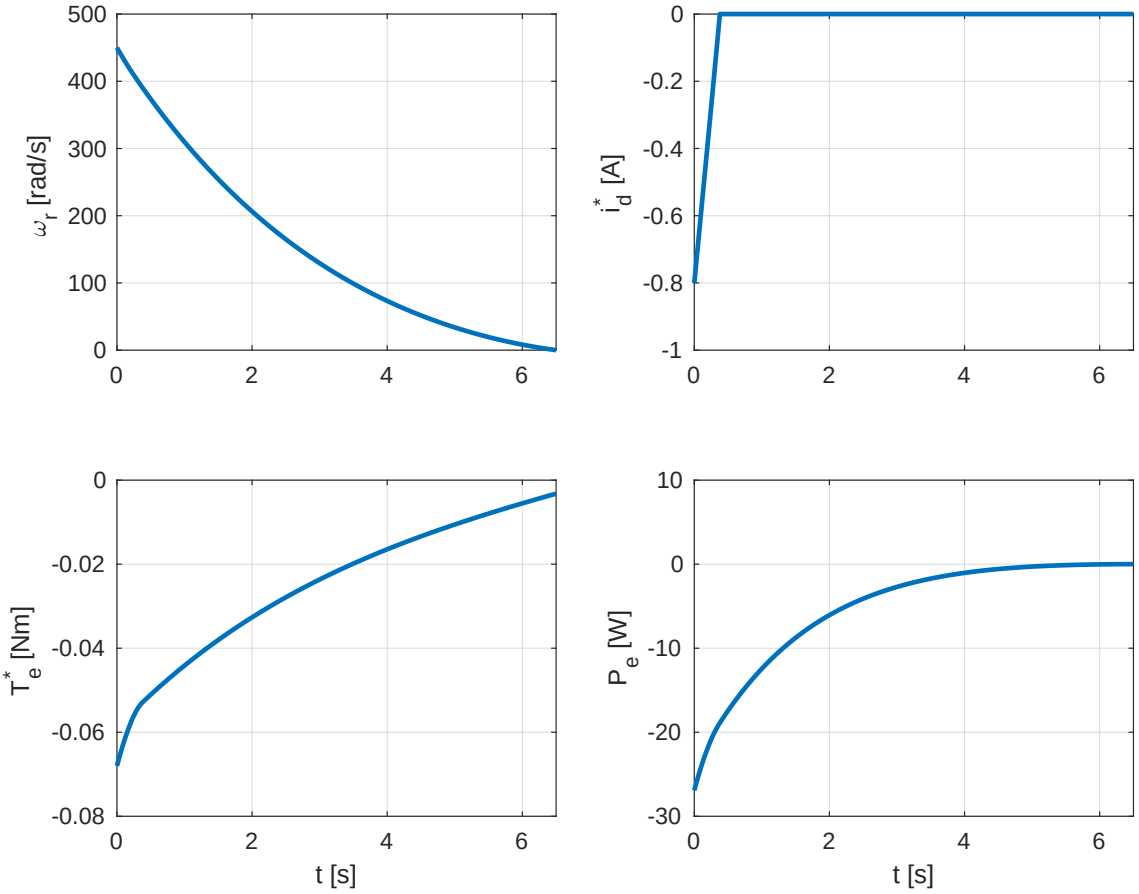

Figure 8.5: Optimal trajectories of rotor speed, direct-axis current, electromagnetic torque, and electrical power for $\omega_{r0} = 450$ rad/s, $\omega_{rT} = 0$ rad/s, and $T = 6.5$ seconds using the numerical optimization tool `bvp4c`.

The trajectories of rotor speed, power converter leg currents and voltages are measured using sensors during the course of the experiment. Leg voltages are measured by sampling the voltage across a voltage divider circuit for each leg. The leg currents are measured by sampling the voltage across shunt resistors located between the low-side switches and the negative battery terminal. The electrical power during the braking time-interval is calculated on the microcontroller using the following equation

$$P_e = v_A i_A + v_B i_B + v_C i_C \tag{8.29}$$

where v_{ABC} are the leg voltages and i_{ABC} are the leg currents. The electrical energy that

is recovered during the braking interval is obtained by integrating the electric power using Euler's Forward Integration method. The trajectories and performance of the experiments are compared with simulation results as shown in Figures 8.6 and 8.7. The black dotted line in Figure 8.7 represents the torque-speed capability boundary. Notice that the direct-axis current is negative for the first half a second of the braking time-interval, indicating that the flux-weakening operation is in effect. Table 8.3 compares the energy recovery ratios of the experiment, which is an average of four trials, and the simulation results. There is good agreement between experiments and simulations for the trajectories and the energy recovery ratios.

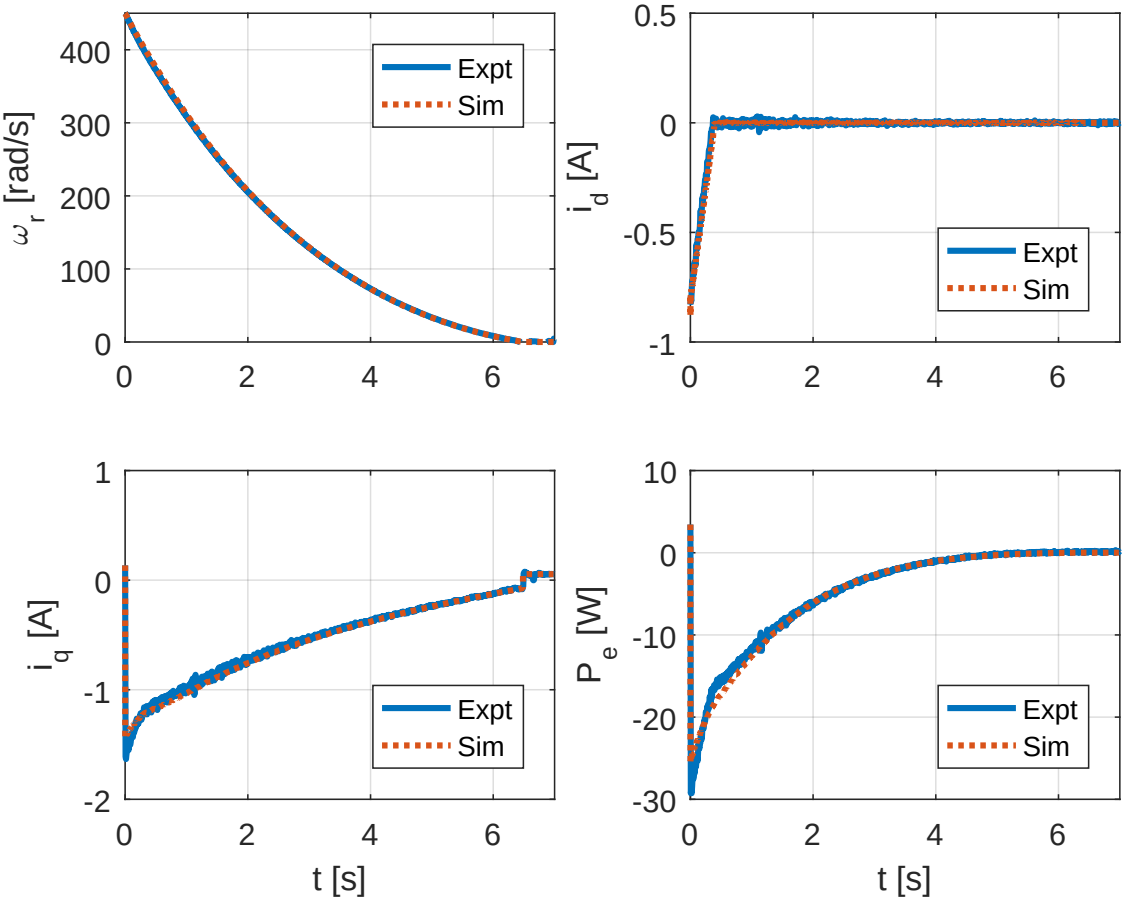

Figure 8.6: Comparison of rotor speed, direct and quadrature axes currents, and electrical power for experiment and simulation implementations of the optimal kinetic energy recovery algorithm using constant-power flux-weakening.

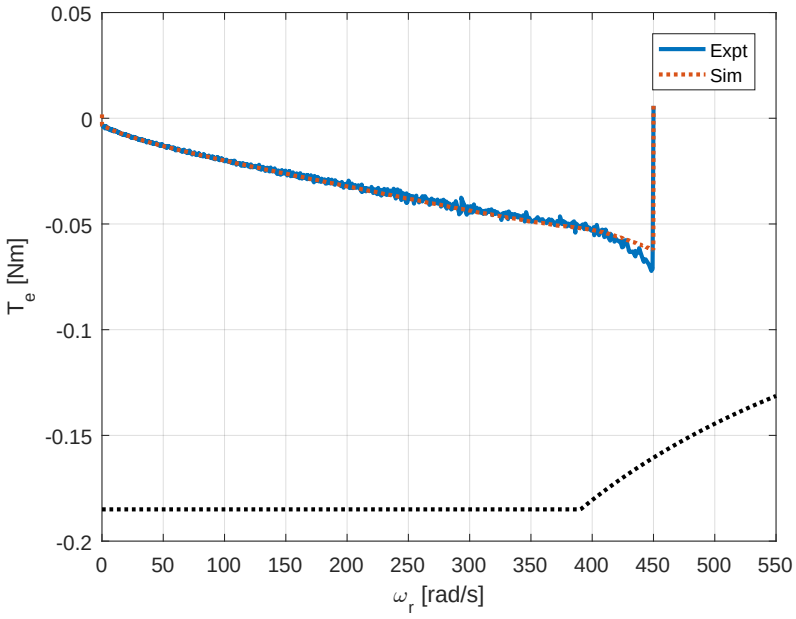

Figure 8.7: Comparison of braking trajectories in the torque-speed plane for experiment and simulation implementations of the optimal kinetic energy recovery algorithm using constant-power flux-weakening.

Table 8.3: Comparison of Simulation and Experiments for the Optimal Braking Controller Under Flux-Weakening

Method	E_{ratio} [%]
Simulation	80.90
Experiment	80.04

8.8 Conclusion

Operating electric machines at high-speeds necessitates implementation of flux-weakening policies due to the presence of voltage and current limit constraints. Therefore, using zero direct-axis current is not a valid option if high-speed operation is desired. This chapter detailed the development, performance, and experiment implementation of the optimal kinetic energy recovery algorithm under flux-weakening operation. The constant-power flux-weakening policy was used to implement flux-weakening. The rotor-speed dependent direct-axis current resulted in a piece-wise non-linear boundary value problem which could not be solved in closed-form. A numerical optimization tool called `bvp4c` was used to solve the non-linear boundary value problem. The performance of the optimal controller was compared with that of a constant-torque braking controller and superiority of the optimal controller was highlighted. The outputs of the `bvp4c` function were then used as lookup tables for implementation in simulations and experiments. The experimental results showed good agreement with the simulation results. Investigating the design of the optimal kinetic energy recovery algorithm using the constant-power flux-weakening policy is a first step in the direction of developing energy recovery algorithms for high-speed operation. Future research in this direction could possibly investigate optimal kinetic energy recovery under more complicated methods of flux weakening such as maximum-torque-per-amp. The complication primarily arises due to the presence of both the torque and rotor speed terms in the expression for the desired direct-axis current for high-speed operation. The resulting two-point boundary-value problem which is lengthy to write down and is piece-wise non-linear can be solved using numerical optimization tools such as the `bvp4c` solver to obtain the optimal rotor speed and torque trajectories.

CHAPTER 9
A VARIABLE-FLUX OPTIMAL KINETIC ENERGY RECOVERY ALGORITHM FOR IPMS IN THE CONSTANT-TORQUE REGION

Interior permanent-magnet synchronous machines (IPMs) have the capability of producing a reluctance torque component that can augment the permanent-magnet torque. This is possible due to the difference between the direct and quadrature axes inductances that produces a reluctance torque that is proportional to the direct-axis current and is expressed as

$$T_{e,\mathrm{rel}} = N\left(L_d - L_q\right) i_d i_q \tag{9.1}$$

As discussed in Chapter 6, there is merit in using a constant non-zero direct-axis current to enhance the rotor flux for IPMs operating in the constant-torque region of the torque-speed plane. This improves the effective back-EMF constant of the machine, thereby reducing the electromechanical loss parameter, $\gamma = \dfrac{B_1 R_e}{K_e^2}$, which improves the controllable energy recovery ratio of the system. This chapter will focus on developing optimal kinetic energy recovery algorithms for IPMs with variable direct-axis stator current under operation in the constant-torque region of the torque-speed capability boundary.

9.1 Maximum Torque Per Ampere

Before developing and solving the optimal control problem for maximum kinetic energy recovery, the classical approach to variable-flux operation in IPMs is discussed first. Assuming ideal sinusoidal permanent-magnet flux, the total electromagnetic torque is the

sum of the permanent-magnet torque and the reluctance torque components

$$T_e = N\left(\Lambda + \left(L_d - L_q\right) i_d\right) i_q \tag{9.2}$$

Since the copper losses are proportional to length of the current vector, the objective of producing a required level of electromagnetic torque can be achieved by using a current vector of minimum length. This policy is called maximum torque per ampere (MTPA) [77]. The length of the current vector is defined as

$$i = \sqrt{i_d^2 + i_q^2}, \quad \Longrightarrow \; i_q = \pm\sqrt{i^2 - i_d^2} \tag{9.3}$$

The resulting electromagnetic torque is

$$T_e = \pm N\left(\Lambda + \left(L_d - L_q\right) i_d\right)\sqrt{i^2 - i_d^2} \tag{9.4}$$

To minimize i for a given T_e is equivalent to maximizing T_e for a given i, resulting in the partial derivative that is set to zero

$$\frac{\partial T_e}{\partial i_d} = \pm N\left(L_d - L_q\right)\sqrt{i^2 - i_d^2} \mp \frac{N\left(\Lambda + \left(L_d - L_q\right) i_d\right)}{\sqrt{i^2 - i_d^2}} i_d = 0 \tag{9.5}$$

The resulting constraint reduces to

$$\left(L_d - L_q\right)\left(i^2 - i_d^2\right) = \left(\Lambda + \left(L_d - L_q\right) i_d\right) i_d \tag{9.6}$$

or equivalently to

$$\left(L_d - L_q\right) i_d^2 + \Lambda i_d - \left(L_d - L_q\right) i_q^2 = 0 \tag{9.7}$$

and application of the quadratic formula leads to

$$i_d = \frac{-\Lambda \pm \sqrt{\Lambda^2 + 4\left(L_d - L_q\right)^2 i_q^2}}{2\left(L_d - L_q\right)} \tag{9.8}$$

If $L_d < L_q$, the positive sign on the square root term results in negative direct-axis current ($i_d \leq 0$) that maximizes the T_e/i factor [79]. The locus of all such points in the (i_d, i_q) plane is plotted below in Figure 9.1 for parameter values corresponding to the Motorsolver IPM as shown in Table 4.3(a). The intersection of this locus with the current limit circle corresponds to the torque maximizing current vector of (4.68). Operation along the MTPA curve allows the user to achieve the requested electromagnetic torque using the shortest length current vector which reduces the stator copper winding losses in the electric machine. The electromagnetic torque corresponding to the MTPA currents is obtained by substituting the value of i_d from (9.8) in (9.13) to obtain

$$T_e = f(i_q, i_q^2) \tag{9.9}$$

which is a non-linear function of q-axis current. A numerical optimization tool, such as Newton's method as discussed in [78], is used to determine values of i_q and corresponding values of i_d using (9.8) that minimizes the length of the current vector for every permissible electromagnetic torque value. The resulting map of dq currents and torque are stored in a lookup table. When the drive requests a certain level of torque in the constant-torque region, current references are selected from the lookup table to produce the requested torque in accordance with MTPA.

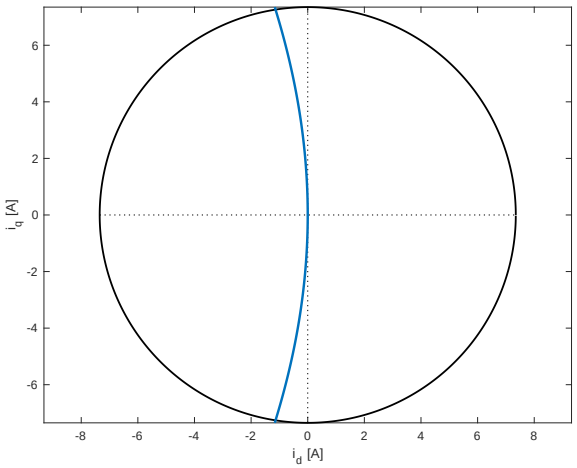

Figure 9.1: The maximum torque per ampere curve for the Motorsolver IPM and the corresponding current limit circle.

9.2 Optimal Kinetic Energy Recovery

The rotor speed dynamics, as described in the previous chapters, satisfies

$$\dot{\omega}_r = \frac{1}{J}\left(T_e^* - T_{\text{load}}\right) \tag{9.10}$$

The mechanical load includes both viscous friction and Coulomb friction components and is described as

$$T_{\text{load}} = B_1\omega_r + B_0\ \text{sgn}\left(\omega_r\right) \tag{9.11}$$

The electrical stator dynamics of an IPM are described using the following differential equations

$$\begin{aligned} L_d\frac{di_d}{dt} &= v_d - R_s i_d + N\omega_r L_q i_q \\ L_q\frac{di_q}{dt} &= v_q - R_s i_q - N\omega_r\left(\Lambda + L_d i_d\right) \end{aligned} \tag{9.12}$$

where v_d and v_q are the direct and quadrature axes voltages. The electromagnetic torque reference, T_e^*, is described in terms of the dq reference frame stator current references, i_d^* and i_q^*, as

$$T_e^* = \left(K + L_e i_d^*\right) i_q^* \tag{9.13}$$

where $K = N\Lambda$ and $L_e = N\left(L_d - L_q\right)$. Substituting the expressions for electromagnetic torque reference and mechanical load into the rotor speed dynamic equation (9.10), results in

$$\dot{\omega}_r = \frac{1}{J}\left(\left(K + L_e i_d^*\right) i_q^* - B_1\omega_r - B_0\,\mathrm{sgn}\left(\omega_r\right)\right) \tag{9.14}$$

The electrical power is

$$P_e = v_d i_d + v_q i_q \tag{9.15}$$

The use of high-bandwidth current control allows approximation of the direct and quadrature axes currents to their respective reference signals, i.e. $i_d \approx i_d^*$ and $i_q \approx i_q^*$. The voltages are approximated as

$$\begin{aligned} v_d &\approx R_s i_d - N\omega_r L_q i_q \\ v_q &\approx R_s i_q + N\omega_r\left(\Lambda + L_d i_d\right) \end{aligned} \tag{9.16}$$

The resulting approximate electrical power reduces to

$$P_e \approx R_s\left(i_d^{*2} + i_q^{*2}\right) + \left(K + L_e i_d^*\right) i_q^* \omega_r \tag{9.17}$$

The objective function that maximizes kinetic energy recovery during the braking time-interval is described from earlier as

$$\text{Minimize } E = \int_0^T P_e \, dt, \; \omega_r(0) = \omega_{r0} \;\text{ and }\; \omega_r(T) = \omega_{rT} \tag{9.18}$$

where ω_{r0} and ω_{rT} are the initial and final rotor speeds, and T is the length of the braking time-interval. According to the theory of optimal control, a Hamiltonian function is described as

$$\begin{aligned} H &= P_e + \chi\dot{\omega}_r \\ &= R_s\left(i_d^{*2} + i_q^{*2}\right) + \left(K + L_e i_d^*\right) i_q^* \omega_r + \frac{\chi}{J}\left(\left(K + L_e i_d^*\right) i_q^* - B_1\omega_r - B_0 \operatorname{sgn}\left(\omega_r\right)\right) \end{aligned} \tag{9.19}$$

If i_d^* and i_q^* are the optimal control variables, then the unconstrained optimality conditions are obtained by setting partial derivatives

$$\begin{aligned} \frac{\partial H}{\partial i_d^*} &= 2R_s i_d^* + \left(\omega_r + \frac{\chi}{J}\right) i_q^* \\ \frac{\partial H}{\partial i_q^*} &= 2R_s i_q^* + \left(K + L_e i_d^*\right)\left(\omega_r + \frac{\chi}{J}\right) \end{aligned} \tag{9.20}$$

equal to zero, which results in non-linear control laws

$$\begin{aligned} i_{d,\text{opt}}^* &= \frac{KL_e\left(\omega_r + \chi J^{-1}\right)^2}{4R_s^2 - L_e^2\left(\omega_r + \chi J^{-1}\right)^2} \\ i_{q,\text{opt}}^* &= -\frac{2KR_s\left(\omega_r + \chi J^{-1}\right)}{4R_s^2 - L_e^2\left(\omega_r + \chi J^{-1}\right)^2} \end{aligned} \tag{9.21}$$

Notice that the substitution of $L_e = 0$, which is the case for SPMs, results in linear control laws

$$\begin{aligned} i^*_{d,\text{opt}} &= 0 \\ i^*_{q,\text{opt}} &= -\frac{K}{2R_s}\left(\omega_r + \chi J^{-1}\right), \end{aligned} \tag{9.22}$$

which is identical to (5.11).

The optimal electromagnetic torque reference is obtained from (9.13) as

$$\begin{aligned} T^*_{e,\text{opt}} &= \left(K + L_e i^*_{d,\text{opt}}\right) i^*_{q,\text{opt}} \\ &= -\frac{8R_s^3 K^2 \left(\omega_r + \chi J^{-1}\right)}{\left(4R_s^2 - L_e^2\left(\omega_r + \chi J^{-1}\right)^2\right)^2} \end{aligned} \tag{9.23}$$

The optimal state and costate dynamics are obtained according to the following partial derivatives

$$\begin{aligned} \dot{\omega}_{r,\text{opt}} &= \frac{\partial H}{\partial \chi} = \frac{1}{J}\left(T^*_{e,\text{opt}} - B_1\omega_{r,\text{opt}} - B_0 \text{ sgn } \left(\omega_{r,\text{opt}}\right)\right) \\ \dot{\chi}_{\text{opt}} &= -\frac{\partial H}{\partial \omega_r} = -T^*_{e,\text{opt}} + \frac{B_1}{J}\chi_{\text{opt}} \end{aligned} \tag{9.24}$$

A non-linear two-point boundary value problem can be formulated as

$$\begin{aligned} \dot{\omega}_{r,\text{opt}} &= \frac{1}{J}\left(T^*_{e,\text{opt}} - B_1\omega_{r,\text{opt}} - B_0 \text{ sgn}\left(\omega_{r,\text{opt}}\right)\right) \\ \dot{\chi}_{\text{opt}} &= -T^*_{e,\text{opt}} + \frac{B_1}{J}\chi_{\text{opt}} \end{aligned} \tag{9.25}$$

subject to

$$\omega_{r,\text{opt}}(0) = \omega_{r0} \text{ and } \omega_{r,\text{opt}}(T) = \omega_{rT} \tag{9.26}$$

The non-linear nature of the above dynamic equations is due to the terms in the denominator of the optimal torque reference in (9.23).

9.3 Numerical Optimization

The non-linear nature of the two-point boundary value problem in (9.25) cannot be solved easily in closed-form. Therefore, numerical optimization tools, such as `bvp4c` in Matlab [74, 75], are used to obtain solutions to the two-point boundary value problem in (9.25). The inputs to the `bvp4c` are the initial rotor speed (ω_{r0}), final rotor speed (ω_{rT}), and the braking time-interval length (T), along with the system parameters. The parameters of the Motorsolver IPM electromechanical system from Table 4.3 are used to obtain the solutions. The output of the `bvp4c` solver is a discrete time grid and the time-dependent optimal trajectories of the state and costate variables. The optimal current references, $i^*_{d,\text{opt}}$ and $i^*_{q,\text{opt}}$, are obtained from the optimal state and costate trajectories using (9.21). Figure 9.2 shows the results of numerical optimization for $\omega_{r0} = 120$ rad/s, $\omega_{rT} = 0$ rad/s, and $T = 0.6$ seconds. The original optimal grid consists of 46 discrete values and the solution is linearly interpolated to produce the trajectories shown in Figure 9.2. Notice that the optimal direct-axis current is a time-varying function of time and is zero at $t = T$.

Superimposing the optimal current trajectories obtained from numerical optimization onto the MTPA trajectory in Figure 9.1, results in an exact match between the two loci as shown in Figure 9.3. Therefore, the solution of the optimal kinetic energy recovery algorithm automatically implements MTPA without using any of the equations that were developed for classical MTPA implementation in Section 9.1. It is known that the MTPA algorithm produces loss minimizing current references for a permissible torque reference. To achieve the objective of maximizing kinetic energy recovery, the optimal algorithm must also minimize stator copper winding losses, which was the basis for MTPA. The result is that the optimal kinetic energy recovery algorithm has "re-derived" the MTPA algorithm as a part of the overall objective of recovering maximum kinetic energy.

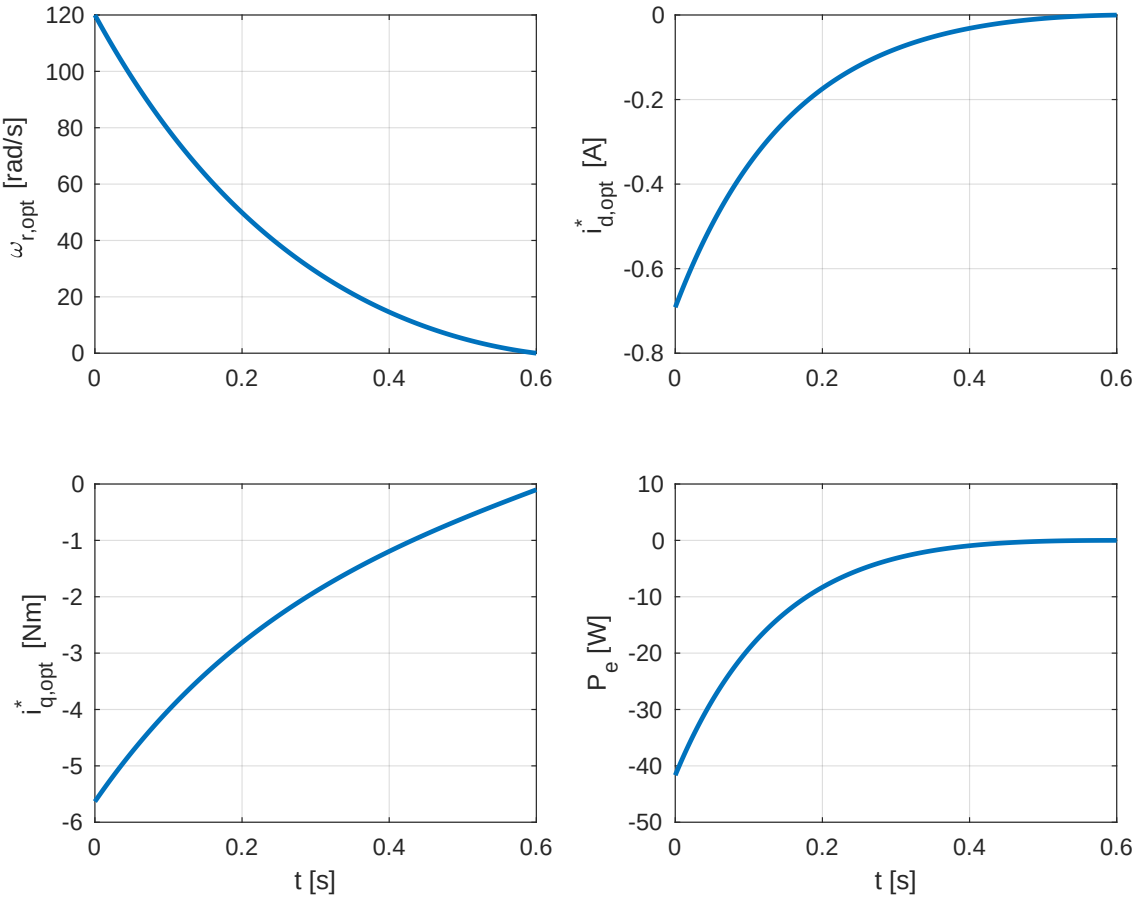

Figure 9.2: Optimal trajectories of rotor speed, direct-axis current, quadrature-axis current, and electrical power for $\omega_{r0} = 120$ rad/s, $\omega_{rT} = 0$ rad/s, and $T = 0.6$ s for the idealized Motorsolver IPM using `bvp4c`.

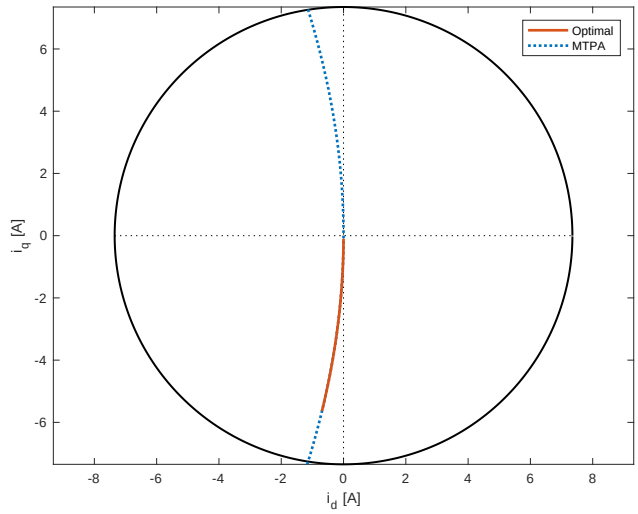

Figure 9.3: Optimal current trajectories superimposed on the MTPA curve.

9.4 Experimental Results

The experiments are performed using the Motorsolver IPM system shown in Figure 4.7 with the DRV-8312 Motor Control Kit from Texas Instruments and a battery pack with terminal voltage equal to 19.6 V as the power source. The optimal braking trajectory is implemented in a manner similar to the methods discussed in Section 5.5.4 that uses closed-loop feedback speed control along with a feedforward torque signal as shown in Figure 5.9. The optimal electromagnetic torque reference is calculated from the optimal dq reference frame currents using (9.23). Once the total torque reference that includes feedback and feedforward torques is calculated, lookup tables are used to determine the dq reference frame current references to implement MTPA, as discussed previously. The optimal rotor speed trajectory that is obtained as a result of numerical optimization is used as a lookup table for the speed reference command inside the microcontroller. The optimal torque reference trajectory is also included as lookup table. The switching frequency is 30 kHz, the current-controller update frequency is 10 kHz, speed-controller update frequency is 5 kHz. The current-controller bandwidth is 2500 rad/s and that of the speed-controller is 2 rad/s. The rotor is made to spin at an initial speed of 120 rad/s and once the braking command is issued, the rotor must come to a complete stop in 0.6 seconds while recovering maximum kinetic energy. The energy recovered during the braking time-interval is measured and logged for multiple experimental trials. The comparison of simulation and experimental responses for rotor speed, direct and quadrature axes currents, and electrical power is shown in Figure 9.4. As discussed previously, the significant cogging torque effect in this system is evident from the ripples in the rotor speed trajectory at low speed. The Motorsolver IPM machine also has non-sinusoidal back-EMF which results in current ripples at high-speeds as seen in both the simulation and experimental trajectories of direct and quadrature axes currents. The comparison of simulation and experimental braking trajectories in the torque-plane is shown in Figure 9.5. The non-sinusoidal back-EMF

also produces torque harmonics as seen from the braking trajectories in the torque-speed plane as shown in Figure 9.5(b). There is good agreement between simulation and experiments. The comparison of energy recovery performance of the simulation and experiments is shown in Table 9.1. The table also lists simulation and experimental energy recovery comparisons using $i_d^* = 0$ as discussed in Section 6.5.2. The optimal algorithm that is developed in this chapter results in operation similar to MTPA and as such recovers slightly more energy than its counterpart that uses zero direct-axis current. This trend is confirmed in both simulation and experiments which show good agreement with each other. The small mismatch in the energy recovery of simulation and experiments is explained due to electric machine core-iron losses and power converter losses that are not included in the model used for simulations.

Table 9.1: Comparison of Energy Recovery Ratios for Simulations and Experiments for the Motorsolver IPM System with $\omega_{r0} = 120$ rad/s, $\rho = 0$, and $T = 0.6$ s

Method	Simulation	Experiment
$i_d^* = 0$	72.41%	71.39%
$i_d^* = i_{d,\text{opt}}^*$	72.89%	71.81%

9.5 Conclusion

The development of an optimal kinetic energy recovery algorithm for an IPM operating under variable-flux in the constant-torque region was studied in this chapter. Application of the optimality conditions resulted in a non-linear two-point boundary value problem. A numerical optimization tool called `bvp4c` was used to solve the non-linear system and the resulting optimal trajectories were stored as lookup tables. The dq reference frame current trajectories obtained from the optimal solution were compared with the classical MTPA algorithm for IPMs and it is shown that the optimal solution "re-derived" the MTPA algorithm. Simulation and experiments were conducted and the results showed good agreement

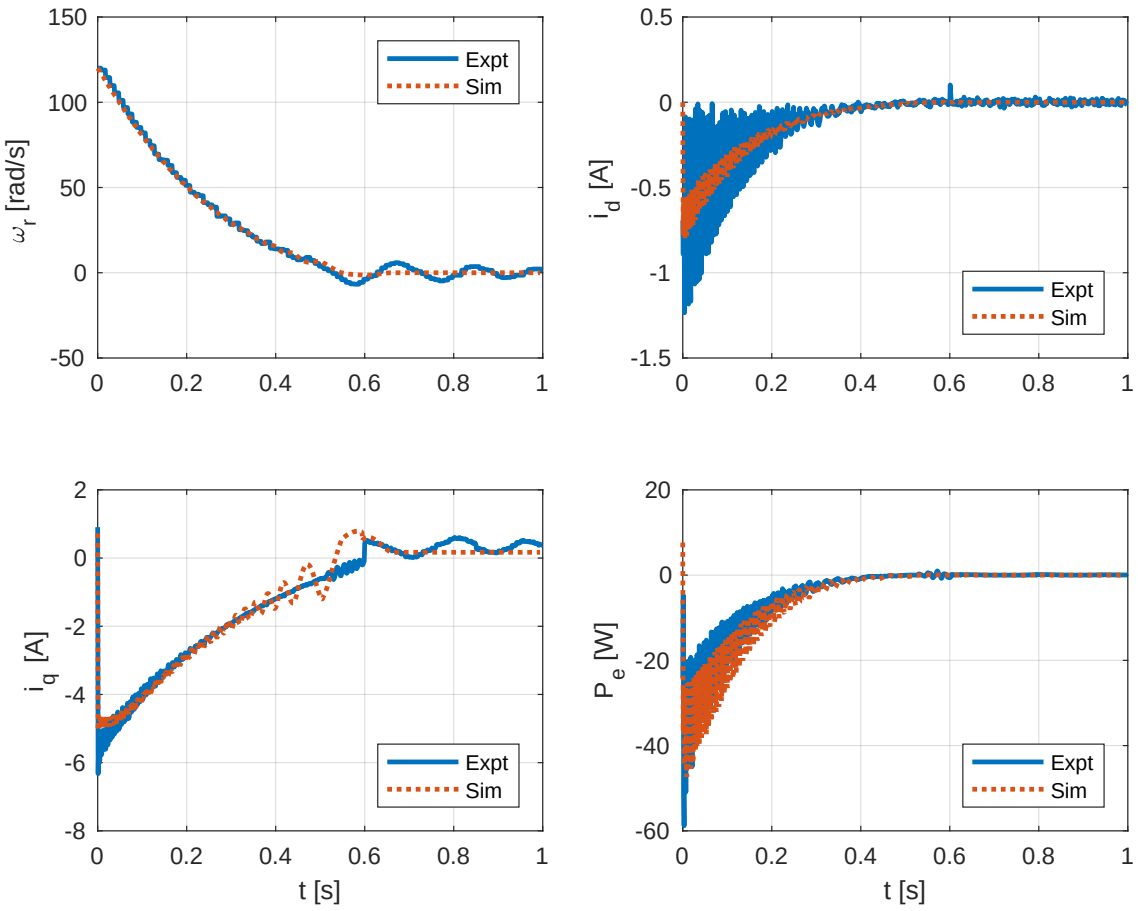

Figure 9.4: Comparison of experiment and simulation implementations using the Motorsolver IPM system for $\omega_{r0} = 120$ rad/s, $\rho = 0$, and $T = 0.6$ s based on numerical optimization.

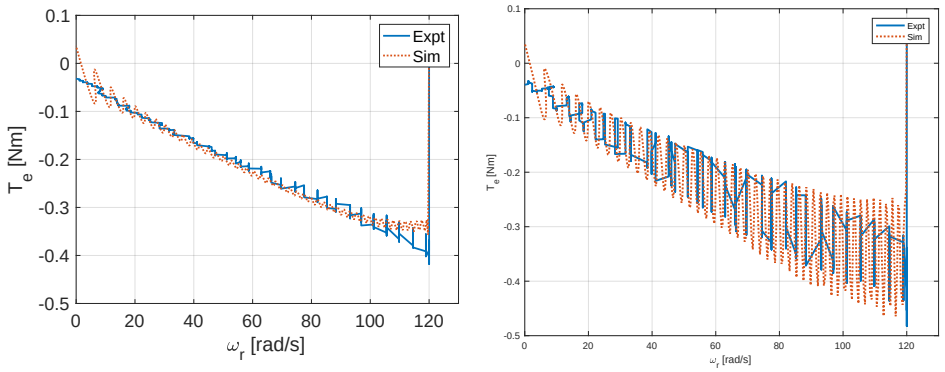

(a) Average torque (b) Including torque-harmonics

Figure 9.5: Comparison of braking trajectories in the torque-speed plane for experiment and simulation implementations using the Motorsolver IPM system for $\omega_{r0} = 120$ rad/s, $\rho = 0$, and $T = 0.6$ s based on numerical optimization.

with each other. The variable-flux optimal energy recovery algorithm performed slightly better than the constant-flux optimal control algorithm that was developed in Chapter 6. This difference in energy recovery will be significant in IPMs that have higher saliency ratios or those that can operate with larger currents or both.

CHAPTER 10
CONCLUSIONS

The world is using an enormous amount of electricity and electric machines account for over 28% of the usage. There are over 300 million electric machines installed worldwide and this number is growing every year. Electric machines are used to accelerate and decelerate mechanical loads in a variety of applications. During the acceleration event, electrical energy is transferred from the electric power source to the mechanical load in the form of kinetic energy. In applications that involve frequent starting and stopping and those that require frequent changes in operating speed, there exists an opportunity to recover a significant portion of the kinetic energy and send it back to the electric power source for storage. Therefore the topic of kinetic energy recovery is important to improve the overall efficiency of the start-stop or variable-speed application. Several researchers have studied this topic previously, however, significant gaps remain that are addressed by this research.

10.1 Contributions of this Research

This research set out to answer a set of key questions such as investigating the possibility of recovering kinetic energy during the braking process, determining the limits of kinetic energy recovery, deducing the factors that influence energy recovery, and so on. This research has addressed all of these open questions by studying the process of kinetic energy recovery in great detail by using a physics-based analysis method. The primary contribution of this research was to provide control engineers with a comprehensive design method that includes development, analysis, and implementation of an optimal kinetic energy algorithm for maximum energy recovery during the braking event. The internal behavior of the system is considered during the development of the algorithms, thereby exposing the role of design parameters in the kinetic energy recovery process. The feedback

interconnections between the electric machine and its power converter are explicitly considered, clearly revealing the influence of the current feedback gains on the overall system. The influence of the electromechanical system parameters on the limits of kinetic energy recovery is clearly illustrated using closed-form expressions wherever possible.

This research illustrates the development of a universal optimal kinetic energy recovery algorithm to include three machine types: surface permanent-magnet synchronous machines, interior permanent-magnet synchronous machines, and induction machines under constant-flux operation. By doing so, this research targets the most commonly used machine types in the electric machine market and removes the need for specialized kinetic energy recovery algorithms for each individual type of electric machine. The optimal braking algorithm is implemented using a standard feedback speed (or position) controller, with a small modification to include a feedforward signal. The performance of the universal optimal kinetic energy recovery algorithm is verified using simulations and experiments.

The performance of the optimal kinetic energy recovery algorithm is compared with that of constant-torque braking. The shortcomings of maximum torque braking, that is suggested by several authors as a method to recover maximum energy, is exposed by developing closed-form expressions and comparing its performance to optimal braking. The performance of the optimal controller is also compared with a maximum power control (based on static optimization as discussed in Appendix A) to provide contrast between the two types of controllers (static optimization versus optimal control). It was found that the optimal controller outperforms the maximum power controller. Braking problems that include both stopping and slowing down to a non-zero speed are studied in this research.

For the first time in published literature on this topic, non-linear loads such as Coulomb friction and aerodynamic drag (Appendix B) are considered in the development of optimal kinetic energy recovery algorithms. This extends the application of the algorithms developed in this research to include the braking operation of electric vehicles and trains. Developing closed-form expressions to evaluate the performance of kinetic energy recovery

is also another unique contribution of this research. The closed-form expressions provide control engineers with a framework to study the trade-off between energy recovery and braking time. Another unique contribution is the development of closed-form or numerical methods to help control engineers determine the optimal length of the braking time-interval for user-defined constraints on initial and final speeds.

The universal optimal kinetic energy recovery algorithm is extended to include constraints on rotor position that are imposed in applications such as robotic manufacturing, elevator drives, etc. Numerical methods are used to solve the two-point boundary value problem and the performance of the algorithm was verified using simulations and experiments. Another unique contribution of this research is to study the optimal kinetic energy recovery process for high-speed operation of electric machines under the influence of flux-weakening. The formulation of the non-linear optimal control problem is illustrated and the optimal control solution is obtained using numerical methods. The veracity of the solution is determined using simulations and experiments. Finally, the variable-flux operation of interior permanent-magnet synchronous machines in accordance with maximum-torque-per-amp (MTPA) is also considered in the development of optimal kinetic energy recovery algorithms for the first time in published literature. The non-linear optimal control problem is formulated and a numerical method is used to obtain the optimal control solution. It was shown that the optimal kinetic energy recovery algorithm "re-derived" the MTPA algorithm and the solution was verified using simulations and experiments.

10.2 Topics for Future Research

However, there are still some topics that remain to be addressed. This research considered the unconstrained version of optimal control for the development of the energy recovery algorithm. If the optimal control solution requires the machine to operate beyond its capability boundary, the constraints on current and voltage will not permit such operation. Methods based on Pontryagin's maximum (or minimum) principle can be considered

to tackle such problems [5, 80] with the current and voltage limits being part of the optimal control problem formulation.

This research primarily focuses on mechanical loads that include viscous and Coulomb friction, with experimental results being shown only for these two types of mechanical loading. However, applications such as electric vehicles and electric trains experience significant aerodynamic resistance. A framework to develop the two-point boundary value problem for mechanical loads that includes aerodynamic drag is shown in Appendix B. Future research can focus on developing optimal kinetic energy recovery algorithms based on this extended framework and testing the algorithms for applications such as electric vehicles and trains.

Induction machines, like permanent-magnet machines, can operate under the policy of maximum-torque-per-amp and minimum copper loss control. However, these policies require variable rotor flux that is a function of the requested electromagnetic torque. This research has focused only on the constant-flux operation of induction machines for the development of optimal kinetic energy recovery algorithms. Preliminary research to include MTPA for induction machines was studied as part of this research, however, only mechanical dynamics were considered and the electrical dynamics were assumed to be at quasi-steady-state. It was observed that the rotor flux did not exhibit quasi-steady-state behavior under variable-flux braking. This is due to the fact that the rotor flux for induction machines has a time constant of L_r/R_r and the settling time of the rotor flux cannot be influenced by the user in any way. Therefore, future work can focus on including the rotor flux dynamics in the optimal kinetic energy recovery problem formulation. Topics such as minimum fuel control and singular arcs [5, 80] can come in handy when dealing with such problems.

For high-speed operation of electric machines, this research considered only the constant-power based flux-weakening policy. Algorithms such as MTPA can be extended to the flux-weakening region as well. However, preliminary research into the inclusion of MTPA-

based flux-weakening in the optimal kinetic energy recovery algorithm framework revealed that the problem formulation is complicated. As shown in Chapter 8, high-speed optimal kinetic energy recovery requires the solution of a piecewise Hamiltonian function. For the simpler case that uses the constant-power flux-weakening policy, the switching logic between the two components of the piecewise Hamiltonian function depended only on the state variable. However, for the complicated problem that uses the MTPA-based flux-weakening policy, the switching logic between the two components of the piecewise Hamiltonian function depended on both the state variable and the optimal control variable. Future work can focus on carefully formulating and solving this complicated version of the problem.

This research used a numerical optimization tool in Matlab called `bvp4c` to solve two-point boundary value problems that were non-linear in nature. The solution was obtained offline and the results were uploaded to the microcontroller in the form of lookup tables. Future research can focus on solving the two-point boundary value problem directly in embedded hardware. This would streamline the process of implementing the optimal control solution when the user-defined parameters change.

This research developed and solved optimal control problems with the objective of maximizing kinetic energy recovery. The solutions were tested using mechanical loads using bench-top experimental setups as a "proof of concept." Future research can deploy these algorithms in specific real-world applications such as washing machine drives, elevator drives, and electric vehicles and trains, and evaluate the performance in target applications.

Appendices

APPENDIX A

MAXIMUM POWER REGENERATIVE BRAKING CONTROL

Maximum power braking is suggested as another method of applying braking torque in [19, 20, 22, 59, 60, 61]. This section discusses the development of the maximum power braking control algorithm and compares its performance with the optimal kinetic energy recovery algorithm.

Consider the rotor speed dynamics equation with only viscous friction mechanical loading

$$\dot{\omega}_r = \frac{1}{J}\left(T_e^* - B_1\omega_r\right) \tag{A.1}$$

Under quasi-steady-state assumptions, the electric power expression for an SPM from (5.5) is

$$P_e \approx R_s\left(i_d^{*2} + i_q^{*2}\right) + Ki_q^*\omega_r \tag{A.2}$$

where R_s is the stator winding resistance and K is the back-EMF constant, and the electromagnetic torque reference is expressed as

$$T_e^* = Ki_q^* \tag{A.3}$$

in terms of the current reference commands i_d^* and i_q^*. Assuming that current magnitude constraints are not active, the current commands for maximum power control are deter-

mined by setting partial derivatives

$$\begin{aligned} \frac{\partial P_e}{\partial i_d^*} &= 2R_s i_d^* \\ \frac{\partial P_e}{\partial i_q^*} &= 2R_s i_q^* + K\omega_r \end{aligned} \tag{A.4}$$

equal to zero, yielding

$$\begin{aligned} i_{d,\mathrm{mpc}}^* &= 0 \\ i_{q,\mathrm{mpc}}^* &= -\frac{K}{2R_s}\omega_r \end{aligned} \tag{A.5}$$

The rotor dynamics under these conditions satisfy

$$\dot{\omega}_{r,\mathrm{mpc}} = -\frac{K^2}{2JR_s}\left(1+2\gamma\right)\omega_{r,\mathrm{mpc}} \tag{A.6}$$

where $\gamma = \dfrac{B_1 R_s}{K^2}$ is the dimensionless electromechanical loss parameter. With an initial condition of $\omega_{r,\mathrm{mpc}}(0) = \omega_{r0}$, the speed trajectory is obtained as

$$\omega_{r,\mathrm{mpc}} = \omega_{r0} e^{-\alpha t} \tag{A.7}$$

where $\alpha = \dfrac{K^2}{2JR_s}\left(1+2\gamma\right)$. The electrical energy is

$$E = \int_0^T P_e \, dt = -\left(\frac{1}{2}J\omega_{r0}^2\right)\frac{1}{2+4\gamma}\left(1-e^{-2\alpha T}\right) \tag{A.8}$$

For the infinite time-horizon problem, $T \to \infty$ results in the energy ratio

$$E_{\mathrm{rat,mpc}} = \frac{E}{E_{\mathrm{avail}}} = \frac{1}{2+4\gamma} \tag{A.9}$$

where $E_{\mathrm{avail}} = \frac{1}{2}J\omega_{r0}^2$.

The maximum value of the energy ratio is $E_{\mathrm{rat}} = \dfrac{1}{2}$ with the substitution of $\gamma = 0$,

and the minimum value of the energy ratio is $E_{\text{rat}} = 0$ with the substitution of $\gamma \to \infty$. In contrast, the energy recovery ratio for the same problem using optimal control is

$$E_{\text{rat,opt}} = 1 + 2\gamma - 2\sqrt{\gamma(1+\gamma)} \tag{A.10}$$

which has maximum and minimum values of 1 and 0 for values of $\gamma = 0$ and $\gamma \to \infty$ respectively. It can be shown that for any non-zero value of γ,

$$E_{\text{rat,opt}} > E_{\text{rat,mpc}} \tag{A.11}$$

APPENDIX B

AN OPTIMAL KINETIC ENERGY RECOVERY ALGORITHM WITH AERODYNAMIC DRAG LOADING

Applications such as electric vehicle and trains experience significant aerodynamic loading especially at high speeds. In this section, the optimal kinetic energy recovery algorithm framework that was developed earlier is extended to include the influence of aerodynamics loading.

Consider the rotor speed dynamic equation that includes viscous friction, Coulomb friction, and aerodynamic drag loading

$$\dot{\omega}_r = \frac{1}{J}\left(T_e^* - B_1\omega_r - B_0\ \mathrm{sgn}(\omega_r) - B_2\omega_r^2\right) \tag{B.1}$$

For an electromechanical system operating under constant-flux, the controllable electric power is

$$P_c = T_e^*\omega_r + \frac{R}{K_r^2}T_e^{*2} \tag{B.2}$$

and the associated electrical energy is

$$E = \int_0^T P_c\ dt \tag{B.3}$$

The Hamiltonian function is described as

$$\begin{aligned} H &= P_c + \chi\dot{\omega}_r \\ &= T_e^*\omega_r + \frac{RT_e^{*2}}{K_r^2} + \frac{\chi}{J}\left(T_e^* - B_1\omega_r - B_0\ \mathrm{sgn}(\omega_r) - B_2\omega_r^2\right) \end{aligned} \tag{B.4}$$

The optimal electromagnetic torque reference signal can now be calculated by setting the following partial derivative

$$\frac{\partial H}{\partial T_e^*} = \omega_r + \frac{2R}{K_r^2} T_e^* + \frac{\chi}{J} \tag{B.5}$$

equal to zero, resulting in

$$T_{e,\mathrm{opt}}^* = -\frac{K_r^2}{2R}\left(\omega_{r,\mathrm{opt}} + \frac{\chi_{\mathrm{opt}}}{J}\right) \tag{B.6}$$

The state and costate dynamics can be derived in terms of the state, costate, and control variables by taking the partial derivatives

$$\begin{aligned} \dot{\omega}_{r,\mathrm{opt}} &= \frac{\partial H}{\partial \chi} = \frac{1}{J}\left(T_{e,\mathrm{opt}}^* - B_1 \omega_{r,\mathrm{opt}} - B_0 \operatorname{sgn}(\omega_{r,\mathrm{opt}})\right) \\ \dot{\chi}_{\mathrm{opt}} &= -\frac{\partial H}{\partial \omega_r} = -T_{e,\mathrm{opt}}^* + \frac{B_1}{J}\chi_{\mathrm{opt}} + \frac{2B_0}{J}\delta(\omega_{r,\mathrm{opt}})\chi_{\mathrm{opt}} + 2B_2 \omega_{r,\mathrm{opt}} \chi_{\mathrm{opt}} \end{aligned} \tag{B.7}$$

The above expression constitutes a two-point boundary value problem with initial and final conditions $\omega_{r,\mathrm{opt}}(0) = \omega_{r0}$ and $\omega_{r,\mathrm{opt}}(T) = \omega_{rT}$ respectively.

REFERENCES

[1] *Key World Energy Statistics*, International Energy Agency, 2015.

[2] *Annual Energy Outlook 2015*, U.S. Energy Information Administration, April 2015.

[3] *Energy Efficiency Technologies: Overview Report*, World Energy Council, March 2014.

[4] *Energy Savings Potential and Opportunities for High-Efficiency Electric Motors in Residential and Commercial Equipment*, Office of Energy Efficiency and Renewable Energy, U.S. Department of Energy, December 2013.

[5] D. KIRK, *Optimal Control Theory—An Introduction*, Prentice Hall, 1971.

[6] R. BELLMAN, *Dynamic Programming*, Princeton University Press, 1957.

[7] *Gen4 Size 8 AC Motor Controller Datasheet*, SEVCON,
Available: http://www.sevcon.com/media/2462/Gen4 Size 8 Aug 2013 web.pdf.

[8] P. SPICHARTZ, L. BUBMANN and C. SOURKOUNIS, "Comparison of recuperation strategies for electric vehicles regarding energy efficiency," *Proceedings of the Annual IEEE Industrial Electronics Society Conference*, pp. 2984 – 2990 , November 2014.

[9] F. WANG, X. YIN, H. LUO and Y. HUANG, "A series regenerative braking control strategy based on hybrid-power," *Proceedings of the International Conference on Computer Distributed Control and Intelligent Environmental Monitoring (CDCIEM)*, pp. 65–69, March 2012.

[10] X. NIAN, F. PENG and H. ZHANG, "Regenerative braking system of electric vehicle driven by brushless DC motor," *IEEE Transactions on Industrial Electronics*, 61(10), pp. 5798–5808, October 2014.

[11] J. GUO, J. WANG and B. CAO, "Regenerative braking strategy for electric vehicles," *Proceedings of the IEEE Intelligent Vehicles Symposium*, pp. 864–868, June 2009.

[12] J. GOU, W. LIFANG, L. CHENGLIN, Z. JUNZHI and Y. XIAOWEI, "The coordinated control of motor regenerative braking torques defined by accelerator pedal and brake pedal of electric vehicle," *Proceedings of the IEEE Vehicle Power and Propulsion Conference (VPPC)*, pp. 119–123, October 2012.

[13] D. PENG, J. ZHANG and C. YIN, "Regenerative braking control system improvement for parallel hybrid electric vehicle," *Proceedings of the International Technology and Innovation Conference (ITIC)*, pp. 1902–1908, November 2006.

[14] L. CAI and X. ZHANG, "Study on the control strategy of hybrid electric vehicle regenerative braking," *Proceedings of the International Conference on Electronic and Mechanical Engineering and Information Technology (EMEIT)*, pp. 253–256, August 2011.

[15] M. PAREDES, J. POMILIO and A. SANTOS, "Combined regenerative and mechanical braking in electric vehicle," *Proceedings of the Brazilian Power Electronics Conference (COBEP)*, pp. 935–941, October 2013.

[16] D. CROMBEZ and J. CZUBAY, "Vehicle and method for controlling regenerative braking," US Patent 8,066,339 B2, November 2011.

[17] M. ZHOU, Z. GAO and H. ZHANG, "Research on regenerative braking control strategy of hybrid electric vehicle," *Proceedings of the International Forum on Strategic Technology (IFOST)*, pp. 300–303, August 2011.

[18] B. LIANG and W. LIN, "Optimal regenerative torque control to maximize energy recapture of electric vehicles," *Proceedings of the World Automation Congress*, pp. 1 – 6 , September 2010.

[19] A. S. MURTHY, "Analysis of Regenerative Braking of Electric Machines," M.S. thesis, Georgia Institute of Technology, Atlanta, GA, 2013.

[20] A. S. MURTHY and D. G. TAYLOR, "Regenerative braking of battery powered converter controlled PM synchronous machines," *Proceedings of IEEE Transportation Electrification Conference and Expo*, Detroit, pp. 1–6, June 2013.

[21] A. S. MURTHY, D. P. MAGEE and D. G. TAYLOR, "Regenerative braking capability of converter-controlled induction machines," *Proceedings of IEEE Transportation Electrification Conference and Expo*, Detroit, pp. 1–6, June 2015.

[22] A. S. MURTHY, D. P. MAGEE and D. G. TAYLOR, "Vehicle braking strategies based on regenerative braking boundaries of electric machines," *Proceedings of IEEE Transportation Electrification Conference and Expo*, Detroit, pp. 1–6, June 2015.

[23] C. JIAXIN and CAIHONG, "The research of energy regeneration system and its reliability in electric vehicles," *Proceedings of the International Conference on Power Electronics and Drive Systems*, pp. 864 – 867 , November 2003.

[24] G. LUO, Z. CHEN, Y. DENG, Y. DENG, M. DOU and W. LIU, "Research on braking of battery-supplied interior permanent magnet motor driving system," *Proceedings of the Vehicle Power and Propulsion Conference*, pp. 270 – 274 , September 2009.

[25] L. HUA, Z. MENG-CHUN, Z. JIAN, X. DA and L. HAI, "Study on regenerative brake method of hybrid electric drive system of armored vehicle," *Proceedings of the International Conference on Instrumentation, Measurement, Computer, Communication and Control*, pp. 970 – 973 , October 2011.

[26] L. CHEN, R. DAVIS, S. STELLA, T. TESCH and A. FISCHER-ANTZE, "Improved control techniques for IPM motor drives on vehicle application," *Proceedings of the Annual Industry Applications Conference*, pp. 2051–2056, October 2002.

[27] D. SHIN, S. LEE, S. SONG, H. KIM andY. LIM, "Regenerative energy control of electric vehicles applied to a dual power system," *Proceedings of the IEEE Vehicle Power and Propulsion Conference*, pp. 441–447, October 2012.

[28] S. MORIMOTO, Y. TONG, Y. TAKEDA and T. HIRASA, "Loss minimization control of permanent magnet synchronous motor drives," *IEEE Transactions on Industrial Electronics*, pp. 511–517, October 1994.

[29] A. MUKHITDINOV, S. RUZIMOV and S. ESHKABILOV, "Optimal control strategies for CVT of the HEV during a regenerative process," *Proceedings of the IEEE Conference on Electric and Hybrid Electric Vehicles*, pp. 1 – 12, December 2006.

[30] L. YUTONG, Z. JUNZHI, L. CHEN, K. DECONG and H. CHENGKUN, "Research of regenerative braking system for electrified buses equipped with a brake resistor," *Proceedings of the Vehicle Power and Propulsion Conference*, pp. 1 – 5 , October 2013.

[31] A. MAHAPATRA and S. GOPALAKRISHNA, "Regenerative braking in induction motor drives in applications to electric vehicles," *Proceedings of the IEEE Students' Electrical, Electronics and Computer Science Conference*, pp. 1 – 5 , March 2014.

[32] M. ALNAJJAR and D. GERLING, "Minimization of energy losses in the traction drive of HEV using optimized adaptive control," *Proceedings of the Vehicle Power and Propulsion Conference*, pp. 1 – 6 , October 2014.

[33] U. SCHAIBLE and B. SZABADOS, "A torque controlled high speed flywheel energy storage system for peak power transfer in electric vehicles," *Proceedings of the Industry Applications Society Annual Meeting*, pp. 435 – 442 , October 1994.

[34] M. DAOUD, A. ABDEL-KHALIK, A. ELSEROUGI, S. AHMED and A. MASSOUD, "DC bus control of an advanced flywheel energy storage kinetic traction system for electrified railway industry," *Proceedings of the Annual Conference of the IEEE Industrial Electronics Society*, pp. 6596–6601, November 2013.

[35] M. DOMINGUEZ, A. FERNANDEZ-CARDADOR, A. CUCALA and R. PECHARROMAN, "Energy savings in metropolitan railway substations through regenerative energy recovery and optimal design of ATO speed profiles," *IEEE Transactions on Automation Science and Engineering*, vol. 9(3), pp. 496–504, July 2012.

[36] S. GUPTA, L. PAVEL and J. TOBIN, "An optimization model to utilize regenerative braking energy in a railway network," *Proceedings of the American Control Conference*, pp. 5919–5924, July 2015.

[37] J. QU, X. FENG and Q. WANG, "Real-time trajectory planning for rail transit train considering regenerative energy," *Proceedings of the IEEE International Conference on Intelligent Transportation Systems*, pp. 2738–2742, October 2014.

[38] B. PENG and N. CHEN, "Energy saving strategies in mass rapid transit systems," *Proceedings of the International Conference on Connected Vehicles and Expo*, pp. 272–277, November 2014.

[39] S. LU, P. WESTON and N. ZHAO, "Maximise the regenerative braking energy using linear programming," *Proceedings of the IEEE International Conference on Intelligent Transportation Systems*, Qingdao, pp. 2499–2504, October 2014.

[40] S. LU, P. WESTON, S. HILLMANSEN, H. B. GOOI and C. ROBERTS, "Increasing the regenerative braking energy for railway vehicles," *IEEE Transactions on Intelligent Transportation Systems*, vol. 17(1), pp. 2506–2515, December 2014.

[41] H. MOGHBELI, M. ZAREI andS. MIRHOSEINI, "Transient and steady states analysis of traction motor drive with regenerative braking and using modified direct torque control (SVM-DTC) ," *Proceedings of the Power Electronics, Drives Systems & Technologies Conference* , pp. 615–620, February 2015.

[42] V. BELDJAJEV, T. LEHTLA and H. MOLDER, "Influence of regenerative braking to power characteristics of a gantry crane," *Proceedings of the Electric Power Quality and Supply Reliability Conference*, pp. 73–78, June 2010.

[43] K. INOUE, K. OGATA and T. KATO, "A control method of a regenerative power storage system for electric machinery," *Proceedings of the IEEE Power Electronics Specialists Conference*, pp. 1–5, June 2006.

[44] K. INOUE, K. OGATA and T. KATO, "A study on an optimal torque for power regeneration of an induction motor," *Proceedings of the IEEE Power Electronics Specialists Conference*, pp. 2108–2112, June 2007.

[45] K. INOUE, K. OGATA and T. KATO, "An effcient induction motor drive method with a regenerative power storage system driven by an optimal torque," *Proceedings of the IEEE Power Electronics Specialists Conference*, pp. 359–364, June 2008.

[46] K. INOUE, M. MINAMIYAMA and T. KATO, "A design methodology of an optimal torque minimizing energy loss under torque limit for an induction motor," *Proceedings of the IEEE Energy Conversion Congress and Exposition*, pp. 163–167, September 2009.

[47] K. INOUE, Y. TERANISHI, M. MINAMIYAMA and T. KATO, "Electric energy comparison of an induction motor driven by optimal torques for various operation time periods," *Proceedings of the International Power Electronics Conference*, pp. 2477–2481, June 2010.

[48] K. INOUE, N. OKADA, H. KIYOSE and T. KATO, "Numerical design methodology of optimal trajectories for efficient induction motor drive based on a loss map," *Proceedings of the IEEE Energy Conversion Congress and Exposition*, pp. 3154–3158, September 2013.

[49] N. SHIRAKI and K. KONDO, "Study on maximization method of output density for an induction motor," *Proceedings of the IEEE International Conference on Intelligent Transportation Systems*, Qingdao, pp. 2499–2504, October 2014.

[50] M. NOMURA, H. IKEJIMA, S. MORITA and E. WATANABE, "Regenerative power control for VVVF motor drive (critical braking method applied to the elevator)," *Proceedings of the IEEE Applied Power Electronics Conference and Exposition*, pp. 95–105, February 1988.

[51] P. KOKOTOVIC and G. SINGH, "Minimum-energy control of a traction motor," *IEEE Transactions on Automatic Control*, vol. 15(6), pp. 92–95, February 1972.

[52] K. INOUE, K. OGATA and T. KATO, "Efficient power regeneration and drive of an induction motor by means of optimal torque derived by the variational method," *Electrical Engineering in Japan*, vol. 173(1), pp. 41–50, October 2010.

[53] K. INOUE, K. KOTERA and T. KATO, "Optimal torque trajectories minimizing loss of induction motor under given condition of rotational angle," *Proceedings of the IEEE Energy Conversion Congress and Exposition*, pp. 1734–1738, September 2011.

[54] K. INOUE, T. KATO and K. KOTERA, "Design methodology of optimal trajectories minimizing loss of induction motor under torque amplitude limit," *Proceedings of the IEEE Workshop on Control and Modeling for Power Electronics*, pp. 1–5, June 2012.

[55] K. INOUE, K. KOTERA and T. KATO, "Optimal motion trajectories minimizing loss of induction motor under amplitude limits," *Proceedings of the IEEE Energy Conversion Congress and Exposition*, pp. 2576–2581, September 2012.

[56] K. INOUE, K. KOTERA, Y. ASANO and T. KATO, "Optimal torque and rotating speed trajectories minimizing energy loss of induction motor under both torque and speed limits," *Proceedings of the IEEE International Conference on Power Electronics and Drive Systems*, pp. 1127–1132, April 2013.

[57] Y. ASANO, K. INOUE, K. KOTERA and T. KATO, "An energy saving drive method of an induction motor with the suppression of sudden acceleration and deceleration," *Proceedings of the IEEE International Power Electronics Conference*, pp. 3872–3876, May 2014.

[58] K. INOUE, Y. ASANO, K. KOTERA and T. KATO, "Optimal energy saving trajectories of induction motor with suppression of sudden acceleration and deceleration," *Proceedings of the IEEE Energy Conversion Congress and Exposition*, pp. 3219–3223, September 2014.

[59] A. S. MURTHY, D. P. MAGEE and D. G. TAYLOR, "Comparison of regenerative braking controllers for permanent magnet synchronous machines," *Proceedings of IEEE International Electric Machines and Drives Conference*, Coeur D'Alene, pp. 884–889, May 2015.

[60] A. S. MURTHY, D. P. MAGEE and D. G. TAYLOR, "Optimal control of regenerative braking for SPM synchronous machines with current feedback," *Proceedings of 2016 IEEE Transportation Electrification Conference and Expo (ITEC)*, Dearborn, MI, pp. 1–6, June 2016.

[61] A. S. MURTHY, D. P. MAGEE and D. G. TAYLOR, "Optimized regenerative braking of induction machines with indirect field-oriented control," *Proceedings of 2016 IEEE Transportation Electrification Conference and Expo (ITEC)*, Dearborn, MI, pp. 1–6, June 2016.

[62] D. G. TAYLOR, "Modeling and Analysis of AC Motor Drive Systems," *ECE 4550 Class Notes*, Georgia Institute of Technology, 2016.

[63] R. GABRIEL, W. LEONHARD, and C. J. NORDBY, "Field-Oriented Control of a Standard AC Motor Using Microprocessors," *IEEE Transactions on Industry Applications*, vol. IA-16(2), pp. 186–192, March 1980.

[64] R. W. DE DONCKER and D. W. NOVOTNY, "The universal field oriented controller," *IEEE Transactions on Industry Applications*, vol. 30(1), pp. 92–100, January 1994.

[65] P. KRAUSE, O. WASYNCZUK, S. SUDHOFF, and S. PEKAREK, *Analysis of Electric Machinery and Drive Systems*, 3rd edition, IEEE Press, 2013.

[66] T. TJAHJOWIDODO, F. AL-BENDER, and H. VAN BRUSSEL, "Friction identification and compensation in a DC motor," *Proceedings of the International Federation of Automatic Control* , vol. 38(1), pp. 554–559, 2005.

[67] F. M. H. KHATER, R. D. LORENZ, D. W. NOVOTNY, and K. TANG, "Selection of Flux Level in Field-Oriented Induction Machine Controllers with Consideration of Magnetic Saturation Effects," *IEEE Transactions on Industry Applications*, vol. IA-23(2), pp. 276–282, March 1987.

[68] I. T. WALLACE, D. W. NOVOTNY, R. D. LORENZ, and D. M. DIVAN, "Increasing the dynamic torque per ampere capability of induction machines," *IEEE Transactions on Industry Applications*, vol. 30(1), pp. 146–153, January 1994.

[69] P. A. IOANNOU and J. SUN, *Robust Adaptive Control*, Prentice-Hall, 1996.

[70] J. LEE, Y. KIM, S. RHYU, I. JUNG, S. CHAI, and J. HONG, "Hysteresis torque analysis of permanent magnet motors using Preisach model," *IEEE Transactions on Magnetics*, vol. 48(2), pp. 935–938, February 2012.

[71] J. H. CHOW and P. KOKOTOVIC, "A decomposition of near-optimum regulators for systems with slow and fast modes," *Proceedings of the IEEE Conference on Decision and Control*, Clearwater, pp. 219–224, December 1976.

[72] P. KOKOTOVIC, H. KHALIL and J. O'REILLY, *Singular Perturbation Methods in Control: Analysis and Design*, Academic Press, 1986.

[73] B. J. DRIESSEN and N. SADEGH, "On the discontinuity of the costates for optimal control problems with Coulomb friction," *Transactions on Optimal Control Applications and Methods*, vol. 22(4), pp. 197–200, July 2001.

[74] J. KIERZENKA and L. F. SHAMPINE, "A BVP Solver based on Residual Control and the MATLAB PSE," *ACM Transactions on Mathematical Software*, vol. 27(3), pp. 299–316, 2001.

[75] L.F. SHAMPINE, I. GLADWELL and S. THOMPSON, *Solving ODEs with MATLAB*, Cambridge University Press, 2003.

[76] D. G. TAYLOR, "Torque-Speed Capability of AC Motor Drive Systems," *ECE 4550 Class Notes*, Georgia Institute of Technology, 2016.

[77] M. F. RAHMAN, L. ZHONE and K. W. LIM, "A DSP based instantaneous torque control strategy for interior permanent magnet synchronous motor drive with wide speed range and reduced torque ripples," *Proceedings of the Thirty-First IEEE Industry Applications Conference*, vol. 1, pp. 518–524, 1996.

[78] J. BONIFACIO and R. KENNEL, "Online maximum torque per ampere control of interior permanent magnet synchronous machines (IPMSM) for automotive applications," *Proceedings of the 8th IET International Conference on Power Electronics, Machines and Drives*, pp. 1–5, 2016.

[79] D. G. TAYLOR, "Homework-3 Solution," *ECE 8803 Class Notes*, Georgia Institute of Technology, 2012.

[80] F. LEWIS, D. VRABIE and V. SYRMOS, *Optimal Control*, John Wiley & Sons, 1995.

VITA

Aravind Samba Murthy was born in Bangalore, India, in 1989. He joined R.V. College of Engineering in 2006 to pursue his Bachelor's degree in Electrical and Electronics Engineering. During his freshman year, he joined a Formula-SAE team called Ashwa Racing and participated in the FSAE-Italy competition in 2009 with the team.

In his senior year, he fell in love with a lovely young lady named Rajatha Bhat and after working together for a year in GE Global Research, they decided to pursue their graduate studies in the United States. He joined Georgia Institute of Technology in the Fall of 2011 to pursue his graduate degrees in Electrical and Computer Engineering. He was elected Chief Engineer of Georgia Tech's Formula-Hybrid team and worked with the team to design, assemble, and test a hybrid-electric racecar. He completed his M.S. degree in May 2013 under the guidance of Prof. David Taylor. He married Rajatha a month later and both of them are pursuing their doctoral degrees in Electrical Engineering at Georgia Tech since then. In 2016, both of them were accepted to the Scheller College of Business at Georgia Tech to pursue their MBA/PhD dual-degrees. During his years of studying, Aravind has worked as a Systems Engineering Intern at Texas Instruments, working on sensorless motor control, regenerative braking control, and parameter identification. Aravind is an IEEE student member since 2015.